UNIVERSITY OF SOUTHAMPTON

FACULTY OF ENGINEERING, SCIENCE & MATHEMATICS
School of Ocean & Earth Science

Upper Ocean Transport Variability in the Subtropical North Atlantic

by

James Alexander Brearley

Thesis for the degree of Doctor of Philosophy

September 2010

UNIVERSITY OF SOUTHAMPTON

ABSTRACT

FACULTY OF ENGINEERING, SCIENCE & MATHEMATICS

SCHOOL OF OCEAN & EARTH SCIENCES

Doctor of Philosophy

UPPER OCEAN TRANSPORT VARIABILITY IN THE SUBTROPICAL NORTH ATLANTIC

By James Alexander Brearley

Many general circulation models predict a reduction in overturning strength in the 21st century as a response to anthropogenic forcing, meaning that novel methods of monitoring individual components of the subtropical North Atlantic circulation are required. This observational study outlines efforts to monitor upper ocean transports near the 36°N latitude line and to identify possible forcing mechanisms. Specifically, an optimal interpolation scheme is employed to synthesise annual and seasonal sections of the Atlantic using *T/S* data from Argo floats and the Line W array from 2002 to 2007. Combining these data with an estimate of the barotropic velocity yields accurate values of the interior geostrophic transport above 1000 dbar. Close to the western boundary, where errors incurred by the scheme are larger, altimetric SSH differences are used to quantify the Gulf Stream transport above 2000 dbar at 10-day resolution. Finally, a detailed analysis of wind stress and wind stress curl fields of the subtropical North Atlantic is used to estimate both the Ekman and Sverdrup transports and to isolate the dominant time and space scales of variability.

The mean zonally integrated interior transport above 1000 dbar between the eastern boundary and the Gulf Stream was -48.0 ± 3.3 Sv, where the error represents the standard error of the seasonal baroclinic transport estimates. The size of the variability between seasons was similar to the interannual variability (standard deviations of 6.6 Sv and 7.7 Sv). Most variability at interannual timescales arises from changes in the density structure of the main thermocline west of 40°W. Neither interannual nor seasonal variability in the interior transport correlate with changes in the Sverdrup transport, though the Sverdrup relation does account for the mean upper ocean transport in the eastern basin. Gulf Stream transport across Line W in the period 2002 to 2008 was estimated to be 87.6 (± 0.8 Sv standard error) in the upper 1000 dbar, with a peak transport in late summer. In line with earlier studies, the seasonal cycle of the transport appears to be correlated with local wind stress curl forcing but determining the precise mechanism requires further theoretical and modelling work.

Contents

List of Figures

List of Tables

DECLARATION OF AUTHORSHIP

I, James Alexander Brearley, declare that the thesis entitled

Upper Ocean Transport Variability in the Subtropical North Atlantic

and the work presented in the thesis are both my own, and have been generated by me as a result of my own original research. I confirm that:

- this work was done wholly or mainly while in candidature for a research degree at this University;
- where any part of this thesis has previously been submitted for a degree of any other qualification at this University or any other institution, this has been clearly stated;
- where I have consulted the published work of others, this is always clearly attributed;
- where I have quoted from the work of others, the source is always given. With the exception of such quotations, this thesis is entirely my own work;
- I have acknowledged all the main sources of help;
- where the thesis is based on work done by myself jointly with others, I have made clear exactly what was done by others and what I have contributed myself;
- none of this work has been published before submission.

Signed:

Date:

Acknowledgements

Firstly, I would like to thank my supervisors Dr Elaine McDonagh, Dr Brian King and Professor Harry Bryden for their enthusiasm and support throughout the course of my PhD. I also acknowledge the help provided by Dr John Toole and Dr Ruth Curry at Woods Hole Oceanographic Institution in making mooring data available to me and discussing the management of the Line W array. I also thank Dr Simon Josey and Dr Lisa Marsh at NOC for speaking informally to me about the processing of wind stress and satellite altimetry data. Finally, I must thank Dr Breck Owens at WHOI for discussing pressure problems on SOLO/FSI Argo floats during my visit in summer 2008.

On a personal level, I thank my office colleagues at NOC, firstly in 166/07 and later in 564/13. Specifically, I express my gratitude to Jill and Jenny who watched me wrestle with MATLAB during my first year. I thank Chris for frequent discussions of wind stress data over tea, Lorna for sharing Argo-related difficulties and John for being such great fun at Ocean Sciences in Portland.

Finally, I am indebted my wonderful wife Sarah, who has shown incredible patience and kindness throughout my PhD and has always fully supported me, even when I have been away from home for many months. Thank you so much.

List of Acronyms and Units

A16	A16 cruise section at 20°W
A20	A20 cruise section at 52°W
A22	A22 cruise section at 66°W
AABW	Antarctic Bottom Water
AAIW	Antarctic Intermediate Water
ACF	Autocorrelation function
ADCP/LADCP/VMADCP	Acoustic Doppler Current Profiler/Lowered ADCP/Vessel Mounted ADCP
APEX	Type of Argo float constructed by Webb Research
CD171	Charles Darwin Cruise 171
CFC	Chlorofluorocarbon
CTD	Conductivity-temperature-depth sensor
dbar	Decibars
DMQC	Delayed mode quality control
DWBC	Deep Western Boundary Current
DT	Absolute dynamic topography (in m)
dyn m.	Dynamic metres
ECMWF	European Centre for Medium-Range Weather Forecasting
EDW	Eighteen Degree Water
EOF	Empirical orthogonal function
FSI	Falmouth Scientific Instruments
GDAC	Global Data Centre
GUSTO	Gulf Stream Observations Mooring

h	Hours
IGY	International Geophysical Year of 1957
Line W	Mooring line between Cape Cod and Bermuda named after Val Worthington
LSW	Labrador Sea Water
MMP	McLane Moored Profiler
MOC/AMOC	Meridional Overturning Circulation/Atlantic Meridional Overturning Circulation
MW	Mediterranean Water
NACW	North Atlantic Central Water
NADW	North Atlantic Deep Water
NAO	North Atlantic Oscillation
NASA	National Aeronautic and Space Administration
NCEP/NCAR	National Center for Environmental Protection/National Center for Atmospheric Research
NOC	National Oceanography Centre Southampton
OI	Optimal Interpolation
PV	Potential vorticity $= f/H$
PW	Petawatts $= 1 \times 10^{15}$ W
QuickSCAT	Quick Scatterometer
RADS	Radar Altimeter Data Service
RAFOS	Type of float. SOFAR (Sound Fixing and Ranging) spelt backwards
RAPID	Mooring array monitoring the MOC at 26.5°N in the Atlantic
RMS	Root mean squared
SBE41	Seabird 41, type of CTD on Argo floats
SNR	Signal-to-noise ratio
SOLO	Type of Argo float manufactured by Falmouth Scientific Instruments
SSHA	Sea surface height anomaly
Sv	Sverdrups

SVD	Singular value decomposition
SYNOP	Synoptic Ocean Prediction Experiment
TOPEX/POSEIDON	First generation satellite altimeter
TW	Terawatt
VACM	Vector averaging current meter
W1/W3	Moorings of the Line W array
WHOI	Woods Hole Oceanographic Institution
WOA	World Ocean Atlas
WOCE	World Ocean Circulation Experiment
WSC	Wind stress curl
XBT	Expendable bathythermograph
YoMaHa	Data product of float velocities. Name is formed by three of the main authors: Yoshinari, Maximenko and Hacker.

List of Symbols

β	North-south gradient in f
$\Delta\Phi$	Geopotential anomaly
η	Noise variance
θ	Potential temperature
ρ	In-situ density
τ	Wind stress
σ_θ	Potential density referenced to the surface
e	Exponential
f	Coriolis parameter
g	Gravitational acceleration (9.81 ms^{-2})
s	Signal variance
S	Salinity
T	Temperature

Chapter 1

Introduction

1.1 Project Motivation

In light of climate change projections suggesting a reduction in the strength of the Meridional Overturning Circulation (MOC) in response to anthropogenic climate change (IPCC, 2007), the importance of direct long-term monitoring of the individual components of the circulation is now widely recognised. The MOC, which moves warm near-surface waters northward towards high latitudes and returns cold, dense waters southward in the deep ocean, transports approximately 1.3 PW (1 PW = 1×10^{15} W) of heat northwards in the subtropical North Atlantic and is responsible for the temperate climate over northwest Europe (Bryden and Imawaki, 2001). Any changes in its size or structure could have significant climatic implications. With the establishment of a long-term monitoring array for the MOC in the Atlantic at 26.5°N, observations from individual cruises many years apart can be evaluated alongside estimates of the intra-annual variability to determine whether any decadal changes are statistically significant (Bryden et al., 2005b; Cunningham et al., 2007). This RAPID array separately quantifies individual components of the overturning including the Gulf Stream, the Ekman Transport, the Deep Western Boundary Current and the zonally integrated mid-ocean transports to provide estimates of the overturning with daily resolution.

In spite of the enormous research effort concentrated at this latitude, our knowledge of MOC variability north of this latitude line remains limited. A large number of individual research programmes have elucidated individual components of the circulation, but full basin-transport estimates have only been achieved from occasional cruise occupations. In particular, there is strong justification for monitoring the individual components of the overturning at 36°N. Current estimates of the meridional heat flux at this latitude differ substantially (Roemmich and Wunsch, 1985; Rintoul and Wunsch, 1991; McDonagh et al., 2010) meaning that the subtropical North Atlantic is either a source or a sink of heat (see Section 1.3). Moreover, the northward mass transport of the Gulf Stream is much stronger here than at 26.5°N due to strong entrainment (Worthington, 1976). Finally, 36°N is the

latitude at which the Mediterranean Outflow Water enters the Atlantic and reaches its level of neutral buoyancy (Iorga and Lozier, 1999), thus contributing to the horizontal density gradient across the basin. Given results suggesting a long-term increase in the size of the gyre circulation (Bryden et al., 2005b) and an accompanying reduction in the overturning component, volume transport variability further north that might affect the size or structure of the mid-ocean transport is of potential importance to understanding the MOC.

This project also provides an opportunity to use temperature, salinity and float displacement measurements from the Argo float programme to examine the year-to-year variability in the upper ocean circulation. The Argo project, started in 2000, has now reached its full array size of 3000 floats. Constructing a time series of volume transports at 36°N with associated uncertainties therefore allows us to make an assessment of the present state of ocean observations in this region and to determine the size of detectable changes. In addition, the mechanisms forcing variability in both Gulf Stream and mid-ocean transports remain unclear. Recent work by DiNezio et al. (2009) has argued that the Florida Current is controlled by wind stress curl changes in the western Atlantic between 28°N and 30°N, but what controls the size and variability of the Gulf Stream and interior flows at 36°N is not known.

The main research question of this thesis is thus:

What is the magnitude of the interannual variability in the geostrophic velocity field of the upper North Atlantic around 36°N *and what mechanisms control this variability?*

In order to answer this overall research question, a number of objectives were set for this thesis, outlined in Section 1.10. However, before moving on to discuss the details of this project, the existing literature is reviewed. Historical perspectives of the large-scale North Atlantic circulation are outlined in Section 1.2, from the earliest qualitative schemes through to the emergence of quantitative transport estimates in the twentieth century. Cruises from the modern hydrographic era at 36°N are discussed in Section 1.3. Important currents and water masses from the section are then discussed in more detail: the Gulf Stream in Section 1.4, the Deep Western Boundary Current in Section 1.5, the Subtropical Mode Water in Section 1.6 and the Mediterranean Outflow in Section 1.7. Recent developments, including the first results from the RAPID mooring array, are discussed in Section 1.8. Literature of the Argo float programme is then reviewed in detail in Section 1.9, specifically covering the operation, quality control procedures and work to date in the subtropical North Atlantic. Finally, the objectives of the project and structure of the remainder of the thesis are outlined in Section 1.10.

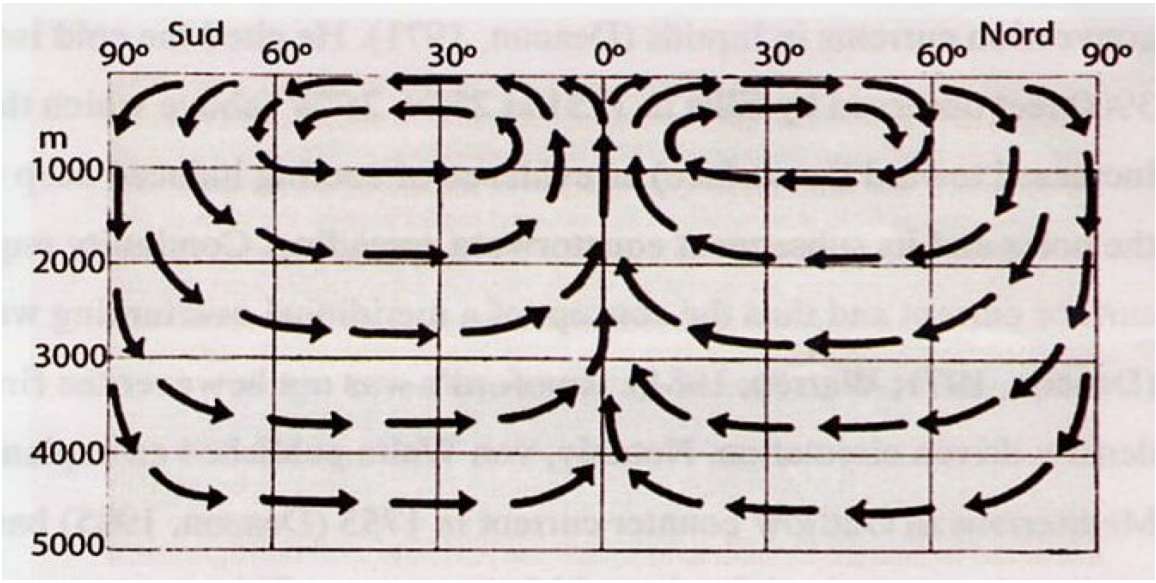

Figure 1.1: The two cell convection scheme proposed by Lenz in 1845. Warm surface currents in both hemispheres are compensated by cold return flows at depth. Upwelling occurs close to the Equator. Image reproduced from Longworth (2007).

1.2 Historical Perspectives on North Atlantic Circulation

For a complete review of circulation schemes related to the meridional overturning, the reader is directed to Longworth (2007) and Richardson (2008), who track the development of models from the early 19th century to the present. In this section, the focus is primarily on those aspects of relevance to the zonal flow structure in the subtropical Atlantic at 36°N.

1.2.1 Qualitative Schemes

Early models characterizing the large-scale circulation of the North Atlantic were largely descriptive in nature. The very first schemes, such as Lenz's (1845) two cell convection model (Figure 1.1), were based on a deduction made by Count Rumford in 1797 that the cold deep ocean water must have been formed in polar regions and then exported equatorwards (Warren, 1981). It was initially assumed that the deep water must then upwell at the Equator, but subsequent observations (e.g. during the *Challenger* expeditions of 1872-1876) confirmed the presence of cross-equatorial flows in the Atlantic.

Later in the 19th century, many of the water masses still used today by physical oceanographers were first documented. For instance, Buchanan (1884) showed that a salinity minimum observed at mid-depth in the Atlantic extended well to the north of the Equator from high southern latitudes. This water mass, termed the Antarctic Intermediate Water (AAIW), is nowadays identified in the western basin of the subtropical North Atlantic by its minimum in CFCs centred around $\theta = 7°C$ (Mémery et al., 2000). Similarly, Buchan (1895) identified a flow of deep water from the North Atlantic to the South Atlantic, later termed the North Atlantic Deep Water (NADW), and formed by deep convection of surface waters during

wintertime. Today it is recognised that this water mass actually comprises three layers: a deep layer of water derived from the Nordic Seas (1.8-3°C) capped by a classical Labrador Sea Water (LSW) layer (3-3.9°C) and an upper LSW layer (3.9-5°C). However, the term NADW remains in common use.

Recognising the importance of these cross-equatorial layers, Brennecke (1911) proposed a scheme in which southward-moving NADW was found between northward moving AAIW above and Antarctic Bottom Water (AABW) below. AABW, found to the west of the Mid-Atlantic Ridge, was identified initially by its very low temperature (less than 1.8°C) and later by its high silicate values. Moreover, high-salinity water originating from the Mediterranean was found in the North Atlantic by Wüst (1935), occupying the 7-12°C temperature range east of the Mid-Atlantic Ridge. A final important water mass of the 36°N section - the 18°C water - was first documented in the 1950s as an isothermal layer with salinity around 36.5 (Worthington, 1959). This water mass forms locally in the region immediately offshore of the Gulf Stream by wintertime convection and is discussed in more detail in Section 1.6.

Whilst most of the water masses recognisable to North Atlantic oceanographers today were thus documented by the early 20th century, purely qualitative schemes were incapable of explaining the horizontal gyre circulation of the subtropical Atlantic. Zonally uniform flows were clearly unrepresentative in light of observations made by *Meteor* showing east-west density gradients, yet Wüst's (1935) scheme continued to focus only on the meridional thermohaline-driven circulation (Figure 1.2). It was not until the application of quantitative methods such as geostrophy that organised currents such as the Gulf Stream could be properly understood.

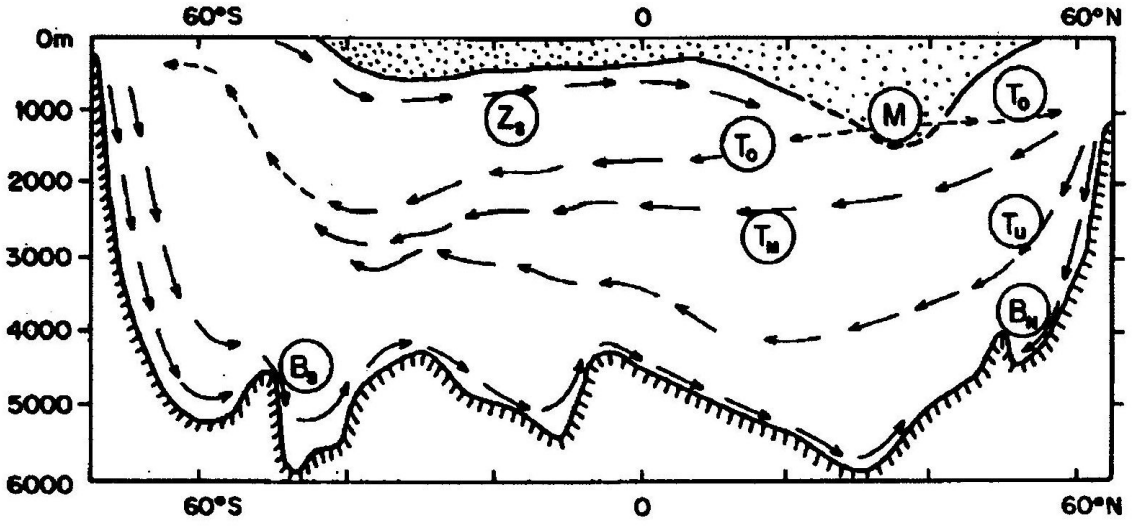

Figure 1.2: Wüst's 1935 scheme showing spreading of water masses in the Atlantic, from Longworth (2007). Z_S is the Subantarctic Intermediate Water; $B_{S(N)}$ is Bottom Water from South (North); T_O is Upper NADW; T_M is middle NADW; T_U is Lower NADW; M is the Mediterranean influence. The stippled area is Wüst's warm water sphere.

1.2.2 Quantitative Circulation Schemes

The development of the geostrophic method, which states that ocean velocities can be determined by the balance between the pressure gradient force and the Coriolis force, was instrumental to the development of our understanding of the horizontal ocean circulation. An early application of the method to the subtropical North Atlantic was by Jacobsen (1929), using data from the *Dana* expedition of 1920-22. He found a strong Gulf Stream-North Atlantic Current along the western boundary with a horizontal return flow across the rest of the basin (which was intensified around 70°W), known now as the subtropical gyre. Further investigation of the density field by Defant (1941) extended the analysis down to 2000 m. The map he produced clearly showed water moving southwards out of the Labrador Sea at 2000 m close to the western boundary, as well as the anticyclonic subtropical gyre and cyclonic subpolar circulation at shallower depths. *The Oceans*, published by Sverdrup a year later, suggested the three separate sources for the deep water in the North Atlantic; one from the Labrador Sea, one from the Iceland-Greenland Sea and one from the Mediterranean Outflow, contributing to a total overturning circulation of 6 Sv (1 Sv $= 1 \times 10^6$ m^{3}s^{-1}).

A further major breakthrough in understanding the near-surface circulation was made with the development of physical theories relating ocean transport to wind stress at the surface. Whilst Ekman theory had been developed early in the 20th century, the concept of Sverdrup transport (Sverdrup, 1947) explicitly stated that the total ocean mass transport could be calculated from the curl of the wind stress divided by the latitudinal gradient in the Coriolis parameter:

$$M_y = \frac{curl_z \tau_\eta}{\beta} \tag{1.1}$$

where M_y is the northward mass transport, $curl_z \tau_\eta = \frac{d\tau_y}{dx} - \frac{d\tau_x}{dy}$ is the wind stress curl and β is the meridional gradient in the Coriolis parameter.

Further contributions from Stommel (1948) and Munk (1950) explained the physics behind western boundary current intensification and gyre circulations. Crucially, Munk obtained an analytical solution for the mass streamfunction ψ in terms of the ocean dimensions, the Coriolis parameter and the latitudinal pattern of zonal wind stress (for simplicity he excluded meridional stresses). His solution for the Pacific (Figure 1.3) showed that the vanishing of zonal wind stress curl at certain latitudes broke the horizontal circulation up into separate subtropical and subpolar gyres.

By the late 1950s, the modern circulation scheme of the Atlantic accepted today was being quantified and formalized. In 1958, Stommel's seminal text *The Gulf Stream* was published, in which he illustrated the increasing transport of the Gulf Stream as it travels between the Florida Straits and Cape Hatteras (see Section 1.4). The offshore deflection at 36°N was also noted, as was the separation of the Gulf Stream into a mid-ocean gyre component and a northeastward-moving North Atlantic Current. He also proposed a stronger overturning

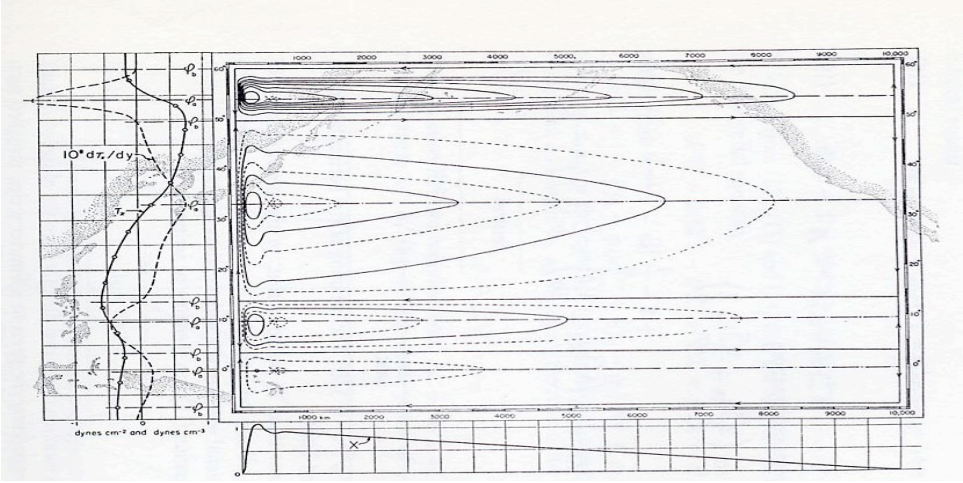

Figure 1.3: The mean annual wind stress τ_x and its meridional gradient across the Pacific (left). Mass transport streamlines (right) are calculated according to Munk's equation and plotted at 10 Sv intervals. The y axis represents latitude. Figure from Munk (1950).

circulation of between 15 and 25 Sv.

Debate over the Atlantic overturning strength continued until the 1970s, with Worthington (1976) suggesting a value of 7 Sv based upon a deep level of no motion, and Stommel (1958) reporting a stronger value of 15 Sv with a shallower reference level. However, Worthington's estimate was soon shown to be physically implausible, as it needed to violate geostrophy in order to conserve heat and salt. Furthermore, Swallow and Worthington (1961) tracked deep floats moving southwards at 33°N, 75.5°W, and found the accompanying hydrographic section to have isobaric slopes which suggested a level of no motion at around 1500 m.

The development of inverse methods at the end of the 1970s, which involve taking an initial estimate of the circulation and adjusting the solution to satisfy various constraints (e.g. mass and salt conservation) confirmed that a vigorous overturning was more realistic (Wunsch, 1978). By the end of the decade, Roemmich (1980) estimated that mass could be conserved to within $\pm 1 - 2$ Sv between two transatlantic sections without requiring large changes to the initial velocity field. However, later analyses (e.g. by Ganachaud (2003)) have argued that a looser mass constraint is more realistic (± 8 Sv in one-time hydrographic sections). Specifically, the presence of internal waves was found to introduce at least 3 Sv of uncertainty into midlatitude transport estimates. The use of inverse methods has continued to the present day, with Lumpkin and Speer (2007) deriving a global circulation scheme based on 18 individual boxes and 45 isopycnal layers (Figure 1.4).

1.3 Modern Hydrographic Cruises

In parallel with the development of theory for the wind-driven circulation and the quantification of the overturning circulation, the first full-width hydrographic sections of the North Atlantic were completed. Taken as part of the 1957 International Geophysical Year (IGY),

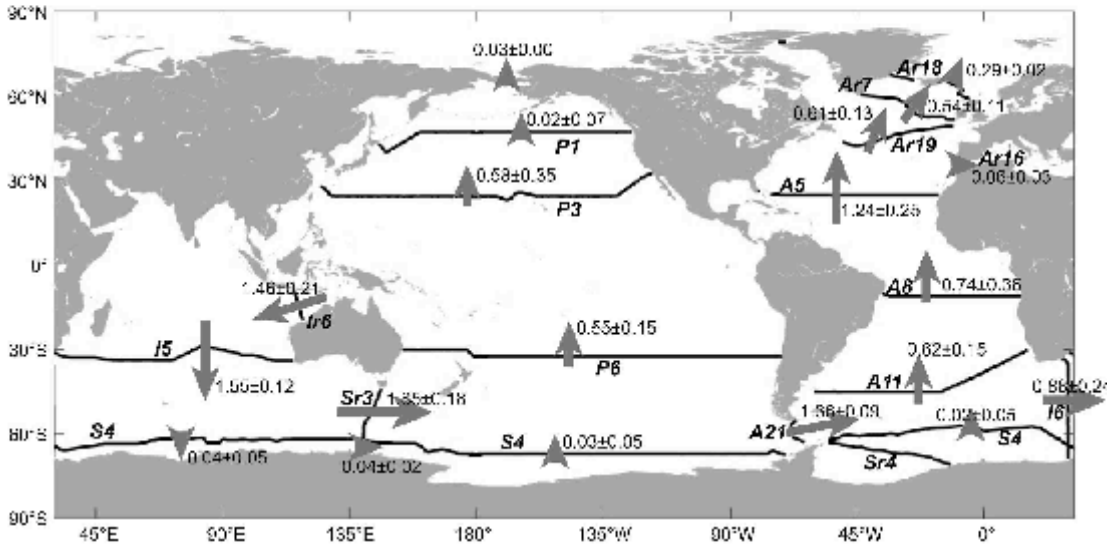

Figure 1.4: The configuration of the inverse box model used by Lumpkin to estimate global meridional overturning. 25 World Ocean Circulation Experiment sections form 18 boxes in which various properties are conserved. Heat transports are in PW. Figure from Lumpkin and Speer (2007).

sections were obtained along 24°N, 36°N and 48°N. Although these cruises provided important information of the cross-basin temperature and salinity structure (Fuglister, 1960), their significance for directly calculating consistent volume and heat transports only became apparent after the development of inverse methods. Roemmich (1980) was the first to reconsider these sections in order to estimate the range of meridional heat flux. Using a combination of mass and salt conservation along isopycnals, along with a 30 Sv Florida Straits transport, he obtained best estimates of heat transport of 1.2 PW at 24°N and 0.8 PW at 36°N.

Refinements of these estimates took place following the 1981 reoccupation of the 24°N and 36°N sections by *Atlantis II* as part of the *Long Lines* project. Using data from both 1959 and 1981, Roemmich and Wunsch (1985) used a series of models of increasing complexity to deduce the meridional flow field and produce a dynamically consistent circulation at both latitudes. The zonally integrated geostrophic transport per unit depth profile is given in Figure 1.5 for both the 1959 and 1981 sections, revealing the velocity structure of the overturning. Northward flowing surface and intermediate waters dominate above 1300 m, whilst southward flows occur between 1300 m and 4500 m, divided into two lobes. The shallower lobe, with its core around 2000 m, originates in the Labrador Sea whilst the deeper lobe is made up of Norwegian and Greenland Seas water. Below 4500 m a lobe of northward-flowing Antarctic Bottom Water can be identified. The mean magnitudes of the transports were estimated at 11.3 $\pm$ 3.2 Sv for the surface layer, -5.8 $\pm$ 0.7 Sv for the intermediate water, -19.9 $\pm$ 4.7 Sv for deep water and 2.9 $\pm$ 2.6 Sv for the bottom water. Through having access to two cruises (albeit separated by 24 years), Roemmich and Wunsch (1985) were also able to perform the first study of the changes in layer transports

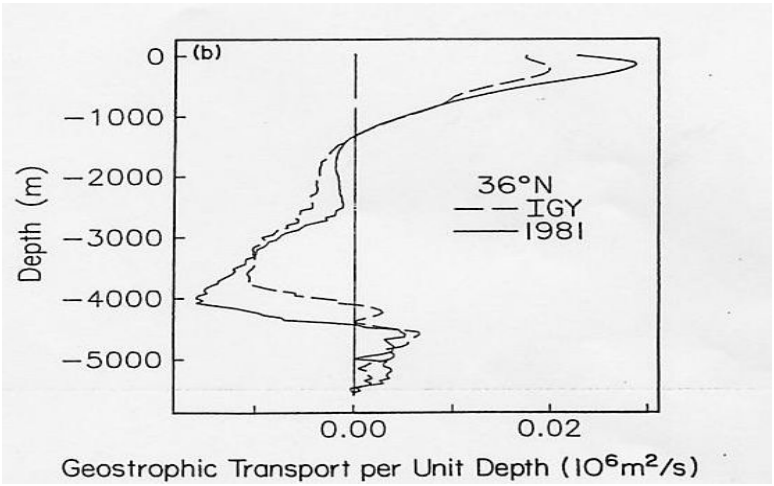

Figure 1.5: Zonally integrated geostrophic transport per unit depth for 36°N sections taken during 1959 and 1981. Positive values represent northward flow. Figure reproduced from Roemmich and Wunsch (1985).

between 1957 and 1981. There was a reduction in Labrador Sea water transport of 3.1 Sv, accompanied by an increase of 6.8 Sv in the lower North Atlantic Deep Water.

More complex models were able to reveal the zonal structure of these flows (Figure 1.6). The Gulf Stream is concentrated on the western side of the section in the upper 1400 m, with southward recirculation extending across the entire width of the ocean, although it is deepest and strongest west of 40°W. The southward flowing deep western boundary current (DWBC) is also present adjacent to the Gulf Stream. Below and slightly to the east of this southward velocity maximum, the northward flowing Antarctic Bottom Water can be identified. Around the same time, the two sets of cruises were also used to estimate the heat storage change of the subtropical Atlantic between 1957 and 1981. Roemmich and Wunsch (1984) found an increase in the overall heat content of the 700 to 3000 m layer with a maximum temperature difference of 0.2°C. However, at depths shallower than 700 m, cooling was observed.

A further reappraisal of the data was published when Rintoul and Wunsch (1991) used an alternative inverse model that incorporated observations of oxygen and nutrients. They made different choices to the earlier analysis, most notably by having a deeper reference level, as they argued that Rintoul and Wunsch's was too shallow to conserve silicate correctly. Furthermore, they suggested that Roemmich and Wunsch's Gulf Stream transport (26 Sv) was too weak, given that several directly estimated literature values put the value nearer 80 Sv (further details in Section 1.4). Richardson and Knuass (1971), using three transport floats, had estimated the strength at 36°N to be 63 Sv, whilst Richardson (1985), using a combination of surface drifters, floats and current meters calculated the mean flow to be 93 Sv. Halkin and Rossby (1985), employing the Pegasus instrument at 73°W, estimated a total Gulf Stream flow of 87.8 ± 17.3 Sv. The Rintoul and Wunsch estimate of 84 Sv thus appeared more realistic.

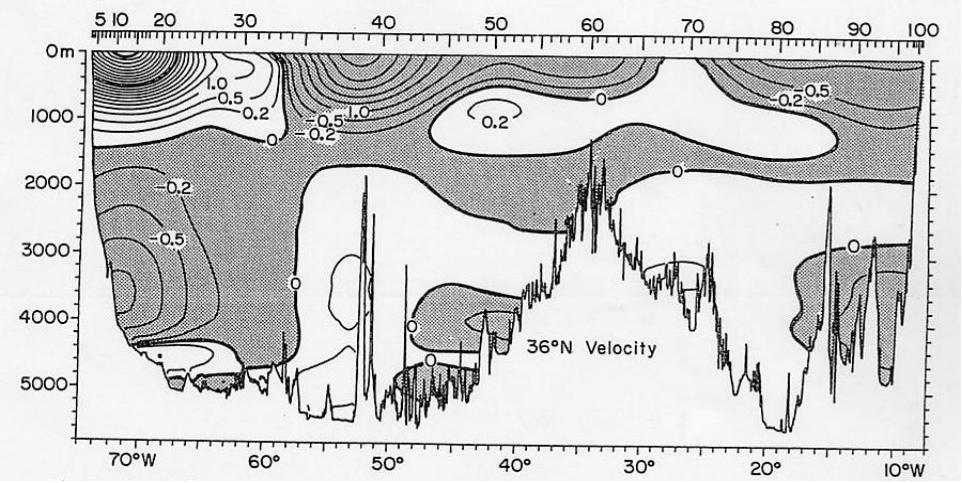

Figure 1.6: Horizontally smoothed geostrophic velocity (in cms^{-1}) at 36°N from 1981 data, based on the reference level calculation with constraints on total transport only. Southward velocities are shaded. Figure reproduced from Roemmich and Wunsch (1985).

However, the most fundamental difference in results was in the heat flux estimates. Whilst Roemmich and Wunsch (1985) had suggested a convergence of heat between the two latitudes, Rintoul and Wunsch (1991) calculated that the poleward heat flux at 36°N was actually 1.3 PW. The estimate at 24°N remained unchanged at 1.2 PW. It was suggested that the reason for the differing values was that Roemmich and Wunsch's original analysis smoothed out a southward-moving Gulf Stream ring, although it has recently been argued that the error actually occurred through over-smoothing of the entire Gulf Stream (McDonagh, personal communication, 2010). The fact that Rintoul and Wunsch's result suggested divergence of heat between 24°N and 36°N raised important questions about the role of the subtropical oceans in the climate system. Some analyses (e.g. Trenberth and Caron (2001)) maintain that ocean heat transport peaks in the tropics and declines rapidly with latitude (consistent with Roemmich and Wunsch's findings) whilst air-sea flux climatologies tend to place the maximum poleward heat flux in the subtropics (supporting Rintoul and Wunsch's interpretation).

A complete repeat of the 36°N section was not obtained during the World Ocean Circulation Experiment (WOCE) (Wunsch, 2002), although hydrographic cruises were conducted at 24°N during 1992 and 1998 as part of the Ocean Atmosphere Carbon Exchange Program (OACES). Despite the lack of new data during the 1990s at 36°N, other WOCE cruises (A20 and A22 along 52°W and 66°W) produced useful results. Joyce et al. (1999), for instance, found that the temperature and salinity of waters above the Antarctic Intermediate Water at 1000 m had increased between 20°N and 35°N. The study also suggested there had been a cooling and freshening of the Labrador Sea Water between 1981 and 1997.

The need to resolve many of the uncertainties in the hydrography, heat transport and nutrient budgets at 36°N led to the establishment of the 36°N consortium, which included a new occupation of the section in 2005. This is discussed in detail in Section 1.8.

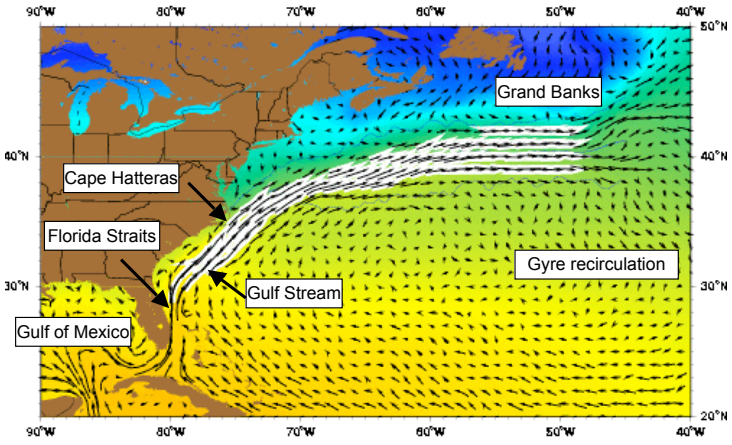

Figure 1.7: The Gulf Stream as represented by the Mariano Global Surface Velocity Analysis (MGSVA). Figure adapted from Ocean Surface Currents pages of Rosentiel School of Marine and Atmospheric Sciences website (`http://oceancurrents.rsmas.miami.edu/atlantic/gulf-stream.html`).

1.4 The Gulf Stream

Forming the largest individual component of the meridional transport across the 36°N section, the Gulf Stream has also received by far the most observational attention. From the Gulf of Mexico, the current moves northeastward through Florida Straits and follows the eastern seaboard of the United States before moving offshore at Cape Hatteras, eventually passing the Grand Banks and forming the North Atlantic Current which separates the subtropical and subpolar gyres (Figure 1.7). Along this path, considerable variation is observed in both the overall transport and structure of the current, which is summarised briefly below.

Historical studies of the Gulf Stream within Florida Straits suggested that the mean transport there is close to 30 Sv (Schmitz and Richardson, 1968; Niiler and Richardson, 1973), a result later confirmed by long-term observations using a calibrated submarine cable (Baringer and Larsen, 2001) that now forms part of the RAPID MOC monitoring array at 26°N. Nevertheless, substantial seasonal variability is observed from this mean figure, with Baringer and Larsen (2001) finding a 3.5 Sv annual cycle with a maximum in July, based on 16 years of data. Moreover, Schott et al. (1988), using repeated moored arrays across the current near 27°N, found the annual cycle to have an asymmetric shape with a broad maximum in spring and summer and a sharp drop-off in transport during the autumn. Recent work has attempted to correlate this variability with external forcing such as the wind stress and indirectly to the phase of the North Atlantic Oscillation, the largest mode of atmospheric variability in the North Atlantic (Baringer and Larsen, 2001; DiNezio et al., 2009).

Between Florida Straits and Cape Hatteras, both the transport and width of the Gulf Stream increase dramatically. Richardson et al. (1969) observed transport increasing from 29.6 Sv near the Florida Keys to 53 Sv off Cape Fear at 34°N, with an accompanying increase in both width and depth of the current. This transport addition was found to be uniform in

depth. Later work by Leaman et al. (1989) confirmed a three-fold increase in transport between the Straits and Cape Hatteras, reaching 93.7 Sv. The strong increase in transport by Cape Hatteras was confirmed by Halkin and Rossby (1985), who estimated a total Gulf Stream flow of 87.8 ± 17.3 Sv above 2000 dbar at 73°W from 16 sections of temperature and velocity obtained using the Pegasus Instrument between 1980 and 1983. Interestingly, the annual cycle they observed had a maximum in April which does not concur with the summertime maximum observed in the Florida Current. Nevertheless, temporal aliasing on such a short time series is likely to be strong so it could not be demonstrated unreservedly that the seasonal cycle is different at this latitude.

Cape Hatteras is an important location in the dynamics of the western boundary current. It is here that the Gulf Stream moves offshore (Richardson and Knuass, 1971), reaching at least 2000 m in depth. This means that the Deep Western Boundary Current, flowing southwards along the continental slope and carrying deep water formed in the Labrador and Norwegian Seas, must cross under the Gulf Stream at this location. Richardson's early schematic had two deep southward flowing layers positioned between the northward flowing Gulf Stream along the continental slope. However, he recognised that in such a strongly sheared region this layered picture was likely to be inadequate and that entrainment and mixing of Labrador Sea Water in the Gulf Stream was inevitable. This was confirmed by Pickart and Smethie (1993), using hydrographic data from a 1990 survey, who found the shallowest layer of the DWBC (500 m to 1200 m) was completely entrained by the Gulf Stream, whilst the deeper 2500 m to 3500 m layer originating in the Nordic Seas underwent very little recirculation. A more recent survey using RAFOS floats (Bower and Hunt, 2000), found that the amount of entrainment of the Labrador Sea Water was heavily dependent on the meandering of the Gulf Stream. With the Stream close to its mean position, upper NADW parcels tended to travel along its northern edge, whilst with a meander trough close to the position of entrainment, DWBC parcels could be expelled to the south. Floats deployed in the Nordic Seas water either move directly beneath the Gulf Stream or exhibit eddy motion before moving into the interior of the Stream, depending on their exact entrainment location. Modelling studies (e.g. Spall (1996)) have confirmed these results.

Downstream of Cape Hatteras, further changes occur in the strength and structure of the Gulf Stream. The transport increases at a rate of roughly 8 Sv per 100 km, reaching 113 ± 8 Sv near 68°W (Johns et al., 1995) and 150 Sv at 55°W (Hogg, 1992), with most of the increases being barotropic in nature. These increases are thought to be due primarily to deep recirculation cells that occur on both sides of the current. To the north of the Gulf Stream and west of the New England Seamounts, Hogg et al. (1986) observed 40 Sv of transport flowing westward between 500 m and the bottom, of which 20 Sv recirculates back to the east, augmenting the lower layers of the Gulf Stream. To the south of the Gulf Stream, a strong recirculation occurs in the 'Worthington Gyre' (Worthington, 1976), which Hogg (1992) observed to extend as far west as 70°W. This recirculation feature is clearly visible in both the 1981 and 2005 cruise sections at 36°N and is at least as important as the northern gyre in supplementing the Gulf Stream transport. Another notable feature of the

Gulf Stream north of Cape Hatteras is the intensification of meandering, with both the size and number of Gulf Stream rings increasing, eventually branching into numerous fronts to the east of the Grand Banks. On average, 22 warm-core rings and 35 cold-core rings are shed by the current each year (Hogg and Johns, 1995), with an example of the latter seen in the 2005 section close to 64°W.

Whilst several short-term measurement efforts of the Gulf Stream have been conducted close to the 36°N latitude line, including the SYNOP and Pegasus lines already discussed at 68°W and 73°W respectively, long-term monitoring of the Gulf Stream akin to that conducted in the Florida Straits has not been achieved. ADCP and XBT data from the container vessel *Oleander* has been used to monitor the upper part of the Stream between 1992 and the present (Rossby et al., 2005) on a weekly basis but this only covers at most the top 800 m of the Stream. In addition, the Line W array close to 68°W, whilst primarily designed to monitor the Deep Western Boundary Current, does provide twice yearly CTD/LADCP cruise sections across the Gulf Stream from 2003 to the present. In this study, these cruise data are combined with satellite data from the JASON altimeter to estimate the Gulf Stream transport near 68.5°W every 10 days from 2002 to 2008.

1.5 The Deep Western Boundary Current

Whilst depth restrictions of the Argo data mean that the volume transport of the DWBC is not explicitly studied in this thesis, a brief discussion of its structure and dynamics in the northern subtropical Atlantic is warranted for completeness. Being the lower limb of the MOC, it flows southwards from the deep water formation regions in the Labrador and Norwegian Seas, turning southwestward near the Grand Banks of Newfoundland before crossing the Gulf Stream at Cape Hatteras (Section 1.4). As the current flows through the North Atlantic, both the volume transport and properties of the current change significantly. For instance, Pickart and Smethie (1998), based on four cruise sections, estimated the total transport of the Labrador Sea Water and Iceland and Denmark Strait Overflow Water at 55°W to be -18.9 $\pm$ 6.3 Sv, with the current located over sloping bathymetry at 2000 to 4000 m. South of the Gulf Stream crossover near Cape Hatteras, the situation is different, with a much stronger DWBC estimated by Leaman and Harris (1990) to be -34.8 ± 14.5 Sv at 26.5°N. However, this latter estimate is probably not representative of the throughflow of deep water, as up to 15 Sv of flow may result from recirculation. Furthermore, other estimates close to this location (Lumpkin and Speer, 2003; Cunningham et al., 2007) have suggested much smaller values (between -17.6 and -18.5 Sv).

In our study region close to 70°W, several features of the DWBC are worthy of discussion. Joyce et al. (2005), using data from eight cruises occupied along Line W between 1994 and 2003, estimated the total flow at -16.5$\pm$2.5 Sv, with the flow being situated between 2500 to 4000 m. The deployment of the Line W mooring array along this line in 2004 has provided a 4 year time series of Deep Western Boundary Current measurement, with a mean transport

of −25.1 Sv (Toole et al., 2010). Interestingly, these surveys all argue that the DWBC remains the primary export pathway for LSW into the North Atlantic, in contrast to recent work by Bower et al. (2009) that suggested that much of the LSW is actually exported into the interior of the North Atlantic.

1.6 The Eighteen Degree Water

Moving east of the Gulf Stream along the 36°N section, one encounters the horizontal recirculation of the subtropical gyre (Figure 1.7). The western part of the gyre is the formation region for the North Atlantic Subtropical Mode Water, known colloquially as the 18-degree water (EDW) mentioned previously in Section 1.2.1. Subtropical mode waters, formed offshore and equatorward of western boundary currents, are found in all major oceans, and the EDW is a dominant feature of the hydrography of the subtropical North Atlantic. Occurring throughout a 200 m thick layer, it is characterised by temperatures of 17.6°C to 18.2°C and salinities between 36.4 and 36.6. Knowledge of the mechanisms and volume of formation have improved significantly since the 18°C thermostad was first documented by Worthington in 1959. Klein and Hogg (1996), using a time series from moored sensors in the eastern Sargasso Sea, found that the subtropical mode waters produced in the 1980s were warmer and saltier than those observed in the 1950s. Wintertime convection is known to be responsible for forming the deep mixed layers associated with the EDW, but Klein and Hogg (1996) found that although cold conditions prevailed in 1988, large volumes of EDW were not incorporated into the gyre due to advection moving the mixed layer eastwards. Both the buoyancy forcing and the prevailing ocean currents are therefore important in determining the thickness and properties of the subtropical mode water.

Long term studies of EDW formation have been carried out by Alfutis and Cornillon (2001) and Kwon and Riser (2004). Using a large number of expendable bathythermograph (XBT) measurements from 1968-1988, Alfutis and Cornillon (2001) found that basin-wide renewal of the NASTMW took place in the winters of 1969, 1970, 1977, 1978, 1981 and 1985, whilst localised convection to the east of 55°W occurred in the other years. Kwon and Riser (2004), using temperature measurements from 1961-2000, found a strong interannual to decadal variability in the volume of EDW produced. Furthermore, a strong negative correlation between EDW temperature and volume was uncovered, suggesting that active EDW formation years have more and colder EDW because the newly formed water is colder than residuals from previous years. From these studies, it is possible that year-to-year differences in the volume and temperature of EDW could have important implications for the size of the inferred interior transports (Chapter 3).

1.7 The Mediterranean Outflow

Another prominent feature of the 36°N section, this time to the east of the Mid-Atlantic Ridge, is the large salinity maximum found in the lower thermocline and centred around 1200 m depth. This high salinity tongue, formed by the outflow of dense Mediterranean Water down the continental slope from the Strait of Gibraltar, was originally observed by Carpenter and Jeffreys (1870) on a cruise aboard *HMS Porcupine*. The outflow is also relatively warm, depressing the 8°C isotherm from a typical depth of 500 m to about 1500 m (Käse and Zenk, 1996). Its total volume transport is estimated at −0.68 Sv (Bryden et al., 1994).

The spatial structure of the outflow as it descends into the Gulf of Cadiz has been documented for several decades, with Wüst (1935) identifying three distinct tongues: one near the Canary Islands, one along 36°N and one directed northwards. In addition to these advective pathways, the discovery of meddies – anticyclonically rotating lenses containing Mediterranean Overflow Water surrounded by other water masses – encouraged further investigation into the dynamics of the overflow (Armi and Stommel, 1983). Specifically, the long lifetime of these features (over two years) provides an alternative mechanism of heat and salt transport into the eastern basin and is therefore of relevance to basin-wide transport estimates of these quantities.

Recently, Álvarez et al. (2005) have attempted to quantify the rate of Mediterranean Water (MW) formation. It is estimated that 2.7 ± 0.2 Sv of MW are formed in the North Atlantic, which includes the entrainment of 0.2 Sv of North Atlantic Central Water, the main thermocline water of the region. Most of this water is advected northwards, with roughly 0.5 Sv exported into the eastern subtropical North Atlantic. Despite the relatively modest contribution to the total volume budget of the North Atlantic, it has been postulated that the Mediterranean Water is a major component of the warm inflow to the Nordic Seas (Reid, 1979). However, uncertainty remains as to whether the MW is advected directly to the Greenland-Scotland Sill or whether it reaches the Nordic Seas by first mixing with the North Atlantic Current (Lozier et al., 1995). A recent paper by (McCartney and Mauritzen, 2001) argues that there is no direct undercurrent moving the Mediterranean Overflow into the Nordic Seas, with the MW instead being discharged into the interior of the subtropical gyre. Questions also remain over the extent of westward penetration of the MW within the basin, with most results now suggesting it is limited to the Tagus Basin (Iorga and Lozier, 1999) east of 20°W. Understanding the nature and dynamics of this overflow is potentially important to understanding the size and variability of the horizontal gyre circulation. As the MW is found at the eastern end of the section, changes in the density structure on a seasonal or interannual basis would affect the size of the zonally integrated transports.

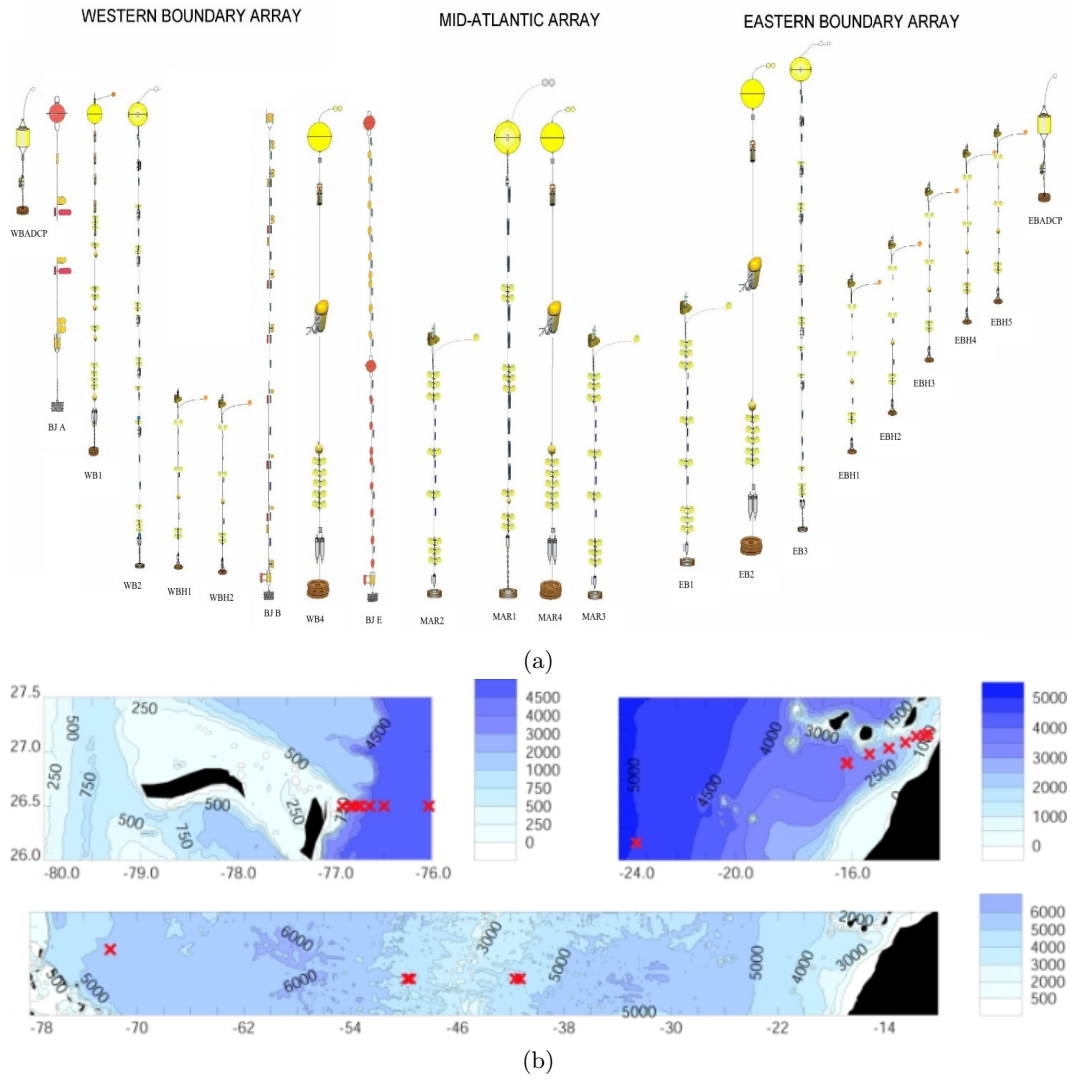

Figure 1.8: Diagrams showing (a) the configuration and (b) the position of the RAPID mooring array at 26.5°N. Figures from Rayner and Cunningham (2005).

1.8 Recent Developments

Two important developments in recent years have improved our understanding of both the overturning and gyre circulations in the subtropical North Atlantic. Firstly, the deployment of the RAPID mooring array (Figure 1.8) means that daily real-time mean estimates for each component of the MOC at 26.5°N are now available. Initial findings suggest that each of the overturning estimates from the five years (1957, 1981, 1992, 1998, 2004) used in Bryden et al.'s (2005) study fall within the subannual variability observed during 2004 by RAPID (Figure 1.9). One surprising feature observed in the first year of RAPID was the large variability in the interior transport (Cunningham et al., 2007). This has been attributed in part to the propagation of transport anomalies from east to west by Rossby waves (Hirschi and Marotzke, 2007).

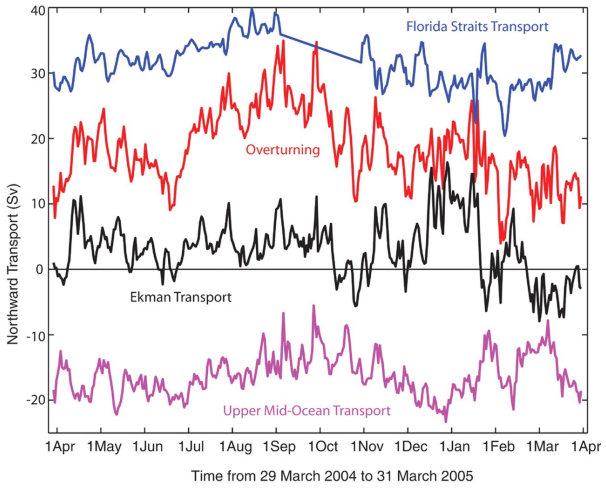

Figure 1.9: Daily time series of Florida Straits transport (blue), Ekman transport (black), upper mid-ocean transport (magenta) and overturning transport (red) for the period 29 March 2004 to 31 March 2005 from the RAPID array. Overturning transport is the sum of the Florida Straits, Ekman, and upper mid-ocean transports and represents the maximum northward transport of upper-layer waters on each day. Figure from Cunningham et al. (2007).

The second advance in understanding, of more direct applicability to 36°N, was the 2005 occupation of the section by R.R.S. *Charles Darwin*. As part of the 36°N Consortium Project, this cruise had a number of aims including resolving the heat budget uncertainties and investigating carbon uptake and nutrient cycling. In total, 144 full depth stations were taken on CD171, in order to resolve mesoscale features, with CTD and ADCP measurements obtained at each location.

Work is still continuing on the interpretation of these data, but early results are now published. Leadbetter et al. (2007) performed the heat content analysis for the section. Examining the temperature fields from 1959, 1981 and 2005, they found that much of the observed heat content increase noted in the mid-depth waters between 1959 and 1981 (Roemmich and Wunsch, 1984) had been reversed by 2005. Indeed, they found an overall reduction in heat content between 800 m and 2500 m, accompanying an increase in heat content of the uppermost 800 m. The pattern was most pronounced in the western portion of the section. Two mechanisms were proposed to explain the temporal variability in ocean heat content. In the upper waters, it was suggested that changes were caused by the vertical displacement of isopycnals, which were uplifted between 1959 and 1981 before sinking in the period between 1981 and 2005. This displacement may have been caused by a change in wind forcing associated with the phases of the North Atlantic Oscillation, with negative NAO (1959-1981) producing strong wind stress leading to a weakening in Ekman downwelling. Conversely, the predominantly positive NAO between 1981 and 2005 caused weaker wind stress and a resulting increase in Ekman downwelling. In the mid-ocean waters, a different mechanism was proposed. In both the Labrador Sea Water and Mediterranean Water, compensating changes in temperature and salinity took place, so that the water masses became warmer

and saltier between 1959 and 1981, thus preserving their density. Cooling and freshening then occurred between 1981 and 2005.

Hydrographic efforts have focused on producing a consistent circulation scheme using inverse methods in order to estimate the meridional heat flux (McDonagh et al., 2010). The principal constraints employed have been zero net volume flux, a Gulf Stream of 87.8±17.3 Sv (Halkin and Rossby, 1985) and transport in the eastern basin below $\theta = 2.05°C$ of 0.3 Sv northwards. Net northward flow was found above 1170 m, with a Gulf Stream solution transport above 2000 m of 67.2 Sv and a cumulated east to west interior transport above 2000 m of around 70 Sv (their Figure 9). The revised heat flux was 1.14± 0.12 PW, comprising an overturning component of 0.75 PW and a horizontal component of 0.39 PW. These estimates are in line with the value proposed by Rintoul and Wunsch (1991) and higher than the 0.8 PW proposed by Roemmich and Wunsch (1985) and the 0.86 PW proposed by Talley (2003). Air-sea flux climatologies that suggest heat transport peaks at 30 to 35°N are thus supported by the results of this inverse solution.

Whilst this inverse modelling has provided a physically consistent mean velocity field for the section, a need still exists for high frequency monitoring of the individual transport components of this section. The Argo float array, discussed in detail in the following section, provides an opportunity to use existing technology to deduce circulation variability in the upper 2000 m at both seasonal and interannual timescales.

1.9 The Argo Programme

Since 2000, a network of free-floating autonomous profiling floats has been deployed throughout the ice-free world ocean. As of 14th May 2010, 3255 Argo platforms were operational, with the aim of cataloguing the temperature and salinity structure of the middle and upper ocean and the velocity field at mid-depth. The motivation for Argo arose from the lack of sustained and systematic temperature and salinity measurements and the consequent sparsity of data for validating climate models or for use in data assimilation schemes. The target array size of 3000 floats at a nominal 3° x 3° spatial resolution was reached on 31st October 2007, with these floats profiling from as deep as 2000 dbar up to the surface every 10 days. In Section 1.9.1, the operational cycle of an Argo platform is described, before a discussion of the quality control procedures performed on Argo data in Section 1.9.2. Problems with Argo pressure sensors are addressed, whilst challenges with the use of Argo data for performing geostrophic calculations are outlined in Section 1.9.3. Results of relevance to our work in the North Atlantic using Argo data are discussed in Section 1.9.4.

1.9.1 Argo Operation

For a more extensive review of Argo operation, the interested reader should refer to Roemmich et al. (1998). Presented here is a brief overview of the features pertinent to this

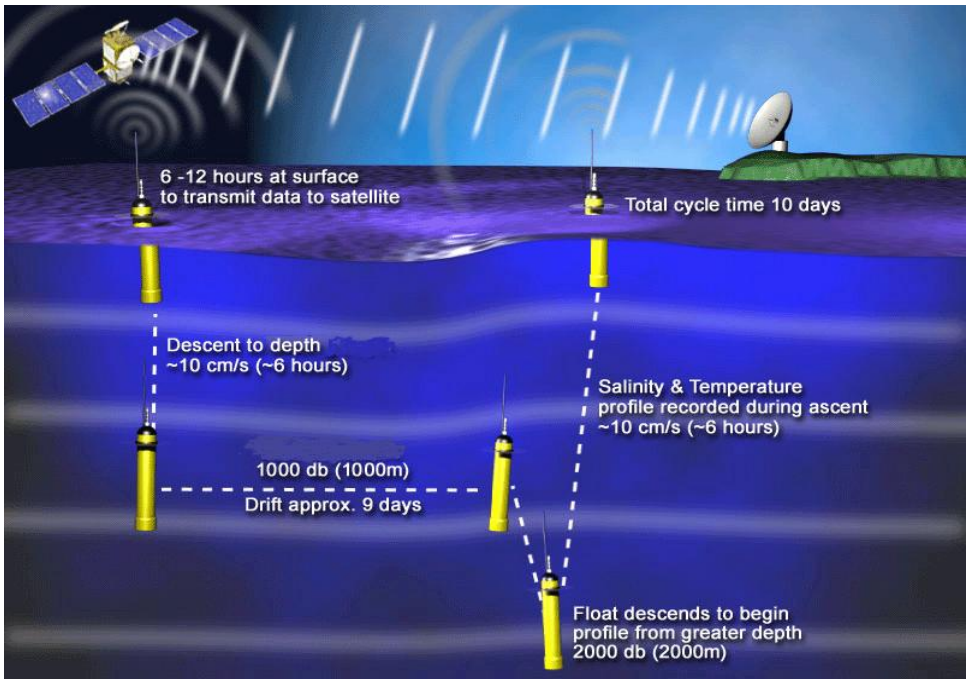

Figure 1.10: Schematic to show the typical cycle of an Argo float on a typical park and profile mission. Image reproduced from `www.argo.ucsd.edu`. Other mission types are used but this is now the most common.

project.

Argo floats on a typical 'park and profile' mission (Figure 1.10) drift freely at a predetermined parking pressure (generally 1000 dbar) for 9 days. After this time, they decrease the volume of a hydraulic bladder and descend to 2000 dbar. The bladder is then re-inflated, causing the float to ascend slowly to the sea surface over a period of ∼6 hours. During the ascent, the onboard sensor suite measures temperature and conductivity at around 70 pressure levels. On reaching the surface, the profile data is transmitted by the Argos system to one of four low-orbiting satellites. The position of the float is calculated from the Doppler shift on the transmitted signals, yielding an accuracy of between 100 and 1000 m. In total, data transmission takes between 6 and 12 hours. After transmission, the bladder decreases in volume and the float descends back to the parking pressure in ∼6 hours. Once transmission through the Argos system is complete, the data is received by the relevant national data centre that manages the particular Argo float. Within 24 hours, the data undergo initial real-time quality control before being distributed to the principal investigator responsible for the float. The data are also sent to the Global Data Centres (GDACs) (Coriolis and USGODAE), which provide online access to users.

In total, over 20 countries are currently part of the Argo programme, with seven different float types currently in operation. Regardless of make, the floats carry a CTD (conductivity, temperature and depth) package manufactured either by Falmouth Scientific Instruments (FSI) or by Seabird Electronics.

1.9.2 Argo Quality Control

Due to the difficulty in recovering Argo floats, repeated calibration of sensors during the float's lifetime is not possible. Therefore, in the absence of a suitable quality control system, temperature, pressure and conductivity measurements would be susceptible to anomalous individual readings, offset values and sensor drift through time. These problems are outlined in detail by Oka and Ando (2004) and Oka (2005). The specification for the Argo programme requires that sensors give readings of temperature that are accurate to 0.005°C and readings of salinity accurate to 0.01. Both Seabird and FSI sensors are generally sufficiently stable to meet the required temperature accuracy throughout the lifetime of a float, but the conductivity sensors (from which salinity is deduced) are more prone to error.

Using recalibrations from six floats that were deliberately recovered, Oka and Ando (2004) and Oka (2005) observed a range of anomalous behaviour in the conductivity sensor. For instance, one Provor float deployed in the North Pacific and fitted with a Seabird SBE41-CP sensor module was found to have an offset in its salinity readings of 0.02. This occurred due to an operational error in which the conductivity cell operated at the sea surface immediately after launch, fouling the sensor. Argo floats are programmed not to measure conductivity at the surface because of the risk of cell contamination by organic material. A second example of irregular behaviour was seen in the later study, where drifts in salinity of between -0.0074 and -0.0125 over 2.5 years were found. These were attributed to a gradual accumulation of biological material within the cell, which decreases its effective conductivity and thus leads to underestimated salinity values.

In order to correct for these types of error, a two-stage quality control mechanism has been established (Wong et al., 2009). Within 24 hours, national data centres should have completed real-time quality control before transmitting the data to the GDACs. This quality control is limited and automated in order to disseminate the data as quickly as possible to the scientific community. It involves 18 separate tests, described in brief in Table 1.1. From this process, a series of quality control flags are assigned to the data, which give a rating of 1 to 9 on the quality of pressure, temperature, salinity and position measurements. An overall profile quality marker is also assigned to indicate the percentage of pressure levels that contain good data.

However, real time quality control is designed only to isolate obvious errors, such as erroneous spikes in the temperature or salinity fields, the presence of density inversions and extreme vertical gradients in properties. As each profile is considered in isolation, it will not detect spurious offsets, jumps or drift between profiles. In view of this limitation, the second-stage 'delayed-mode' quality control process was introduced in 2005. This procedure, first described in detail by Wong et al. (2003), aims to remove spurious data by a statistical comparison between float salinities on θ surfaces and background climatological data derived from historical hydrographic measurements. Typically, for any float profile, 600 historical profiles are used. Temporal variations in water mass properties are accounted for using an

Test performed	Comments
Platform identification	Checks float ID is valid.
Impossible date test	Checks date is sensible.
Impossible location test	Checks latitude and longitude are both within the ranges -90 to +90.
Position on land test	Checks the float is located in an ocean.
Impossible speed test	Checks float has not drifted at an impossible speed from the last position.
Global range test	Applies a gross filter on observed T and S values.
Regional range test	Applies a filter to ensure T and S lie inside certain ocean-specific ranges.
Pressure increasing test	Checks that pressures are monotonically increasing.
Spike test	Checks T and S profiles do not contain anomalous spikes.
Gradient test	Checks vertical gradients in properties are not unrealistically steep.
Digit rollover test	Detects data rollover (technical test).
Stuck value test	Looks for all measurements in a profile being identical.
Density inversion	Checks for density inversions from T and S data.
Grey list	Prevents real time dissemination of measurements from a poorly operating sensor.
Gross S or T drift	Used to detect a sudden sensor drift (e.g. change in S more than 0.5).
Visual QC	Manual subjective inspection by an operator (optional).
Frozen profile test	Checks a float is not reproducing the same profile over and over again.
Deepest pressure test	Checks the bottom profile does not have an unrealistically high value.

Table 1.1: Summary of the tests performed as part of the real time quality control process.

objective estimate method, to yield a set of calibrated data with error estimates. Since the work of Wong et al. (2003), two further papers have been published that aim to improve the delayed mode quality control algorithm in certain circumstances. Boehme and Send (2005) take into account the planetary vorticity when obtaining a background field of salinity, to give more weight to historical measurements that have a PV that matches that at the Argo observation point. This method is particularly suitable for float data from oceans with high spatial and temporal variability, where multiple water masses exist on the same isotherm or where water mass distribution is affected by topographic barriers. Finally, Owens and Wong (2009) aimed to improve the method of Wong et al. (2003) by performing an optimal linear piecewise continuous fit in potential conductivity space. Further details of the DMQC process are found in the Argo Quality Control Manual (Wong et al., 2009).

Unfortunately, because of the need to accumulate a time series to calculate a stable slope correction term (e.g. for sensor drift), delayed mode quality control can only occur around 6 months after the data are obtained. In practice, the delayed mode calibration can take much longer, because of the large backlog of data that accumulated prior to the adoption of this system in 2005. However, substantial progress has now been made so that by March 2009, 253941 delayed profiles were available worldwide out of a total of 519754.

Argo Pressure Problems

Since the start of the Argo programme, three substantial problems with pressure sensors on floats have been identified. The first issue, initially identified in February 2007, involved Woods Hole Oceanographic Institution SOLO floats with FSI CTD sensors, most of which were in the Atlantic Ocean. The nature of the error was that profile data were offset upward by one or two pressure levels, leading to a significant cold bias in the data. Of the 211

affected floats, 59 were easily correctable by automated procedures, whilst the remainder were 'greylisted' as they required expert examination. Many of these were subsequently corrected (with an associated uncertainty contained in the PRES_ADJUSTED_ERROR field of the netcdf profile files) but a substantial number were deemed uncorrectable and thus continue to be greylisted. In the course of this investigation, a number of WHOI floats with SBE sensors were also found to have smaller pressure offsets, but these were relatively easily corrected.

A second problem, identified in December 2008, involved long-term drift in the pressure sensors on APEX floats. These were generally small (from an array average of -2 dbar in 2003 to 0 dbar in 2008. Most of these profiles have been corrected, although a subset with APF8 controller boards are not easily correctable.

The final more serious problem, initially identified in September 2008, involved a failure of the Druck pressure sensor used in SBE41 and SBE41CP CTDs. This was manifested as a negative drift in pressure followed by an eventual failure in the pressure transducer. The cause of the problem was identified to be oil leaks from the sealed inner sensor chamber via micro-cracks in the glass-to-metal seals. As this occurred, a flexible diaphragm used to transmit seawater pressure to the oil chamber was deflected downwards causing a negative pressure error (Wong and King, 2009). Initially, this problem was thought to affect only around 3% of SBE CTDs, but by October 2008 it was found that up to 35% of SBE floats had pressure sensors that were failing prematurely. A moratorium on Argo float deployment with these sensors thus started in May 2009, with many floats returned to Seabird for pressure sensor replacement. It is hoped that all remaining pressure bias issues will be resolved by the end of 2010 with the corrected data stored in the PRES_ADJUSTED variable field. Until this time, users were advised to use only DMQC data and to check the size of the PRES_ADJUSTED_ERROR field before using the data.

1.9.3 Argo Data and Transports

Whilst the excellent spatial and temporal resolution of Argo data provide a unique opportunity for examining ocean variability over months and years, several characteristics of the data mean that using it for geostrophic transport calculations is challenging. Firstly, the irregular spatial distribution of the data (Figure 1.11) means that a robust method of interpolation is required to put the Argo θ/S measurements onto a single latitude line (in our case 36°N). In the presence of ocean noise, this procedure is non-trivial and is discussed in detail in Chapter 2. Secondly, the depth restriction of the data (a maximum of 2000 dbar) means that the programme is *only* capable of resolving the upper ocean transports and cannot be used to determine transports in the deep layers such as the North Atlantic Deep Water or Antarctic Bottom Water. Thirdly, the Argo θ/S alone can only be used to infer geostrophic shear relative to a pressure level. Exact determination of velocity requires a well-defined reference velocity field at a particular pressure level. Whilst this can be obtained from Argo trajectories at the float parking depth, this in itself involves a number of assumptions and

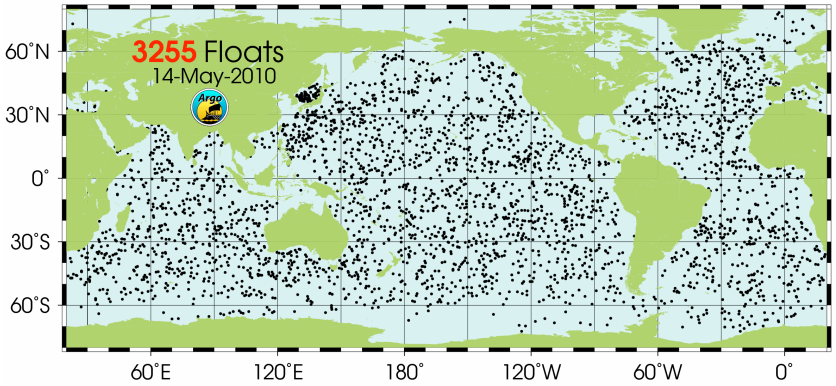

Figure 1.11: Map showing position of Argo floats that delivered data in the period 14th April to 14th May 2010.

again requires careful projection onto a latitude line. This process is discussed in more detail in Chapter 3. Finally, the irregular temporal distribution of Argo data in the period 2001 to 2007 as the array was gradually deployed means that any transport estimates for individual years will vary in absolute accuracy and will be potentially subject to temporal aliasing (e.g. a bias in float measurements towards a particular season). Careful analysis of the temperature and salinity errors is conducted in Chapters 3 and 5 to identify these uncertainties.

1.9.4 Argo Results in the Subtropical North Atlantic

Despite Argo's limitations, the program has been highly successful in increasing our understanding of circulation variability in the subtropical North Atlantic. An early analysis at 36°N was conducted by Hadfield et al. (2007), who showed that Argo data could be used successfully to estimate both upper ocean temperature and heat storage. Specifically, they used an optimal interpolation technique to deduce that the RMS temperature difference between the CD171 cruise section and a synthesised section along the same latitude using Argo floats could be reduced to 0.6°C. This compared favourably with the 0.8°C RMS error incurred by using the World Ocean Atlas. Furthermore, they found that the Argo dataset had sufficiently small errors to estimate the mixed layer seasonal heat storage to within 10 Wm^{-2}, suggesting that Argo might be used to investigate mixed layer heat storage within the subtropical gyre on interannual timescales.

Other studies have focused on the use of Argo data to infer circulation variability. An early attempt was made by Fraile-Nuez and Hernandez-Guerra (2006), who used 500 Argo profiles in the subtropical gyre east of 45°W to compute the geostrophic transport streamfunction at 24.5°N. Using a Successive Correction Interpolation Scheme, they calculated T and S on a 1-degree grid with sections at 24.5°N and 30.5°N. Assuming a zero velocity at 2000 dbar, they found that the total southward mass transport in the thermocline at 24.5°N was not significantly different from the hydrographic cruises in 1957, 1981 and 1992. Moreover, the total geostrophic minus Ekman transport showed good agreement with the total Sverdrup

transport estimated from QuickSCAT data, suggesting the wind stress curl is the controlling influence on the interior transport.

More recently, the same group of researchers have extended their analysis to produce a box inverse of the subtropical North Atlantic contained within the latitudes 24°N and 36°N in the period 2003 to 2007 (Hernandez-Guerra et al., 2010). A number of constraints are used in the inverse including mass conservation, Florida Straits transport and Ekman layer transport. Solutions with and without transformation due to Mediterranean Water formation are included. It is found that by using all the Argo T/S data from the five-year period, the transports have significantly less eddy noise than individual cruise sections. From this inverse, the size of the upper limb of the MOC at is estimated as 14.9 ± 3.0 Sv and not significantly different from previous cruise-based estimates stretching back to 1957. However, they do not attempt to infer variability in the MOC from the Argo float array.

Work by another group (Willis et al., 2003; Willis and Fu, 2008; Willis, 2010) has focused on combining ocean density fields from the Argo float array with estimates of SSH from satellite altimetry to detect long term changes in Atlantic Ocean overturning. They note that one of the largest sources of error in estimates of the mean ocean circulation based on subsurface float displacements is the temporal variability caused by the mesoscale eddy field. Their technique makes use of the strong relationship between sea surface height anomaly and anomalous reference level velocities to reduce mesoscale eddy variability. Their first study was conducted for the region north of 33°N in the period 2004 to 2006, and in most regions they found that inclusion of altimeter data caused a 1-2 cm change in the dynamic height field. In their latest paper, the analysis was extended to estimate the size of the AMOC at 41°N. They computed maps of the time-varying density field in the upper 2000 m for each month using overlapping three-month periods. The AMOC was then estimated from the dynamic height difference of the section end points, with the transport integrated above 958 m. The final MOC estimate, 15.5 ± 2.4 Sv is somewhat smaller than the 18.7 Sv mean value estimated at 26.5°N by Cunningham et al. (2007). Furthermore, the variability is generally smaller than at 26.5°N with a weaker seasonal cycle. The authors also note that it is not possible to compute a similar Argo-based time series south of 41°N due to a substantial portion of the meridional flow resting on the shelf, where Argo float coverage is non-existent.

1.10 Research Objectives

Many research questions have been identified throughout the review of literature, yet the focus of this study remains on problems related to the volume transport at 36°N. Firstly, understanding of the interannual and seasonal variability in the zonal structure of the gyre recirculation at this latitude remains limited. Specifically, we would like to produce a time series of basin-wide geostrophic interior transports for the period 2002 to 2007 from the Argo float data and for each meteorological season. From these estimates, it will be possible to identify both the longitude and depth range that sets the dynamic height difference across

the basin and thus controls the size of the baroclinic interior transport. Secondly, a long-term time series of Gulf Stream transports similar to that at Florida Straits is required close to the separation point of the Gulf Stream at Cape Hatteras. Whilst the Argo float array alone is found to be inadequate for this purpose, a time series of ten-day temporal resolution is produced by utilising both cruise and altimeter data along the Line W mooring line. Finally, the mechanisms controlling the interannual variability in the gyre recirculation remain to be determined. This work focuses in particular on the role of the theoretical Sverdrup transport on controlling the size of the interior flow from a year-to-year basis. Fundamental questions such as the size and timescales of variability in both the wind stress and wind stress curl fields are addressed before a direct comparison is made with the Argo-based interior transport estimates and the Gulf Stream time series.

To address these questions, the structure of the thesis is as follows:

1. Chapter 2 sets out the methodology used in the analysis. The geographical distribution of Argo profile data in the North Atlantic is discussed, along with the necessary quality checking. Details of how the Argo data are mapped onto 36°N are included, along with how the decorrelation length scales used in the interpolation were determined. The chapter also includes discussion of the wind stress products used to estimate the Sverdrup and Ekman transports of the section. A detailed overview is given of the Line W mooring and cruise data and the JASON satellite altimeter, with the focus on using the two datasets to produce a time series of Gulf Stream transports. Finally, the OCCAM model is introduced, which is used later in Chapter 5 to help identify mechanisms of transport variability.

2. Chapter 3 discusses the results of the Argo data interpolation. The size of the potential temperature and salinity errors are assessed and the year-to-year changes in these fields are identified. The interannual and seasonal changes in the dynamic height gradients across the basin are outlined before time series of Argo interior transports are presented. Difficulties in establishing an accurate background reference field are discussed and the comparative size of the interannual and seasonal interior transport variability is evaluated. Finally, the results of our Gulf Stream transport time series are presented and compared with previous historical estimates in the same region.

3. Chapter 4 investigates the main modes of variability controlling the wind stress and wind stress curl in the subtropical North Atlantic, which in turn drive the Ekman and Sverdrup transports respectively. After a brief overview of theoretical considerations, the latitudinal structure of both Ekman and Sverdrup transports in the subtropical North Atlantic is examined using four different wind stress products. Spectral analyses of both wind stress and wind stress curl and then conducted to identify the dominant timescales of variability, with EOF analysis employed to identify the main spatial patterns. The relationship between both these fields and the North Atlantic Oscillation is also discussed.

4. Chapter 5 compares the interior transport estimates derived from the Argo float data

with the Sverdrup minus Ekman transport derived from the wind stress products. Whilst some agreement is found in the eastern basin (east of 40°W), deviations from Sverdrup balance of up to 15 Sv are observed in the western basin, meaning that the Sverdrup transport does not provide a useful predictor of total geostrophic flow in the interior at interannual or seasonal timescales. A comprehensive error analysis is also carried out. Gulf Stream transport and wind stress/wind stress curl is correlated to help identify forcing mechanisms of Gulf Stream variability. Results from the OCCAM model are also presented to further support the case made previously by Hirschi et al. (2009) for baroclinic Rossby waves affecting the size of interior and Gulf Stream transports. Finally, concluding remarks from the study are made.

Chapter 2

Data and Methods

A number of data sources and methods were used to investigate the main research question posed in Chapter 1. In the early part of this chapter, the geographical and temporal distribution of Argo data in the subtropical North Atlantic is examined (Section 2.1.1). Details of early experiments to investigate the magnitude of transport variability are documented along with the methodological problems encountered in this approach in Section 2.1.2. The optimal interpolation scheme used to map the Argo θ/S data is then introduced, with discussion focused on the use of the World Ocean Atlas 2001 climatology and on the determination of appropriate zonal and meridional length scales to use in the OI (Sections 2.2 and 2.3). The use of Argo float trajectory data to establish a reliable reference velocity field is also discussed (Section 2.4). The second part of the chapter covers the geographical and temporal coverage of the wind stress data used to investigate the source of the transport variability. Specifically, four different wind stress products are introduced in Section 2.5 and the methods used to deduce the Ekman and Sverdrup transports at 36°N are outlined. The North Atlantic Oscillation is also introduced as an important mode of meteorological variability (Section 2.6). In the third part of the chapter (Section 2.7), the Line W mooring array that occupies the region between Cape Cod and Bermuda is discussed, with the emphasis on its role in providing supplementary data to the Argo float array near the boundary and on its use in estimating Gulf Stream transport. The altimeter data collected by the JASON satellite is then introduced and it is shown how the data can be used in conjunction with Line W to infer a time series of Gulf Stream transports. Finally, the OCCAM $\frac{1}{4}^{\circ}$ model is introduced in Section 2.8, as results from this product are discussed in Chapter 5 in relation to mechanisms forcing the interannual variability in interior and Gulf Stream transports.

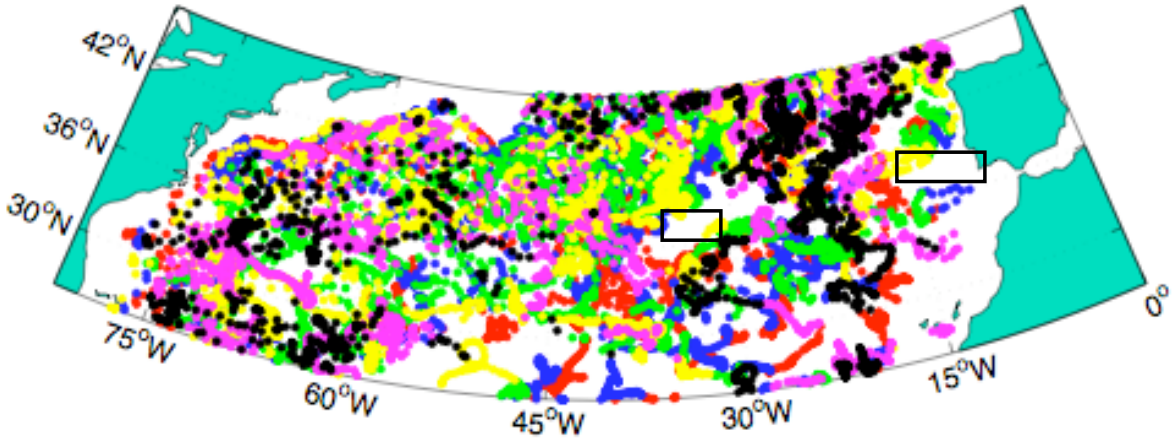

Figure 2.1: Map to show locations of good quality delayed mode Argo profiles between 26°N and 46°N taken in the period 2002 to 2007. The colour coding is as follows: red 2002, blue 2003, green 2004, yellow 2005, magenta 2006 and black 2007. Large data gaps near 36°N are shown with black boxes.

2.1 Argo Floats in the North Atlantic

2.1.1 Geographical and Temporal Distribution

The first Argo profile in the northern subtropics of the North Atlantic (defined for our purposes as between 26°N and 46°N) was collected in the year 2000. However, the focus of our study is only on the period from 2002 onwards as it was only after this time that there were sufficient profiles to attempt to determine the geostrophic shear at 36°N. In the period 2002 to 2007, 14384 good quality profiles were collected in this latitude band: 1572 in 2002, 2044 in 2003, 2465 in 2004, 2144 in 2005, 2518 in 2006 and 3641 in 2007. By 24th February 2009, 9025 of these profiles had gone through the delayed mode quality control process: 1386 in 2002, 1761 in 2003, 1977 in 2004, 1554 in 2005, 1203 in 2006 and 1144 in 2007. At the time of float selection, there were an insufficient number of delayed mode float profiles to extend the analysis after 2007. The distribution of delayed-mode floats by year is shown in Figure 2.1. Float profile distribution close to 36°N is generally good throughout the time period, with the exception of the region east of 15°W and between 30°W and 35°W where very few Argo profiles are found. Elsewhere, there appears to be reasonable coverage in every year, with the exception of the region between 60°W and 75°W in 2002. The exclusion of many SOLO/FSI floats with inaccurate pressure readings has a substantially reduces the number of available profiles in that year, especially west of the Mid-Atlantic Ridge (Section 1.9.2). Over the entire time period, profiles from 159 floats (out of a total of 765) were excluded from the analysis on the basis of being greylisted for pressure errors.

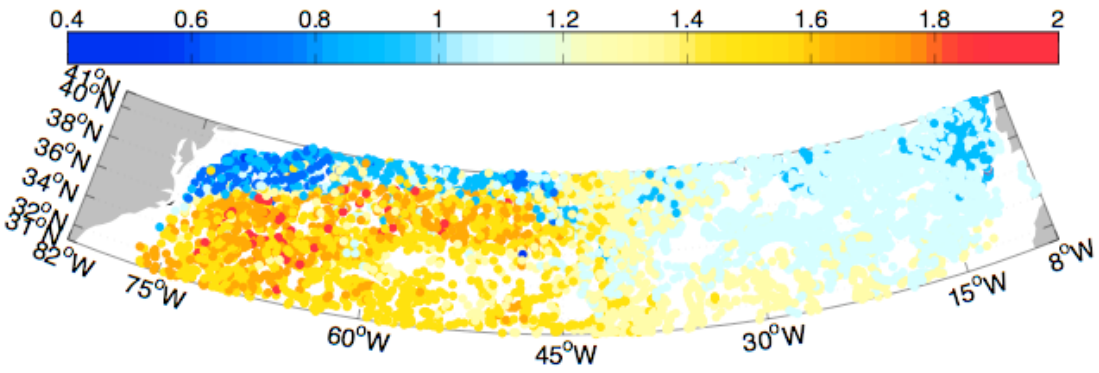

Figure 2.2: Scatter plot of dynamic height (in dyn. m) at the surface relative to 1000 db for all usable Argo profiles in the domain in the period 2000 to 2007.

2.1.2 Early Experiments

Our earliest experiments involved using all available good-quality profiles to plot the dynamic height field of the subtropical North Atlantic between 31°N and 41°N. In total, over 6300 profiles were used to calculate the dynamic height relative to 1000 dbar in the period January 2000 to November 2007 (Figure 2.2). A clear zonal gradient in dynamic topography is observed, with values increasing from 0.9 dyn. m in the Iberian Basin to 2 dyn.m in the Sargasso Sea around 70°W. A sharper gradient denotes the position of the Gulf Stream and North Atlantic Current, with values inshore and to the north of the stream being as low as 0.5 dyn. m (at around 38°N, 75°W).

The horizontal circulation can also be described from the scatter plot. The asymmetrical subtropical gyre is the dominant feature, with a peak in dynamic height in the Sargasso Sea around 36°N, 70°W. Strong recirculation of the Gulf Stream is apparent from the zonal gradient in topography around 45°W, with weaker recirculation east of 30°W where the dynamic topography is much flatter. The eastward offshore movement of the Gulf Stream at Cape Hatteras is also visible. These results thus qualitatively support the circulation scheme of the subtropical North Atlantic outlined in Chapter 1.

The initial method of determining the magnitude and variability of the interior transport (the east to west cumulated transport between the eastern boundary and the offshore limit of the Gulf Stream) was to use an end point method trialled successfully by Longworth (2007) at 26°N. In theory, this technique circumvents the irregular spacing issue of the Argo data set, allowing the geostrophic velocity profile to be estimated from a single pair of hydrographic stations at either end of a mid-ocean section (Hall and Bryden, 1982). The equation used by the technique is:

$$(V - V_R) = \frac{1}{f\Delta x}(\Delta\Phi_E - \Delta\Phi_W) \tag{2.1}$$

where V is the average geostrophic velocity between western and eastern stations relative to the reference pressure with a reference velocity V_R. $\Delta\Phi_E$ and $\Delta\Phi_W$ are the geopotential anomalies at the western and eastern end stations respectively, f is the Coriolis parameter and Δx is the horizontal distance between the two profiles. Three implicit assumptions are made. Firstly, there should be no intervening topography between the stations and the transport between each end station and the boundary should be negligible. Secondly, if the method is to be used to construct a time series of interior transport changes along 36°N, end stations must be carefully selected so that the temporal changes observed in their density structure are representative of those at 36°N. Finally, it considers variability at each end of the section in isolation, thus assuming that baroclinic transport changes are independent.

Two instantaneous Argo profiles roughly representative of mean end station conditions at either end of the interior section were selected (a western profile at 34.89°N, 66.83°W and an eastern profile at 38.67°N, 10.40°W). Using a level of no motion at 1000 dbar, the zonally integrated transport between these points found to be 32.6 Sv southwards. From these 'reference' profiles, a time series of transport anomalies was calculated at each boundary from 'representative' profiles at each end of the section. A careful sampling strategy was devised for the selection of these eastern and western stations, which is outlined below.

The Eastern Boundary Box

A geographical box was used to isolate profiles near the eastern boundary 'representative' of end station conditions at 36°N. The southern boundary of the box was chosen to be 35°N, in order to avoid including water from south of the meandering Azores Current, which detaches from the Gulf Stream near the Grand Banks and produces a meridional gradient in dynamic height close to 33°N in the eastern basin (Gould, 1985), seen in Figure 2.2. The western limit of the box was defined as 16°W, a position designed as a compromise between being sufficiently close to the boundary to reflect full-width changes and including a large enough number of profiles to ensure a good temporal resolution to the time series. 41°N was chosen as the northernmost limit of the box as the subtropical recirculation does not extend as far north as Cape Finisterre.

As this was an initial study done early in the course of the project, 729 Argo profiles were found in the box between May 2002 and November 2007, but only 3 had undergone delayed mode quality control. Initial data checking was thus carried out to identify and remove profiles with poor quality flags, along with those that exhibited anomalous drift or jumps in their θ-S relationship. From this procedure, one float (6900372) was excluded. In total, this left 685 usable profiles, with most of the box relatively well sampled, the exception being the southeastern corner near 35°N, 10°W.

The Western Boundary Box

Defining suitable profiles at the western end of the interior section was more difficult and is ultimately why the end station method was rejected in favour of optimal interpolation. Specifically, Gulf Stream and slope waters had to be excluded as we wished to evaluate the interior transport only. Unfortunately, a simple latitude-longitude selection criterion was inadequate to filter out these profiles due to temporal meandering of the Gulf Stream (Webster, 1961), visible in Figure 2.2 as the zone of mixed high and low dynamic height values near 36°N, 70°W. Furthermore, complete detachment of Gulf Stream meanders into the ocean interior to produce cyclonic cold-core eddies (Richardson et al., 1973) mean that anomalously cold and fresh slope water was sometimes sampled by Argo floats in the Sargasso Sea west of 60°W (Parker, 1971).

Extensive experimentation was carried out to remove these anomalously cold and fresh profiles. Eventually, it was decided to exclude profiles with an 18°C isotherm depth of less than 300 m. A histogram of the depths (not shown) revealed no clear separation between the different water masses, so this cut-off is rather arbitrary. The geographical box used in conjunction with the isotherm depth criterion was 35°N to 41°N, 71°W to 65°N. As before, profiles with poor quality data and signs of drift/jump were excluded. In total, 326 usable profiles were identified.

The Transport Anomaly Time Series

Given that instantaneous profiles in eastern and western boundary boxes were not acquired at the same time, it was not possible to produce a time series of interior transport using Equation 2.1. To circumvent this problem, the method outlined by Longworth (2007) was followed, which produces two individual time series, one for the western and one for the eastern boundary. The method has the additional advantage of showing how either side of the basin contributes to the total interior transport variability.

The principle behind the method is to assume that the density structure of one boundary is constant in time. A reference profile taken at time t_r is then identified at the other boundary. A series of transport anomalies are then calculated between the reference profile and all other profiles in the boundary box surrounding it. For instance, if one assumes the dynamic height structure at the eastern boundary is constant, the transport anomaly per unit depth resulting from changes at the western boundary is:

$$\Delta x(V_1 - V_R) - \Delta x(V_r - V_R) = \frac{(\Delta\Phi_{W_r} - \Delta\Phi_{W_1})}{f} \tag{2.2}$$

where V_1 is the velocity at time t_1, V_r is the reference velocity at time t_r, V_R is a background reference velocity at pressure p_R, $\Delta\Phi_{W_1}$ is the geopotential anomaly at the western boundary at time t_1 and $\Delta\Phi_{W_r}$ is the reference geopotential anomaly at the western boundary at time t_r.

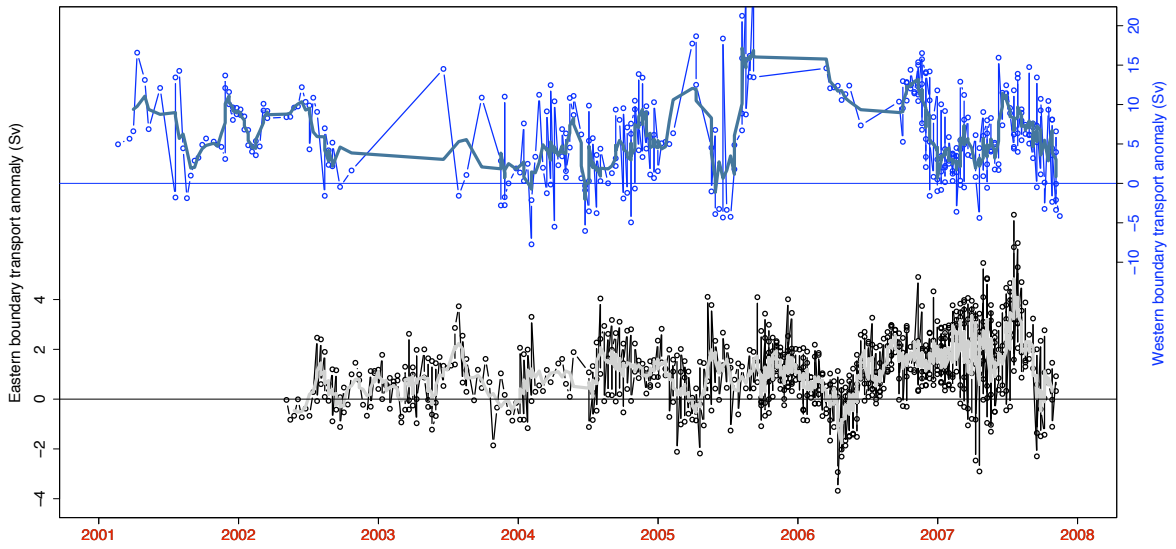

Figure 2.3: Interior geostrophic transport anomalies at the western boundary (top) and the eastern boundary (bottom) with a 5 point symmetrical moving average added in bold. Note the different y axis scales. The observation that the anomalies do not average to zero is due to the selection of reference end stations (which were not statistical 'mean' profiles but instantaneous Argo profiles).

The corresponding equation for the eastern boundary assuming no change at the west is:

$$\Delta x(V_1 - V_R) - \Delta x(V_r - V_R) = \frac{(\Delta\Phi_{E_1} - \Delta\Phi_{E_r})}{f} \tag{2.3}$$

where $\Delta\Phi_E$ represents geopotential anomalies at the eastern boundary. After converting to a volume transport, two time series of anomalies were thus produced and analysed (Figure 2.3). A level of no motion of 1000 dbar was used.

Several observations can be made from Figure 2.3:

1. The western time series has significant temporal gaps, especially in early 2003 and late 2005/early 2006. At the eastern boundary, the temporal resolution is much better with the only gaps longer than one month occurring in 2004.

2. In line with observations made by Longworth (2007) at 25°N, variability at the western end of the interior section is greater than that at the eastern boundary (5.5 Sv standard deviation compared with 1.6 Sv). No clear seasonal cycle is apparent at either boundary. Furthermore, no statistically significant linear trend in transport occurs at either end of the section, with linear regression analyses suggesting a 0.30 Sv per year reduction in transport at the eastern boundary and a 0.03 Sv per year increase at the western boundary. Both values are small when compared with the high-frequency

variability of each time series, with R^2 values of 0.09 and 0.01 respectively ($p > 0.05$ in both cases).

3. Although direct correlation between the boundary transports was impossible due to the irregular nature of the time series, no visible correlation is seen between the two time series, suggesting that short-term geostrophic transport changes do not occur simultaneously at both ends of the section.

Methodological Problems

Unfortunately, this data set has several undesirable features which led to its abandonment as the main approach for determining the transport variability at 36°N.

1. Most importantly, the method does not allow us to separate unequivocally the temporal variability from the spatial variability in each boundary box. Whilst at the eastern boundary this effect is relatively small (Figure 2.4), the strong eddy field at the western end of the section means that small geographical separations strongly affect the estimate of interior transport. A method is thus required that explicitly accounts for the spatial variability in producing a time series.

2. The method produces two separate time series on an irregular temporal grid. In order to compare the variability of geostrophic transport with estimates based on wind stress curl (Section 4.2.2), interior transport measurements on a regular time grid (in our case annual) are required.

3. The method only gives estimates of single-point changes (at the eastern and western ends of the section) and does not resolve the zonal structure of the transport changes along the section.

4. The method does not provide a rigorous estimate of transport error incurred by the background spatial variability.

For each of these reasons, it was decided instead to use an objective mapping based on the optimal interpolation method, outlined in Section 2.2.

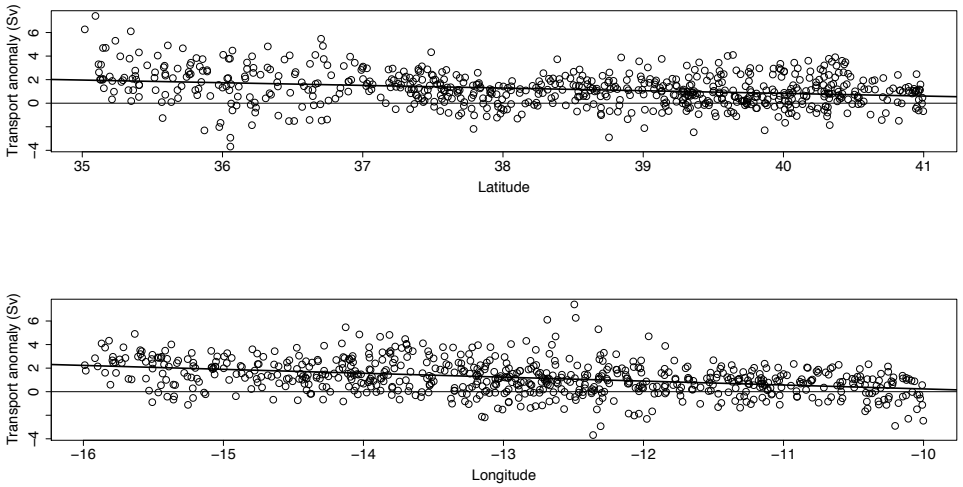

Figure 2.4: Graph of eastern boundary transport anomalies against the latitude and longitude of the profile, with least squares regression line fitted. The transport anomaly becomes more southward with increasing latitude and increasing longitude, although in both cases the slopes are small (0.23 Sv per degree and 0.33 Sv per degree respectively). Associated R^2 values are 0.069 and 0.13.

2.2 The Optimal Interpolation Scheme

Given the inherent difficulties in disentangling spatial and temporal variability in the original methodology, it was decided to use an optimal interpolation method to calculate the geostrophic transport field along the 36°N latitude line. The algorithm used (known hereafter as the optimal interpolation or OI) is based on the Gauss-Markov theorem and has been successfully employed in several ocean studies. Introduced by Gandin (1963), the method yields a least squares estimate of the value of temperature or salinity at a grid node, from a number of non-uniformly distributed observations around the node in the presence of noise. This noise includes both measurement error and natural short-scale ocean variability. The procedure also provides an estimate of the error variance based on the distribution of the data. The technique has previously been used by Bretherton et al. (1976) in the Sargasso Sea to estimate the velocity field from a network of 100 current meters on 23 moorings arranged in a circle of radius 200 km. More recently, Hadfield et al. (2007) inferred monthly changes in heat content in the subtropical North Atlantic from Argo data using the method and Getzlaff (2009) has applied the technique in the South Indian Ocean.

In order to provide an objective estimate of the desired ocean parameter, the algorithm requires an *a priori* estimate of the background structure of the mean field. The annual mean World Ocean Atlas 2001, comprising objectively analysed temperature and salinity measurements on a 1° x 1° grid, provides this background climatology in our study. WOA01 contains around 5 million measurements of surface temperature worldwide (Stephens et al., 2002) and 1.3 million measurements of surface salinity (Boyer et al., 2002), principally from

historical ocean station data, CTDs and XBTs. A revision of WOA took place in 2005 (Antonov et al., 2006), enhancing the size of the dataset to around 5.3 million surface temperature measurements and 1.6 million surface salinity measurements. A further update was done in 2009, taking the number of temperature measurements to over 9 million (Locarnini et al., 2010). We elected to use WOA01, but as the analysis in Section 5.3.5 shows, the final solution is relatively insensitive to the choice of background climatology.

In addition, knowledge of the correlation structure of the field on pressure levels is required to apply the OI. In Section 2.3, the method of determining anisotropic length scales (Lx and Ly) for the subtropical North Atlantic is discussed and the results of these analyses are given. However, the theoretical considerations of the OI method are firstly considered in more detail.

2.2.1 Theoretical Considerations

From the irregularly spaced Argo data in the North Atlantic, it was decided to map both temperature and salinity onto the station positions of the CD171 cruise and onto the Line W cruise/mooring line (Figure 3.1 and Section 3.1). This selection was made in order to facilitate easy comparison between objective estimates of temperature and salinity and the results from CD171 cruise. The 23 mapping points on the Line W line (Section 2.7) between 36°N and the W1 mooring at 39.6°N, 69.7°W were included to make use of data from two Line W moorings inshore of the Gulf Stream. For this section, a station spacing of close to 10 km was used between the W1 and W3 moorings, around 15 km between W3 and W6 and around 25 km between mooring W6 and 36°N (Figure 3.1). The following discussion refers to mapping of salinity but exactly the same principles apply to the mapping of temperature.

The final estimate for salinity S_{obj} at each mapping point on every 20 dbar surface is given by:

$$S_{obj} = S_{WOA} + w \cdot (S - S_{WOA}) \tag{2.4}$$

where S_{WOA} indicates the salinity from the WOA01 climatology at that point, w is the coefficient weighting matrix using the decorrelation length scales and $S = [S_1, ..., S_N]$ is the set of salinity measurements from the relevant float profiles for each grid point. The *a priori* estimate of salinity (and temperature) is provided by the World Ocean Atlas. To obtain the WOA01 value of temperature and/or salinity at the mapping point, a simple two-dimensional linear interpolation was used from the $1^\circ \times 1^\circ$ gridded climatology.

Application of the OI algorithm comprises two steps. Step one involves preselection of the data whilst the mapping of that data is carried out in step two. Some previous authors using this algorithm have incorporated a third step (Wong et al., 2003; Boehme and Send, 2005), which includes a 'small-scale' distance mapping that also incorporates temporal separation. The purpose of using this step is to give additional weighting to measurements that are

close to the grid point in both space and time and give larger error estimates where recent historical data are not available. This third step uses shorter length scale estimates than the anisotropic decorrelation scales, representing the length scale of the mesoscale variability. However, given the relative sparsity of data that occurs at very short distances (< 100 km) from the grid points, it is not felt that small-scale eddy variability could be adequately incorporated into our estimate and this third step is therefore omitted.

First Step of the OI

In this initial step the profiles contributing to each mapping grid point are preselected, which improves the computational efficiency of the algorithm. Firstly, Argo data points that are separated by topography from the mapping point are excluded (including the coasts and the bottom). A 0.5° x 0.5° topographic grid is created from the TerrainBase 5′ elevation database and data points are excluded from the analysis if it is found that there is intervening topography between them and the mapping point. Secondly, a distance weighting scheme is applied to the remaining data points based on the decorrelation length scales we have defined below, assuming a Gaussian distribution of the data. Only data points with a weighting $wd_{i,g}$ exceeding e^{-3} are included in the analysis. The weighting is calculated as:

$$wd_{i,g} = exp\left\{-\left[\frac{Dx_{i,g}^2}{Lx^2} + \frac{Dy_{i,g}^2}{Ly^2} + \frac{F_{i,g}^2}{\Phi^2}\right]\right\} \text{for } i = 1 : N \tag{2.5}$$

where $Dx_{i,g}$ and $Dy_{i,g}$ are the zonal and meridional distance in km between the i-th data point and the mapping grid point with index g. Lx and Ly represent the length scales calculated in the autocorrelation function analysis. The final term $(F_{i,g}^2/\Phi^2)$ is a weighting by potential vorticity: F is the fractional distance in PV representing the cross-isobath separation (Boehme and Send, 2005). F is calculated by the following formula:

$$F = \frac{|PV(a) - PV(b)|}{\sqrt{PV^2(a) + PV^2(b)}} \tag{2.6}$$

where PV is the barotropic potential vorticity, defined as f/H where H is the full ocean depth. The cross-isobath scale, Φ, is set to 0.3, and is designed to reduce the influence of profiles inside the basin on mapping points near the boundary (and vice versa). For computational efficiency, if there are more than 40 profiles with a weighting exceeding e^{-3}, only the 40 profiles with the highest weighting are selected.

Second Step of the OI

Once the weights are defined for each contributing data point, the objective estimate at the grid node (mapping point) is calculated. The algorithm assumes that each individual measurement of salinity S_i can be separated into a true signal s_i and random noise η_i,

which comprises measurement errors, unpredictable processes and natural ocean variability that can all cause deviations from the mean state. Provided noise is uncorrelated over distance with uniform variance and the signal has a longer correlation distance than the data separation, the signal and noise variance of the data can be estimated as $S_i = s_i + \eta_i$. Signal variance can be approximated as:

$$s^2 = \frac{1}{N}\sum_i (S_i - S_{WOA_i})^2 \tag{2.7}$$

and the noise variance η^2 is estimated from the difference of S from neighbouring measurements,

$$\eta^2 = \frac{1}{2N}\sum_i (S_i - S_k)^2 \tag{2.8}$$

where S_k is the salinity measurement that has the shortest distance from S_i on each isobar. The signal and noise variance are then used to calculate the coefficient weighting matrix w used in the final estimate equation 2.4.

$$w = \mathbf{Cdg} \cdot [\mathbf{Cdd} + I \cdot \langle \eta^2 \rangle]^{-1} \tag{2.9}$$

where I denotes the identity matrix and **Cdg** and **Cdd** are the data-grid and data-data covariance matrices given by:

$$\mathbf{Cdg} = \langle s^2 \rangle \cdot wd_{i,g} \tag{2.10}$$

and

$$\mathbf{Cdd} = \langle s^2 \rangle \cdot exp\left\{ - \left[\frac{Dx_{i,j}^2}{Lx^2} + \frac{Dy_{i,j}^2}{Ly^2} \right] \right\} \tag{2.11}$$

Here, $Dx_{i,j}$ and $Dy_{i,j}$ are the zonal and meridional distances between the two data points with indices i and j. The error variance of the OI is then given by:

$$\sigma_{OI}^2 = s^2 - \mathbf{Cdg} \cdot \mathbf{Cdg^{-1}} \cdot \mathbf{Cdg^T} \tag{2.12}$$

cruisemap.pdf which takes into account the number of profiles to calculate degrees of freedom with which to scale the standard deviation. The OI procedure thus produces a robust estimate of mapping error for each variable. The size of these errors is investigated in detail in Section 3.1.1.

Mapping Salinity on Temperature Surfaces

Some consideration was given to mapping salinity on temperature surfaces as opposed to pressure surfaces. The advantage of this method is that it generally yields longer correlation scales as $S(T)$ variance is smaller than that on pressure surfaces. However, Haines et al. (2006), investigating data assimialtion at both 300 and 700 m, found that $S(z)$ variance exceeded $S(T)$ in much of the Mediterranean Water outflow region of the eastern basin. Furthermore, as mapping salinity on temperature surfaces can exclude much of the seasonal variability (e.g. Ekman pumping) which may affect the baroclinic transport on these timescales.

2.3 Decorrelation Length Scales

Following the methodology of Getzlaff (2009), decorrelation length scales for both temperature and salinity were estimated from the residuals either between cruise data (Figure 2.5) and the WOA01 climatology or between the Argo data set and WOA01. Such an approach allows us to investigate whether the decorrelation length scales are significantly different depending on the time period under consideration.

In both instances, a two dimensional linear interpolation of the annual World Ocean Atlas to the float profile position or CTD station was used as an estimate for temperature and salinity at that location. The differences between the climatology and the Argo or cruise data were then calculated and these residuals (after being detrended and demeaned) were used to calculate the decorrelation length scales through a spatial autocorrelation. In this section, the main results of this analysis are highlighted, with a fuller description given in Appendix A.

Seven cruise sections were chosen from which to evaluate the length scales, displayed in Figure 2.5. The zonal CD171 section, occupied in May 2005, was already described in Section 1.8. CTD data from the six meridional sections, two each along World Ocean Circulation Experiment cruise tracks A16, A20 and A22 respectively, were obtained from `http://cchdo.ucsd.edu/atlantic.html` (retrieved August 2008).

2.3.1 Selection of Data

In deciding zonal (Lx) and meridional (Ly) length scales for the *interior* of the subtropical North Atlantic, any cruise CTD stations falling within the Gulf Stream region were excluded. Large scale meanders and extensive eddy activity are known to dominate in western boundary currents, reducing the spatial correlation of ocean temperature and salinity fields on pressure surfaces. Examination of potential temperature and salinity fields (Figures 3.10a and 3.11a) for the CD171 cruise at 36°N showed that Gulf Stream waters are found west of 68°W and therefore only stations to the east of this longitude were included in the length

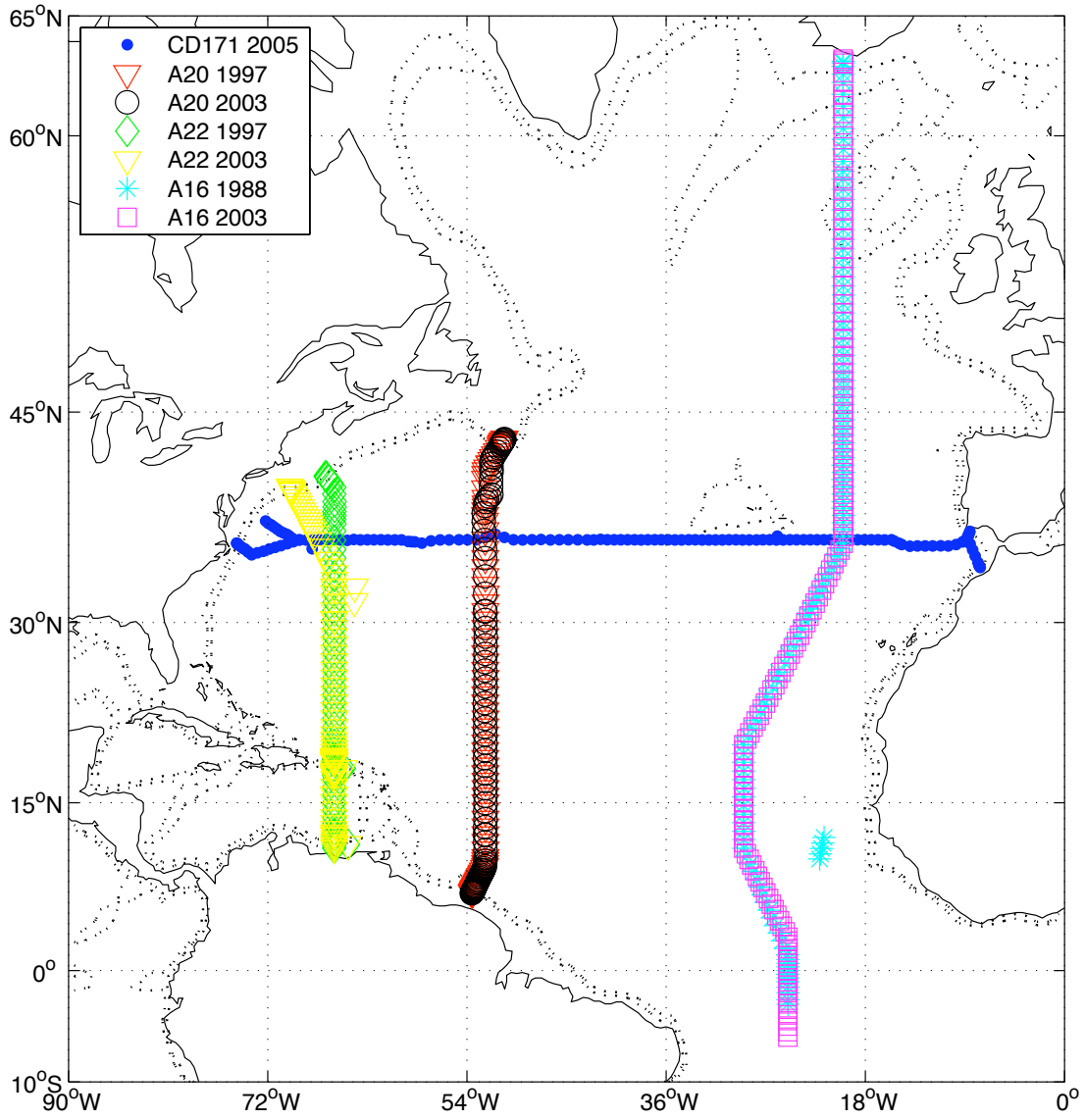

Figure 2.5: Seven cruise tracks in the North Atlantic Ocean from which decorrelation length scales were estimated. The latitudinal section at 36°N is the *Charles Darwin* CD171 cruise occupied in June 2005. The four longitudinal cruise tracks at 52°W and 66°W (all occupied by *R.V. Knorr*) are 1997 and 2003 cruises on the WOCE A20 and A22 lines. The two longitudinal tracks near 20°W (occupied by *R.V. Oceanus* and *R.V. Ronald H. Brown*) are occupations of the WOCE A16 line in 1988 and 2003. The 1000 m and 2000 m isobaths are displayed.

scale analysis (116 stations in total). For the meridional sections to the west of the basin (A20 and A22), Gulf Stream waters were excluded by removing stations located north of 41°N and 39°N respectively. On the A22 section, profiles located south of 18°N were also excluded as they are located within the Caribbean Sea and are thus unrepresentative of interior ocean conditions. Length scale analysis on the A16 section included data between 5°N and 40°N, as data north and south of these latitudes are not representative of conditions in the subtropical gyre. To the south, one encounters the tropical North Equatorial Countercurrent, whilst to the north one moves north of the North Atlantic Current into the subpolar gyre.

Once the relevant zonal section stations (from CD171) or meridional stations (From A16, A20 or A22) have been selected, the distance between CTD stations on each section was calculated and a new axis generated along 36°N, 20°W, 52°W or 66°W (for CD171, A16, A20 and A22 sections respectively). This new axis was divided into 200 equally spaced mapping points, each with a separation between two and three times that of the original data. Potential temperatures and salinities for each station (with good quality control flags) were then linearly interpolated onto 20 dbar surfaces and the interpolated data projected onto the new axis. The autocorrelation function (ACF) of the demeaned and detrended potential temperature and salinity anomalies at each pressure level was then calculated as the correlation of the signal against a space-shifted version of itself. The decorrelation length scale is defined as the first crossing point of the ACF.

In order to improve the temporal resolution of the length scale estimates and to reduce the effects of short-lived eddies on the length scale estimate, all Argo data collected from 2° either side of the four cruise sections were also used to estimate zonal and meridional scales. The choice of how wide to define latitude and longitude bands is a compromise; they need to be sufficiently narrow to ensure that length scales are representative of the section and sufficiently wide to ensure there is no temporal bias introduced by the fact that the band does not include sufficient profiles from a particular period of the Argo programme. The chosen data are then sorted by longitude or latitude and interpolated onto a new axis with 200 evenly-spaced stations. As with the cruise data, the first zero crossing of the autocorrelation function is used to estimate the scales.

The annual number of profiles contributing to the length scale analysis within the 4° band around 36°N is given in Figure 2.6. In total, 2866 profiles are used to evaluate the length scale at this latitude. For comparison, a 1° band would only included 656 profiles, with only 6 profiles from the year 2001 and 54 from 2005.

2.3.2 Zonal Scales

Following the methodology outlined in Section 2.3.1, the zonal decorrelation length scale (L_x) was estimated along the 36°N line using both CD171 cruise data and Argo data. In the interior (east of 68°W), a single length scale of 350 km was found to be most appropriate.

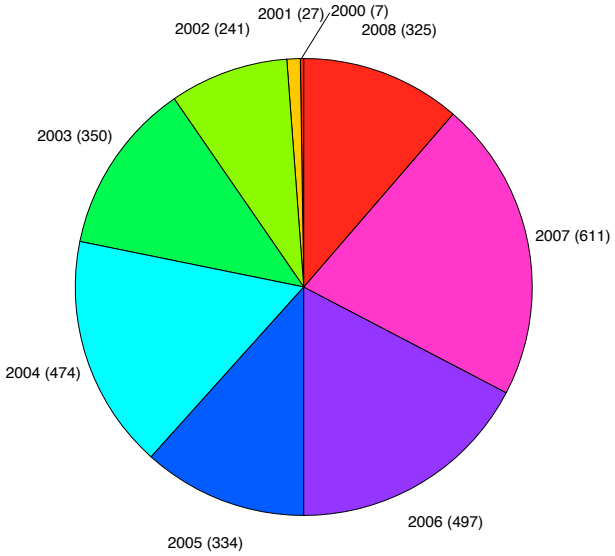

Figure 2.6: Annual number of good-quality float profiles within ±2° of 36°N over the lifetime of the Argo programme up to October 2008).

Some differences in the vertical structure of the length scales were observed when comparing length scales derived from the cruise data compared with those derived from the Argo data (Figure 2.7). Whilst the cruise data show a gradual reduction in length scale with increasing depth (Figure 2.7a), stabilising below 900 dbar at close to 250 km, the Argo estimates have increasing length scales at depth and a more complex vertical structure (Figure 2.7b). The reason for Argo having shorter temperature length scales in the mixed layer is that the data are collected throughout several years, whereas the cruise data were obtained during a single month. As the variability in temperature is mainly controlled on large spatial scales by the seasonal surface fluxes in the mixed layer, including data from all seasons markedly reduces the spatial correlation near the surface.

A detailed examination of the normalised residuals for both potential temperature and salinity explains the difference in depth structure (Figure 2.8). In the case of the cruise data (Figures 2.8a and 2.8c), increasing mesoscale variability with depth due to strong isopycnal displacements in the more weakly stratified deep ocean is the cause of the decreasing length scale (more details in Appendix A). In comparison, there is weaker station-to-station variability at 1500 to 1900 dbar in the Argo data (Figures 2.8b and 2.8d). This is because most of the tranisent eddies are removed, the Argo data having been collected over eight years. As a result, such large scale isopycnal displacements are not found and the zonal scales are consequently much longer.

In order to test the robustness of the scales estimated from the cruise data, the length scale analysis was repeated with various levels of randomly-generated Gaussian noise added to the temperature and salinity anomalies. The noise levels selected varied from 0.005 to 0.2 for salinity and 0.005°C to 0.2°C for temperature, the lower values being the approximate instrumental error on the CTD. The resultant plots for noise levels of 0.005/0.005°C and

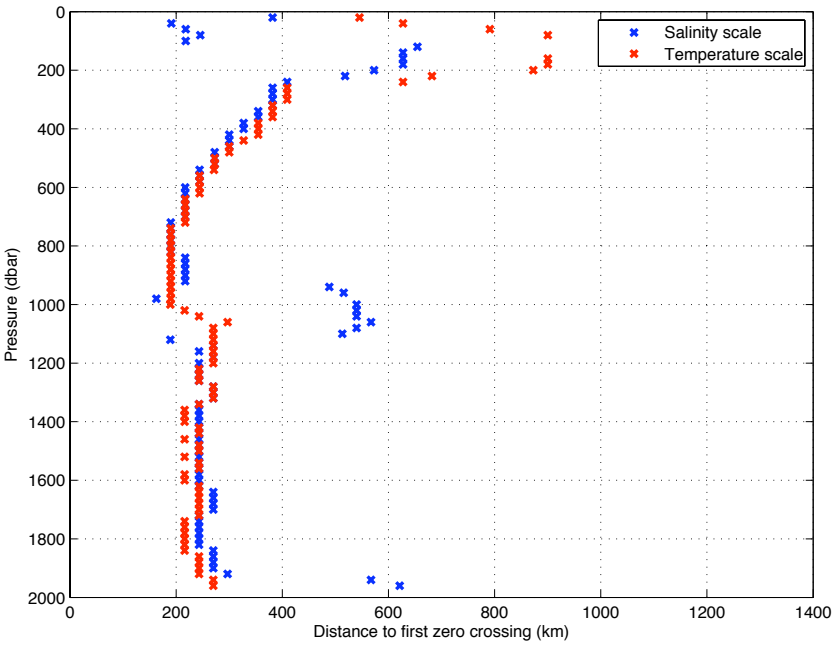

(a) CD171 cruise data

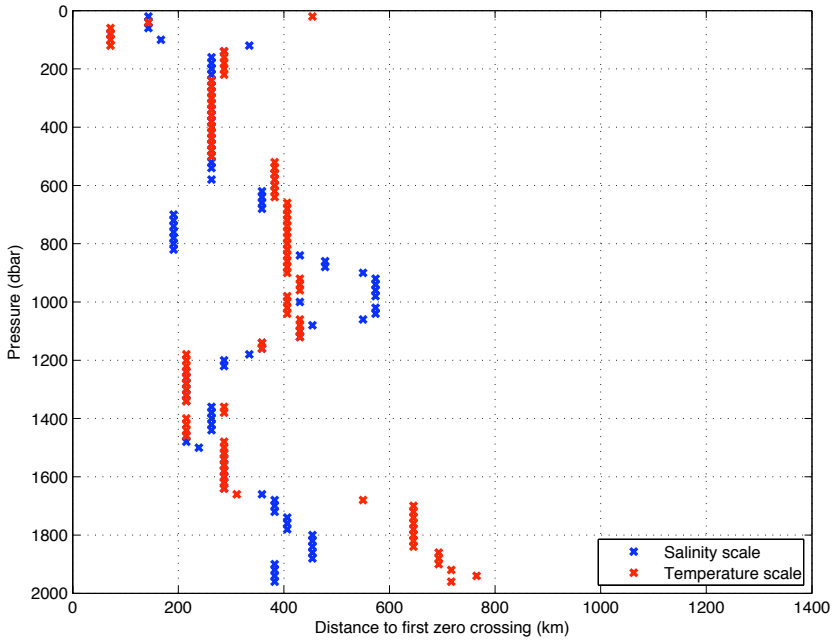

(b) Argo data

Figure 2.7: Zonal decorrelation length scales for (a) CD171 cruise data east of 68°W and (b) Argo profiles within 2° of 36°N east of 68°W.

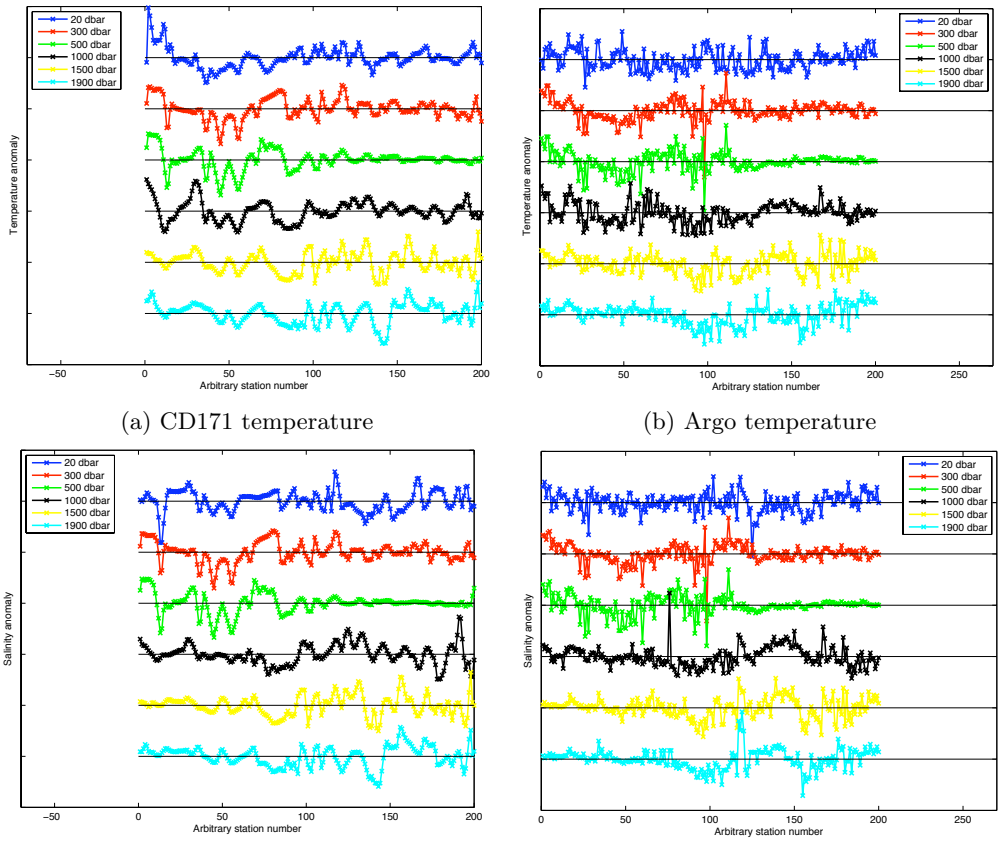

(a) CD171 temperature

(b) Argo temperature

(c) CD171 salinity

(d) Argo salinity

Figure 2.8: Detrended potential temperature and salinity residuals for various pressure levels normalised by their standard deviation for both the 2005 CD171 section and for Argo data collected within 2° of 36°N east of 68°W. Station 1 is located at 68°W and station 200 at the eastern boundary.

0.1/0.1°C are shown in Figure 2.9. At noise levels comparable to the size of the instrumental error, our estimate is found to be robust, with almost no change in the vertical structure of the length scales. It is only when very large noise levels are added (0.1 or greater) that the structure breaks down, although even at a noise of 0.1 the reduction in length scales between 300 dbar and 1000 dbar is still observable (Figure 2.9b).

More detailed analysis of the individual ACFs is given in Appendix A, but after careful consideration we find insufficient evidence to adopt a depth-varying length scale. As a result, a final choice of 350 km was made for the ocean interior. In contrast, obtaining accurate length scales in a dynamically active region as the Gulf Stream is difficult, especially given the strong meandering and high levels of eddy activity associated with the current. The abundance of transient features such as rings has the potential to impact significantly on the decorrelation length scales, causing small regions to exhibit very short length scales during relatively short time periods. However, as this study does not attempt to resolve individual eddies, we have repeated the earlier zonal length scale analysis, but included only Argo float data west of 68°W. The results are shown in Figure 2.10.

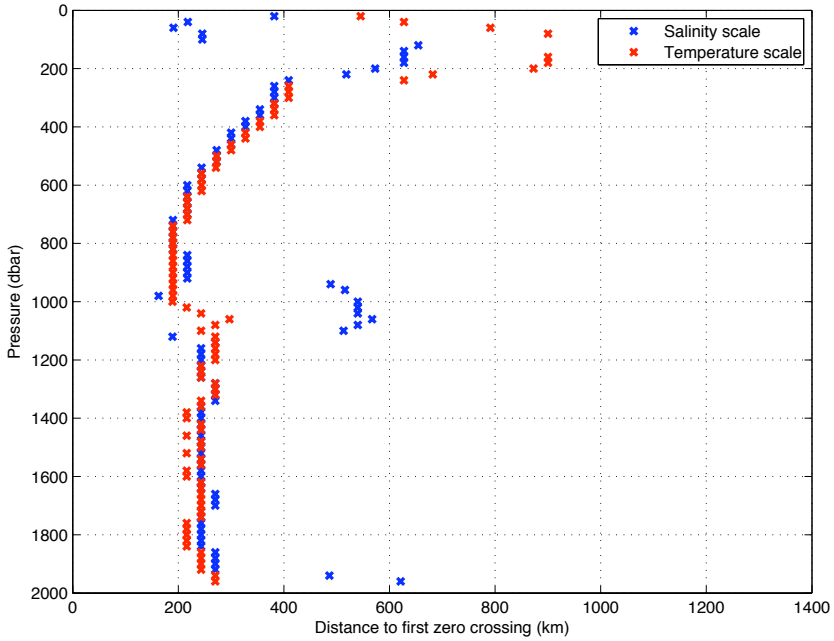

(a) Random noise of standard deviation 0.005

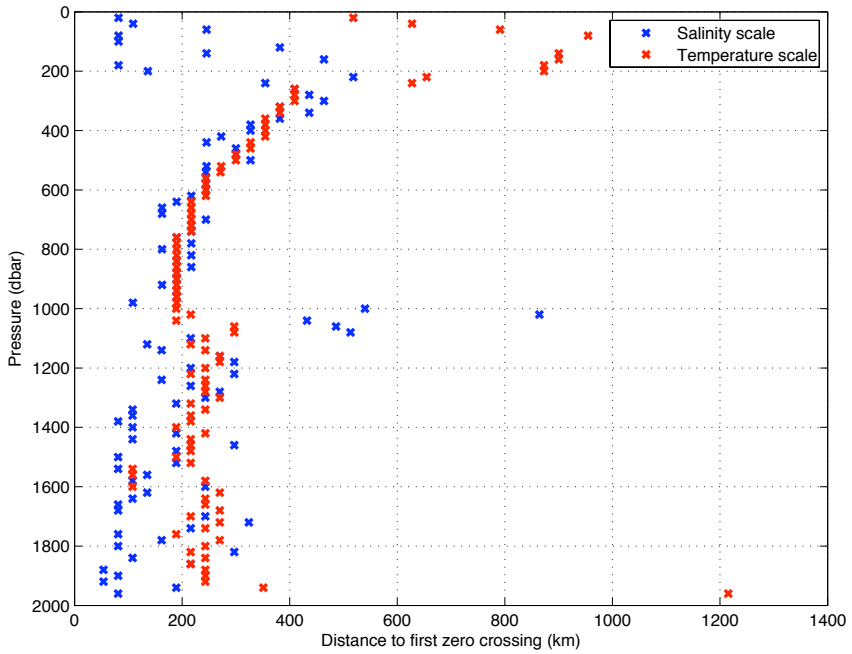

(b) Random noise of standard deviation 0.1

Figure 2.9: Zonal length scales for the CD171 section after the application of Gaussian random noise of standard deviation 0.005 and 0.1 for both potential temperature and salinity.

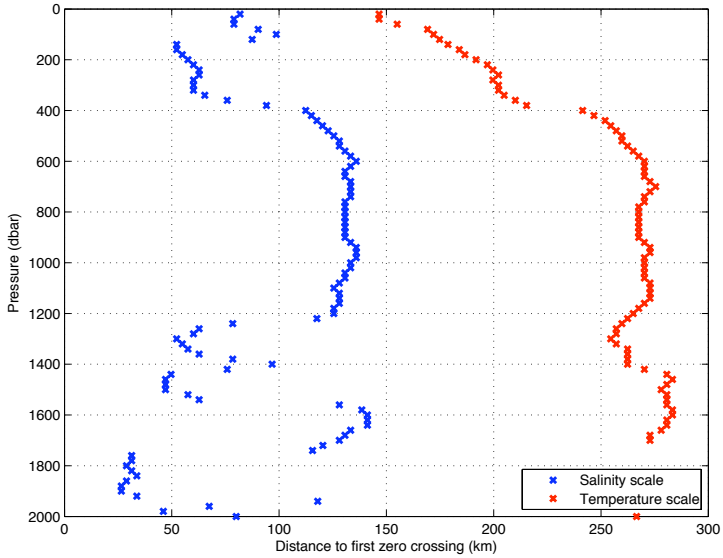

Figure 2.10: Zonal decorrelation length scales for Argo floats within 2° of 36°N in the Gulf Stream region west of 68°W.

As expected, length scales are relatively short throughout the water column, varying from as little as 25 km for salinity at 1800 dbar to as much as 270 km for potential temperature below 600 dbar. It is notable that scales tend to be shorter in the upper 400 dbar where the effects of mesoscale eddies on the potential temperature and salinity fields is largest. Moreover, salinity has a shorter length scale than potential temperature at all depths. The reason for a salinity having a shorter length scale than temperature in the Gulf Stream is not immediately apparent, but given the relatively small region over which these scales are evaluated, we cannot be fully confident that they are statistically different. Therefore, as a conservative estimate of a length scale to use in the Gulf Stream, 150 km would appear to be a sensible choice.

2.3.3 Meridional Scales

In total, six cruises and three interpolated sections made using Argo data were used to infer the meridional decorrelation length scale (L_y). In all instances, the meridional length scales were shorter than the zonal counterparts estimated at 36°N. However, there was substantial variability in the length scales, both between the individual cruise sections and between the Argo and cruise data. At the A16 line (20°W), both 1988 and 2003 cruises yield typical length scales of between 100 and 200 km, though the earlier year has a more pronounced decay in length scale with depth (Figures 2.11a and 2.11b). In contrast, the Argo-derived length scale estimate at this longitude (from 979 float profiles) yields estimates between 60 and 250 km, with salinity having longer length scales than temperature below 1400 dbar (Figure 2.11c). Further discussion of the depth structure is given in Appendix A, but an overall value of around 150 km appears appropriate at this longitude.

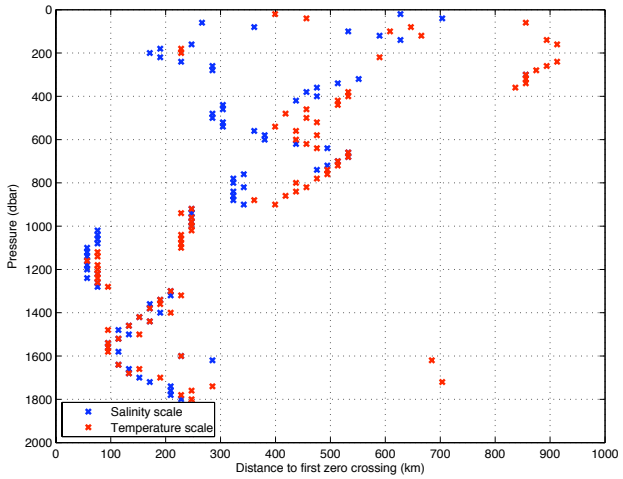

(a) 1988

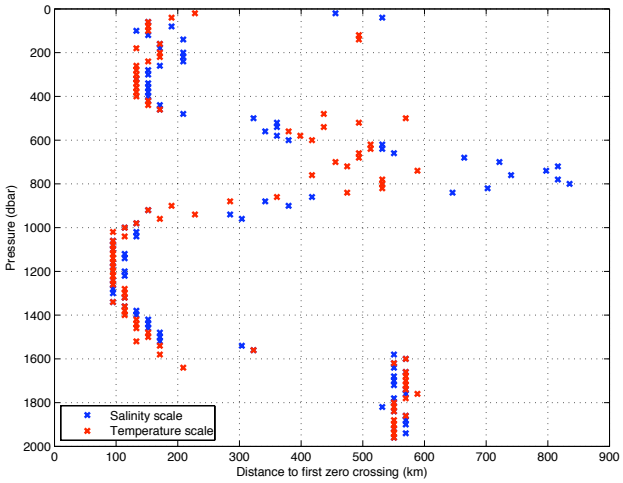

(b) 2003

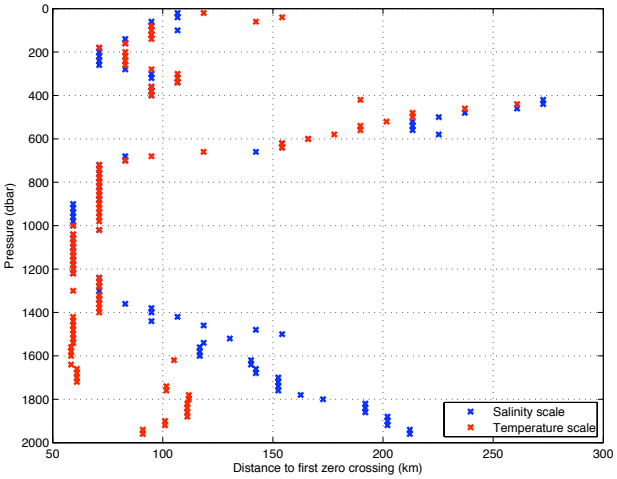

(c) Argo

Figure 2.11: Length scales for potential temperature and salinity at 20°W. The top two panels show results for the A16 cruises in 1988 and 2003 using the stations between 5°N and 40°N, whilst the bottom panel uses Argo profiles located within 2° of that longitude.

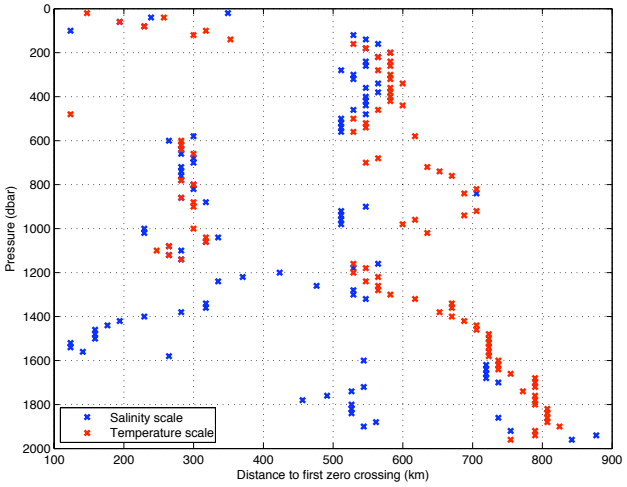

(a) 1997

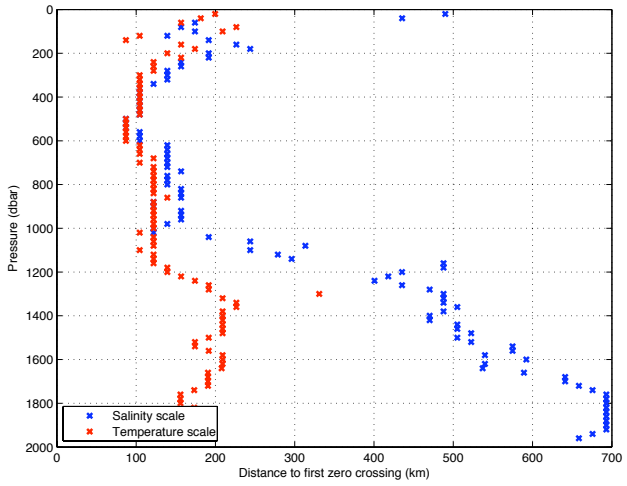

(b) 2003

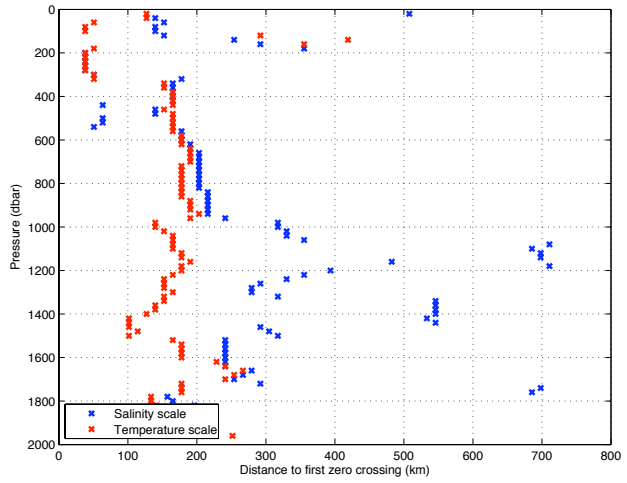

(c) Argo

Figure 2.12: Length scales for potential temperature and salinity at 52°W. The top two panels show results for the A20 cruises in 1997 and 2003, whilst the bottom panel uses Argo profiles located within 2° of that longitude.

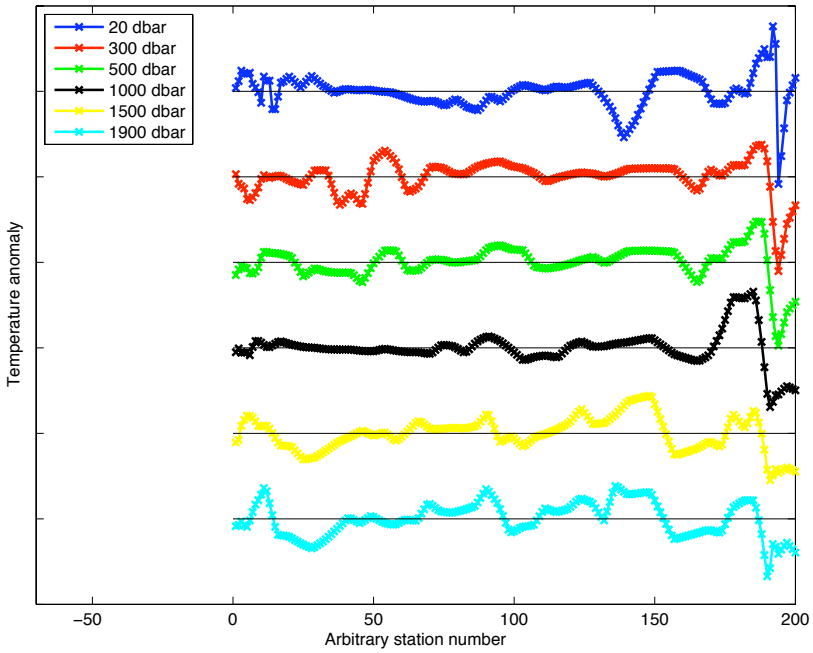

(a) Potential temperature

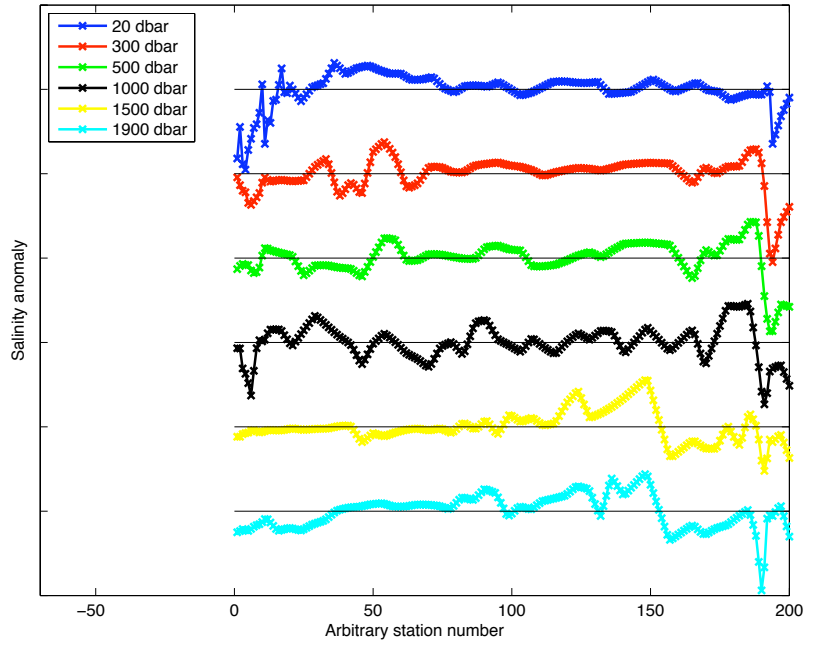

(b) Salinity

Figure 2.13: Detrended potential temperature and salinity residuals for various pressure levels normalised by their standard deviation on the 2003 A20 section. The x axis is arbitrary station number from south to north, with station 1 located at 5°N and station 200 at 41°N.

Contrasting results are also found for the two A20 cruises at 52°W (Figures 2.12a and 2.12b). Whilst the 2003 occupation yields mean values of around 150 km with longer salinity scales below 1000 dbar, the mean values in 1997 are generally longer, but have a much noisier depth structure. The Argo data generally agrees with the later cruise in having length scales close to 150 km, though again the salinity scale is generally longer than for potential temperature between 1000 and 1600 dbar (Figure 2.12c). In both the 2003 cruise data and the Argo realisation, it would appear that the longer salinity length scale occurs because of weaker salinity anomalies towards the northern end of the section nearest the edge of the Gulf Stream (Figure 2.13). If the region north of 35°N is excluded, the salinity and temperature scales are in much better agreement (not shown).

At 66°W, both cruises (in 1997 and 2003) suggest length scales of between 100 and 200 km (Figure 2.14a and 2.14b). Similar results are found using Argo data, though there is a more complex vertical structure (Figure 2.14c). Further details are given in Appendix A.

Finally, meridional length scales in the Gulf Stream region west of 68°W were evaluated using the Argo data. As with the zonal length scales, the meridional scales are close to 150 km (Figure not shown), reflecting the short length scales of variability within the boundary current.

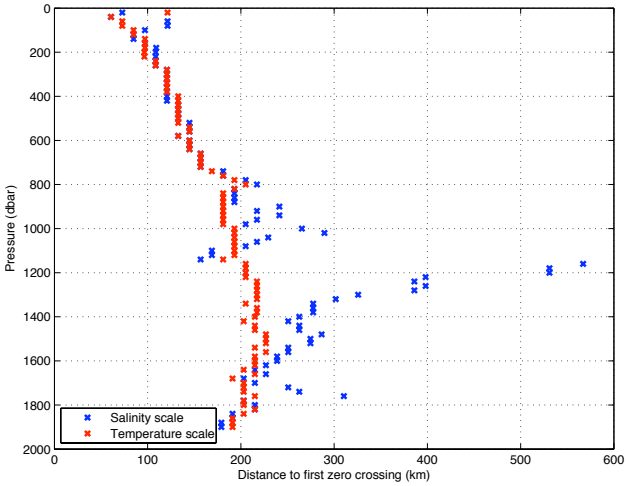

(a) 1997

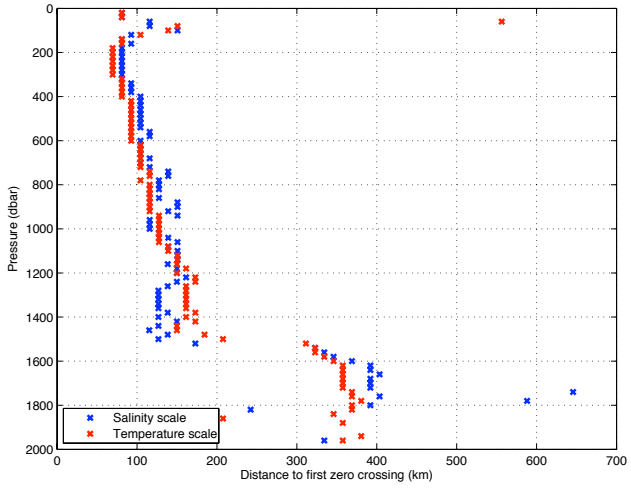

(b) 2003

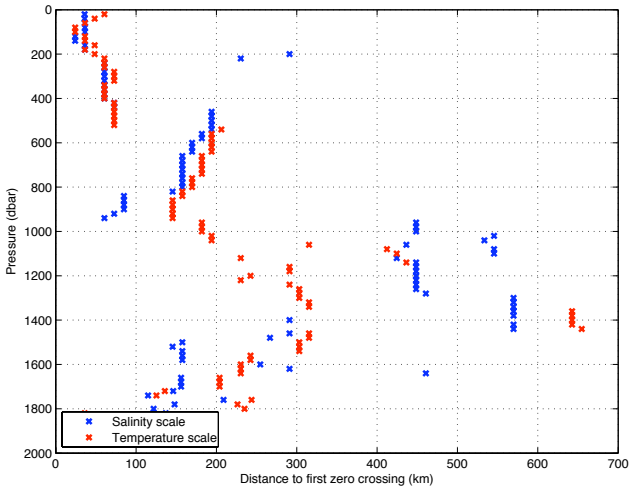

(c) Argo

Figure 2.14: Length scales for potential temperature and salinity at 66°W. The top two panels show results for the A22 cruises in 1997 and 2003, whilst the bottom panel uses Argo profiles located within 2° of that longitude.

2.3.4 Final Choice of Length Scales

After considering both the cruise and the Argo data, the final choice of zonal length scales was 350 km in the ocean interior east of 68°W and 150 km in the Gulf Stream region. A meridional length scale of 150 km was used throughout the section. These values are a little less than the depth-mean length scale estimated from the decorrelation analyses and are thus fairly conservative in their use of Argo data. After further experimentation, it was decided not to include a temporal weighting within the OI as the highest temporal resolution that could accurately be determined was annual. All readings within the year thus receive equal temporal weighting within the OI.

2.4 Reference Velocities from Argo Float Data

Once a reliable T/S field has been mapped at 36°N, a robust background velocity is needed to reference the geostrophic shear. Whilst at the parking depth, the Argo floats themselves act as Lagrangian drifters: their float displacement can be used as a measure of the velocity vector over the 9 day period. However, these velocity estimates are subject to a number of errors, discussed in detail by Park et al. (2005). An important limitation is the fact that the end time of the descent of the Argo float (T_{desc_end}) and the start time of its ascent (T_{asc_start}) are not recorded for all float models. The closest approximation that can therefore be used for these times are the descent start time (T_{desc_start}) and the ascent end time (T_{asc_end}). However, these times are also not generally recorded in the Argo meta data. For instance, the ascent end time is often missing because an Argos satellite will not necessarily be directly overhead when the float reaches the surface. Generally, the best estimate that is achieved is the time of first and last data transmission at the surface (Figure 2.15).

Several attempts have been made to improve the accuracy of the trajectories, reviewed in detail by Prytherch (2008). For APEX type floats with a fixed cycle length starting at the first descent time, if the 'reference' time of first descent (T_R) can be calculated, each subsequent descent time can be determined (Park et al., 2005). The ascent end time can generally be recovered from the meta data of APEX floats. A more difficult issue is to determine the *position* of T_{asc_end} and T_{desc_start}. The simplest method is simply to use the position of the first and last transmission packet, but several extrapolation techniques have been used to improve the reliability of these estimates. Davis et al. (1992) assumed that the surface trajectory was the sum of linear drift, inertial motion and noise. Later methods (Park et al., 2005; Prytherch, 2008) have improved these estimates by determining the linear and inertial velocity scales independently for each trajectory, rather than using a prior choice. This requires a minimum of three position fixes, and, if four or more fixes are available, an error estimate of the extrapolated positions can be made. Three principal improvements are achieved by Prytherch (2008): a time weighting is added to the position fixes, an evaluation of the quality of Argo position fixes is made and a technique for minimising position error by selecting the optimal extrapolation method is instituted.

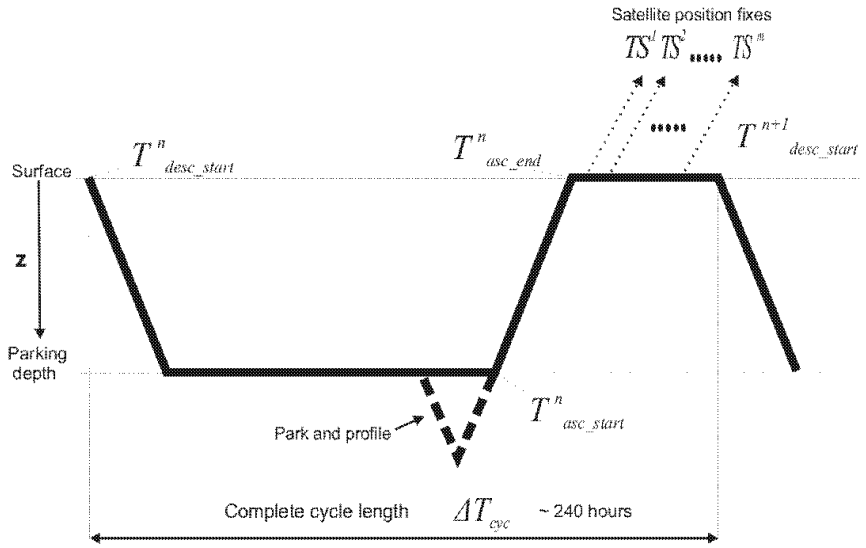

Figure 2.15: Typical cycle for an APEX-type Argo float, where n represents the cycle number. T_{desc_start} and T_{asc_end} are not generally recorded by the float. The YoMaHa′07 database uses the first and last surface fix (TS^1 and TS^m) to calculate the float trajectory. Image from Prytherch (2008).

These advances have made substantial improvements to the estimates of Argo parking depth velocities, with Park et al. (2005) suggesting that errors from all sources contribute to an overall velocity error of 0.2 cms^{-1} (the other major sources of error include clock jumps and clock drifts). However, in spite of these developments, parking depth velocities using the most up-to-date and accurate techniques are not yet available as a routine data product. However, a database of float velocity data has been collated by a team at the Asia-Pacific Data-Research Center at the University of Hawaii. Known as YoMaHa′07, this data set includes all Argo floats worldwide with accurate position data and provides estimates of both surface and parking depth velocities for each float, with associated errors due to vertical shear of the horizontal flow (Lebedev et al., 2007). The methodology used by YoMaHa′07 is to utilise the last and first surface fixes by the Argos satellite, and hence is less accurate than methods that estimate the positions and times of diving and surfacing. The possibility of creating our own database of parking depth velocities for the subtropical North Atlantic using the methodology of Prytherch (2008) was explored but eventually deemed too time-consuming.

YoMaHa′07 is available as both a collection of the raw float trajectories *and* as a gridded product, box averaging data in $3° \times 3°$ bins. It was decided that the raw trajectories would be used, as the gridded product box averages all data with a parking pressure of greater than 750 dbar together, not discriminating between different pressure levels. This is clearly not acceptable for providing a reference to a geostrophic calculation. Furthermore, it was felt that the crude latitude-longitude boxes in which the averaging of trajectory data is done is not suitable for deriving an accurate reference velocity field at 36°N, especially in the Gulf Stream region where large latitude-longitude boxes will smooth out the horizontal structure

of the velocity field. Further details of the trajectory selection process and averaging used to achieve the reference velocities are given in Section 3.3.1.

The analysis was originally done using the main version of the YoMaHa′07 database (Section 3.3), but the database is now updated in near real-time to include the most up-to-date Argo trajectories. Moreover, many incorrectly-recorded parking pressures within the Argo meta data have been corrected. A recent version of the data set, accessed in April 2010 and containing over 620000 Argo trajectories worldwide since the start of the programme, was therefore used in the final estimate of interior transport (Section 3.4).

2.5 Wind Stress and Wind Stress Curl Estimates

One of the main proposed mechanisms for transport variability in the North Atlantic is through changes in the Sverdrup transport, outlined in Section 1.2.2. In order to evaluate this quantity on a monthly basis, four wind stress products were used. The first product – the NOC Climatology – is based on ship measurements and is currently available at $1^\circ \times 1^\circ$ resolution from 1980 to 2005 (Josey et al., 1998). A substantial revision of the product was recently carried out (Berry and Kent, 2009), which included error estimates of the individual flux fields, but at present this updated version does not include fluxes for specific months. Data were obtained from `http://www.noc.soton.ac.uk/noc_flux/noc1_1.php`. The second source of wind stress data used was the QuickSCAT satellite scatterometer. This instrument, which orbits the earth every 101 minutes, measures the backscatter of echoed radar pulses from the ocean surface, which in turn correlates well with wind speed (Chelton and Freilich, 2005). Monthly averages of the wind stress and wind stress curl are produced on a $0.875^\circ \times 0.875^\circ$ grid, with data available for the period between August 1999 and November 2009. Late in 2009, the mechanism spinning the scatterometer antenna failed and no data has subsequently been collected (NASA press release, 23rd November, 2009). Data were retrieved from `http://cersat.ifremer.fr/data/discovery/by_parameter/ocean_wind/mwf_quikscat`.

The two other sources of wind stress data – from the European Centre for Medium Range Weather Forecasting (ECMWF) and the National Center for Environmental Protection (NCEP/NCAR) – are both reanalysis products. These are meteorological data assimilation projects, which use both a general circulation model and historical observations to minimise a cost function and yield an optimal state of the atmosphere at each time step. The NCEP/NCAR Reanalysis (Kalnay et al., 1996) provides 6-hourly estimates of the state of the atmosphere on a $2^\circ \times 2^\circ$ grid. Initially, the reanalysis was run for the period 1957 to 1996, but has subsequently been extended to cover the period 1948 to the present. The ECMWF Reanalysis, by contrast, has a $1.5^\circ \times 1.5^\circ$ grid and was initially run for 15 years (December 1978 to February 1994), before being extended to 45 years under the name ERA-40 (1957 to 2002) (Uppala et al., 2005). However, this thesis uses data from the ERA Interim Product, which covers the period 1989 to the present and forms

a precursor to a revised extended analysis that will replace ERA-40. ECMWF Reanalysis data were accessed via `http://www.ecmwf.int/research/era/do/get/era-interim`, whilst NCEP/NCAR Reanalysis data were retrieved via `http://www.esrl.noaa.gov/psd/data/gridded/data.ncep.reanalysis.derived.html` .

For each product, the x and y wind stress data were isolated at the closest latitudes to 36°N (35.5°N for NOC, 35.2375°N for NCEP/NCAR, 36°N for ECMWF and 35.75°N for QuickSCAT). For the NCEP/NCAR, NOC and ECMWF products, wind stress curl was calculated using finite differencing to approximate the differential terms, whilst the QuickSCAT data includes a field of wind stress curl as a routine product. The Sverdrup and Ekman transports per unit width were then calculated and cumulated across the basin, with the results plotted and discussed in Chapter 4. Moreover, wind stress and wind stress curl were also extracted for the entire subtropical North Atlantic between 28°N and 40°N and spatial mean values taken in order to isolate the dominant time and space scales of variability (Sections 4.3.1 and 4.3.2).

2.6 The North Atlantic Oscillation

As the leading mode of variability in the atmospheric pressure field of the North Atlantic (Rogers, 1990), the NAO was considered as a possible control on the strength of the Ekman, Sverdrup and interior geostrophic transports. The NAO index, usually expressed as the normalized pressure difference between the quasi-stationary Azores High and Icelandic Low pressure systems, has been shown to have wide-ranging atmospheric impacts, including on surface air temperatures and storm track position (Rogers, 1997). More recently, correlations have been found between the index and oceanic phenomena, such as sea ice (Hu et al., 2002) and sea surface temperature (SST), although the nature of the relationship is not simple and linear. Taylor and Stephens (1998), for instance, found a statistically significant correlation between the latitude of the Gulf Stream and the NAO at a 2-year time lag, which they attributed to the adjustment time of the oceanic circulation. Furthermore, Curry and McCartney (2001) found that a time-integrated winter NAO was correlated with the baroclinic mass transport in the upper 2000 m between Bermuda and the Labrador Basin.

In order to investigate the relationship between the NAO and the wind stress/wind stress curl, the monthly mean NAO index from the National Oceanic and Atmospheric Administration's Climate Prediction Center (`http://www.cpc.noaa.gov/products/precip/CWlink/pna/nao.shtml`) was used. This index uses a principal component analysis (PCA) to identify the dominant patterns in the 500 mbar height anomalies in each month. The strength of the NAO-type mode in each individual month is then evaluated, with account being taken of the differing absolute strength of the mode throughout the year by normalisation. Results of the analysis are given in Section 4.4.

2.7 Line W Data

2.7.1 Aims and Objectives of Line W

Started in spring 2004, a sustained measurement programme was instituted along a section between Cape Cod and Bermuda with the aim of returning high-resolution observations of the Deep Western Boundary Current, the lower limb of the Atlantic MOC. The section, named Line W in memory of prominent oceanographer Val Worthington, comprises a six-element moored array on a line underlying a satellite altimeter ground track and a programme of repeated ship-based hydrographic/direct velocity sections along the array and extending into the Sargasso Sea.

2.7.2 Sampling Strategy

The sampling strategy of the Line W moorings, outlined in more detail in Section 3.5.1, involves a mixture of fixed-depth and profiling sensors. Moorings 1, 3 and 5 (Figure 2.16) are equipped with McLane Moored Profiler Instruments along with Vector Averaging Current Meters (VACMs) and Sea Bird temperature/conductivity sensors above and below each profiled depth segment. Moorings 2 and 4 were only fitted with VACMs and T/C sensors, whilst mooring 6 had VACMs only. The MMPs were programmed to burst sample a set of 4 one-way profiles every fifth day, with the profiles typically initiated every 9.5 h (roughly half the local inertial period and three quarters of the semi-diurnal tidal period). The mooring instruments have generally functioned well during their period of deployment, with the exception of mooring 1 in 2006/2007. Further details are provided by Toole et al. (2010).

Two streams of data from the MMPs were used in this study. Firstly, temperature and conductivity data from moorings 1 and 3 (which profile to within 100 m of the surface) were used to provide additional temperature and salinity data for the optimal interpolation inshore of the Gulf Stream (Sections 2.2 and 3.1). Secondly, velocity data at 1000 dbar were added to the most recent version of the YoMaHa dataset in Section 3.3. In both cases, a mean of the data from each set of burst samples was used in order to reduce the ageostrophic velocities and vertical displacement energy as compared to the individual profiles. Moorings W1 and W3 (Figure 2.16) are both located in the slope water region inshore of the Gulf Stream, at 39° 36.0′N, 69° 43.1′W and 38° 50.6′N, 69° 11.1′W.

Cruises along the Line W section have typically been occupied twice a year since May 2004 in order to service the moorings and permit shipboard sampling of the section. The slope waters were sampled on every cruise, but only those cruises detailed in Table 3.7 were judged to have crossed the Gulf Stream. The earliest cruise in the table (in November 2003) is the northernmost part of the A22 section used in establishing the decorrelation scales in Sections 2.3.2 and 2.3.3. For each cruise, continuous temperature, salinity and dissolved oxygen data were acquired at each station, together with discrete water samples analysed for salinity,

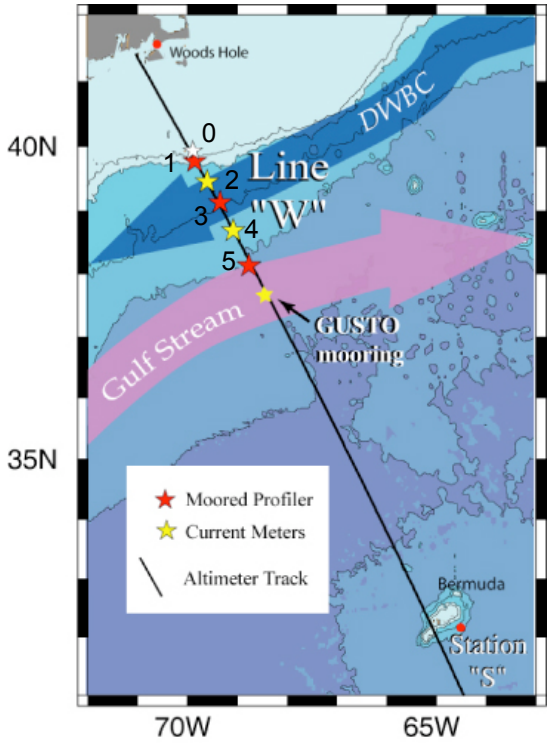

Figure 2.16: Map to show the moorings comprising the Line W array between Cape Cod and Bermuda. Image from Line W web pages `http://www.whoi.edu/science/PO/linew/about/index.htm`.

dissolved oxygen and tracers. Direct measurements of velocity were made both by hull-mounted Acoustic Doppler Current Profilers and lowered ADCPs. Temperature sections for each of the cruises used in the analysis are shown in Figure 2.17. Moving west to east across the Gulf Stream, the isotherms descend by up to 600 m.

2.7.3 Line W and Altimeter Data

The principal use of the Line W cruise data in this study is to 'calibrate' sea surface height differences across the Gulf Stream from the JASON satellite altimeter. Using the regression relationship between zonally integrated Gulf Stream transport and inferred SSH differences from the cruise data, the SSH differences from each altimeter pass yielded a Gulf Stream transport every 10 days. The full methodology for the procedure is described in Section 3.5.1, but the history and operation of the JASON satellite altimeter is discussed below.

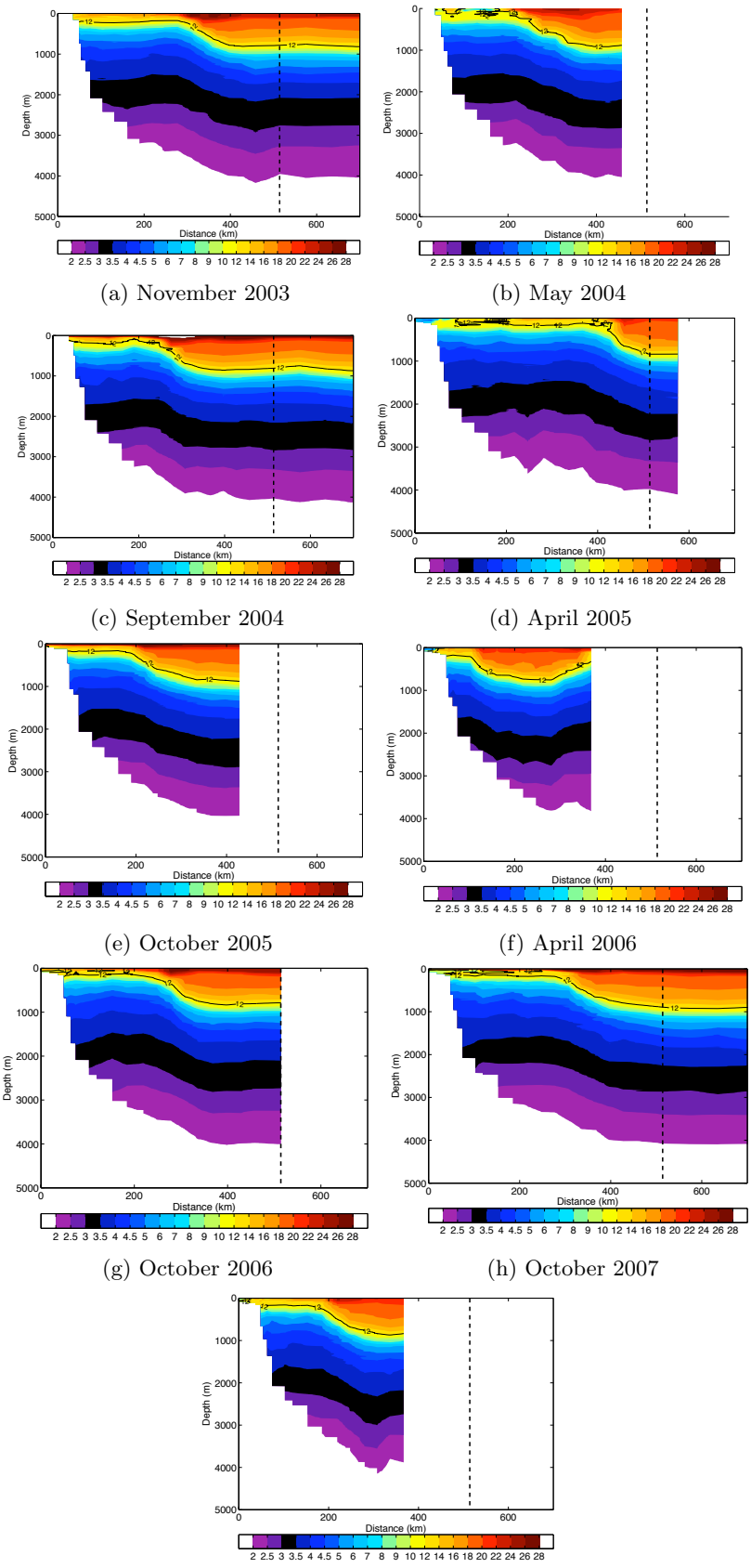

(a) November 2003

(b) May 2004

(c) September 2004

(d) April 2005

(e) October 2005

(f) April 2006

(g) October 2006

(h) October 2007

(i) May 2008

Figure 2.17: Potential temperature (in °C) for nine Line W sections that cross all or the majority of the Gulf Stream. The 12°C isotherm, the depth of which is commonly used to denote the position of the Gulf Stream, is marked. The dashed line marks the position where Line W intersects the 36°N section.

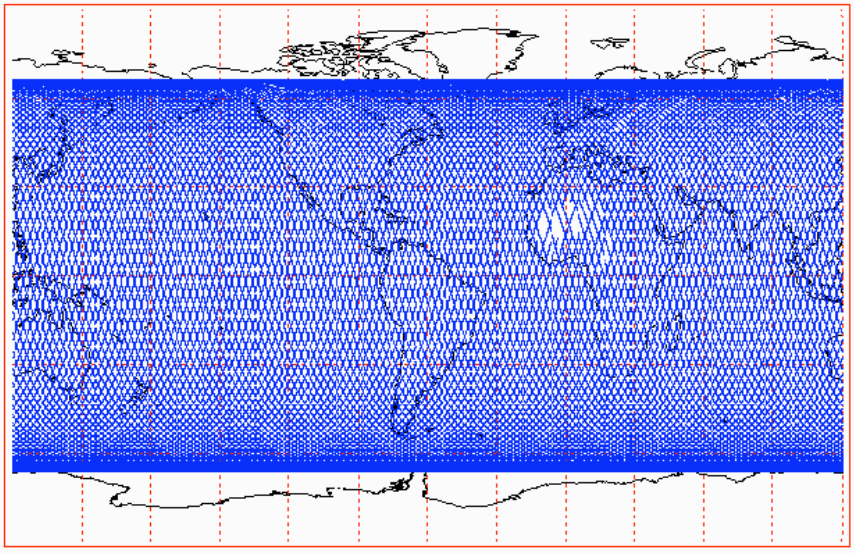

Figure 2.18: Map to show the 254 passes of the JASON satellite altimeter. Image from AVISO and PODAAC User Handbook.

2.7.4 History and Operation of the JASON altimeter

Launched on 7th December 2001, JASON-1 was a follow-on mission to the highly successful TOPEX/POSEIDON mission, which measured ocean surface topography from 1992 to 2005. Whilst partially designed as an instrument to measure global sea level change, gradients in sea surface height can also be used to infer both the speed and direction of ocean currents. The orbit of the satellite is accurate to 2.5 cm and sea surface height is measured with an accuracy of 3.9 cm (`http://topex-www.jpl.nasa.gov/mission/jason-1.html`). The 500 kg satellite comprises a multi-mission PROTEUS communications platform and a JASON-1 specific scientific payload module. Five instruments are included on the satellite, including a Solid-State Radar Altimeter, the DORIS Precise Orbit Determination System and a Microwave Radiometer to measure total water vapour in the troposphere along the altimeter beam (AVISO Group, 2008).

The JASON-1 satellite flies the same ground track as the original TOPEX/POSEIDON mission, with a 254 pass 10-day exact repeat cycle (Figure 2.18). Line W was originally chosen to be on T/P track number 126 (Pena-Molino and Joyce, 2008). Between January 2002 and December 2008, 249 altimeter passes of Line W were made.

2.8 OCCAM Model

In order to supplement our observational study and to understand better some of the mechanisms controlling transport variability both in the interior and at the western boundary, 19 years of model output were obtained from the $\frac{1}{4}^{\circ}$ OCCAM model (Ocean Circulation and Climate Advanced Modelling Project). OCCAM (Webb et al., 1998) is a primitive equation

numerical model of the ocean, based on the GFDL MOM version of Bryan-Cox-Semtner, with an improved advection scheme and a free sea surface (Bryan, 1969; Semtner, 1974; Cox, 1984). It differs from many other ocean models in its use of a rotated grid for the North Atlantic and Arctic Oceans, which prevents the need for a very short timestep as the meridians converge near the North Pole. Wind stress at the surface is prescribed using the ECMWF monthly wind stress climatology. The model was spun up for 4 years and then run for a further 4 years to allow transients to dissipate. Model analysis was then carried out for 19 years from 1985 to 2003. More recently, the spatial resolution of the model has been increased to $\frac{1}{12}^{\circ}$ but time constraints prevented analysis of the model at this increased resolution. Full details of the model analysis are given in Section 5.6.

2.9 Summary

In this section, the main data sources and methods used to quantify the variability in both the interior and Gulf Stream transports have been discussed, along with the wind stress and NAO data that might force that variability. Further details of some of the methods are given in the results sections (e.g. the spectral and empirical orthogonal function analysis of the wind stress data). The remainder of the thesis details our results, with the magnitude and variability of the transports covered in Chapter 3 and the wind stress/NAO analysis in Chapter 4. Comparisons between the interior transport time series, Gulf Stream and wind stress/wind stress curl follow in Chapter 5.

Chapter 3

Results: Density Structure and Transports

In this chapter, the density structure and transport variability of the transatlantic section along 36°N and Line W are discussed. In Section 3.1, the results of the potential temperature and salinity interpolation are presented for each year and season, with the size and structure of the variability at both timescales quantified. The uncertainty in the mapping of each variable is analysed and the accuracy of the interpolation is investigated by attempting to replicate the θ/S section of the CD171 cruise. In Section 3.2, the density variability of the section is examined with reference to the dynamic height field, specifically focusing on the role of the seasonal and main thermoclines in controlling density changes across the section. The calculation of reference velocity fields at both 1000 dbar and 1500 dbar from Argo float trajectories is discussed in Section 3.3, along with refinements found to be necessary to the technique. The interior transport results are then discussed in Section 3.4, with the annual and interannual variability linked to changes in the density field of the section. Finally, efforts towards constructing a ten-day time series of Gulf Stream transport from differences in altimetric sea surface height anomaly are presented in Section 3.5.

3.1 Potential Temperature and Salinity Interpolation

The sections of potential temperature and salinity discussed below each use the mapping points shown in Figure 3.1. The blue mapping points comprise the stations from the CD171 cruise east of 68°W, using the northern crossing of the eastern boundary to the coast of Iberia, along with 24 mapping points along the Line W section. The closest Line W mapping point to the coast coincides with the position of the W1 mooring. For all the annual and seasonal sections, along with the estimates of the interior and full-basin transports, the section defined by the blue points is used. For the comparison between the objectively mapped fields of θ/S and the cruise-derived fields, the mapping points close to the western boundary do not follow Line W but instead use the northern crossing of the Gulf Stream

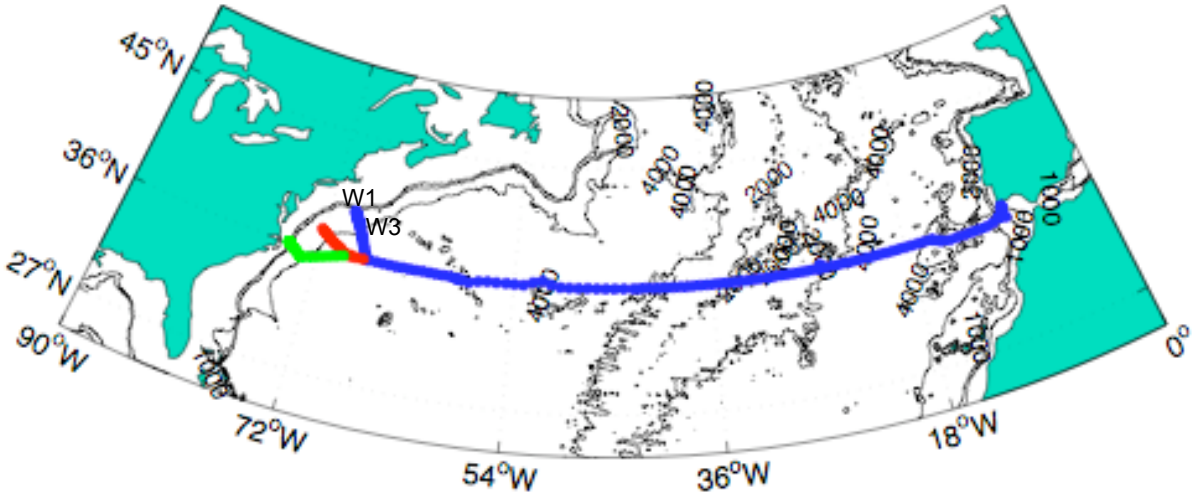

Figure 3.1: Mapping points used in the interpolation of θ/S fields. Blue points indicate the main section used (the CD171 cruise stations east of 68°W along with 23 mapping points along Line W). The position of the W1 and W3 moorings are marked. The red points indicate the alternative western boundary points used when comparing the interpolated θ/S data with the cruise section. The green points, showing the southern cruise crossing of the Gulf Stream, are included for information only. Further details are given in the text. 1000 m, 2000 m and 4000 m isobaths are marked.

made by CD171 (the red points). A topographic map of the section formed by the blue points is given in Figure 3.2.

3.1.1 Annual Sections

Potential temperature and salinity sections for the six years 2002 to 2007 from the optimal interpolation of the Argo float and Line W mooring data are shown in Figures 3.3 and 3.4. As the sections do not follow 36°N along Line W, the x axis displays distance along the section from the westernmost mapping point.

In all years, some regions with missing data can be identified. The largest persistent gap is close to the eastern boundary, especially in the region east of 4500 km along the baseline. In some years (e.g. 2005), no interpolated temperatures or salinities exist east of 5300 km, meaning that the 15 mapping points closest to the eastern boundary have no data. In other years, such as 2003, there are no data points deeper than 1000 dbar. This situation reflects the fact that there have been relatively few Argo float profiles collected close to the mouth of the Mediterranean, and even those that do exist generally do not profile deeper than 1000 dbar.

A second smaller region of missing data is found immediately east of the Mid-Atlantic Ridge. This gap, originally identified in Section 2.1.1, is generally found below 1500 dbar, but is larger in both vertical and zonal extent in 2007. Investigation of this region reveals that

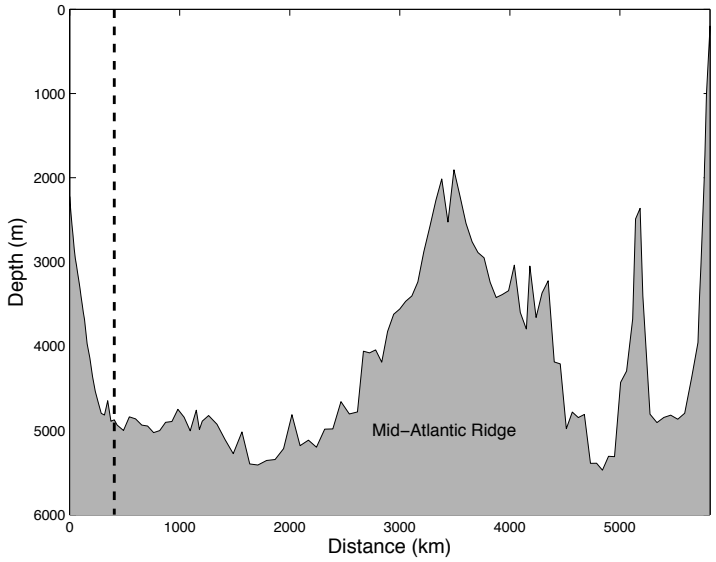

Figure 3.2: Topographic detail of our mapped section along 36°N and Line W. Data were obtained from the 5 minute TerrainBase database of global topography. The vertical dashed line indicates the point at which Line W meets the CD171 cruise track.

most of the available floats are of the Webb Research APEX type, which were programmed to profile only as deep as 1500 dbar, with occasional profiles reaching 2000 dbar. The larger data gap extending to the surface in 2007 occurs because of a lack of float profiles close to the 36°N mapping line in this year.

Despite these missing data, the main zonal trends in potential temperature and salinity across the basin can be identified. Close to the western boundary, the sharp zonal gradient in both potential temperature and salinity associated with the Gulf Stream is found. The extra data provided by the W1 and W3 Line W moorings improves determination of this structure west of 200 km along the baseline. Immediately east of the Gulf Stream, the core of the subtropical gyre is located, identifiable by its maximum in both potential temperature (up to 26°C) and salinity (up to 36.8) in the upper 200 m. Furthermore, a thick (around 200 m) layer of water in the 17°C to 19°C temperature range is found in most years, this being the ubiquitous Eighteen Degree Water formed by wintertime convection and discussed at length in Chapter 1. Across the rest of the basin, a gradual reduction in both potential temperature and salinity is observed in the upper 600 m, with isopycnals shoaling by roughly 300 m. Beneath the North Atlantic Central Water and east of 3000 km, the warm and salty core of Mediterranean Water can be found, identifiable by a maximum of salinity in all years close to 1200 m. The salinity maximum is especially pronounced east of 4500 km, with salinity falling rapidly west of 20°W. This accords with analysis by Iorga and Lozier (1999) which argues that Mediterranean Water is only advected as far west as 20°W, with pathways in the rest of the eastern basin being solely diffusive (Section 1.7). The interpolated fields thus successfully reproduce, in a qualitative sense, the main hydrographic features of the section observed previously (Fuglister, 1960; Roemmich and Wunsch, 1985; McDonagh et al., 2010).

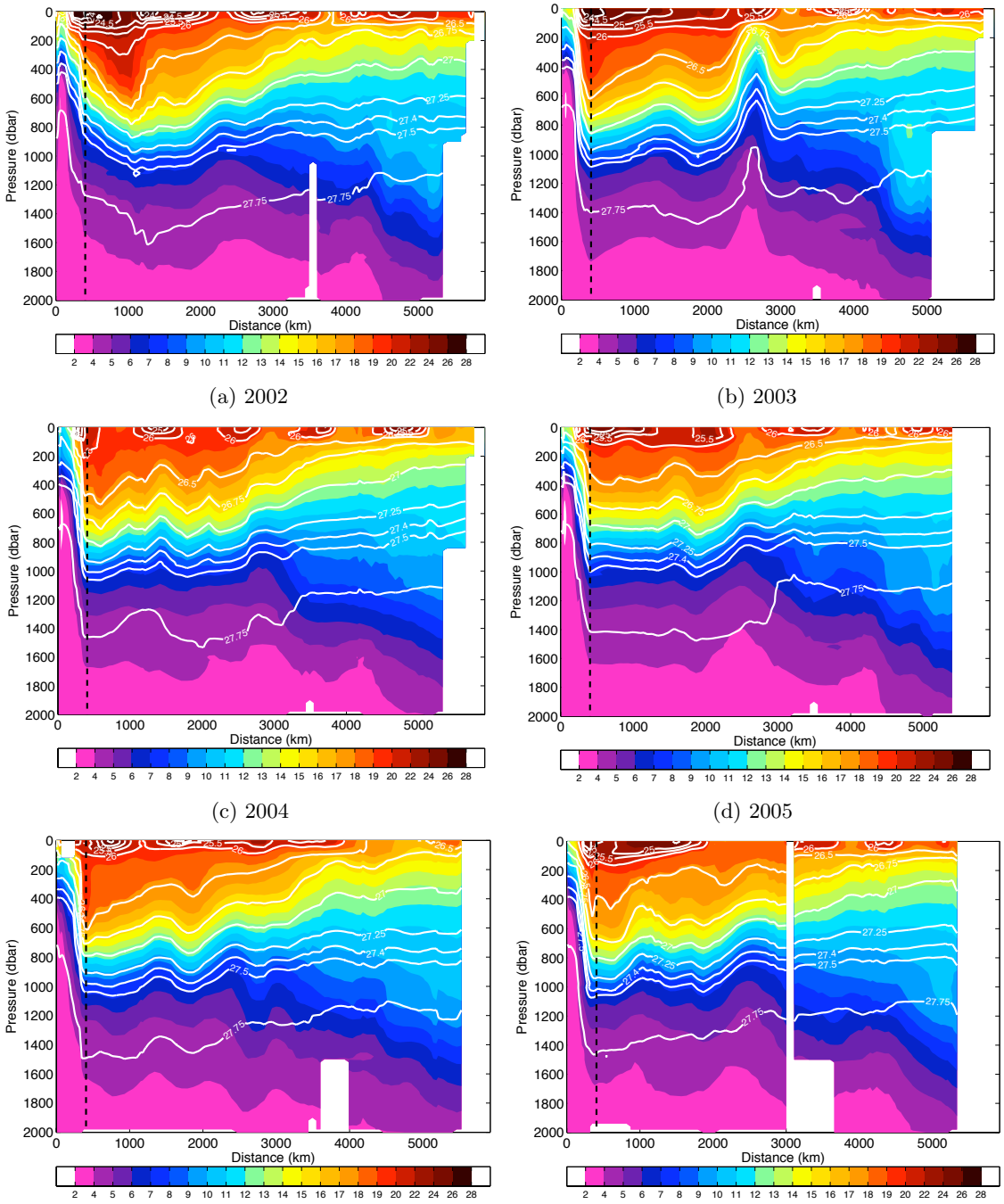

(a) 2002 (b) 2003

(c) 2004 (d) 2005

(e) 2006 (f) 2007

Figure 3.3: Potential temperature (in °C) for 2002-2007 with potential density (σ_0) contours overlaid. The vertical dashed line close to 400 km indicates the point at which Line W meets the CD171 cruise track. The crest of Mid-Atlantic Ridge is located between 2700 km and 3700 km along the baseline, with the crest close to 3200 km. White regions show areas of missing data.

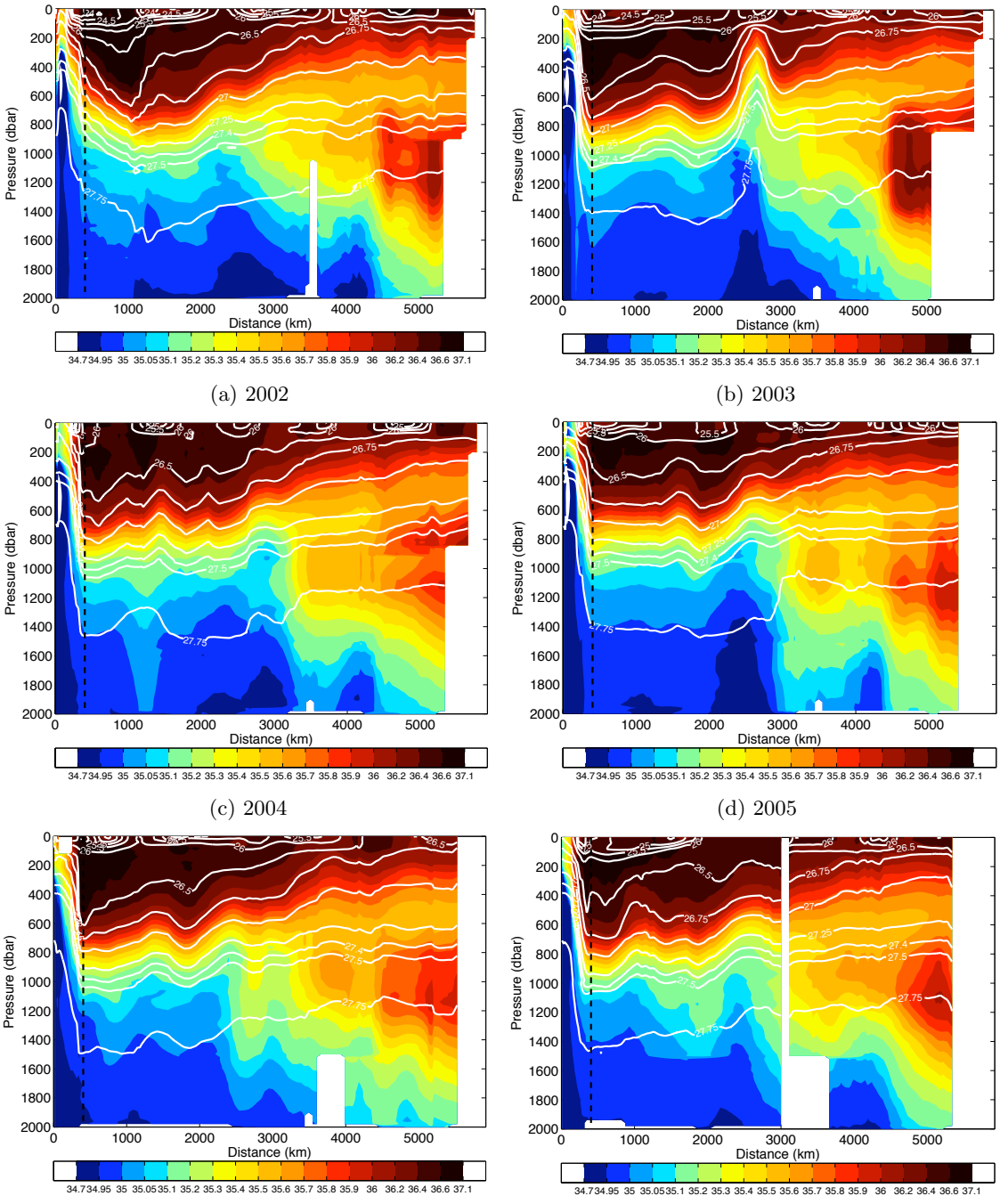

(a) 2002 (b) 2003

(c) 2004 (d) 2005

(e) 2006 (f) 2007

Figure 3.4: Salinity for 2002-2007 with potential density (σ_0) contours overlaid. The vertical dashed line close to 400 km indicates the point at which Line W meets the CD171 cruise track. The crest of Mid-Atlantic Ridge is located between 2700 km and 3700 km along the baseline, with the crest close to 3200 km. White regions show areas of missing data.

Mapping Errors in the Annual Sections

Prior to using these sections to estimate the geostrophic shear, a consideration of the limitations and errors of the optimal interpolation is needed. Whilst the general features of the sections (Figures 3.3 and 3.4) are qualitatively sound, close inspection of the temperature and salinity sections in some years reveals some unexpected features. These raise questions about the whether the output from the OI really represents an 'annual mean' of the section or is still subject to eddy variability caused by undersampling. The most obvious example is in 2003, where an anomalous cold and fresh feature is found between 200 and 1500 m close to 2500 km along the baseline (42°W). Furthermore, the temperature and salinity structures at the western boundary in 2002, 2003 and 2004 appear rather unrealistic, with a strong deepening of the isopycnals inshore of the Gulf Stream (e.g. Figures 3.3a and 3.4a). Such a feature is not observed on any of the cruise sections taken as part of the Line W programme (Toole et al., 2010), or in the CD171 cruise section. Finally, the number of profiles available to the OI appears to be seasonally biased towards summer and autumn in 2002 (Table 3.1).

To investigate the first of these issues, the data contributing to the mapping points near 42°W in 2003 were identified. Although 40 Argo profiles were found to contribute to the estimate of temperature and salinity at the 2 mapping points closest to 42°W, by far the largest weighting was given to a single profile collected on 4th October 2003 at 42.188°W, 35.987°W. This profile, collected by float 6900168, was located in a cyclonic cold core eddy with a raised thermocline, leading to the anomalous feature observed in the optimal interpolation. Some smaller eddy features are also observed in the surface layer (e.g. in 2004) but are not found beneath the main thermocline. As the quantity of delayed mode quality control data close to the 36°N latitude line increases later in the period, temporal aliasing as observed in 2003 is not as apparent, though it cannot be guaranteed to be absent if a strong eddy lies very close to an individual mapping point.

The second error, characterised by deepening isopycnals onshore at the western boundary in the years 2002 to 2004, is the result of the large geographical variability in this region. In 2002 to early 2004, the profiles contributing to the estimates of temperature and salinity at the mapping point coincident with mooring W1 (located at 39.44°N, 69.60°W) were those from mooring W3 along with a variety of float data (W1 itself was not deployed until mid-2004). As the variability in this region is so great, even the reduced 150 km length scale means that data not necessarily representative of the mapping point is being included within the interpolation. Reducing the scale further, however, would lead to a large data gap. After 2004, the problem does not appear as the deployment of the W1 mooring improves the estimate at the mapping points close to the continental shelf. However, a data gap is found in the top 100 m during 2006 as a result of a lack of Argo profile data (the W1 and W3 moorings only profile up to 100 m).

Given the seasonal bias identified in the 2002 data, the final interior transport estimates

Season	Spring	Summer	Autumn	Winter	Annual
Months	MAM	JJA	SON	DJF	Total
Number of 2002 profiles	258	305	337	251	1151
Number of 2003 profiles	307	332	393	353	1385
Number of 2004 profiles	427	431	425	456	1739
Number of 2005 profiles	349	314	264	346	1273
Number of 2006 profiles	222	228	224	241	915
Number of 2007 profiles	209	228	238	219	894
Number of 2000/2001/2008 profiles	89	88	128	254	559
TOTAL NUMBER OF PROFILES	1861	1926	2009	2120	7916

Table 3.1: Number of delayed mode Argo float profiles/ Line W mooring profiles available in each season in the latitude band 30°N to 45°N.

(Section 3.4) do not include data from this year, as it is shown later that the transports in the western basin are unrealistic (Figure 3.37).

Through discussion of these errors, it is clear that careful interpretation is required by the oceanographer to identify problems in the OI fields. The OI technique does not have any inbuilt process that makes the solution realistic from an oceanographic perspective (e.g. no density inversions). Furthermore, the 2002 section is probably affected by seasonal bias and should not be automatically interpreted as an annual mean. Nevertheless, there is less evidence of temporal aliasing is apparent after 2004 as the volume of delayed mode data close to the mapping point increases.

Interpolated Temperature and Salinity Errors

A primary advantage of the OI is that robust estimates of the mapping error for temperature and salinity are produced (Equation 2.12). In brief, the error variance gives an estimate of the likely error based on the size of both the covariance within the Argo data used at the mapping point and the covariance between the Argo data and the annual background climatology. The size of these errors for each year is shown in Figures 3.5 and 3.6 for both potential temperature and salinity.

For both variables, the magnitude of the error variance generally decreases slightly in the later years (2005-2007). In both 2002 and 2003, the potential temperature error variance within 1000 km of the western boundary is as large as 3°C, but improved data coverage in this region in later years confines the region with errors as large as 2°C to the Gulf Stream only. The situation for salinity is broadly similar, with the largest errors (0.5) near the western boundary in years 2002 and 2003. Whilst the overall number of profiles eligible for inclusion in the mapping is *not* greater in later years (Table 3.1), a large improvement is found in the number of available profiles receiving large weighting by virtue of being close to the mapping points in the Sargasso Sea. For instance, in 2002, the mean number of profiles contributing to the potential temperature estimate at each mapping point in the western basin was 24; by 2003 this had increased to 39.

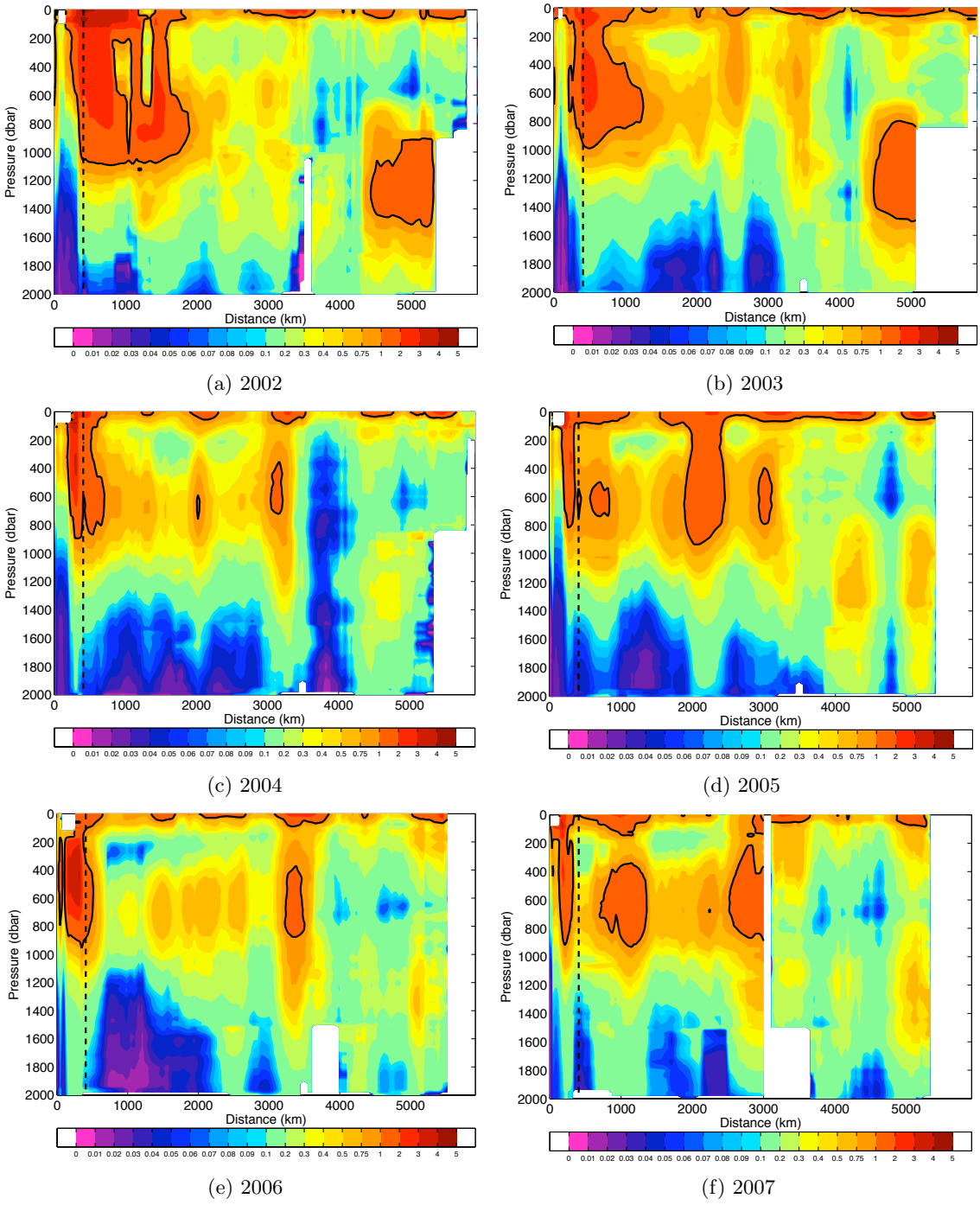

(a) 2002

(b) 2003

(c) 2004

(d) 2005

(e) 2006

(f) 2007

Figure 3.5: Potential temperature error variance as diagnosed by the OI for 2002-2007. Areas with an error of greater than 1°C are enclosed by the bold black contour. White regions denote data gaps.

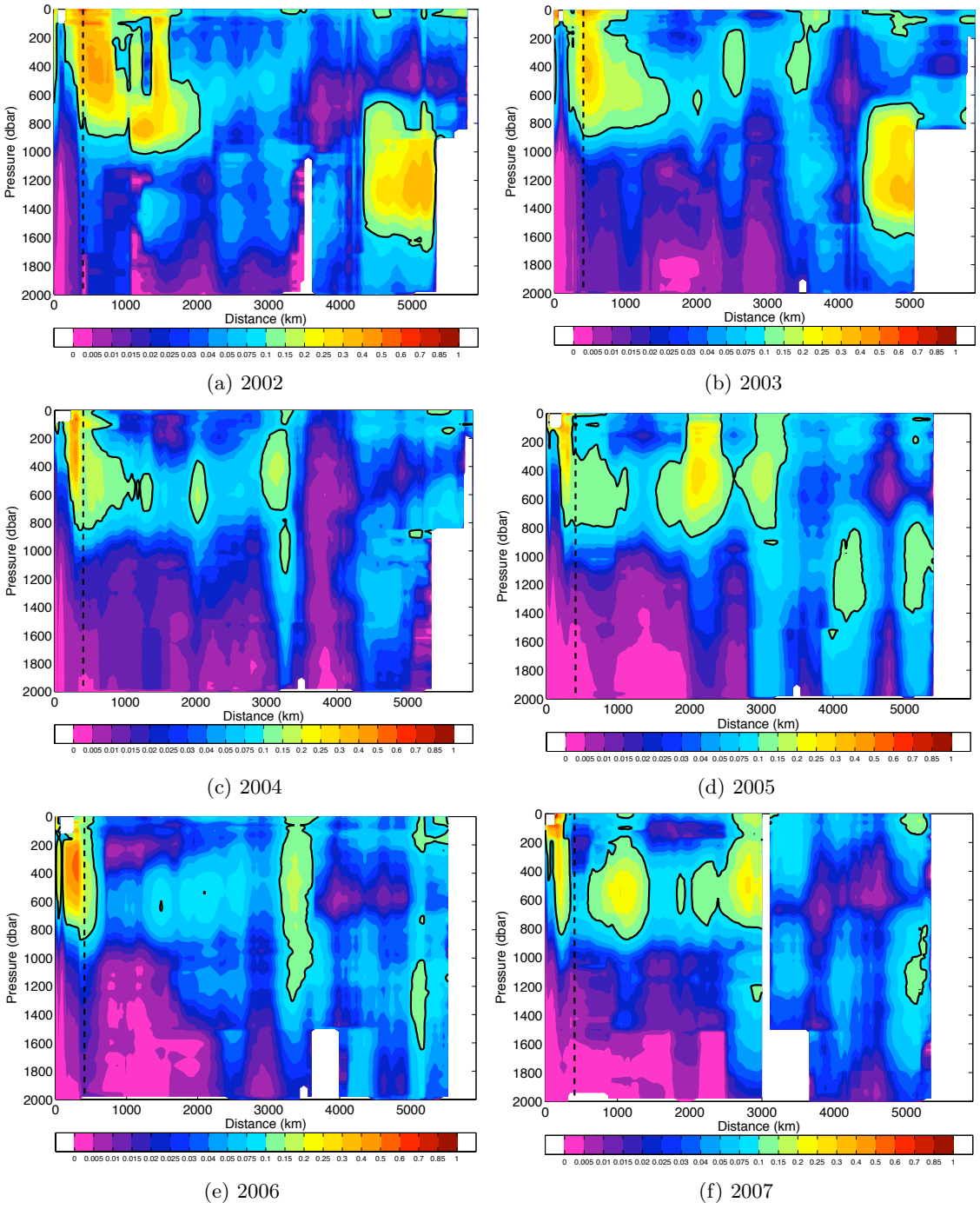

(a) 2002 (b) 2003

(c) 2004 (d) 2005

(e) 2006 (f) 2007

Figure 3.6: Salinity error variance as diagnosed by the OI for 2002-2007. Areas with an error of greater than 0.1 are enclosed by the bold black contour. White regions denote data gaps.

Across the rest of the ocean, the largest errors are generally found above 500 m and especially in the region above 100 m where seasonal and mesoscale variability is strongest. Large errors are also found in 2002 and 2003 in the Mediterranean Water layer. As much of the movement of Mediterranean Water into the interior of the Atlantic is known to be through meddies as opposed to mean advection (Iorga and Lozier, 1999), the potential temperature and salinity characteristics of this layer are temporally and spatially variable, leading to the greater error variance in this region. After 2004, there is generally improved data coverage in the region, minimising the size of the error, although it still reaches 0.5°C in 2007. How these errors affect the magnitude of the interior transport variability will be discussed in Section 5.3.

The large magnitude of the error variances in the surface layer (especially above 100 m) that extend across most of the basin might be reduced by using a seasonal climatology to calculate the θ and S anomalies in Equation 2.4. All recent versions of the World Ocean Atlas have incorporated monthly means for temperature and salinity; the accuracy of the θ and S estimates for individual years might be improved by calculating each of the anomalies in the annual estimate relative to its *monthly* mean. This would ensure that any variability caused simply by seasonal aliasing is removed, thus making the conclusions in Section 3.4 more robust. The advantage of using seasonal anomalies is discussed in more detail when comparing the OI data with the cruise data below.

Signal-to-Noise Ratio

In addition to the error variance, the method also allows the size of the signal to noise ratio (SNR) to be evaluated at each mapping point. The signal to noise ratio is expressed as s^2/η^2 (Equations 2.7 and 2.8). If the signal-to-noise ratio is less than 1, the large amplitude of the variance within the data set makes the data indistiguishable from the climatological background state, whereas with a higher signal to noise ratio there is confidence that the ocean state at the observing point is different to the climatology. It is important to note here that WOA01 does not incorporate any Argo data, whereas later versions (WOA05 and WOA09) do contain Argo T and S data. As a result, it might be expected that WOA01 will yield a higher signal-to-noise ratio than the later climatologies, especially if long-term changes in T or S have taken place. Figure 3.7 shows the zonal structure of the vertically averaged signal-to-noise ratio for potential temperature and Figure 3.8 shows the vertical structure.

The vertically averaged plots (Figure 3.7) show that the size of the signal to noise ratio (SNR) is generally above one across the whole of the basin, with the exception of the eastern and western boundaries. In 2002, there is also a significant region between 1500 and 3500 km where the SNR is close to one, whilst it dips slightly below one in 2003 in the Sargasso Sea. The vertical structure of the SNR, shown in Figure 3.8, confirms these patterns, with low SNR observed throughout the entire pressure range (surface to 2000 m) at the western boundary. The low SNR found in 2002 in the western basin is largely confined to below 800 m, whilst the low SNR region observed in 2003 occurs throughout the entire pressure

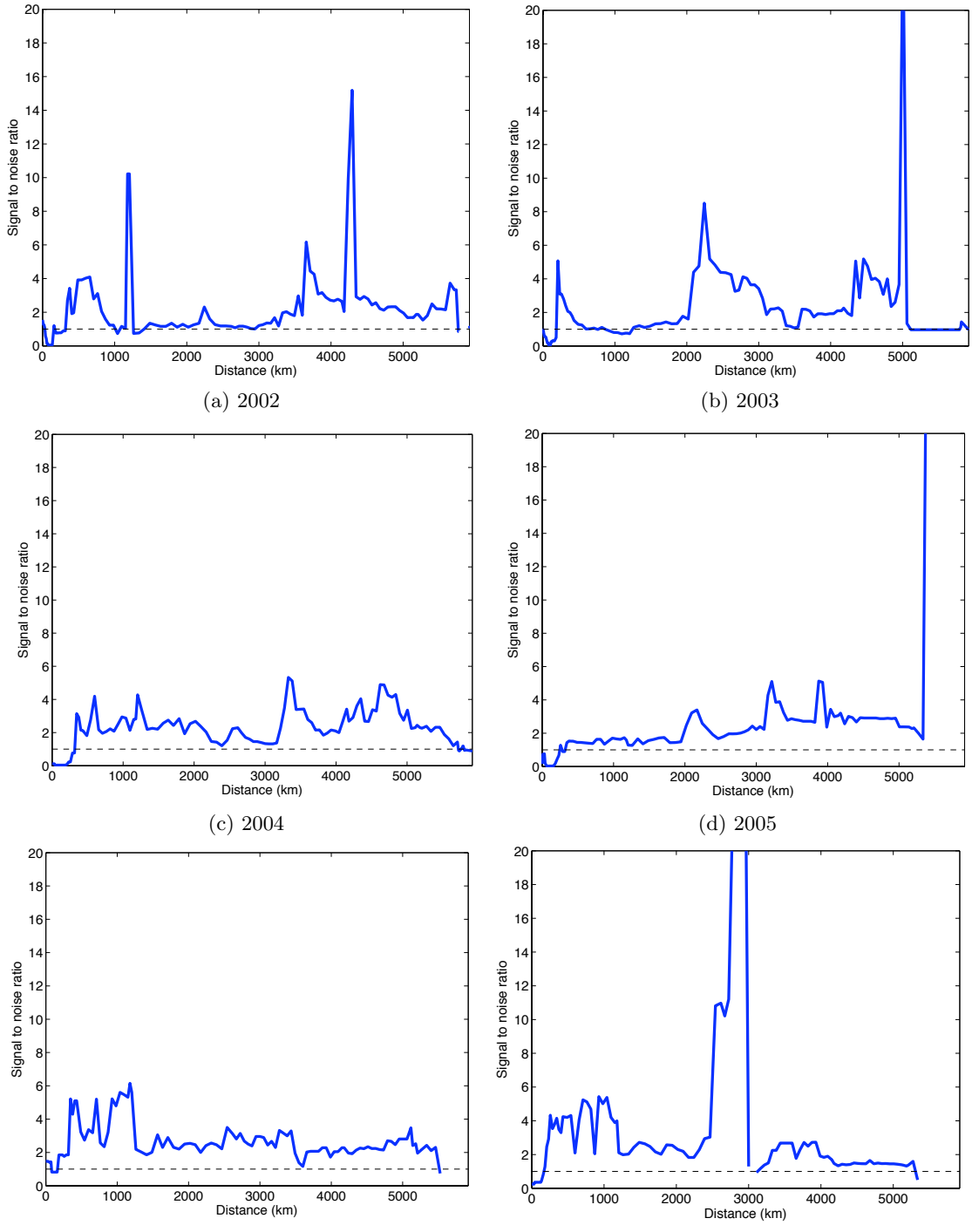

(a) 2002 (b) 2003

(c) 2004 (d) 2005

(e) 2006 (f) 2007

Figure 3.7: Vertically-averaged signal-to-noise ratio for potential temperature as diagnosed by the OI. The horizontal dashed line signifies a signal-to-noise ratio of 1.

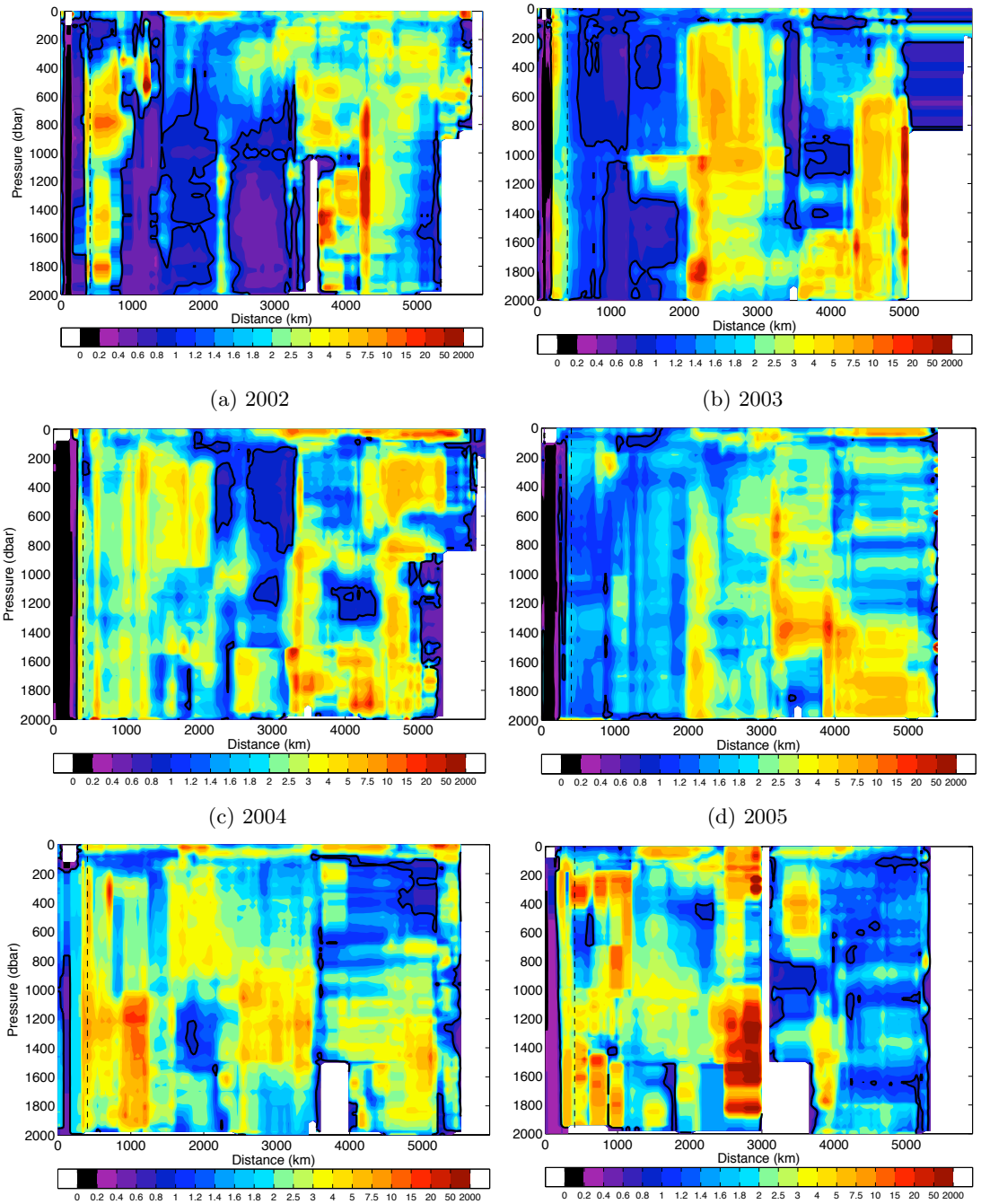

(a) 2002 (b) 2003

(c) 2004 (d) 2005

(e) 2006 (f) 2007

Figure 3.8: Signal-to-noise ratio diagnosed from the OI for potential temperature for the years 2002 to 2007. Areas with a signal-to-noise ratio of less than 1 are outlined with a black contour.

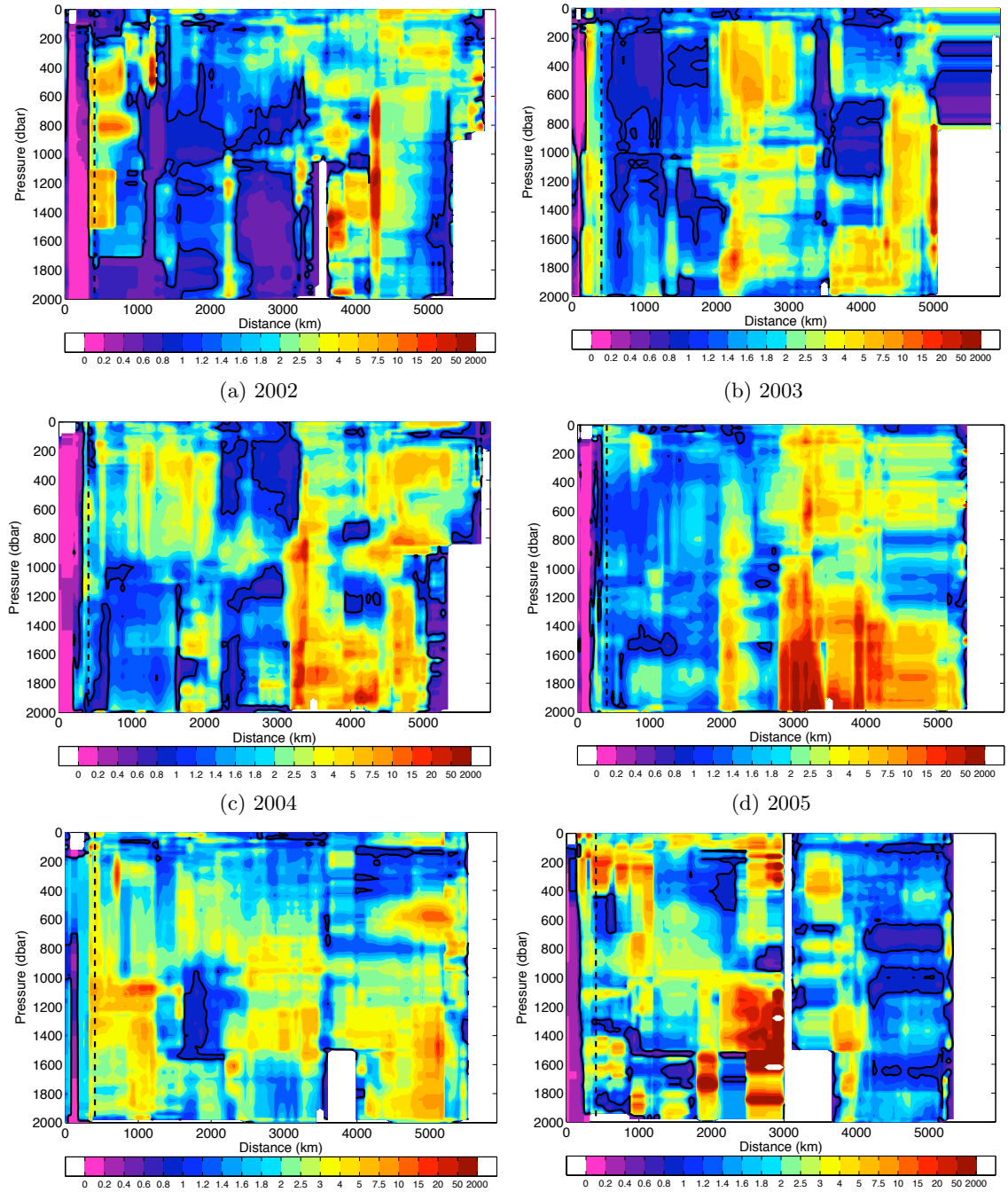

(a) 2002 (b) 2003

(c) 2004 (d) 2005

(e) 2006 (f) 2007

Figure 3.9: Signal to noise ratio diagnosed from the OI for salinity for the years 2002 to 2007. Areas with a signal-to-noise ratio of less than 1 are outlined with a black contour.

range. From 2004 onwards, the SNR in the western basin improves, with regions of low SNR becoming confined to isolated patches. The SNR for salinity (Figure 3.9) has very similar results.

In conclusion, the error analysis has revealed that the error variance in potential temperature is less than 0.5°C over the majority of the basin, with the value for salinity being generally less than 0.05. The largest errors are found in 2002 and 2003 in the Gulf Stream close to the western boundary (where the background variability in temperature and salinity is greatest). Examination of the signal-to-noise ratio confirmed the larger background noise in the western basin and the improvement in signal with better data coverage especially after 2004. It is also apparent from this analysis that mapping errors from the interpolation are a much larger source of uncertainty than the instrumental error in temperature or salinity measurement, which are typically reduced to 0.01°C for temperature and 0.01 for salinity after delayed mode quality control (Wong et al., 2003).

Comparison with Cruise Data

As a final check on the ability of the interpolation to produce accurate potential temperature and salinity fields, the θ/S sections from the 2005 cruise CD171 were compared with sections constructed from the optimal interpolation. Specifically, it was decided to test the relative size of the root mean squared differences of potential temperature and salinity between the optimal interpolation and a five-point moving average of the CD171 cruise data. Analysis was also conducted to test whether the five-point moving average cruise data falls within the error bars defined by the OI (Equation 2.12). The methods used were as follows:

1. All delayed mode Argo θ/S data within the latitude band 30°N to 45°N during the period of the cruise (1st May to 15th June 2005) were extracted. This was supplemented at the western boundary by θ/S data from the W1 and W3 Line W moorings for the same time period. In total, there were 170 available profiles, each of which was linearly interpolated onto a 20 dbar vertical grid as deep as 2000 dbar.

2. Using the same length scales as used for the annual estimates (350 km/150 km), optimal potential temperature and salinity estimates were produced. As the analysis of zonal length scales from the CD171 cruise data in Section 2.3.2 did not give significantly different results to the Argo data, these scales were deemed appropriate even though this is a short time window. At the western boundary, the northern cruise mapping points were used (the red points in Figure 3.1).

3. The root mean squared differences between the optimal estimate and five-point moving average cruise data were calculated for both potential temperature and salinity. The cruise data were smoothed prior to calculating the RMS differences as the OI is not capable of resolving small-scale eddy features in the cruise data with a length scale of less than 350 km. The station spacing (60 km to 70 km) means that using a five-point moving average is equivalent to smoothing the cruise data to around 350 km. For

comparison, the RMS difference between the WOA01 Climatology and the cruise data was also evaluated, in order to establish the extent to which the float and mooring data improves the climatological estimate.

4. The interpolation was repeated using Argo and Line W data collected from 1st April to 15th July (i.e. adding an additional month of data before and after the cruise) and using data collected from 1st March to 15th August (adding an additional two months). Hereafter, the three time windows are referred to as the ±0 month, ±1 month and ±2 month cases respectively.

In total, 170 Argo and Line W profiles were collected during the cruise period (1st May to 15th June), 387 profiles in the ±1 month period and 615 in the ±2 month period (Figure 3.12). The potential temperature and salinity sections for each of these cases are shown in Figures 3.10 and 3.11 respectively, along with those taken from the cruise and the WOA01 Climatology.

The interpolation using data collected only during the cruise period (Figures 3.10b and 3.11b) most closely matches the moving average cruise data for both potential temperature and salinity. When compared with the background climatology (Figures 3.10e and 3.11e), the interpolated fields provide a more realistic representation of the shape of the thermocline during May 2005, especially in the western basin. There is also a small improvement in the temperature and salinity properties of the Mediterranean Water east of 30°W. In comparison, the ±1 month and ±2 month realisations do not match the cruise data as closely, with both realisations tending to overestimate the near-surface temperature and salinity west of 1000 km along the baseline and in the region east of the Mid-Atlantic Ridge. These observations are formalised into RMS differences in Table 3.2, along with the RMS difference between the moving average cruise section and the WOA01 annual climatology.

Several observations can be made from Table 3.2. Whilst the interpolation using only data collected during the cruise yields an RMS error over 20% smaller than that from the WOA Climatology (0.63°C for potential temperature compared with 0.80°C), the errors for the ±1 and ±2 month cases are larger. Indeed, the ±2 month realisation is actually a worse representation of the smoothed cruise data than the annual WOA01 Climatology. Nevertheless, the relatively small RMS errors for the ±0 month case indicates that the interpolation is a substantially better at estimating the actual ocean conditions at monthly timescales than simple annual climatology, provided sufficient Argo data are available.

Two possible reasons exist for the improvement in RMS error value achieved by using Argo data collected only during the cruise (as opposed to including data from 1 or 2 months either side of the cruise). The first is simply that the data collected only during that time window are most representative of the conditions observed by the hydrographic section, and are not subject to temporal aliasing caused by sampling data from a longer period. However, as our OI scheme does not calculate anomalies relative to a monthly or seasonal value of WOA01, it is also possible that longer time windows could be affected by seasonal bias that does not reflect a 'real' difference in temperature or salinity.

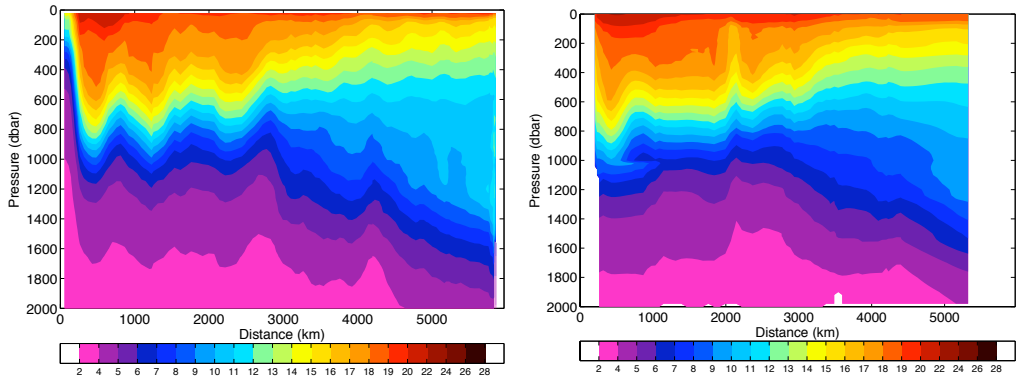

(a) CD171

(b) ±0 month

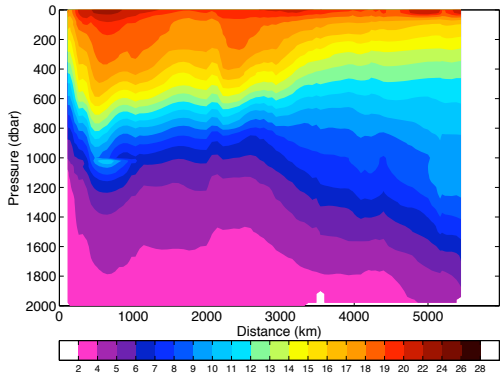

(c) ±1 month

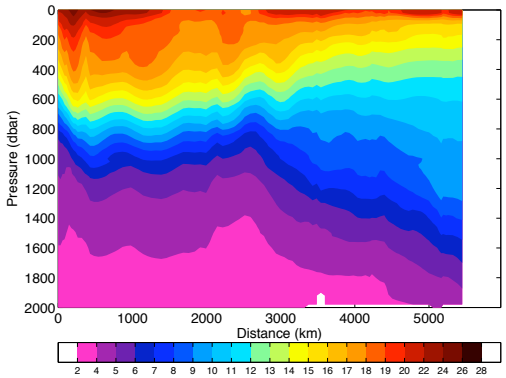

(d) ±2 month

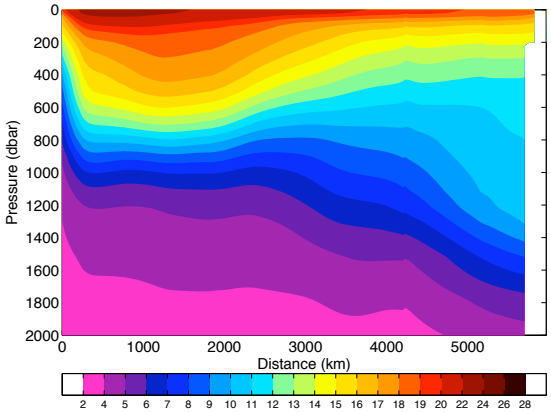

(e) WOA01

Figure 3.10: Potential temperature (in °C) along the CD171 cruise track. (a) Five-point moving average data from cruise; (b) Result of OI for period 1st May to 15th June 2005; (c) Result of OI for period 1st April to 15th July 2005; (d) Result of OI for period 1st March to 15th August 2005; (e) Result from WOA01 Climatology.

Time window	**Number of profiles**	**RMS error (° C) for θ**	**RMS error for S**
±0 month	170	0.63	0.089
±1 month	387	0.65	0.090
±2 month	615	0.84	0.112
Annual WOA01	-	0.80	0.114

Table 3.2: RMS errors for different Argo realisations of the CD171 cruise section (see text).

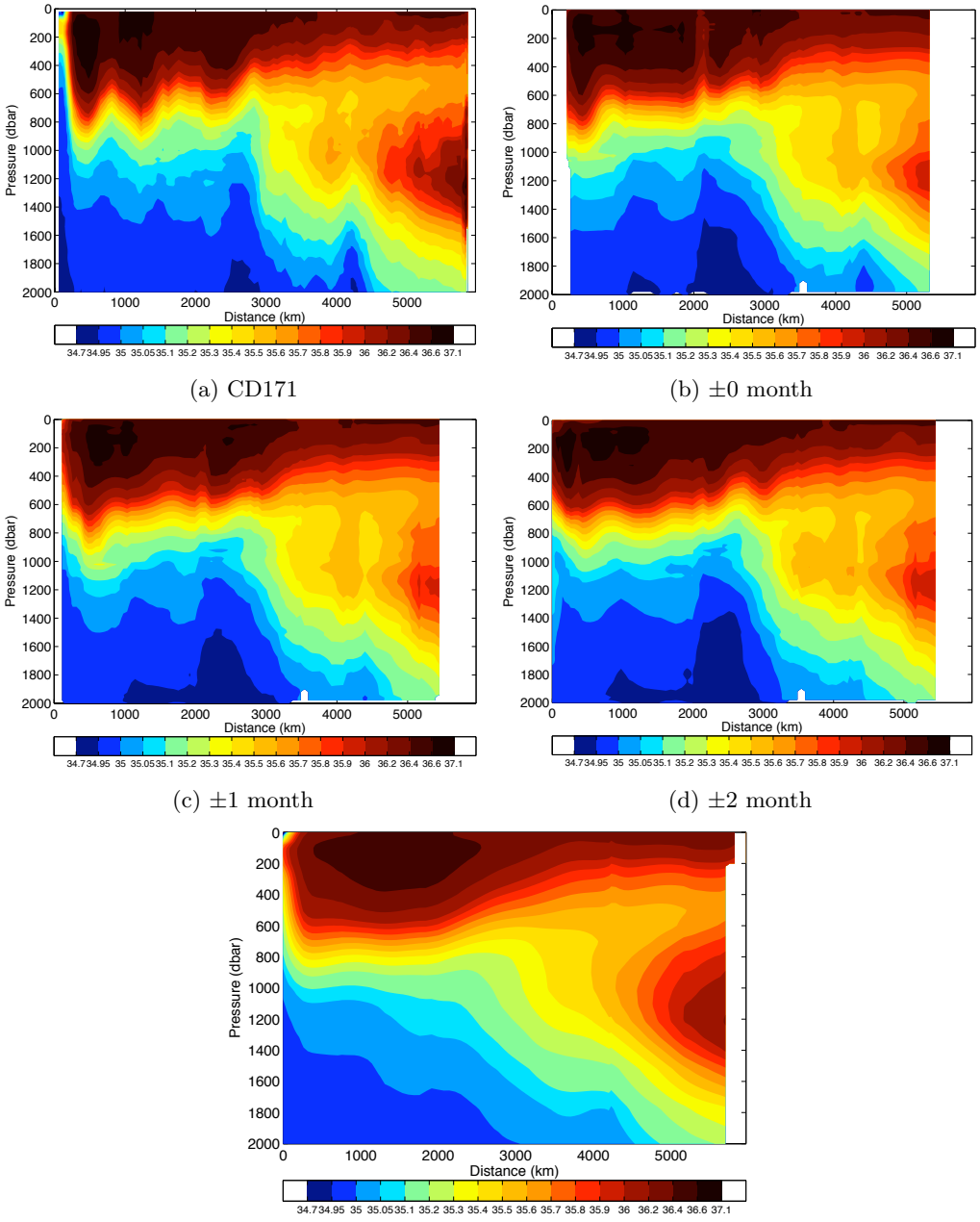

(a) CD171

(b) ±0 month

(c) ±1 month

(d) ±2 month

(e) WOA01

Figure 3.11: Salinity along the CD171 cruise track. (a) Data from cruise; (b) Result of OI for period 1st May to 15th June 2005; (c) Result of OI for period 1st April to 15th July 2005; (d) Result of OI for period 1st March to 15th August 2005; (e) Result from WOA01 Climatology.

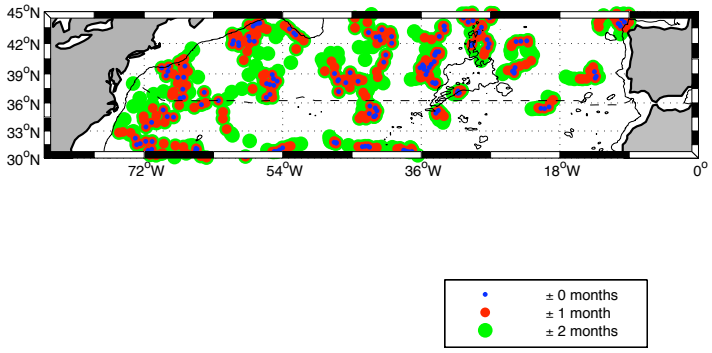

Figure 3.12: Map to show locations of θ/S profiles used in the interpolation for 1st May to 15th June 2005 (blue dots), 1st April to 15th July 2005 (red dots) and 1st March to 15th August 2005 (green dots).

To understand the difference made by the selection of a longer timeframe, plots of the difference between the five-point moving average cruise data and the ± 0 month and ± 1 month realisations are given in Figure 3.13. Whilst there is some increase in the error in the top 100 m between the ± 0 month and ± 1 month cases, which may reflect seasonal bias, many of the differences between the two realisations occur in the main thermocline (200 m to 1000 m) of the western basin. This suggests that temporal variability not related to the formation and erosion of the seasonal thermocline is responsible for much of the difference between each realisation. It might therefore be expected that using a monthly or seasonal WOA to reduce seasonal aliasing would not cause a significant decrease in the RMS errors of the ± 1 month or ± 2 month realisations. However, this remains to be tested formally.

As a final test of the OI, it was decided to investigate whether the smoothed cruise data fell within the error bounds defined by Equation 2.12. The error variances of temperature and salinity were first converted to standard deviations and then multiplied by two to yield a 2σ error bound on the ± 0 month OI estimate. The absolute size of the error (from the difference between the OI and the cruise estimate) was then extracted and the difference between this error and the 2σ error bound was plotted (Figure 3.14). The results show that the smoothed cruise data fall within the 2σ error bound of the OI across almost the entire basin, with the exception of a few small parts of the western basin and in the Gulf Stream. This verifies that our OI technique can reproduce a cruise section to within the specified mapping error along the 36°N line east of the Gulf Stream and can therefore be used to monitor the interannual and seasonal variability in the baroclinic transport (Section 3.4).

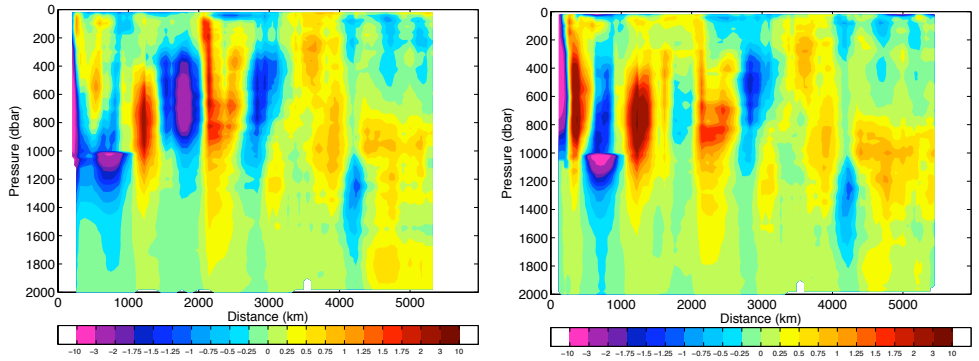

(a) ±0 month potential temperature (in ° C) (b) ±1 month potential temperature (in ° C)

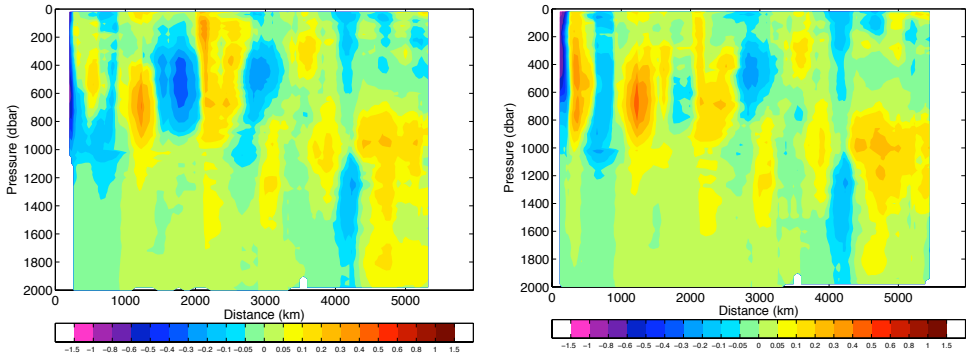

(c) ±0 month salinity (d) ±1 month salinity

Figure 3.13: Difference between the CD171 cruise data values and the results of the optimal interpolation for (a) Potential temperature (1st May to 15th June 2005); (b) Potential temperature (1st April to 15th July 2005); (c) Salinity (1st May to 15th June 2005); (d) Salinity (1st April to 15th July 2005).

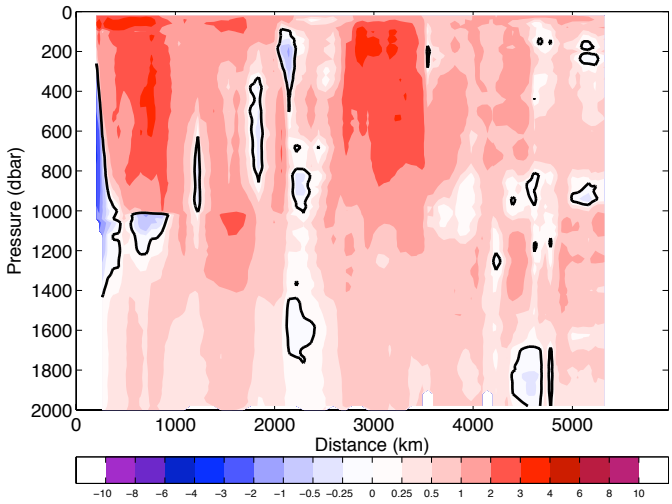

Figure 3.14: Difference between the 2σ OI mapping error for the ±0 month realisation and the actual error between the realisation and the 5-point moving average cruise data. Areas where the cruise data fall within the 2σ error band are shown in red. Regions where the mapping error underestimates the actual error are shown in blue.

3.1.2 Interannual Variability in the Potential Temperature and Salinity Fields

Given that the OI is capable of successfully capturing the year-to-year θ/S changes, attention turns to the size and structure of the interannual variability in these fields. As these variables are the primary controls on in-situ density in the equation of state, changes could strongly influence the dynamic height field and consequently the baroclinic part of the interior transport. Decadal-scale changes in temperature and salinity at 36°N have previously been observed by Leadbetter et al. (2007), explained in detail in Section 1.8.

Our results (Figure 3.15a) for the period 2003 to 2007 do not show such an organised change in potential temperature as Leadbetter's study, with greater variability instead over short distances. Nevertheless, there is a general cooling of the waters in the top 100 m, with a basin-averaged temperature change of −0.75°C. This general cooling of the surface layer exceeds the mapping error in a large region between 2000 km and 3000 km along the baseline, along with a smaller region immediately offshore of the Gulf Stream. Surface warming is only observed in three small areas: close to 100 km (the Gulf Stream), 3200 km (the Mid-Atlantic Ridge) and 4200 km. The plot of differences between 2003 and 2005 (Figure 3.15c) suggest that the surface cooling was concentrated in this period (especially in the western basin), with near zero basin-averaged change in the top 100 m from 2005 to 2007. The result is confirmed by the basin-averaged top 100 m temperature change values, which were −0.79°C and +0.04°C for the periods 2003 to 2005 and 2005 to 2007 respectively.

At thermocline depths (200 m to 1000 m), the temperature trends are highly heterogeneous, with warming between 2003 and 2007 near 2800 km and 4000 km and cooling in much of the western basin and the Mediterranean Water. The strong warming close to 2800 km is caused by the large cold anomaly observed on the section in 2003 (Figure 3.3b), which has previously been discounted as a single eddy; the rest of the changes appear to be more robust. Once again, the cooling in the western basin appears to be concentrated in the period 2003 to 2005, especially in the region immediately offshore of the Gulf Stream where a significant temperature change of up to 4°C is observed. In the later period (Figure 3.15e), a more general slight warming is observed in most of the section. Below 1500 m, temperature changes are generally smaller and only exceed the total mapping error at the bottom of the Mediterranean Water layer and in small parts of the western basin.

The results for salinity, shown in Figures 3.15b, 3.15d and 3.15f, display a strong similarity with those for potential temperature, with an increase in potential temperature being accompanied by an increase in salinity. Therefore, many changes are density-compensating. For instance, the general thermocline cooling of the western basin between 2003 and 2007 (and especially between 2003 and 2005) is accompanied by freshening of the water column. However, many of the surface water changes do not compensate in density: whilst the top 100 m of the western basin cools by up to 3°C between 2003 and 2005 (Figure 3.15c), the salinity changes are mixed, with some regions (e.g. in the Gulf Stream) showing surface

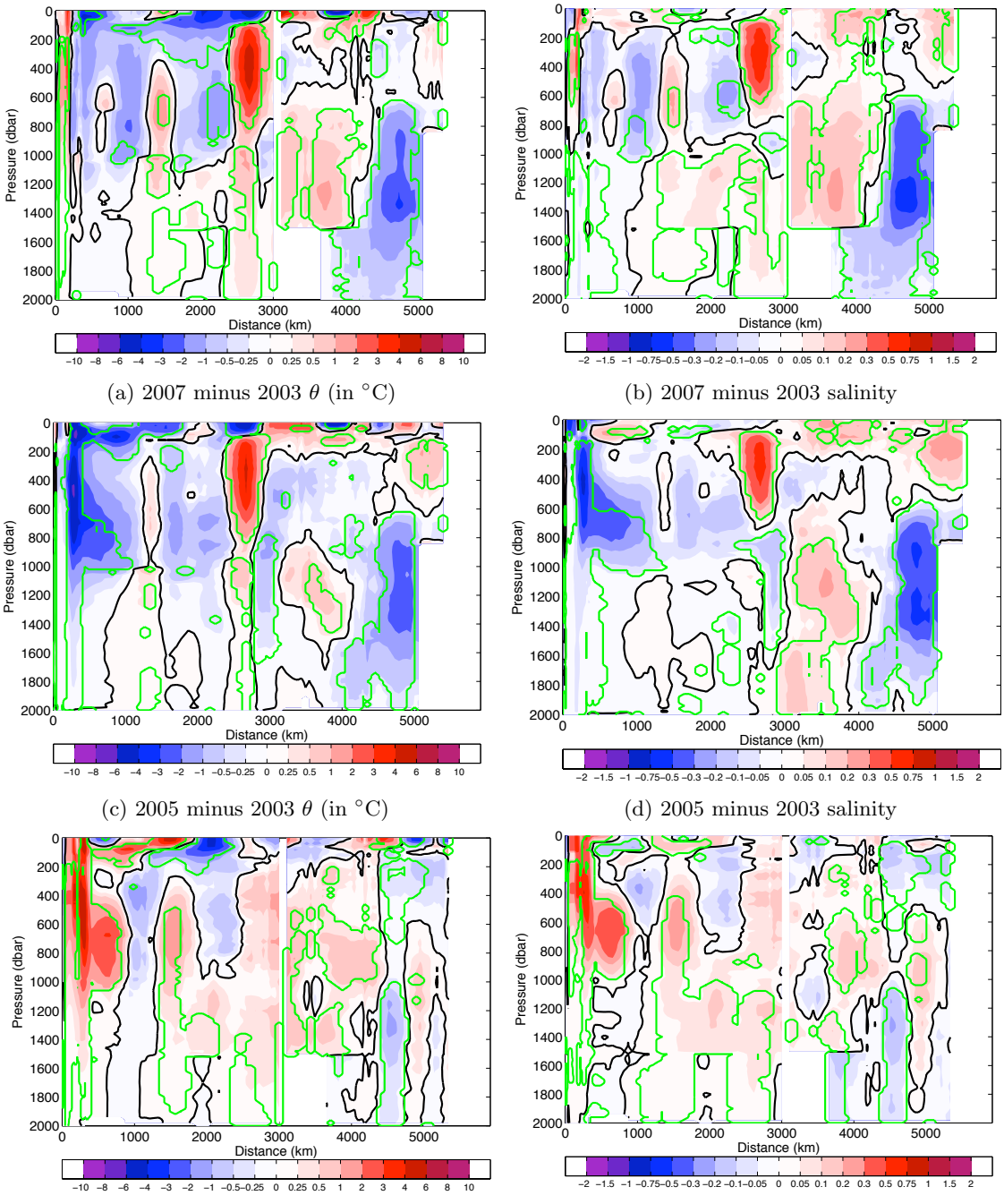

(a) 2007 minus 2003 θ (in °C)

(b) 2007 minus 2003 salinity

(c) 2005 minus 2003 θ (in °C)

(d) 2005 minus 2003 salinity

(e) 2007 minus 2005 θ (in °C)

(f) 2007 minus 2005 salinity

Figure 3.15: Potential temperature and salinity changes on pressure surfaces along the 36°N and Line W section for 2007 minus 2003 (top row), 2005 minus 2003 (middle row) and 2007 minus 2005 (bottom row). The green contour encloses the areas where the temperature/salinity change exceeds the sum of the error variances from the two years.

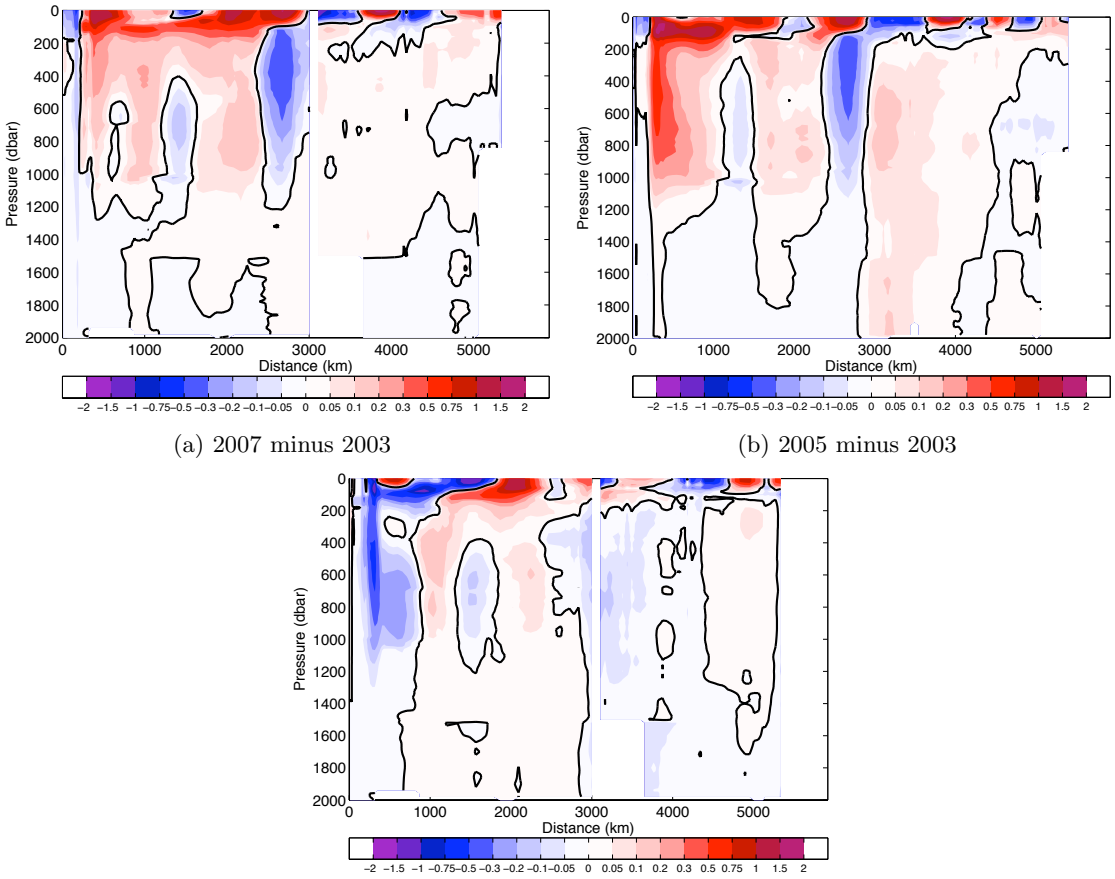

(a) 2007 minus 2003

(b) 2005 minus 2003

(c) 2007 minus 2005

Figure 3.16: Potential density changes (in kgm^{-3}) along the 36°N and Line W section for years: (a) 2007 minus 2003; (b) 2005 minus 2003 and (c) 2007 minus 2005.

freshening and others (e.g. between 500 and 1200 km along the baseline) becoming more saline.

The overall effect of these temperature and salinity changes on potential density relative to the surface (σ_0) is shown in Figure 3.16. Overall, temperature has the dominant influence, with the cooling in the upper 100 m causing an increase in the potential density of the surface layer between 2003 and 2007 (Figure 3.16a). This increase in density extends as deep as 1000 m in part of the Sargasso Sea. At the eastern end of the section, the density change below the seasonal thermocline is close to zero, meaning that there is an overall decrease in the dynamic height difference between the ends of the interior section. The baroclinic transport across the interior of the section in 2007 is thus expected to be smaller than in 2003, a conclusion confirmed in Section 3.4. Once again, the majority of the density changes appear to take place between 2003 and 2005, with density changes being smaller between 2005 and 2007 (Figures 3.16b and 3.16c).

In conclusion, the size of the interannual potential temperature and salinity changes over the six years is of comparable magnitude to the changes observed by Leadbetter et al. (2007) between three individual sections in 1957, 1981 and 2005 (Figure 3.17). Caution does need

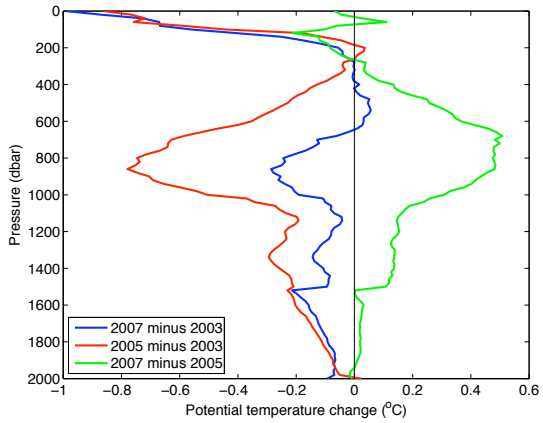

Figure 3.17: Basin-averaged potential temperature changes (in °C) for the periods 2003 to 2005, 2005 to 2007 and 2003 to 2007. Comparison with results from Leadbetter's paper (their Figure 2) reveals that the maximum temperature change between 1959 and 2005 (0.7°C in the upper 500 m) is similar in size to the largest changes observed in the period 2003 to 2007.

to be exercised given the large size of the error variance, particularly in the western basin during 2003 (Figure 3.5 shows a region of values greater than 1°C). However, given that there is no reason to believe that there is a systematic bias in the density at either end of the section (Section 2.1.2), or that the errors at the western and eastern end of the section are correlated, the changes in the density gradient observed between the years commonly exceed the mapping error and are thus likely to be real. Further error analysis focusing specifically on the transport fields is given in Section 5.3.

A more complete investigation of annual temperature and salinity changes would require decomposition of the changes into those resulting from changes *along* isopycnals and those due to vertical displacement of the isopycnals (heave). Such an analysis is not performed here but would help to determine whether year-to-year variability is dominated by water mass property changes or by variable Ekman-driven downwelling of isopycnal surfaces.

3.1.3 Seasonal Variability in the Potential Temperature and Salinity Fields

The interseasonal variability of both potential temperature and salinity fields was also investigated and compared with the interannual changes. The interpolation was repeated with the same length scales, but using only data collected within each meteorological season. The number of available profiles for each season is given in Table 3.1. This number is fairly constant throughout the seasons, suggesting no strong seasonal bias in the accuracy of the temperature and salinity estimates. Furthermore, each year between 2003 and 2007 is relatively well-represented, with the largest number of profiles in 2004 in all seasons. Some data were included from the years 2000, 2001 and 2008 in order to improve the seasonal estimates, but each of these years lacked sufficient delayed mode data to produce a reliable optimal estimate for the whole year. θ and S sections for the four seasons from the optimal interpolation of Argo float and Line W mooring data are shown in Figures 3.18 and 3.19.

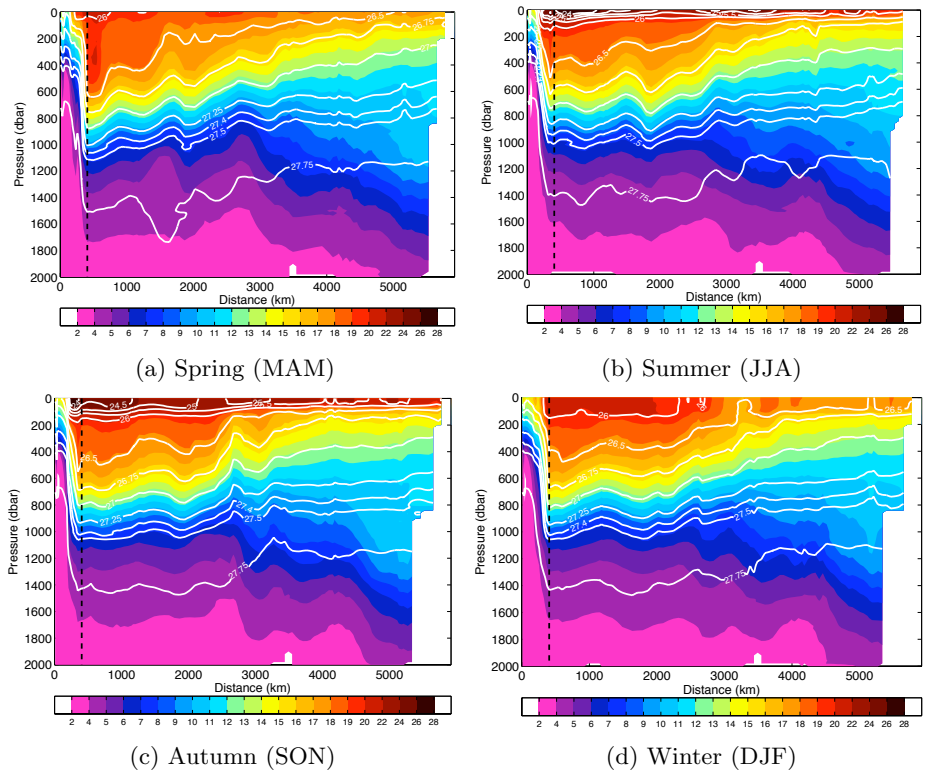

(a) Spring (MAM) (b) Summer (JJA)

(c) Autumn (SON) (d) Winter (DJF)

Figure 3.18: Potential temperature (in °C) by meteorological season with potential density contours overlaid.

Plots showing the mapping error variance for each season are found in Figures 3.20 and 3.21 for potential temperature and salinity respectively. As in the annual sections, the largest errors are found near the Gulf Stream in the upper 1000 m, where potential temperature errors can exceed 1°C and salinity errors can be greater than 0.1. In addition, a region of relatively large uncertainty is found in the proximity of the Mediterranean Water layer, owing to the large temporal and spatial variability in this region. Nevertheless, the seasonal estimates generally have smaller error variance than the individual years (Figures 3.5 and 3.6), primarily because of the larger number of available profiles for the seasonal estimates (around 2000) when compared with the annual estimates (around 1000). As was the case with the annual estimates, the θ/S anomalies could have been calculated relative to seasonal or monthly values of the World Ocean Atlas, which should further reduce the error variances in Figures 3.20 and 3.21, especially in the surface layer.

A number of observations regarding seasonal variability can be made. Near surface temperatures are 2 to 4°C higher throughout the section in summer and autumn compared with winter and spring (Figure 3.18), due to the formation and erosion of the seasonal thermocline. Meanwhile, the layer immediately below (200 m to 400 m) is warmer in the winter months. This pattern is particularly pronounced immediately offshore of the Gulf Stream, where cooler temperatures are observed in the summer between 100 and 1000 m. The reason for the summertime cooling of this layer is not obvious, but may be connected to the formation of EDW discussed in Chapter 1 (Worthington, 1959). In winter and spring, strong

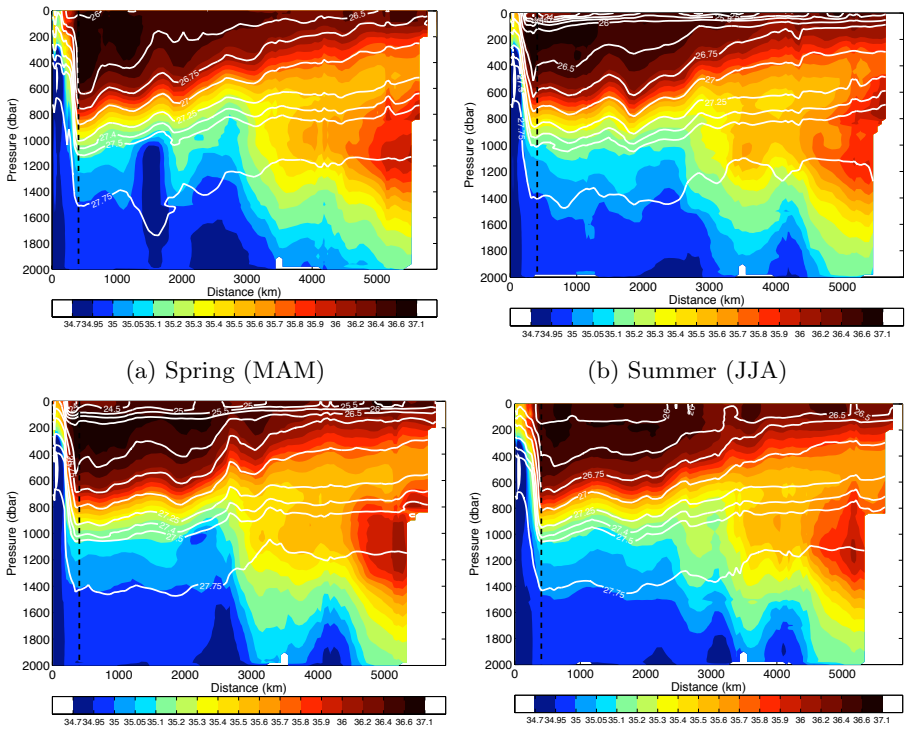

(a) Spring (MAM)

(b) Summer (JJA)

(c) Autumn (SON)

(d) Winter (DJF)

Figure 3.19: Salinity by meteorological season with potential density contours overlaid.

seasonal cooling leads to the formation of a 200 m deep homogeneous temperature layer (Figure 3.18d), eventually causing the formation of the EDW water thermostad, evidence of which is seen in Figure 3.18a between 2000 km and 3000 km along the baseline (50°W to 40°W). However, the water column then restratifies during spring and summer (Figure 3.18b). One possible explanation for the cooler subsurface layer is that this depth range becomes insulated from the surface by the seasonal stratification, allowing it to mix instead with deeper (and colder) water masses.

This seasonal cycle we have observed, including winter cooling of the surface layer with the accompanying formation of an 18°C thermostad, was previously found in the time series from the Panulirus station near Bermuda (32.17°N, 65.5°W) presented by Klein and Hogg (1996) (their Figure 8a).

For the salinity field (Figures 3.19 and 3.23), no obvious large-scale modes of variability can be observed, with almost all changes being less than 0.5. Towards the western end of the section, surface salinity decreases during summer, reinforcing the reduction in density, whilst east of 2000 km, surface salinity is generally greater during summer, partly compensating for the reduced density brought about by increasing temperature. In the region between 100 m and 300 m, where warmer temperatures were observed in winter, the salinity changes are mixed, with much of the western basin becoming fresher in winter and much of the eastern basin becoming saltier. This difference makes it difficult to interpret the reasons behind the sub-surface cooling in summer, as one might expect freshening to accompany

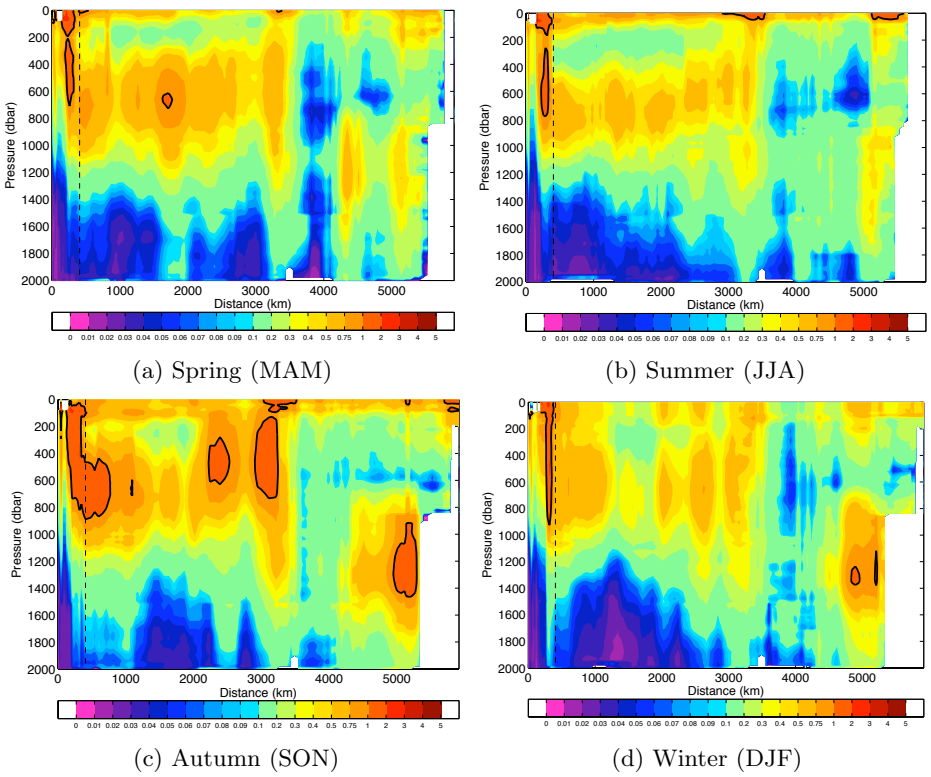

(a) Spring (MAM)

(b) Summer (JJA)

(c) Autumn (SON)

(d) Winter (DJF)

Figure 3.20: Potential temperature error variance as diagnosed by the OI (in °C) for each meteorological season.

the cooling if the water was mixing with deeper layers. The analysis in this project is not sufficient to provide an unequivocal answer to the source of the summertime cooling; work studying the dynamics of Eighteen Degree Water formation and its relationship with air-sea fluxes remains an active area of research as part of the CLIMODE project (Marshall et al., 2009).

Below 300 m, most of the changes appear to be density-compensating, with regions of increased temperature being accompanied by increased, and vice versa. The large apparent increase in salinity during summer in the vicinity of the Gulf Stream is likely related to a seasonal shift in its latitudinal position. Below 1000 m, little change is observed. The mechanisms behind these observations are not discussed in detail here. However, the interested reader is directed to Ivchenko et al. (2008), who discusses North Atlantic steric height varibility in terms of both thermosteric and halosteric components.

Finally, the difference in summer and winter σ_0 fields is examined (Figure 3.24). As expected, the surface layer is less dense across the entire basin in summer as a result of the increase in temperature, with the change exceeding 2 kgm^{-3} near the western end of the section. Beneath the seasonal thermocline, at 200 m to 1000 m, a general increase in density is found during summer, especially in the western basin, once again as a result of the temperature changes observed in this depth range (Figure 3.22). The density changes between seasons are at least as strong as the interannual changes implying substantial changes in the dynamic height field of the top 1000 dbar at timescales of both months and years (see below).

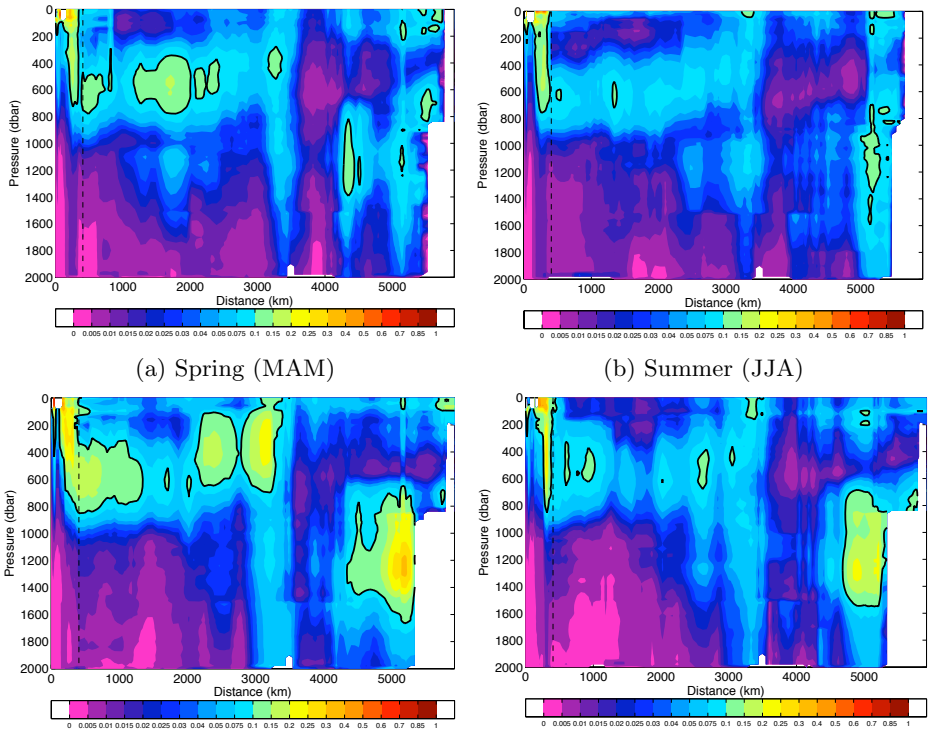

(a) Spring (MAM)

(b) Summer (JJA)

(c) Autumn (SON)

(d) Winter (DJF)

Figure 3.21: Salinity error variance as diagnosed by the OI for each meteorological season.

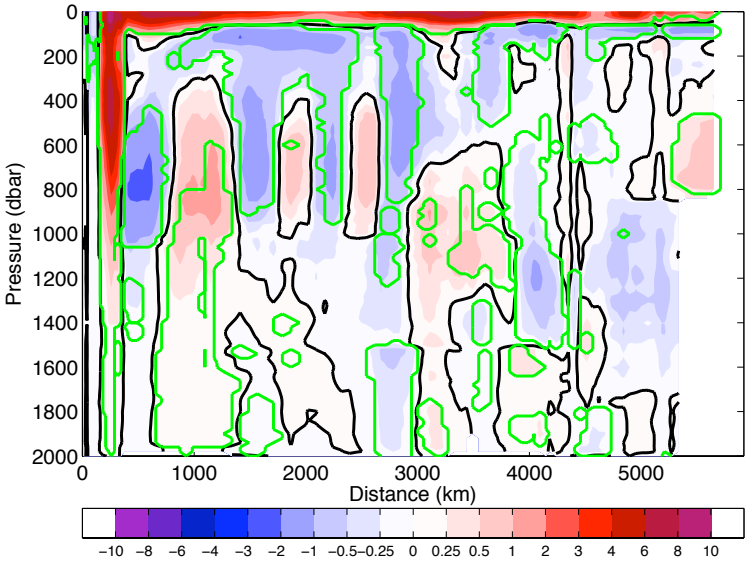

Figure 3.22: Difference between summer and winter (summer minus winter) potential temperature fields across the North Atlantic along 36°N and Line W (in °C). The black contour is the zero line and the green contour encloses those areas where the potential temperature change exceeds the sum of the mapping errors.

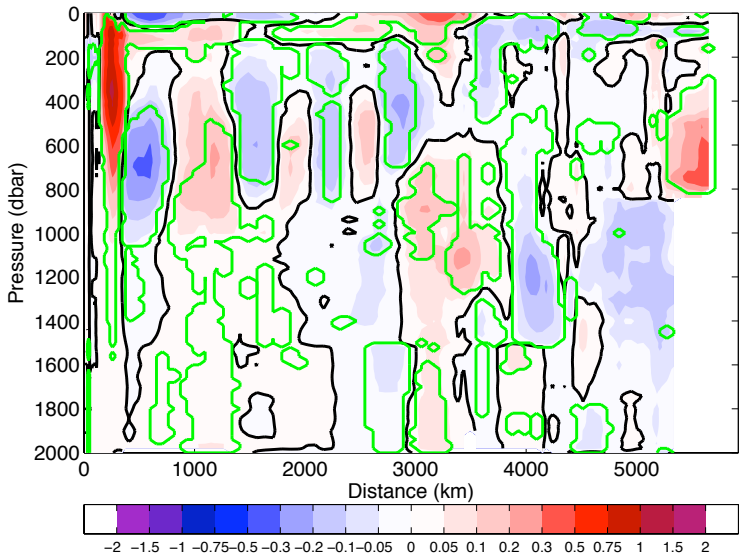

Figure 3.23: Difference between summer and winter (summer minus winter) salinity fields across the North Atlantic along 36°N and Line W. The black contour is the zero line and the green contour encloses those areas where the salinity change exceeds the sum of the mapping errors.

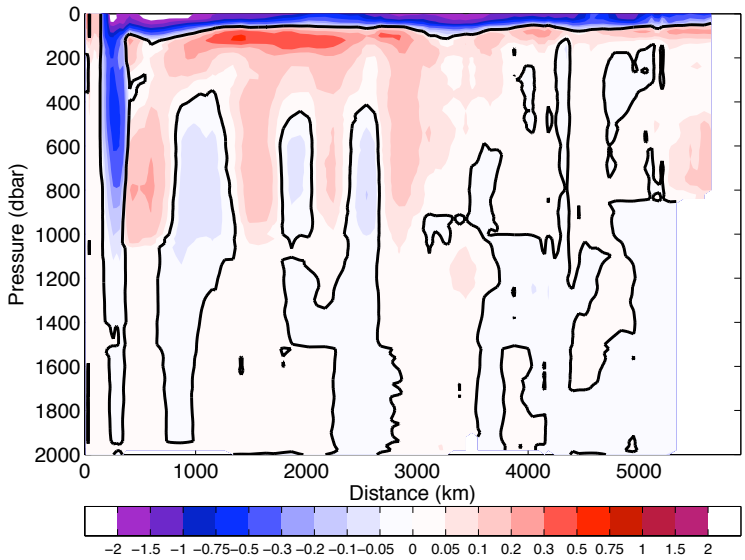

Figure 3.24: Difference between summer and winter potential density fields across the North Atlantic along 36°N and Line W.

3.2 Dynamic Height Variability

Before quantifying the density-driven changes in the interior transport field deduced from the temperature and salinity sections, the seasonal and interannual variability in the dynamic height field is analysed. For each of the seasonal and annual θ/S sections, the dynamic height was examined in pressure layers in order to identify whereabouts in the water column the variability in the density field is strongest and hence to identify the areas driving the baroclinic changes in the interior transport.

3.2.1 Annual Sections of Dynamic Height

Sections of dynamic height for each year in the various layers are found in Figure 3.26. The layers used were:

1. 1500 dbar relative to 1900 dbar: this is the approximate depth range of the upper Labrador Sea Water (Pickart, 1992).
2. 1000 dbar relative to 1500 dbar: this broadly covers the lower thermocline and Mediterranean Water.
3. 500 dbar relative to 1000 dbar: this broadly covers the middle and upper thermocline water.
4. 300 dbar relative to 500 dbar: this includes the 18-degree water.
5. 100 dbar relative to 300 dbar.
6. Surface relative to 100 dbar: the seasonal mixed layer.

For completeness, plots of dynamic height at the surface relative to 1000 dbar and 1500 dbar are included in Figure 3.25. The gaps in several plots near the eastern boundary (e.g. Figures 3.25a, 3.25b, 3.26a and 3.26b), are due to a lack of Argo floats profiling deeper than 1000 dbar in this region.

Figures 3.25a and 3.25b show the same general pattern in each year, with a sharp increase in dynamic height moving west-to-east across the Gulf Stream, followed by a much shallower decline across the subtropical gyre to the eastern boundary. In general, there is very little year-to-year variability in the dynamic height of the eastern basin. Much greater variability is seen in the western basin, both in the magnitude of the dynamic height maximum and in its position. The location of the maximum is generally immediately offshore of the Gulf Stream (600 km along the baseline), but in both 2002 and 2005, the peak was significantly further east. In terms of the interannual variability, there is good agreement between Figures 3.25a and 3.25b with both displaying the largest dynamic height peak in 2003 and the lowest in 2005.

Examining the dynamic height in layers (Figure 3.26), several important comments can be made. Firstly, the gentle east to west slope of dynamic height across the recirculation region

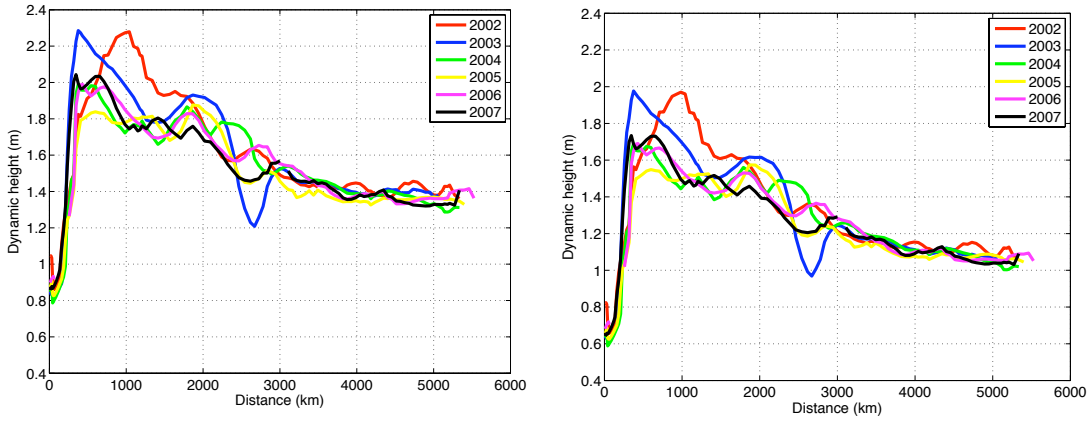

(a) Relative to 1500 dbar

(b) Relative to 1000 dbar

Figure 3.25: Dynamic height (in dyn. m) at the surface by year relative to (a) 1500 dbar and (b) 1000 dbar.

is largely confined to the upper 1000 dbar, with layers below 1000 dbar having a relatively flat dynamic height profile away from the western boundary (Figures 3.26a and 3.26b). This observation implies that the baroclinic part of the recirculation is largely confined to the top 1000 dbar with relatively weak flows beneath this level. However, all plots show a strong gradient in dynamic height across the Gulf Stream itself suggesting this feature extends to at least 2000 dbar. Secondly, in all layers above 1000 dbar, there is much stronger interannual variability in the region west of 3000 km along the baseline than in the eastern basin. This conclusion does not hold in the 1000 dbar to 1500 dbar layer as the influence of the Mediterranean Water east of 4500 km increases the variability of this region. Finally, there is a strong increase in interannual variability in all regions in the surface to 100 dbar layer due to the influence of the annual cycle in solar insolation on this part of the water column.

To investigate the geographical and depth range of the variability more carefully, the standard deviation in dynamic height per unit pressure is plotted in Figure 3.27. The overall pattern is that the interannual variability in dynamic height increases towards the surface, but this masks a more complicated result. In the deepest two layers (the Upper Labrador Sea Water and lower thermocline), the variability in dynamic height is low across the entire basin, suggesting these layers are relatively unimportant in controlling the variability in the baroclinic component of the interior transport. Whilst the Mediterranean Water increases the *relative* importance of the eastern basin compared to the west, it is not important in controlling the overall dynamic height gradient from year to year. In contrast, the 1000 dbar to 500 dbar layer, whilst continuing to have a small standard deviation east of 3000 km, has a much larger standard deviation in the western basin, suggesting that year-to-year changes in the middle and lower thermocline of this region are strongly affecting the dynamic height field. A similar pattern is observed in both the 500 dbar to 300 dbar and 300 dbar to 100 dbar layers, with strong variability west of the Mid-Atlantic Ridge and weak variability close to the eastern boundary. The surface layer has the strongest variability in all regions,

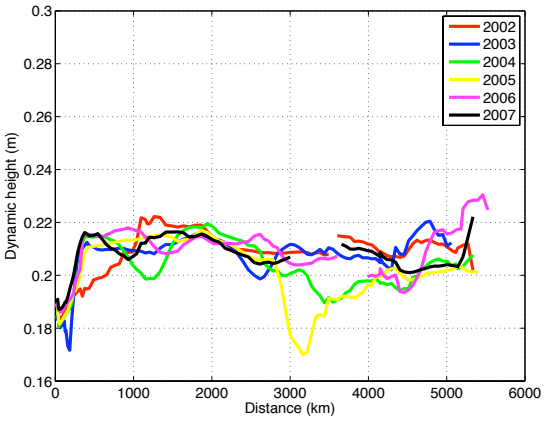

(a) 1500 dbar relative to 1900 dbar (depth range of Upper Labrador Sea Water)

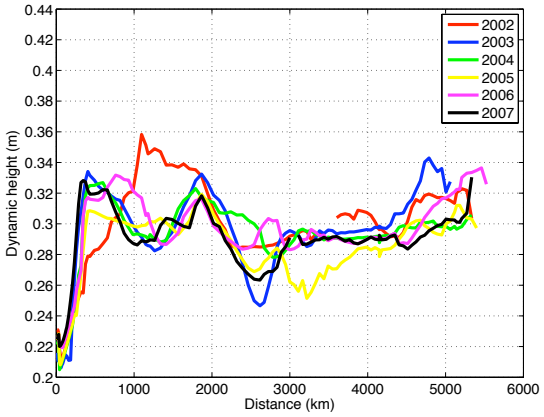

(b) 1000 dbar relative to 1500 dbar (depth range of lower thermocline and Mediterranean Water)

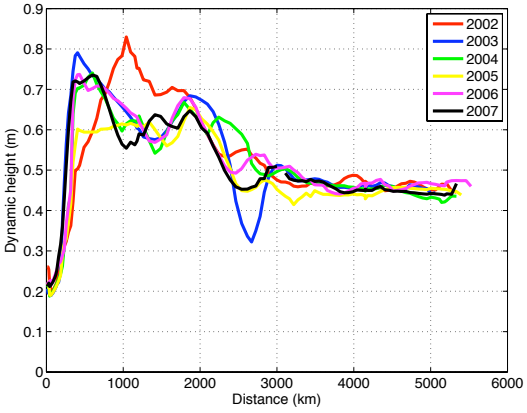

(c) 500 dbar relative to 1000 dbar (depth range of middle and upper thermocline water)

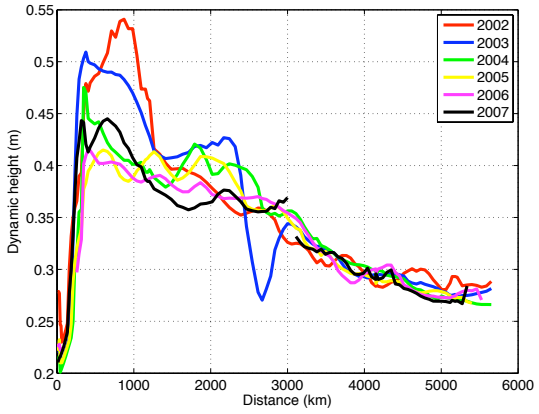

(d) 300 dbar relative to 500 dbar (depth range of EDW)

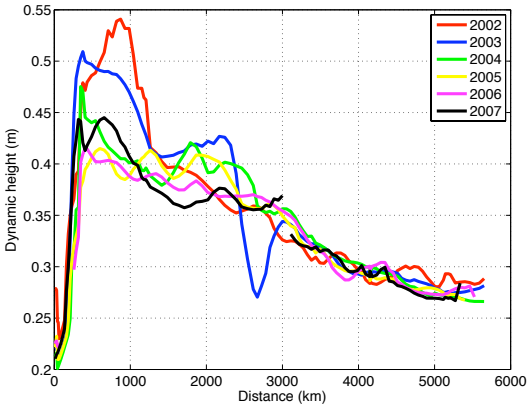

(e) 100 dbar relative to 300 dbar

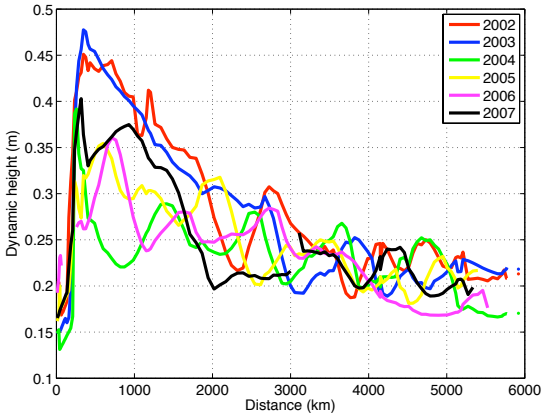

(f) Surface relative to 100 dbar (seasonal mixed layer)

Figure 3.26: Dynamic height (in dyn. m) by year in various depth layers. Note the different vertical scales on each plot.

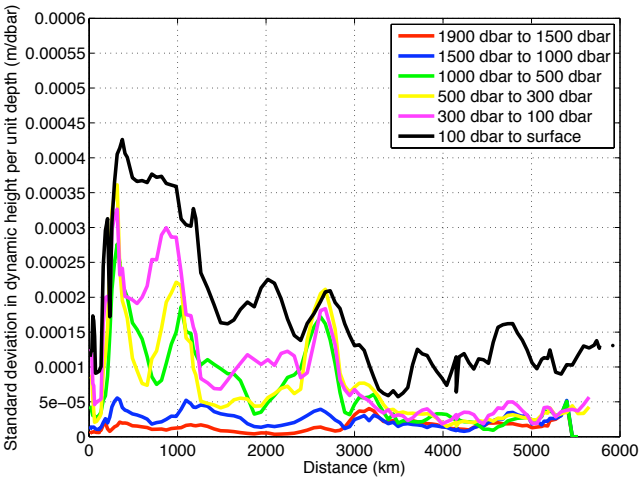

Figure 3.27: Standard deviation in dynamic height per unit pressure for six pressure layers from the annual estimates of 2002 to 2007.

controlling the majority of the variability in the eastern basin. Therefore, two different mechanisms of variability emerge from this analysis. Year-to-year variations in dynamic height in the western basin are controlled in part by density changes within the thermocline and in part by density variability in the surface layer caused by differential solar heating from year-to-year. In contrast, almost all of the variability at the eastern end of the section occurs in the surface layer. Our results concur with the findings of Sato and Rossby (1995), who found that the main source of variability on the Sargasso Sea side of their Gulf Stream transects was the vertical displacement of the main thermocline (their Figure 4).

3.2.2 Seasonal Sections of Dynamic Height

A similar analysis to that outlined in Section 3.2.1 was conducted for each meteorological season (Figures 3.28 and 3.29) to identify the size and sources of variability in dynamic height throughout the year.

In line with the annual sections, Figures 3.28a and 3.28b show no change in the overall density structure of the gyre between the seasons. Once again, the variability in the eastern basin is smaller than in the western basin, though it would appear that dynamic height does tend to be highest here in the autumn. The maximum in dynamic height immediately offshore of the Gulf Stream is also largest in autumn irrespective of the choice of reference level. The largest dynamic height gradient across the basin is found in spring, suggesting southward baroclinic transport is at a maximum in this season.

Splitting the dynamic height into layers (Figure 3.29) yields a number of interesting observations. As with the interannual variability, the two deepest layers contribute little to the dynamic height gradient of the gyre away from the western boundary. Variability again appears to be concentrated in the top 1000 dbar, though the variability over relatively short horizontal scales appears to be smaller than between the individual years. The cooling of

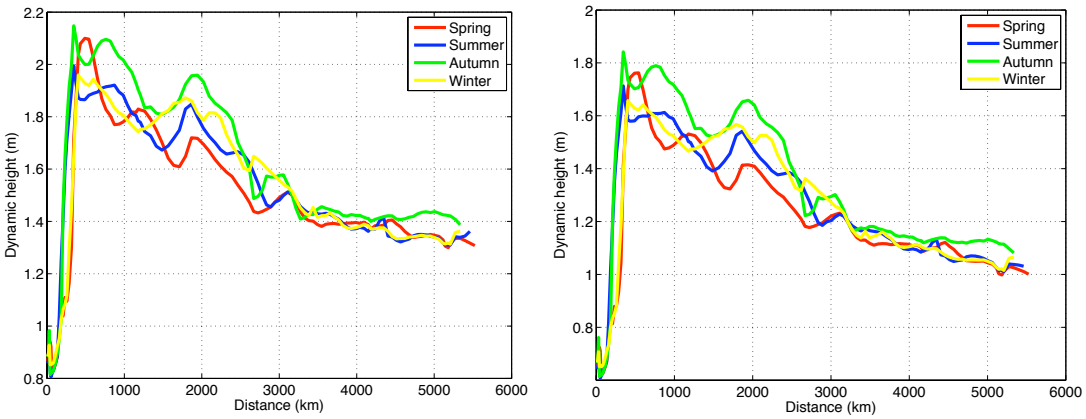

(a) Relative to 1500 dbar

(b) Relative to 1000 dbar

Figure 3.28: Dynamic height (in dyn. m) at the surface by season relative to (a) 1500 dbar and (b) 1000 dbar.

the 100 dbar to 300 dbar layer during summer (Figure 3.22) is observed in the lower dynamic height values west of the Mid-Atlantic Ridge in that season (Figure 3.29e), though the difference in the dynamic height between each end of the section does not change substantially between the seasons. Another clear difference from the interannual variability is found in the top 100 dbar, where the seasonal heating and cooling within the mixed layer produces strong inter-seasonal variability in the total dynamic height at the surface relative to 100 dbar. The highest values here are found in autumn (peaking at 0.46 m) with the lowest values in spring (peaking at 0.24 m). A significant change in the gradient of dynamic height is also found in this layer between the seasons, with the largest dynamic height differences across the basin found in summer and autumn (up to 0.25 m) and weaker gradients in spring and winter (0.05 m to 0.1 m). This change most likely reflects differential sensible heat flux into the mixed layer during summer causing a larger temperature increase on the western side of the basin (Figure 3.22). The change in the dynamic height gradient throughout the year suggests a stronger southward baroclinic transport in the surface layer during summer and autumn compared to winter and spring.

From examination of the standard deviation in dynamic height per unit depth (Figure 3.30), the variability in the density fields between the seasons is dominated in most of the basin by heating and cooling in the surface layer, with variability at most other pressure levels being less important. However, dynamic height changes in the main thermocline between 100 m and 1000 m do continue to influence the baroclinic transport field west of the Mid-Atlantic Ridge, particularly in the region immediately offshore of the Gulf Stream. These changes are responsible for the enhanced dynamic height gradient across the basin during spring. However, across most of the basin, these mid-depth changes are less important on seasonal timescales than for interannual variability.

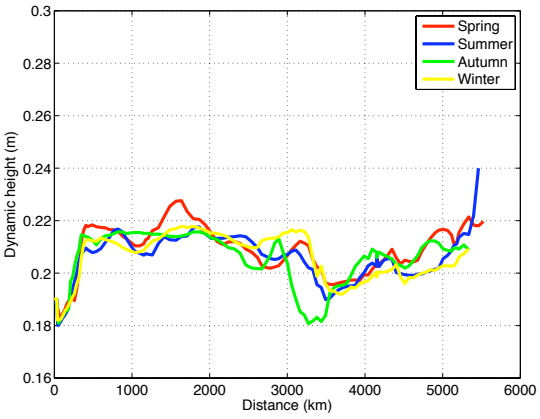

(a) 1500 dbar relative to 1900 dbar (depth range of Upper Labrador Sea Water)

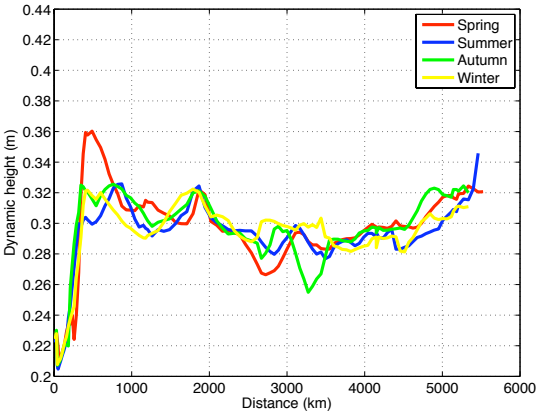

(b) 1000 dbar relative to 1500 dbar (depth range of lower thermocline and Mediterranean Water)

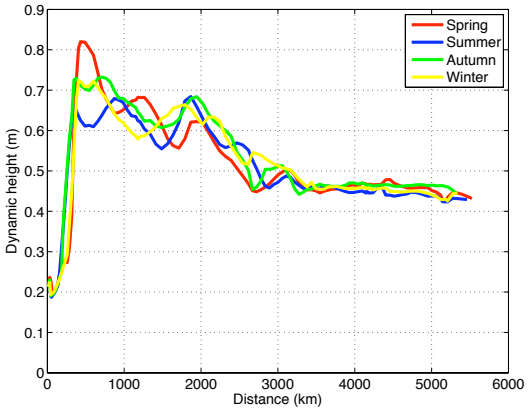

(c) 500 dbar relative to 1000 dbar (depth range of middle and upper thermocline water)

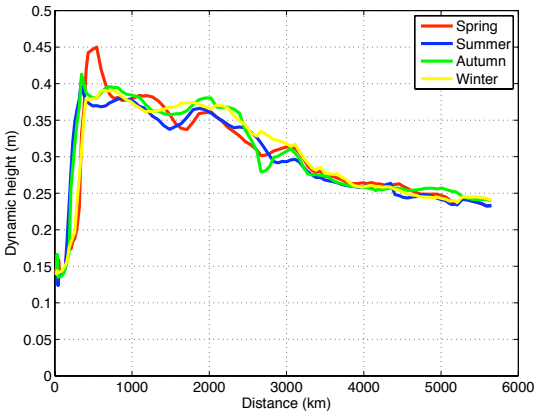

(d) 300 dbar relative to 500 dbar (depth range of EDW)

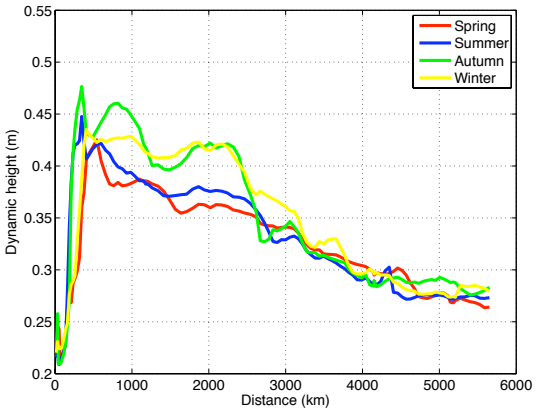

(e) 100 dbar relative to 300 dbar

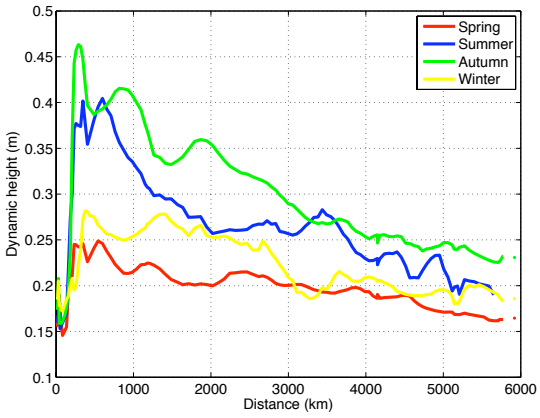

(f) Surface relative to 100 dbar (seasonal mixed layer)

Figure 3.29: Dynamic height (in dyn. m) by season in various depth layers. Note the different vertical scales on each plot.

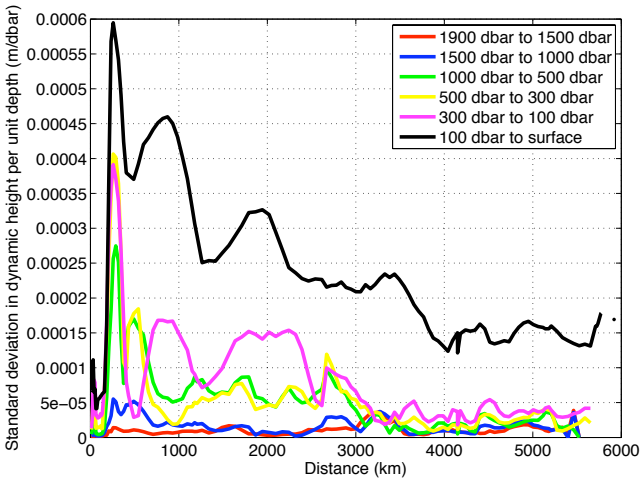

Figure 3.30: Standard deviation in dynamic height per unit pressure for six pressure layers from the seasonal estimates.

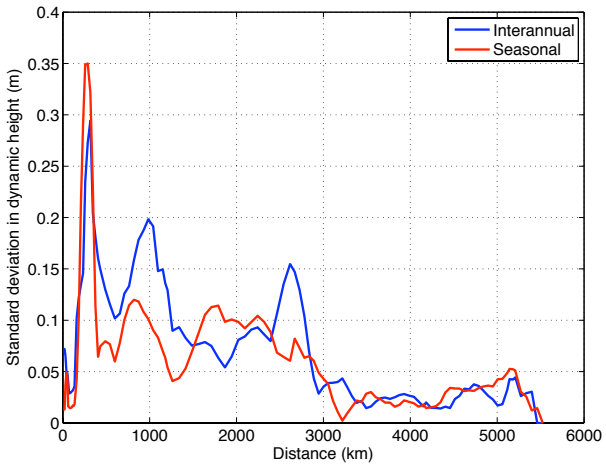

Figure 3.31: Standard deviation in dynamic height at the surface relative to 1000 dbar for annual and seasonal estimates.

Year	1000 dbar floats	1500 dbar floats	1975/2000 dbar floats	Total
2001	4	21	23	**48**
2002	155	241	82	**478**
2003	144	416	173	**733**
2004	357	352	327	**1036**
2005	495	502	134	**1131**
2006	701	569	40	**1310**
2007	333	173	4	**510**
Totals	2189	2274	783	**5246**

Table 3.3: Number of Argo float trajectories collected between 34°N and 40°N in the Atlantic at various parking pressures for each year.

3.2.3 Comparing Seasonal and Interannual Changes

From the results of Sections 3.2.1 and 3.2.2, several conclusions can be reached about the nature of dynamic height variability at seasonal and interannual timescales:

1. The overall size of variability on interannual and seasonal timescales is broadly similar (Figure 3.31), suggesting year-to-year changes in the interior transport field may be difficult to disentangle from higher-frequency variability.

2. The interannual variability is driven in part by the formation and erosion of the seasonal thermocline across the entire basin and in part by changes in the temperature of the main thermocline west of the Mid-Atlantic Ridge.

3. The seasonal variability in dynamic height is mainly caused by the formation and erosion of the seasonal thermocline, with variability of the main thermocline being relatively less important.

3.3 Reference Velocity Calculation

In order to convert the dynamic height variability discussed in Section 3.2 into a time series of absolute interior transport variability, a suitable background velocity needed to be applied at each mapping point across the section to reference the geostrophic shear. Initially, the YoMaHa'07 dataset (Lebedev et al., 2007) was used to estimate the subsurface velocity of each of the Argo floats in the North Atlantic between 34°N and 40°N. In total, 5246 estimates of deep velocity were obtained in this region between the inception of the Argo programme and May 15th 2007, with the numbers of trajectories collected in each individual year given in Table 3.3.

Table 3.3 shows a reasonable number of available float trajectories throughout the period 2002 to 2007 at both 1000 dbar and 1500 dbar. The geographical distribution of these float trajectories is shown in Figure 3.32. Whilst there is a reasonable zonal coverage at both 1000 dbar and 1500 dbar, all the float trajectories at 2000 dbar are found west of 30°W and

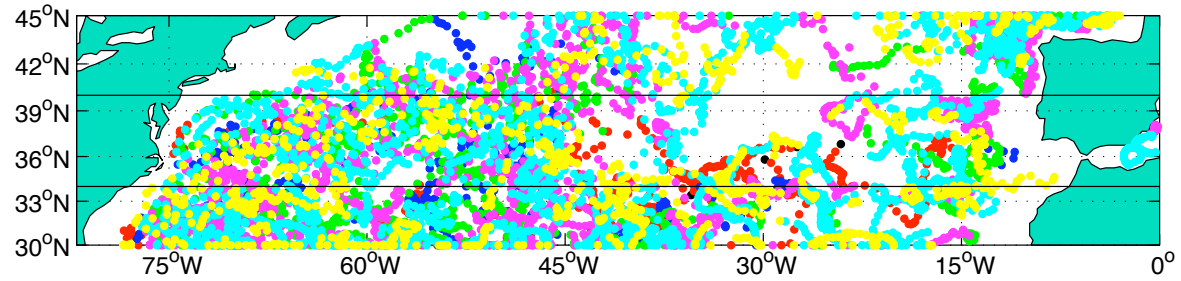

(a) 1000 dbar

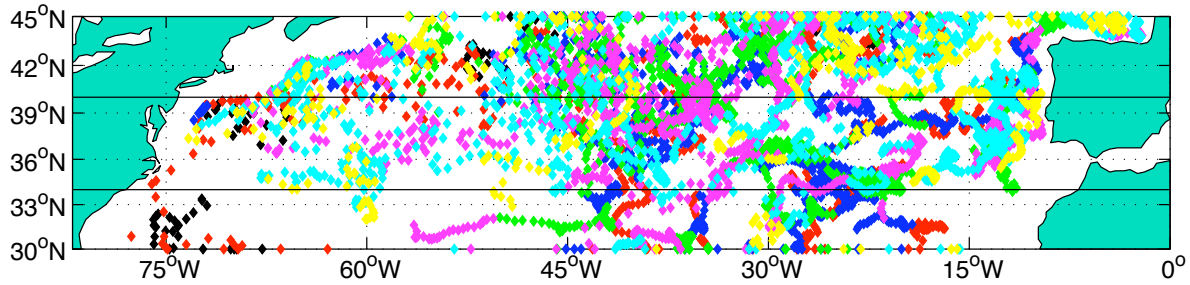

(b) 1500 dbar

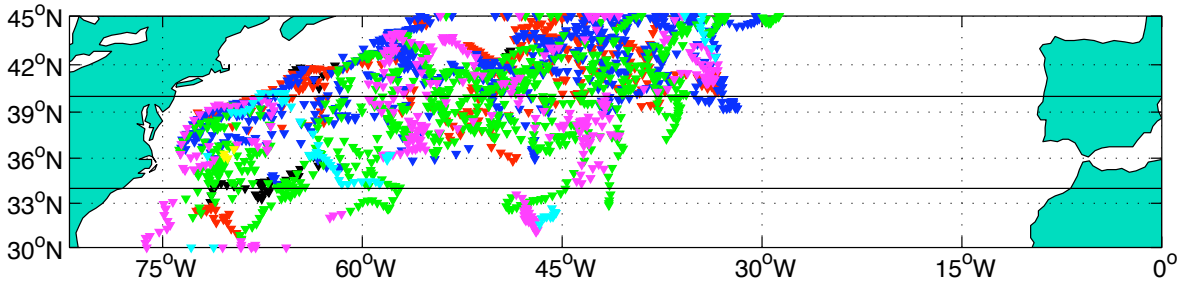

(c) 1975/2000 dbar

Figure 3.32: Positions of Argo float trajectories in the YoMaHa'07 database at (a) 1000 dbar parking pressure; (b) 1500 dbar parking pressure and (c) 1975/2000 dbar parking pressure (for convenience these two depths are grouped together). Black markers represent trajectories in 2001, red markers 2002, blue markers 2003, green markers 2004, magenta markers 2005, cyan markers 2006 and yellow markers 2007. The 34°N and 40°N latitude lines are marked.

the vast majority are west of 45°W. It is also unfortunate that the eastern boundary is so poorly sampled at any pressure level, with only 18 trajectories east of 10°W during the entire time series.

A vector plot of subsurface trajectories at each level is given in Figure 3.33. At 1000 dbar, several important features can be identified. The strong northeastward-directed Gulf Stream is the most prominent velocity feature of the section, with a continuous line of red velocities exceeding 20 cms^{-1} extending from Cape Hatteras to a position near 40°N, 50°W. The exact orientation of the Stream varies because of meandering, with some vectors being directed almost northwards whilst others have southeastward orientation (blue arrows). This results from the extensive meandering and eddy formation that takes place in the Gulf Stream (Richardson et al., 1973). To the west of the Gulf Stream, a relatively narrow band of

weak southwestward velocities can be found, which extend to at least 2000 m in depth (Fratantoni and Pickart, 2003). The lowest part of this current forms the Deep Western Boundary Current that comprises the lower limb of the Atlantic meridional overturning circulation (MOC). To the southeast of the Gulf Stream, but west of 45°W, relatively strong (greater than 10 cms^{-1}) velocities predominate at 1000 dbar, though no dominant direction is apparent. East of 45°W, velocities are weak (less than 10 cms^{-1}) and do not exhibit a dominant orientation.

Velocities at 1500 dbar exhibit a similar spatial pattern, although their magnitude is generally smaller than at 1000 dbar. There is also some evidence at this depth level of westward velocities close to the eastern boundary related to the Mediterranean outflow, particularly from a float that drifted between 15°W and 20°W at 35°N to 36°N (Figure 3.33b). Whilst this float has a generally westward trajectory, two anticyclonic circular trajectories can be identified, consistent with the float being trapped within a meddy of warm and salty Mediterranean Water as described previously by Armi and Zenk (1984).

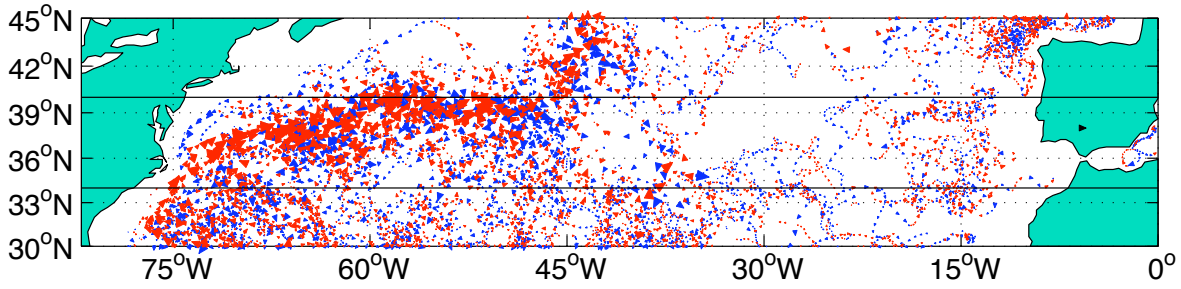

(a) Float trajectories at 1000 dbar

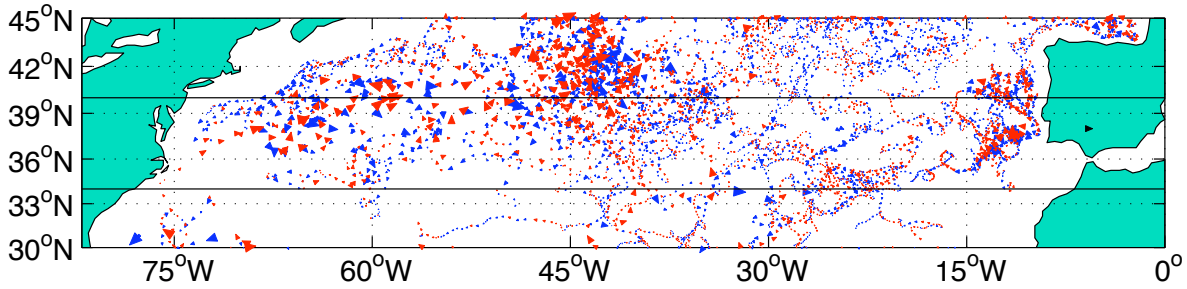

(b) Float trajectories at 1500 dbar

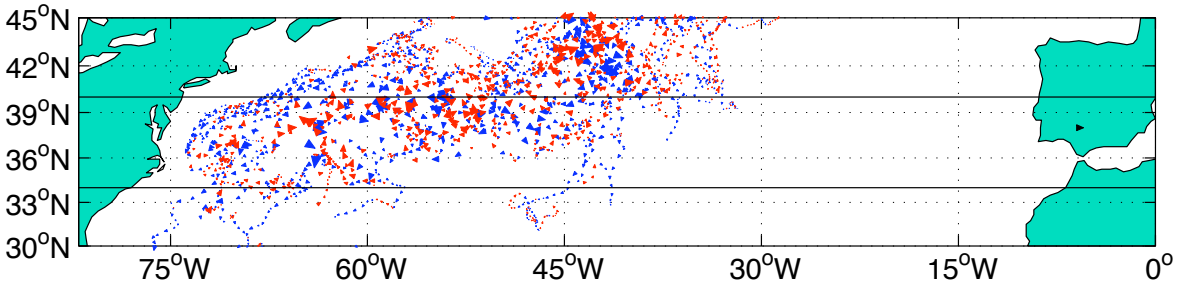

(c) Float trajectories at 1975/2000 dbar

Figure 3.33: Vector plot of subsurface float velocities of the trajectories identified in Figure 3.32. Red vector arrows indicate northward displacements and blue vector arrows indicate southward displacements. The black vector arrow over Iberia, given for scale, represents an eastward velocity of 20 cms^{-1}. The 34°N and 40°N latitude lines are marked.

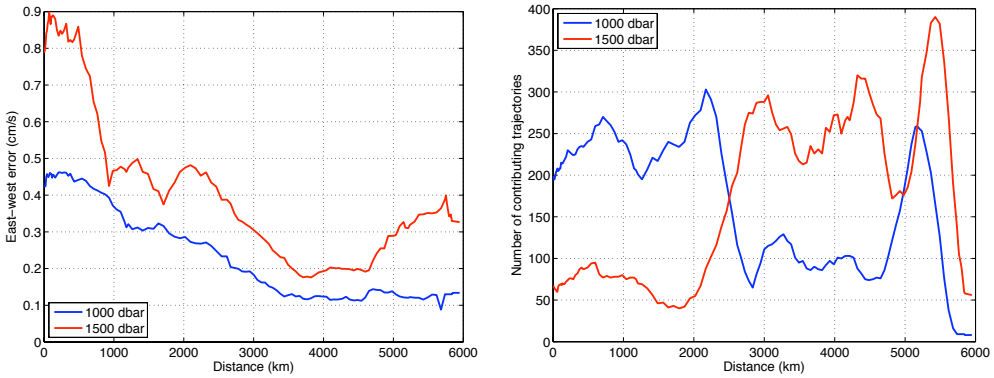

(a) YoMaHa shear error (b) Number of contributing trajectories

Figure 3.34: (a) u velocity errors at 1000 dbar and 1500 dbar at each mapping point across the 36°N/Line W section from the box averaging of data in the YoMaHa '07 database. (b) Number of profiles contributing to each mapping point.

3.3.1 Selection of Velocities

Extensive experimentation was carried out to determine the best method of interpolating these velocities onto the mapping points of the 36°N and Line W sections. Unfortunately, an OI approach of the type used for the potential temperature and salinity measurements is not easily applied to the velocity measurements, because eddy variability and inertial oscillations can strongly bias the velocity field if the mapping point lies close to one of these features. Experimentation using the same OI method as applied for potential temperature and salinity (and a zonally uniform climatological background velocity) did indeed introduce spurious structure into the reference velocity at both 1000 dbar and 1500 dbar, meaning another method was required. The technique was not tried for the 2000 dbar trajectories because of the lack of data coverage east of 30°W (4000 km along the baseline).

Given the relatively large volume of available data, it was instead decided to reduce this noise by simple averaging over a large number of float trajectories. The initial choice was to use a median value of all u and v velocities within 2.5° of longitude of each mapping point and bounded by the latitude lines 34°N and 40°N. At both 1000 dbar and 1500 dbar, this yielded small u and v velocities across the entire section (less than 3 cms^{-1}), with the exception of close to the eastern boundary where a lack of profiles resulted in a large median velocity at 1000 dbar (close to 4 cms^{-1} northeastward).

In view of the smaller shear errors incurred at 1000 dbar compared with 1500 dbar (Figure 3.34a) and the relatively small number of 1500 dbar velocities in the western basin (Figure 3.34b), it was decided to use the 1000 dbar velocities to reference the annual and seasonal estimates of geostophic shear. This process involved rotating the u and v velocities into cross-track coordinates and interpolating onto positions midway between the mapping points to ensure the same number of reference velocities as shear estimates. From this a velocity offset was calculated which was then applied over the top 1000 dbar. The velocity field was then multiplied by the size of the depth bins (20 dbar) and the distance between the midpoints

Longitude range of mapping points	Latitude limits	Longitude limits
68°W to 65°W	34°N to 36.2°N	Mapping point longitude ±1°
65°W to 60°W	34°N to 38°N	Mapping point longitude ±2.5°
60°W to 55°W	34°N to 38°N	Mapping point longitude ±2.5°
55°W to 50°W	34°N to 39°N	Mapping point longitude ±2.5°
50°W to 45°W	34°N to 40°N	Mapping point longitude ±2.5°
45°W to 7°W	34°N to 40°N	Mapping point longitude ±2.5°

Table 3.4: Longitude/latitude boxes from which Argo float trajectories were drawn in the region east of the Gulf Stream. The first column gives the longitude range in which the mapping point lies and the other two columns give the latitude and longitude range over which a mean u and v velocity is calculated.

to give a volume transport in the top 1000 dbar in m^3s^{-1}. This was then cumulated from east to west across the basin to give a total volume transport for each year and season.

Through a series of experiments, it was found that a number of refinements were needed to this initial reference velocity field to improve its reliability:

1. The YoMaHa database is now updated in near real-time, meaning that float trajectories are now available up to April 2010. Some early problems, including inaccurate reporting of the parking depth of some floats, have also been corrected. We thus used this updated database, which improved the number of available deep trajectories in the region to over 7200, with almost 4000 at 1000 dbar. The data were accessed on 1st May 2010.

2. More careful profile selection was found to be required in the western basin, as the geostrophic transport sections that emerged from the analysis generally contained a southward transport maximum over 1000 km to the east of the Gulf Stream edge. A weak northward transport was observed between this position and the outer edge of the Gulf Stream. As the maximum in dynamic height is found immediately offshore of the Gulf Stream (Section 3.2), there was clearly an error in the reference velocity field causing a distortion in the transport structure of the gyre. The source of the anomalous northward transport bias in the western basin was that the box-averaging technique was including some profiles within the Gulf Stream. Several techniques were trialled for removing these unrepresentative profiles, but eventually it was decided simply to apply different northern latitude limits to different parts of the western basin to exclude Gulf Stream profiles from selection (Table 3.4). A mean value was then taken of the remaining profiles.

3. The estimated background velocities both within and inshore of the Gulf Stream (typically 3 cms^{-1}) were much weaker than observations in the literature. For instance, Halkin's (1985) results at 73°W from the Pegasus profiler measured 1000 dbar velocities approaching 20 cms^{-1} in the Gulf Stream, whilst Johns et al. (1995) found a peak velocity at this level of almost 70 cms^{-1}. Including velocities from 5 degrees of

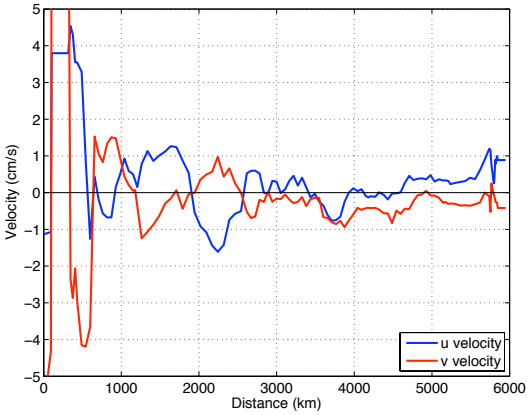

Figure 3.35: u and v velocities at 1000 dbar at each mapping point across the 36°N/Line W section from the final data selection of the updated YoMaHa database and Line W mooring velocities at 1000 dbar.

longitude clearly over-smoothes the data and eliminates the fine spatial features of the boundary current. To address this issue, the limited number of Argo trajectories were supplemented by velocities at 1000 dbar from the W1 and W3 McLane Moored Profilers of the Line W array. In total, this added 475 velocity measurements to the inshore side of the Gulf Stream. Secondly, instead of employing simple box averaging that resulted in the western boundary velocity structure being over-smoothed, a more complex approach was followed. For mapping points in the Gulf Stream itself (between 69.1°W and 68°W), a mean value of the velocities in the latitude-longitude box 69°W to 66°W, 36.2°N and 38.2°N was used. Although this method provided a 'stepped' velocity field (as all the mapping points have the same velocity value), there were an insufficient number of Argo floats to resolve the detailed structure adequately. Inshore of the Gulf Stream (69.7°W to 69°W), virtually all of the available velocities came from the two Line W moorings, so a different strategy was again employed. The velocities at the mapping point at 39.51°N, 69.65°W, closest to Line W mooring W1, were calculated from a mean of all the profiles taken in the box 38.2°N to 40°N, 72°W to 69.4°W. Almost all the velocities at 1000 dbar came from the W1 mooring itself. Similarly, the velocities at mapping point 38.79°N, 69.11°W, closest to Line W mooring W3, were calculated from a mean of all the profiles taken in the box 38.2°N to 40°N, 69.4°W to 69.1°W. Again, almost all the velocities at 1000 dbar came from the W3 mooring. For the 8 mapping points between the two moorings, values of velocity were linearly interpolated from these two mapping points.

The final estimate of the background velocity is given in Figure 3.35. Taking the cross-track component of this estimate and accumulating the transport in the top 1000 dbar from east to west across the basin yields a maximum southward transport of −15.6 Sv (Figure 3.36). The significance and errors of this barotropic transport are discussed further in Section 5.3.4.

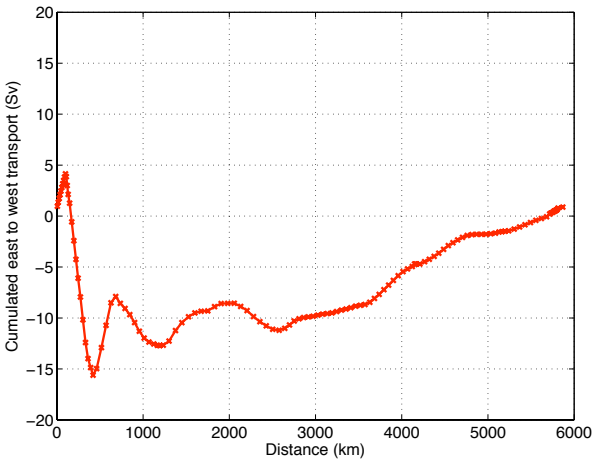

Figure 3.36: Cross-stream east to west cumulated barotropic transport above 1000 dbar along the interpolated section, using the reference velocities at 1000 dbar given in Figure 3.35.

3.3.2 Further Reference Velocity Experiments

Experimentation was carried out on applying annually/seasonally variant background reference velocity at 1000 dbar to reflect the year-to-year or season-to-season changes in the background velocity. The rationale behind this investigation was to determine whether the interior transport variability was primarily driven by density changes or by variability in the barotropic velocity field. Unfortunately, data coverage was found to be too sparse to produce statistically different estimates of the reference velocity for any individual year or by season, so the size of the variability reported in Section 3.4 reflects only the density-driven changes.

One possible extension to the analysis would be to use the record of annual/seasonal 1000 to 1500 dbar dynamic heights (Figures 3.26b and 3.29b) to obtain an estimate of the deep geostrophic shear in each individual year or season. This could then be applied to the reference velocity in Figure 3.36 to get an estimate of the reference velocity field at 1500 dbar for each year or season. This would have the additional advantage of yielding a deeper reference velocity, thus allowing us to estimate the total transport over a larger depth range. This will be pursued in work subsequent to this project.

3.4 Interior Transport Results

With a reliable reference velocity field at 1000 dbar established, annual and seasonal estimates of the interior transport above 1000 dbar were produced. The zonal structure of the cumulated east to west transport is given for each year in Figure 3.37. Most of the interannual variability occurs west of the Mid-Atlantic Ridge (around 3000 km along the baseline), in line with our earlier observation that temperature changes in the main thermocline of the western basin control the dynamic height variability from year-to-year. The

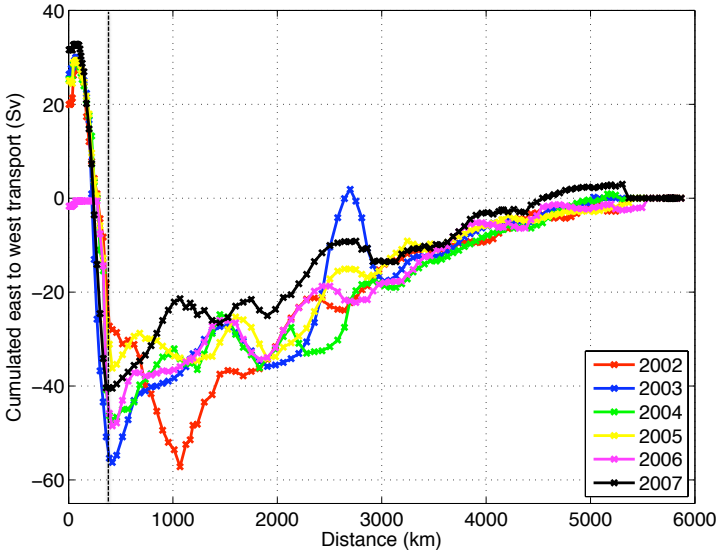

Figure 3.37: Cumulated east to west transport above 1000 dbar for each year calculated using the interpolated θ/S fields and the background reference velocity at 1000 dbar given in Figure 3.35. The western limit of integration at 67.61°W is marked with the dashed line.

Year	**Total transport to** 67.61°W **(Sv)**
(2002)	(−28.0)
2003	−56.3
2004	−47.3
2005	−36.2
2006	−48.5
2007	−40.5
MEAN ± S.E.	-45.8 ± 3.4

Table 3.5: Total zonally integrated transport in the layer above 1000 dbar estimated from optimal interpolation of the θ/S fields and the background reference velocity at 1000 dbar given in Figure 3.35. The transport is cumulated to 67.61°W, the position where the zonal 12°C isotherm gradient becomes negative (see Figure 3.38). The values from 2002 are included for completeness but excluded from the mean value.

eastern end of the section, including the upper part of the Mediterranean Water, is relatively unimportant in terms of interior transport variability, with all the transport estimates being very consistent in the eastern basin. In all years except 2002, the transport reaches a southward maximum immediately offshore of the Gulf Stream, coincident with the position of maximum dynamic height relative to 1000 dbar (Section 3.2). Total accumulated values of interior transport are given in Table 3.5 for the years 2002 to 2007, with the anomalously low transport in 2002 (−28.0 Sv) excluded from the mean calculation because of the lack of data coverage and suspected seasonal bias in this year. Extensive experimentation was carried out to define a suitable western boundary to this integration. Eventually, it was decided to integrate to the position where the zonal gradient of 12°C isotherm depth becomes negative (Figure 3.38). In all years, this point was close to 67.61°W (405 km along the baseline), and this mapping point thus became the western limit of integration.

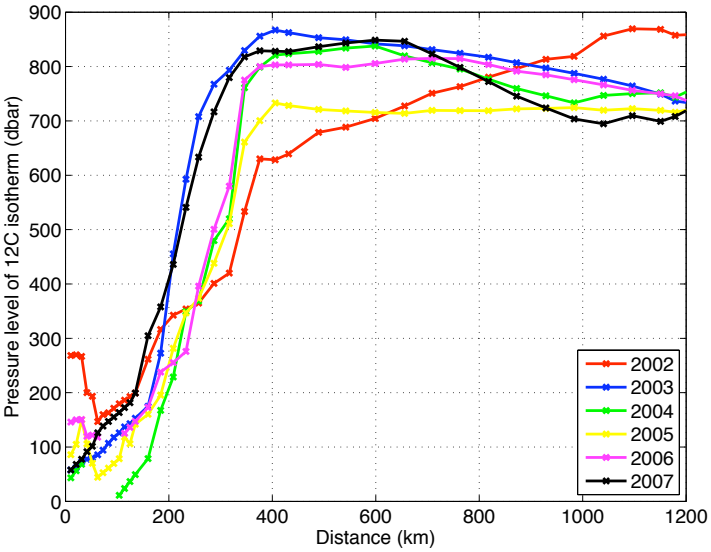

Figure 3.38: Pressure level corresponding to the 12°C isotherm near the western boundary. A rapid increase in isotherm depth is observed as the Gulf Stream is crossed, followed by a gradual decline across the western part of the gyre (except in 2002). In all years (with the exception of 2004) the east-to-west gradient of isotherm pressure becomes negative close to 405 km along the baseline (at 67.61°W, 36.25°N).

The largest value of interior transport was observed during 2003, followed by a gradual reduction up to 2005 and fluctuating values in 2006 and 2007. The reduction in transport in the early part of the time series was primarily caused by the overall increase in density in the upper 1000 dbar west of 2500 km along the baseline (Figure 3.16b). As discussed in Section 3.1.2, this change was brought about by a decrease of up to 3°C in the temperature of the thermocline water in the western basin between 2003 and 2005. The reversal of this trend in the period 2005 to 2007 primarily occurs as a result of strong thermocline warming between 200 and 1000 dbar close to the western boundary (Figure 3.15e). Whilst the salinity changes have opposing effects on density, the potential temperature changes have the dominant impact and thus control the baroclinic transport. In contrast, θ and S changes near the eastern boundary are weaker and thus do not contribute substantially to the interannual variability in transport.

Despite the improvements made to both the θ/S interpolation and the reference velocity field, the western boundary remains poorly resolved, with full basin transports for the six years varying from a minimum of -2 Sv in 2006 to a maximum of 33 Sv in 2007 (see Figure 3.37). Unfortunately, the lack of Argo and Line W data in this highly sheared region remains a serious limitation, meaning that this method is only reliable in the interior. As a result an alternative method for evaluating the Gulf Stream transport is described in Section 3.5.

Examination of the transports by meteorological season (Figure 3.39) yields a similar result to the interannual variability. In the eastern basin, the annual cycle of cumulated transport is small, with transports accumulated to the 3000 km baseline point agreeing to within 3 Sv in all seasons. Virtually all the variability between seasons arises in the Sargasso Sea, and

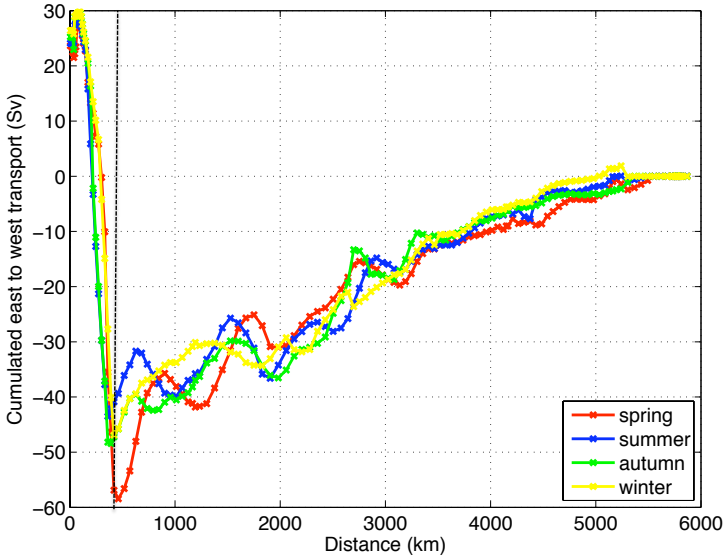

Figure 3.39: Cumulated east to west transport above 1000 dbar for each season calculated using the interpolated θ/S fields and the background reference velocity at 1000 dbar given in Figure 3.35. The western limit of integration at 67.61°W is marked with the dashed line.

particularly in a narrow band immediately offshore of the Gulf Stream. Comparison of these results with the dynamic height results presented earlier once again demonstrates that changes in the main thermocline control the seasonal variability in transport. This result may appear surprising after the discussion in Section 3.2.2, which highlighted the role of the seasonal thermocline in changing the slope of the dynamic height field as being the largest mode of variability (Figure 3.29f). Baroclinic changes in this layer alone would suggest a summer or autumn maximum in transport, as this is when the dynamic height gradient is largest. However, the small depth of the seasonal thermocline (around 100 m) compared with the total interior transport means that changes in the density structure of the main thermocline are more important to the overall gyre transport. Specifically, a strong warming of the main thermocline between 300 and 800 dbar observed in spring towards the western end of the section is responsible for the maximum in southward transport at this time of the year. It seems likely that the warming of the thermocline during this season is related to deep wintertime mixing that leads to EDW formation immediately offshore of the Gulf Stream (Section 1.6).

It is notable from Table 3.6 that the mean value of transport derived from the four seasons of data is not numerically equal to that derived from the annual estimates (Table 3.5). Whilst this may appear a curious result, there is no requirement in the OI for the mean of the seasonal estimates to be equivalent to the mean of the annual estimates. It has already been argued that the transport estimate for 2002 is seasonally-biased, whereas the mean transport in Table 3.6 weights data from each season equally. Furthermore, the seasonal estimates do include some data from outside the 2002 to 2007 time window. However, the overall size of the standard deviation (6.6 Sv) is almost identical to the size of the standard deviation for the individual years (7.7 Sv), indicating the magnitude of the seasonal versus

Season	**Total transport to** 67.61°W **(Sv)**
Spring	−56.9
Summer	−40.9
Autumn	−47.2
Winter	−46.9
MEAN ± S.E.	-48.0 ± 3.3

Table 3.6: Total zonally integrated transport in the layer above 1000 dbar estimated from optimal interpolation of the θ/S fields and the background reference velocity at 1000 dbar given in Figure 3.35. The transport is cumulated to 67.61°W, the position where the zonal 12°C isotherm gradient becomes negative (see Figure 3.38).

interannual variability is similar. It is thus the case that interior transport variability over the course of a year is quantitatively similar to the size of the interannual changes.

3.4.1 Summary of Interior Transport Findings

After considering both the dynamic height and interior transport fields, a number of conclusions can be drawn:

1. On interannual timescales, dynamic height variability within the basin is primarily controlled by temperature changes within the main thermocline in the western basin (Figure 3.27). In the eastern basin, most of the variability in dynamic height occurs because of temperature changes in the seasonal thermocline (the top 100 dbar).

2. On timescales of less than one year, the largest dynamic height changes occur in the seasonal thermocline. However, there is also significant variability in the density structure of the layers between 100 and 1000 dbar in the western Sargasso Sea. The formation a deep mixed layer in the region offshore of the Gulf Stream during winter in the process of EDW formation is likely to be responsible for this variability.

3. Results from Section 3.1.2 confirm that changes in potential temperature observed from year-to-year are as large as the decadal changes between cruise sections observed by Leadbetter et al. (2007); hence their findings from three hydrographic sections are unlikely to represent a decadal trend. In the period 2003 to 2007, there was a general basin-wide reduction in the temperature of the water above 100 m and a thermocline cooling of up to 1°C in the western basin. In both cases, these changes were concentrated in the period 2003 to 2005. Later in the period (2005 to 2007), a region of strong thermocline warming is found just offshore of the Gulf Stream. Whilst many of the salinity changes were found to be partially density-compensating, the dominance of temperature in the equation of state in this θ/S range means that it is these changes that are responsible for the interannual baroclinic mass transport variability in the interior.

4. Careful float trajectory selection is required to establish a reliable background velocity field at 1000 dbar with which to reference the geostrophic shear. Unfortunately a lack

of trajectories within the Gulf Stream means that the strongly sheared horizontal structure of the Gulf Stream remains poorly resolved. In combination with the large θ/S uncertainty within this region (e.g Figure 3.5), this means that our OI technique is not capable of monitoring full-basin transport changes. Instead, calibrated altimetry data are used in the next section to infer Gulf Stream transports.

5. However, the interpolation does yield accurate transports in the interior of the ocean. The mean interior transport above 1000 dbar for the period 2003 to 2007 was -45.8 ± 3.4 Sv. Of this, 15.6 Sv was contributed by the barotropic background velocity at 1000 dbar. The largest southward transport occurred in 2003 when the main thermocline at the western end of the section (67.61°W) was warmest, thus causing a large dynamic height gradient across the basin. Cooling of this region in subsequent years reduced the size of the gradient and consequently the transport. Changes in transport between the seasons are controlled by the similar mechanisms, with a warmer main thermocline at the western end of the section during spring increasing the interior transport. Whilst the main variability in dynamic height on seasonal timescales is caused by seasonal thermocline changes in the top 100 m, this is confined to a small depth range, thus yielding a only small interior transport change in response.

3.5 Gulf Stream Sections and Transport

Given the lack of Argo float coverage in the vicinity of the Gulf Stream and the complex horizontal and vertical shear of the current, the optimal interpolation methods outlined above are inadequate to examine the annual and interannual variability of the western boundary current. As a result, it was decided to seek an alternative strategy to obtain a time series of Gulf Stream transports.

The Line W array (Section 2.7), managed by Woods Hole Oceanographic Institution, was deliberately located beneath a JASON-1 altimeter track. In addition to the moorings, twice yearly CTD-LADCP occupations of the section have been conducted since November 2003, several of which have fully traversed the Gulf Stream. In this study, the methodology of Imawaki et al. (2001) was loosely followed by using the inferred surface velocities from the CTD/LADCP sections to infer the sea surface height difference across the Gulf Stream. A linear regression model was then fitted between these sea surface height differences and the cross-stream integrated Gulf Stream transport. Various depth integrals were used. Finally, this relationship was used to calculate Gulf Stream transport at 10-day resolution from the Line W JASON altimeter data collected in the period 2002 to 2008. These stages are discussed in more detail in Section 3.5.1, before a discussion of the results is presented in Section 3.5.3.

3.5.1 Methodology

In designing the Line W array to monitor the Deep Western Boundary Current, the line was chosen to coincide with track 126 of the TOPEX/Poseidon altimeter (Pena-Molino and Joyce, 2008). Between January 2002 and December 2008, 249 passes of Line W were made by successor mission JASON, yielding an estimate of sea surface height anomaly every 10 days. These altimeter data were accessed using the Radar Altimeter Database System (`http://rads.tudelft.nl/rads/index.shtml`), which provides access to a harmonised, validated and cross-calibrated version of the data set (Naeije et al., 2000). Unfortunately, these data only provide sea surface height anomalies from a temporal mean and not the absolute SSH referenced to the geoid. Rio and Henrandez (2004) have recently constructed a global mean dynamic topography from a combination of altimetry, in situ measurements and a geoid model on a $1^\circ \times 0.5^\circ$ grid; however this product lacks the spatial resolution along the Line W section to provide an accurate mean background field. In situ cruise data from Line W is thus used to estimate the absolute SSH differences, as outlined below.

Line W Cruise Sections

Nine CTD/LADCP sections taken as part of the Line W programme were used to estimate surface velocities and full-depth Gulf Stream transport. Details of these cruises are given in Table 3.7. A tenth section, occupied during April 2007, only occupied the slope waters inshore of the Stream and consequently was not used. Prior to estimating the Gulf Stream transport, the data were processed as follows:

1. The nine CTD sections were downloaded in the WOCE .ctd format from the Line W world wide web pages (`http://www.whoi.edu/science/PO/linew/data/index.htm`). These CTD data were interpolated onto 2 dbar pressure surfaces and have an attached quality control flag, with one file per station. Temperature is reported correct to 0.001°C and salinity to 0.02 after laboratory calibration. All data flagged as good (quality flag 2) were used.

2. The lowered ADCP files for each station were downloaded from the same location as .dat files. These data had previously been detided using the Oregon State University Ocean Model (Egbert et al., 1994). In order to check the consistency of the data, the final processed u and v velocities in the bottom bin were compared with the bottom velocities derived using the bottom tracking only. Visual examination revealed strong agreement in the velocities near the bottom (an example is given in Figure 3.40) and the velocity values at the deepest common level between each set of stations were thus used to reference the geostrophic shear.

3. Geostrophic shear between each station was calculated from the CTD data and referenced using the deepest common level velocity of the LADCP between each station. In a handful of cases where LADCP data were missing at a particular station (e.g. at

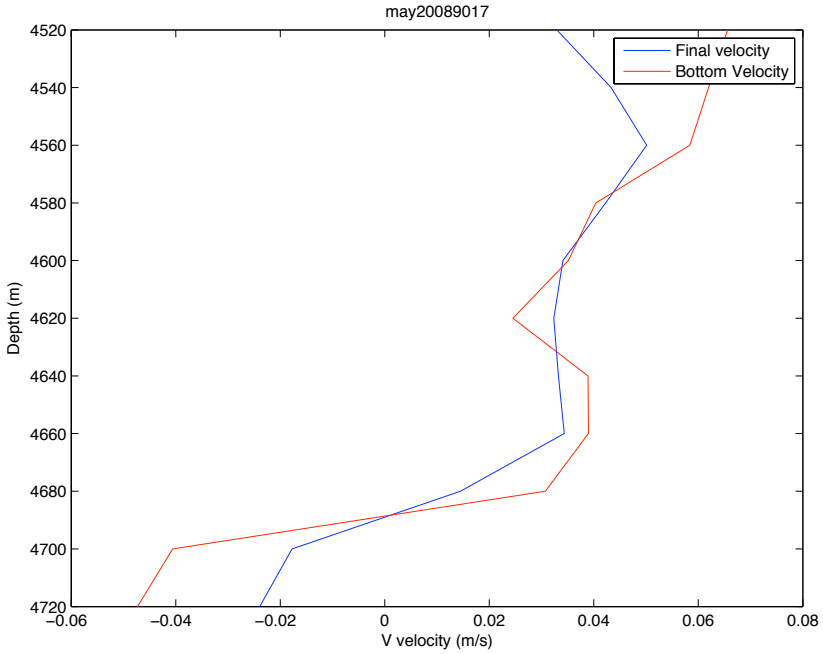

Figure 3.40: Comparison of bottom v velocities derived from bottom tracking (in red) and the final choice of LADCP velocity (in blue) for Station 17 of the May 2008 section.

Station 9 in April 2006), deepest common level velocities were linearly interpolated from the nearest stations. The nine alongstream velocity sections are shown in Figure 3.41.

4. Bottom triangle transports were calculated by reproducing the deepest common level velocity throughout the bottom triangle and multiplying it by the triangle's area. For the 10 sections used, the total bottom triangle transports of the section sum to between +0.04 Sv and −0.49 Sv.

5. The Gulf Stream transport was calculated by cumulating the cross-stream transport in the top 1000 dbar west to east across the Line W line and defining the inshore edge as the position of minimum cumulated northward transport and the outer edge as the location of maximum cumulated northward transport. This leads to different integration limits between the sections as the Gulf Stream meanders substantially between the individual sections. Whilst it is apparent from Figure 3.41 and from previous studies (e.g. Johns et al. (1995)) that northward Gulf Stream velocities extend to the bottom, the 1000 dbar level was used as the default bottom boundary in our study to make the results more easily comparable with the upper ocean interior transports of the mid-ocean section. The analysis was also repeated for the top 2000 dbar and for the full-depth.

It is apparent from Figure 3.41 that there is substantial interannual variability in the position, structure and peak velocity of the Gulf Stream. In April 2006, for instance, the Gulf Stream extends only to around 2000 dbar and is displaced inshore compared to most other years. In contrast, the April 2005 section has a strong Gulf Stream with peak velocities

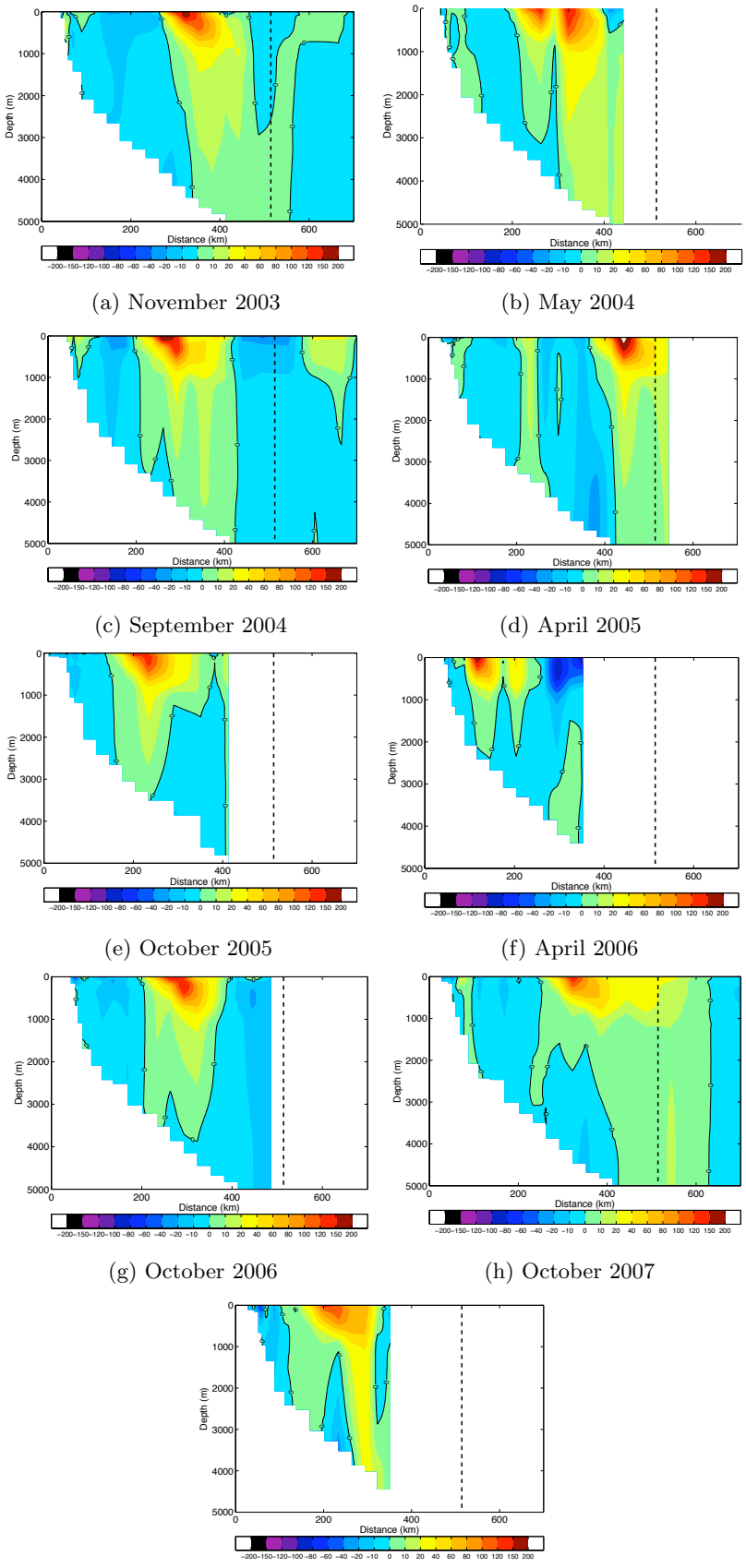

(a) November 2003

(b) May 2004

(c) September 2004

(d) April 2005

(e) October 2005

(f) April 2006

(g) October 2006

(h) October 2007

(i) May 2008

Figure 3.41: Alongstream absolute geostrophic velocity (positive polewards and negative equatorwards) in cm/s for nine Line W cruises. The thick contour is at 0 cm/s. The vertical dashed line shows the position of 36°N.

Cruise dates	Research Vessel	Measurements taken
November 2003	*R/V Knorr*	Shipboard measurements
May 2004	*R/V Oceanus*	Full moored array deployed, shipboard measurments
September 2004	*R/V Cape Hatteras*	Shipboard measurements
April 2005	*R/V Oceanus*	MMP turnaround, shipboard measurements
October 2005	*R/V Oceanus*	Shipboard measurements
April 2006	*R/V Oceanus*	MMP/VACM turnaround, shipboard measurements
October 2006	*R/V Oceanus*	Shipboard measurements
October 2007	*R/V Endeavor*	Shipboard measurements
May 2008	*R/V Oceanus*	Mooring turnaround, shipboard measurements

Table 3.7: Cruises conducted as part of the Line W programme with results included in our regression analysis. A further cruise conducted in April 2007 aboard *R/V Oceanus*. MMP stands for McLane Moored Profiler.

exceeding 2 ms^{-1} and the core of the current is located further offshore; indeed some of the current is actually located south of 36°N. Moreover, the Stream is commonly separated into more than one velocity core (e.g. in May 2004 and April 2006). Integrating the transport from west to east above 1000 dbar yields transports of between 43 and 98 Sv, with the smallest transport in April 2006 and the largest in May 2004 (Figure 3.42). Some sections extend into the recirculation region to the east of the Gulf Stream (e.g. September 2004 and October 2007), whilst in other sections it is not clear that the Gulf Stream has been completely crossed (e.g. October 2005).

In order to quantify the relationship between the Gulf Stream transport and the sea surface height difference across the current, a correlation analysis was undertaken. The horizontal profile of sea surface height for each section was obtained using the absolute geostrophic velocity at the sea surface between the inner and outer edges of the Gulf Stream. This was obtained from the following equation:

$$\eta_2 - \eta_1 = v_s \times \frac{f}{g} \times (x_2 - x_1) \tag{3.1}$$

where η_2 and η_1 are the sea surface heights at either end of the Gulf Stream, $x_2 - x_1$ represents the horizontal distance and v_s is the mean velocity at the surface between x_1 and x_2. A value of f at 38°N is used. The scatter plot of SSH difference against the total transport in the top 1000 dbar is shown in Figure 3.43, with the correlation and regression statistics presented in Table 3.8. A very high correlation coefficient (0.96) is observed, demonstrating that SSH changes are a reliable indicator of Gulf Stream transport variability. This result is even stronger than the 0.90 correlation observed by Imawaki et al. (2001) in the Kuroshio, and suggests that transport changes in the top 1000 dbar of the Gulf Stream are primarily driven by equivalent barotropic transport variability (i.e. an increase in total northward transport results from increased northward velocities in all layers down to 1000 dbar) . This is confirmed by Figure 3.44, which displays the mean transport per unit depth between the inner and outer edges of the Gulf Stream normalised by the mean surface velocity. The fact

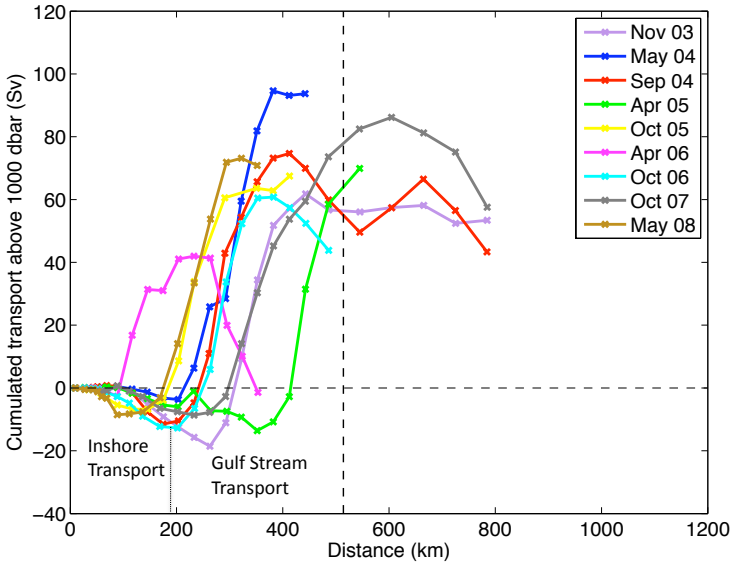

Figure 3.42: Total cumulated west to east transport (in the upper 1000 dbar) for the nine CTD sections reference to the deepest common level of the LADCP. Most sections show a southward transport close to the western boundary associated with the upper parts of the DWBC and then strong northward transport associated with the Gulf Stream further offshore. The dashed line indicates the position of the 36°N section.

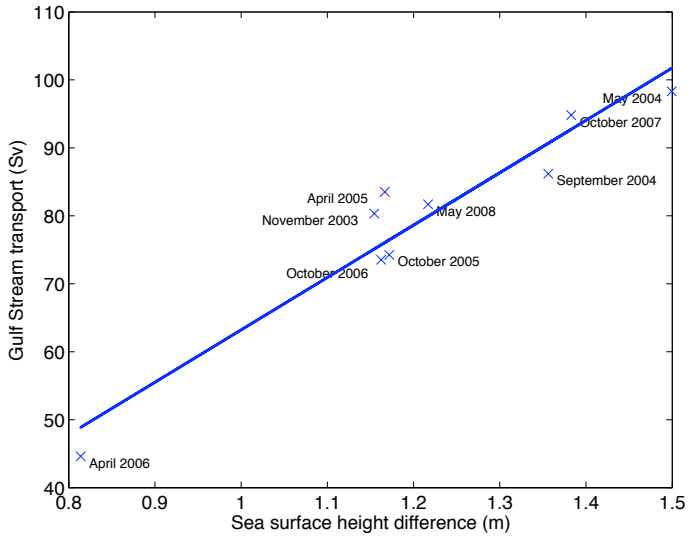

Figure 3.43: Scatter plot of the Gulf Stream transport above 1000 dbar (in Sv) and the sea surface height difference across the current. The solid line shows the linear regression line. For each cruise the inner and outer edges of the Stream are defined by the minimum and maximum cumulated transport (Figure 3.42).

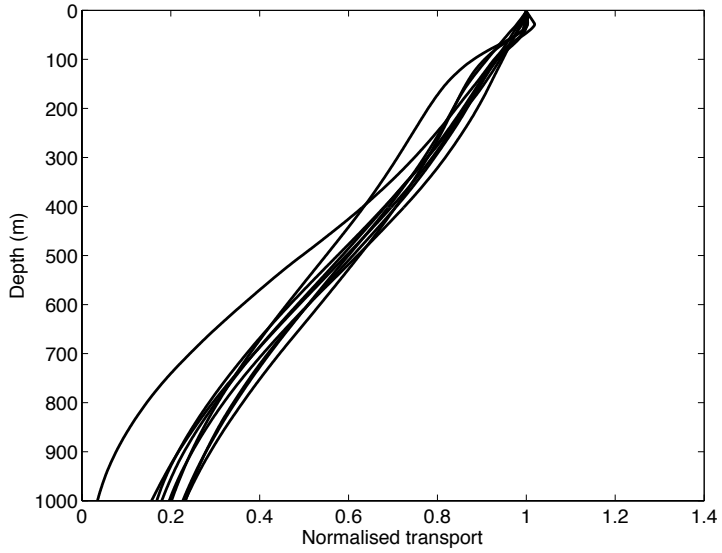

Figure 3.44: Mean transport per unit depth in the upper 1000 dbar between the inner and outer edges of the Gulf Stream normalised by the transport per unit depth at the sea surface for the nine sections. The profile to the left of the others below 500 dbar is the April 2006 section where the Gulf Stream is displaced onshore and largely confined to the upper 1000 dbar (Figure 3.41f).

that most curves overlie one another suggests that transport changes occur simultaneously across all layers, meaning the sea surface height is a reliable expression of the total transport change.

It is acknowledged here that the cruise-derived SSH differences only reflect the geostrophic changes and do not take into account the difference caused by the Ekman transport across the section. Nevertheless, the excellent agreement between SSH difference from the CTD and total Gulf Stream transport implies that the Ekman transport error is likely to be small. Furthermore, the barotropic tide is largely removed from the data by the ADCP processing.

This correlation exercise was repeated for Gulf Stream transport in the upper 2000 dbar and for the full depth transport including the bottom triangles. As the depth range of the integration increases, the overall transport of the Gulf Stream increases but the size of the correlation coefficient decreases (Table 3.8). Although the regression relationship remains statistically significant at the 5% level even when the full depth transport is used, the first linear regression coefficient between SSH difference and transport is not significant for the 1000 to 2000 dbar depth range, with a strong anticorrelation for the region between 2000 dbar and the bottom. These results indicate that whilst the relationship *can* be used to infer transport changes down to 2000 dbar, the results are less certain than for the 0 to 1000 dbar depth range as baroclinic effects become important. The SSH is clearly not a suitable indicator of full-depth changes.

Depth range of transport integration	**Correlation coefficient**	**Regression coefficients (a and b)**	**R^2 value**	**F statistic**	**p value**
$0 - 1000$ dbar	0.9605	77.05/13.87	0.9221	83.4053	$< 1 \times 10^{-5}$
$0 - 2000$ dbar	0.8843	47.76/45.07	0.7820	25.1106	0.0015
0− bottom	0.6892	64.18/41.86	0.4751	6.3347	0.0400
$1000 - 2000$ dbar	0.4175	4.38/16.44	0.1743	1.4775	0.2636
2000 dbar− bottom	−0.6828	−28.26/51.40	0.4717	5.3565	0.0599

Table 3.8: Linear regression statistics for the regression of sea surface height difference determined from absolute surface velocity on Gulf Stream transport in different depth ranges. The relationship expressed by the regression coefficients is GS transport (in Sv) = $a\times$ SSH difference (in m) $+b$.

3.5.2 Possible MOC Compensation at Line W

The strong negative correlation between Gulf Stream transport (as inferred by SSH differences) and transport in the region below 2000 dbar at Line W raises the possibility that changes in the strength of the Gulf Stream in the upper ocean are compensated instantaneously at the western boundary by a volume transport increase in the Deep Western Boundary Current (Table 3.8). It is important to bear in mind that our SSH difference is calculated between the inner and outer edge of the Gulf Stream and *not* the limits of the DWBC, which typically lies slightly inshore of the Gulf Stream at Line W (Figure 3.41). Nevertheless, this is an intriguing result similar to that observed by Bryden et al. (2009) at 26°N, who found that changes in the strength of the Florida Straits transport were compensated by barotropic transport fluctuations very close to the western boundary of the mid-ocean section (p= 0.61 for a ten-day low pass filtered time series). It was found that this depth-independent compensation near the boundary minimised the total size of MOC changes as an increase in the northward limb of the overturning (through an increased northward Gulf Stream transport) was mostly compensated by an enhanced southward upper mid-ocean transport east of the Bahamas (in addition to an increased DWBC).

The geographical configuration of the MOC components at Line W is different to that at 26°N, as the Deep Western Boundary Current lies inshore of the Gulf Stream and the mid-ocean flows are not physically separated from the western boundary current. It will thus require further work beyond the scope of this study to analyse the impact of the negative correlation on long-term monitoring of the DWBC. A useful source additional source of information to investigate our observation is the suite of bottom pressure recorders (BPRs) installed on the bottom of the Line W moorings as part of the RAPID-WAVE array (Elipot et al., 2010), discussed at more length in Section 5.10. Specifically, it would be possible to correlate Gulf Stream transport variability inferred from SSH differences with time series of bottom pressure fluctuations on the five BPRs. This would establish whether changes in the northward limb of the MOC were indeed compensated in a depth-independent manner similar to that observed at 26°N and, in conjunction with the Line W DWBC current meter measurements, would quantify the relationship between the Gulf Stream and the DWBC

on timescales between ten days and interannual.

3.5.3 Time Series of Gulf Stream Transports from Altimetry

Once the regression coefficients between the SSH difference and the Gulf Stream transport for the 9 sections had been established, the altimeter dataset itself could be used to construct a time series of Gulf Stream transport for the period 2002 to 2008. The steps followed were as follows:

1. The mean sea surface height profile across the Gulf Stream was constructed from the nine CTD/LADCP profiles. This was achieved by linearly interpolating the sea surface height differences for each section onto a 5 km grid, with the nearest inshore point being the furthest inshore limit of any of the cruises (40.29°N, 70.20°W). This point was chosen to have an arbitrary sea surface height of zero in all the sections. Finally, a mean of the nine gridded SSH sections was taken (hereafter known as DT_{M9}, DT standing for dynamic topography). This mean profile is shown in Figure 3.45.

2. The altimeter sea surface height anomaly (SSHA) data were extracted for each ten-day period corresponding to the times of the cruise sections. These data were gridded onto the same 5 km grid and averaged to yield $SSHA_{M9}$.

3. All the SSHA data (249 passes in total) were extracted and for each timestep i, the difference between the SSHA at that timestep ($SSHA_i$) and $SSHA_{M9}$ was calculated.

4. The absolute dynamic topography at each 10-day time step DT_i was calculated using Equation 3.2. The inferred mean dynamic topography of the section ($DT_{M9} - SSHA_{M9}$) is displayed in Figure 3.45. Each individual altimeter-derived SSH section is plotted in Figure 3.46.

$$DT_i = DT_{M9} + (SSHA_i - SSHA_{M9}) \tag{3.2}$$

5. Finally, the sea surface height difference between the minimum and maximum points for each DT_i was found. These points were constrained to be north of 36°N as we wished to identify the maximum associated with the southern edge of the Gulf Stream and not any other maxima in SSH in the gyre itself. The Gulf Stream transport above 1000 dbar could then be calculated using the regression coefficients in Table 3.8.

The final time series of Gulf Stream transports above 1000 dbar is found in Figure 3.47. A maximum value of 123.7 Sv was observed in July 2003 and a minimum value of 45.7 Sv in December 2008. The mean value of Gulf Stream transport in the period 2002 to 2008 across Line W was 87.6 Sv. Linear regression of the time series suggests a reduction of 1.04 Sv per year between 2002 and 2008, with the trend being statistically significant at the 99% level (p-value= 0.009). However, if the final 3 months of extremely low Gulf Stream transport are excluded, the value is 0.76 Sv per year, which is not significant at the 5% level.

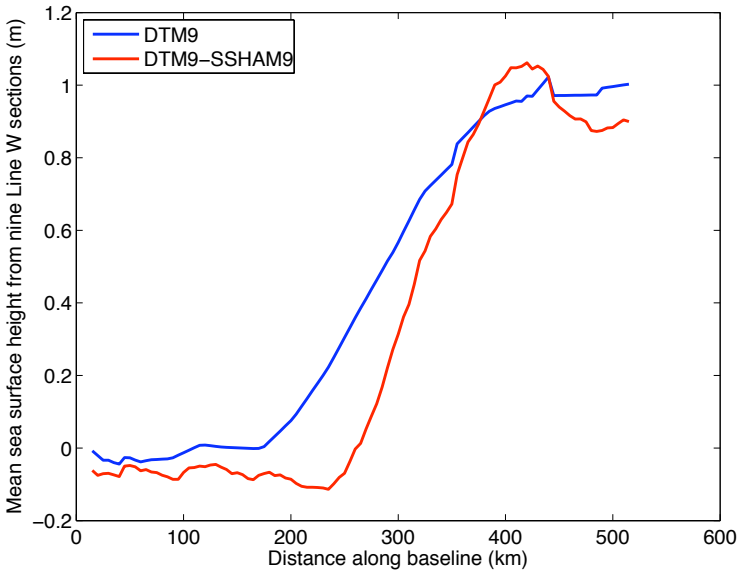

Figure 3.45: Plot to show mean dynamic topography of the nine sections inferred from the hydrographic data (DT_{M9}), along with the assumed long-term mean dynamic topography calculated from $DT_{M9} - SSHA_{M9}$. The region south of 36°N is excluded.

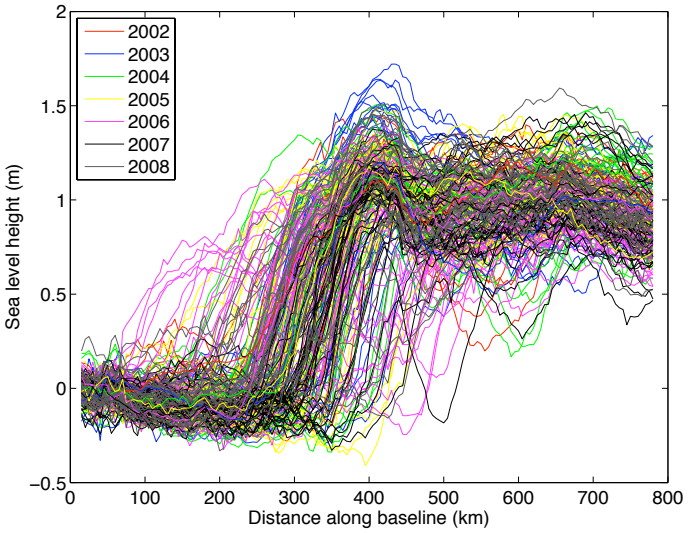

Figure 3.46: Absolute dynamic topography sections (in metres) for each altimeter pass in the period January 2002 to December 2008. The sections are colour-coded by year.

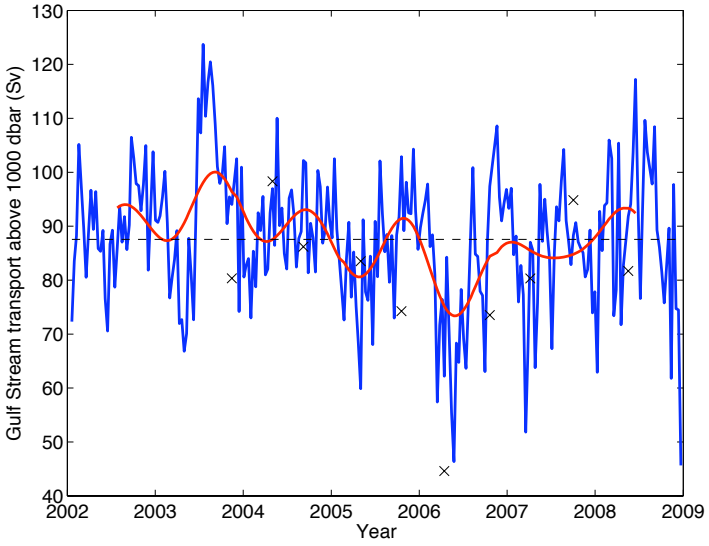

Figure 3.47: Transport of Gulf Stream transport in the top 1000 dbar for the period 2002 to 2008, with 10-day resolution. The red line shows a 12-month low pass Butterworth-filtered version of the time series. Blue crosses show the cruise estimates.

The application of a 12-month filter reveals a Gulf Stream fluctuating in strength by up to 20 Sv, with a substantial reduction in transport during the first half of 2006, supported by the cruise data in April and October 2006.

There was a weaker correlation between SSH difference and the 0 to 2000 dbar Gulf Stream transport, as shown both in Table 3.8 and by the poorer agreement between cruise estimates and altimeter estimates of transport in Figure 3.48. Nevertheless, a time series was produced of top 2000 dbar Gulf Stream transports for comparison with Halkin and Rossby's study. The mean transport was 107.9 Sv, with a maximum of 130.3 Sv and a minimum of 82.0 Sv (again in December 2008 and April 2006 respectively). Linear regression implies a reduction in the Gulf Stream transport of 0.65 Sv per year between 2002 and 2008, with this again being statistically significant at the 99% level (p-value = 0.009). Application of the 12-month filter yields a very similar pattern to the Gulf Stream transports above 1000 dbar, with a notable reduction in strength during 2006 also being observed over this increased depth range.

Given the high temporal resolution of these transport time series, spectral analyses were conducted on the Gulf Stream transports to identify the dominant timescales of variability (see Figure 3.49 for the upper 1000 dbar results). No obvious annual or semiannual peaks can be found in the spectra, although there is some evidence of raised power at periods close to 1 month. This result agrees with Gulf Stream layer transport inferred from the Oleander line (Rossby et al., 2005), which showed no dominant time period of variability in the years 1993 to 2004 (their Figure 7). However, a boxplot of the Gulf Stream in the top 1000 dbar (Figure 3.50a) does show evidence of an annual cycle with a peak transport in August and a minimum in March. The size of this annual cycle (using mean monthly transports) is close to 12 Sv, but with substantial interannual variability. For instance, the three largest

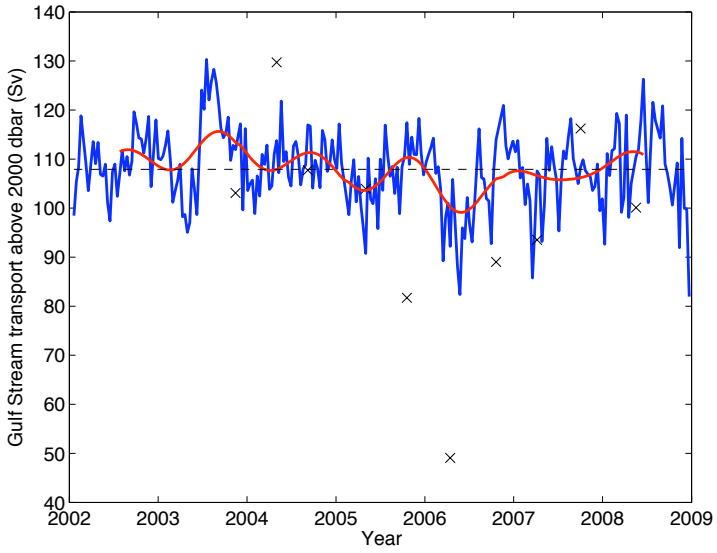

Figure 3.48: Transport of Gulf Stream transport in the top 2000 dbar for the period 2002 to 2008, with 10-day resolution. The red line shows a 12-month low pass Butterworth-filtered version of the time series. Blue crosses show the cruise estimates.

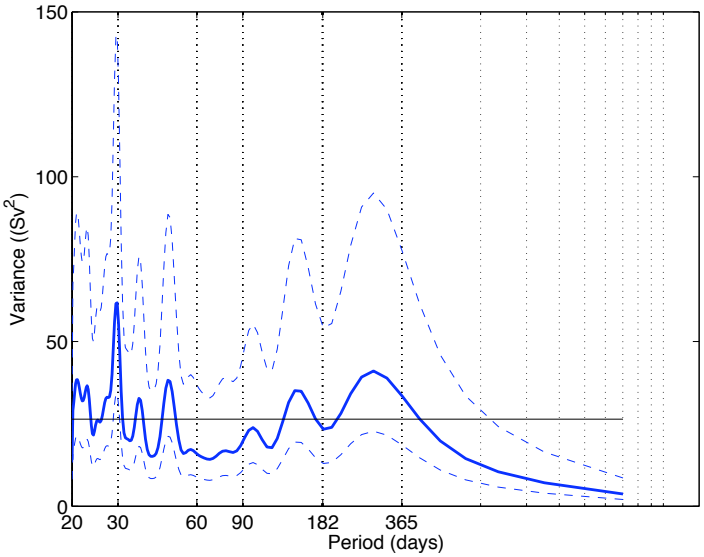

Figure 3.49: Welch spectral analysis (8 windows, 50% overlap) of the horizontally and vertically integrated Gulf Stream transport above 1000 m in the period 2002 to 2008. The dashed lines represent the 5% and 95% confidence intervals and the solid horizontal line represents the mean variance.

10 day transports are in July 2003, June 2004 and August 2003 respectively, showing that the largest transports do not occur in August every year.

The 2000 dbar results can now be compared directly with Halkin and Rossby (1985), who obtained 16 Gulf Stream sections from 1980 to 1983. In their study, they found an annual cycle of magnitude 18 Sv in the top 2000 dbar, with larger values in February to July than in August to January. This cycle was dominated by baroclinic changes, with barotropic changes caused by the changing reference velocity at 2000 dbar being relatively unimportant. Whilst it is not possible from the SSH method to infer baroclinic variability, the strength of the correlation coefficient has shown that, at least in the top 1000 dbar, transport changes affecting all layers in the same direction *are* a strong component of boundary current variability, causing annual transport changes of around 12 Sv. Therefore, our study suggests that barotropic variability *is* a significant cause of Gulf Stream transport variability. Furthermore, a boxplot of our results shows a maximum Gulf Stream transport in August and a minimum in March (Figure 3.50b), which is significantly different to that observed by Halkin and Rossby.

It should be recognised that Halkin and Rossby's conclusions were drawn from just 16 Gulf Stream sections taken over a three-year period, and they acknowledged that this is insufficient to determine the amplitude or phase of the annual harmonic. Nevertheless, their result is supported by an earlier review of 32 hydrographic sections across the Gulf Stream in the Chesapeake Bay-Bermuda-Long Island area by Worthington (1976), which suggested stronger Gulf Stream transport in the first six months of the year. In order to test our finding of larger transports towards the end of the year, the year was split into halves from January to June and July to December. Over the top 2000 dbar, the mean transport for the first half of the year derived from all the individual altimeter passes was 105.8 Sv. The mean for the second half of the year was 110.0 Sv. To investigate whether these means were statistically different, a one-tailed student's t-test was instituted. The t statistic of 4.32 has a p-value of less than 0.001, indicating that the mean value of Gulf Stream transport in the second half of the year is greater than that in the January to June period. Despite the lack of agreement with Halkin and Rossby's work, our results *do* more closely match work by Baringer and Larsen (2001) at Florida Straits, who uncovered a weak annual cycle with a maximum in July and a minimum in January. However, in their results, both the magnitude and phase of the annual cycle changed from the first eight years of the record to the second eight years, with a distinct semi-annual cycle observed during this later period (1990-1998). The most recent appraisal of the Florida Straits cable transport over 26 years (Atkinson et al., 2010) confirmed the presence of a 3.3 Sv seasonal cycle, with a minimum in January and a maximum in July. The cycle was rather more symmetric than in the earlier study by Baringer and Larsen (2001).

Support for our seasonal cycle results is also found in Sato and Rossby (1995), who argue for a maximum in Gulf Stream transport in the top 2000 dbar during July. In their study of 130 pairs of historical hydrographic stations close to Line W, they found that the upper 300 dbar

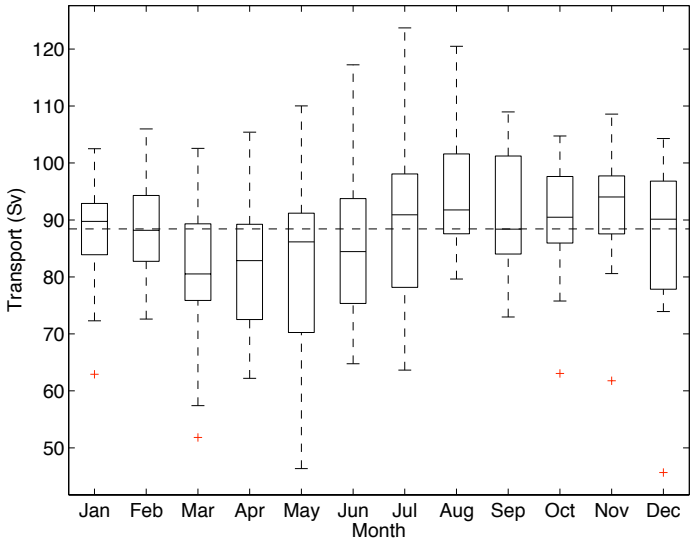

(a) Top 1000 dbar

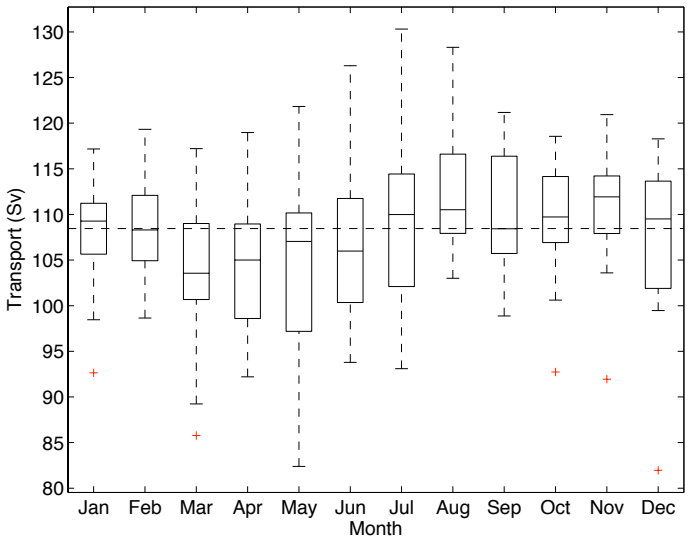

(b) Top 2000 dbar

Figure 3.50: Boxplots of Gulf Stream transport in (a) the top 1000 dbar and (b) the top 2000 dbar, organised by month. The boxes show the lower (Q_1) and upper quartiles (Q_3) and median value, with the upper whiskers extending to furthest data point that lies within the region $Q_3 + 1.5(Q_3 - Q_1)$ and the lower whiskers extending to the further data point that lies within the region $Q_1 - 1.5(Q_3 - Q_1)$. The dashed line shows the median transport.

transport reached a maximum during the autumn, when the difference in the amplitude of the seasonal thermocline to either side of the stream was greatest. However, over the entire 2000 dbar, an annual cycle with a phase similar to the Line W line was observed (their Figure 7b), though the minimum transport in their study occurs earlier in the year (during January).

3.6 Final Comments

Discussion in this section has focused on the annual and interannual variability in the Gulf Stream and interior transport that constitute the major volume transports of the subtropical gyre. In neither component was a large long term trend in transport observed, though the length of each time series is relatively short (6 or 7 years). As measured by the standard deviation, the size of the variability in the interior transport between seasons is very similar to the interannual variability (6.6 compared with 7.7 Sv). The interior transport reached a maximum of 56 Sv during 2003 and is typically at a maximum during spring (58 Sv). In contrast, the Gulf Stream has a maximum transport during August (93 Sv in the top 1000 dbar) and a minimum during March (81 Sv).

The OI and altimeter-based methods have yielded robust transport estimates for the two largest components of the transport above 1000 dbar, and it is legitimate to ask whether these can be used to estimate the size of the meridional overturning circulation along the 36°N/Line W section. Before this can be done, two other components of the transport need to be quantified, these being the zonally integrated Ekman transport (estimated in Chapter 4) and the transport inshore of the Gulf Stream. Nine cruise-based estimates of transport in the upper 1000 dbar are available for the region between the most inshore station and the inner edge of the Gulf Stream (Figure 3.42). These have a mean value of -9.6 Sv with a standard error of 1.7 Sv. However, it is not clear whether this time series can be extended using the same altimeter methods as applied to the Gulf Stream. Some data are available from the Line W moorings, but only W1 and W3 extend as shallow as 100 m, limiting the horizontal resolution of the transport field. In addition, transport has not been quantified on the slope between Cape Cod and the innermost cruise station; an altimeter-type analysis also becomes more difficult in this region as it is known that measurements within 30 km of the coast are subject to contamination by radar return from both the coastal sea-surface state and land topography (Deng et al., 2002).

Despite these difficulties, the mean size of the total northward transport above 1000 dbar for the period 2002 to 2007 is estimated in Section 5.8. Comparisons with existing literature values and remaining difficulties in quantifying the total MOC using our methods are also outlined.

Chapter 4

Which Processes are Driving the Transport Variability?

The focus of this chapter is on the role of wind forcing in driving the variability of the ocean transports in the North Atlantic at 36°N. Classical oceanographic theory suggests that surface wind stress drives two main types of large-scale ocean flow. The first, detailed by Ekman (1905), and now known universally as Ekman transport, predicts that a steady wind stress acting in conjunction with the Coriolis force will produce a transport of water to the right of the wind in the Northern Hemisphere (Section 4.1.1). Analysis of QuickSCAT scatterometer data from the period of cruise CD171 showed that the total horizontally integrated Ekman transport across 36°N in May 2005 was 2 Sv southwards. The second type of wind-driven flow, known as Sverdrup transport (Section 4.1.2), relates the curl of the wind stress to the total mass transport in the upper ocean. The zonal integral of this quantity is substantially larger than the Ekman flow. In the North Atlantic between 27°N and 29°N, Bryden et al. (2005a) estimated it to be 22.1 Sv southwards. Both Ekman and Sverdrup relations rest on a number of assumptions that are discussed in Sections 4.1.1 and 4.1.2.

Time series of Ekman and Sverdrup transports at 36°N from four different wind stress products are then presented and the results analysed. The individual time series are covered in detail in Section 4.2 and differences between the individual products highlighted. In order to deduce the principal timescales and spatial patterns of variability in the Ekman and Sverdrup transport fields in the subtropical North Atlantic, both spectral estimation and empirical orthogonal function (EOF) analysis are used on fields of zonal wind stress and wind stress curl in the latitude band 28°N to 40°N. The principles of these methods are outlined in Sections 4.3.1 and 4.3.2 and the results discussed. Section 4.4 relates these time series and their dominant modes of variability to the North Atlantic Oscillation, the largest mode of atmospheric variability in the Northern Hemisphere (Rogers, 1990). The findings are summarised in Section 4.5.

The time series of Sverdrup minus Ekman transport derived in this chapter is then com-

pared with our OI-based estimate of interior transport variability in Chapter 5 to test the hypothesis that the upper ocean gyre transport is controlled on an annual and interannual basis by changes in the basin-integrated wind stress forcing.

4.1 Theory of Wind Driven Circulation

4.1.1 Ekman Transport

In Ekman's (1905) seminal paper, the effect of friction imparted by wind on the surface of the ocean was treated rigorously for the first time. Assuming no acceleration, the horizontal equations of motion are written as:

$$\begin{aligned} fv + F_x - \alpha\frac{\partial p}{\partial x} &= 0 \\ -fu + F_y - \alpha\frac{\partial p}{\partial y} &= 0 \end{aligned} \tag{4.1}$$

where f is the Coriolis parameter, F_x and F_y are the friction in the x (eastward) and y (northward) directions respectively, α is the inverse of density and p is pressure. In the turbulent ocean where the Reynolds Number exceeds 1000, Ekman deduced that friction force per unit mass in x and y directions can be expressed as a function of an eddy viscosity A_z, causing Equations 4.1 to take the form:

$$\begin{aligned} fv + \alpha\frac{\partial \tau_x}{\partial z} = fv + A_z\frac{\partial^2 u}{\partial z^2} &= \alpha\frac{\partial p}{\partial x} \\ -fu + \alpha\frac{\partial \tau_y}{\partial z} = -fu + A_z\frac{\partial^2 v}{\partial z^2} &= \alpha\frac{\partial p}{\partial y} \end{aligned} \tag{4.2}$$

where τ_x and τ_y are the zonal and meridional wind stresses.

By scaling arguments, Ekman showed that the friction term is important within around 100 m of the surface, a depth referred to as the Ekman depth (D_E). From these equations, Ekman made a number of assumptions:

1. No ocean boundaries.
2. A constant eddy viscosity.
3. A steady wind blowing for a long time.
4. f is a constant.
5. Infinitely deep water (to avoid the bottom friction term becoming important).

6. Homogeneous water ($\frac{\partial p}{\partial x} = \frac{\partial p}{\partial y} = 0$), and thus the geostrophic velocity components are zero.

The u and v velocities can then be determined as a function of depth (assuming here that the wind is blowing in the y direction):

$$\begin{aligned} u_E &= \pm V_0 \cos\left(\frac{\pi}{4} + \frac{\pi}{D_E} z\right) \exp\left(\frac{\pi z}{D_E}\right) \\ v_E &= \pm V_0 \sin\left(\frac{\pi}{4} + \frac{\pi}{D_E} z\right) \exp\left(\frac{\pi z}{D_E}\right) \end{aligned} \tag{4.3}$$

where u_E and v_E are the eastward and northward Ekman velocities, V_0 is the total Ekman surface current and D_E is the Ekman depth. The equations are positive in the northern hemisphere and negative in the southern hemisphere. These equations predict the classic Ekman current spiral, which has been observed both in the laboratory and by current meters in the subtropical North Atlantic (Price et al., 1987).

In order to measure the total basin-wide Ekman transport, Equation 4.2 can be written as:

$$\begin{aligned} \rho f v_E + \frac{\partial \tau_x}{\partial z} &= 0 \\ \rho f u_E + \frac{\partial \tau_x}{\partial z} &= 0 \end{aligned} \tag{4.4}$$

Integrating these equations yields:

$$\begin{aligned} \int_{-2D_E}^{0} u_E \, dz &= \frac{\tau_y}{\rho f} \\ \int_{-2D_E}^{0} v_E \, dz &= -\frac{\tau_x}{\rho f} \end{aligned} \tag{4.5}$$

A further integration across the width of the basin gives the total volume transport in $\mathrm{m^3 s^{-1}}$.

In conclusion, the Ekman transport quantifies the non-geostrophic portion of the wind-driven flow caused directly by the frictional action of the wind stress on the ocean surface. Being confined to the upper 100 m, the meridional Ekman transport is a relatively small component of the volume transport budget of the upper ocean in the subtropical North Atlantic (e.g. Cunningham et al. (2007)).

4.1.2 Sverdrup Transport

Whilst Ekman chose simply to ignore the pressure gradient terms of the equations of motion (Equation 4.2), these terms in reality *do* contribute significantly to the volume transport of the layer affected by the wind. Sverdrup, in his 1947 paper, thus chose instead to retain the pressure terms but did not attempt to determine u and v velocities as a function of depth. Integrating the equations of motion gives:

$$\begin{aligned} \int_{-h}^{0} \frac{\partial p}{\partial x}\, dz &= \int_{-h}^{0} \rho f v\, dz + \tau_x = f M_y + \tau_x \\ \int_{-h}^{0} \frac{\partial p}{\partial y}\, dz &= -\int_{-h}^{0} \rho f u\, dz + \tau_x = -f M_x + \tau_y \end{aligned} \tag{4.6}$$

where $h > D_E$ and is the depth of the ocean at which the vertical velocity goes to zero. M_x and M_y is the mass transport in zonal and meridional directions. Differentiating the first of Equations 4.6 by y and the second by x, then subtracting the two equations from one another gives:

$$\beta M_y = \frac{\partial \tau_y}{\partial x} - \frac{\partial \tau_x}{\partial y} \tag{4.7}$$

where β is the north-south gradient of the Coriolis parameter f. This equation is equivalent to Equation 1.1.

In other words, the total mass transport of the upper ocean, including both Ekman and geostrophic components, is defined by the spatial derivatives of the wind stress and the meridional gradient of the Coriolis parameter. Converting mass transport into volume transport and integrating across the width of the section yields the total Sverdrup transport in $\mathrm{m^3 s^{-1}}$.

Unlike the Ekman equation, the Sverdrup solution in not bound by the homogeneous ocean limitation, but it still contains a number of simplifications. Firstly, it ignores strong horizontal friction terms in regions such as the Gulf Stream making its solutions only valid in the interior of the gyre at 36°N. Secondly, the differential equations allow only one boundary condition to be satisfied (in the east). Finally, it can only provide a measure of the depth integrated mass transport and not its variation with depth.

In conclusion, both the Ekman and Sverdrup solutions are closely related through the equation:

$$M_{yS} = M_{yE} + M_{yg} \tag{4.8}$$

where S, E and g refer to the Sverdrup, Ekman and geostrophic contributions respectively.

The geostrophic component has been estimated independently on an annual and seasonal basis by the optimal interpolation of Argo float and Line W data (Chapter 3) and the consistency of this relationship will be examined in more detail in Chapter 5.

4.2 Time Series of Ekman and Sverdrup Transports

4.2.1 Ekman Transport

Time series of zonally integrated meridional Ekman transport at 36°N are given in Figure 4.1, based on monthly estimates from the four wind stress products introduced in Chapter 2. The four products show close agreement both in their mean values and in their standard deviation in their overlapping period – August 1999 to December 2005 – with all displaying a southward transport of close to 2 Sv southwards (Table 4.1). Regression analysis was performed over the full length of each time series (Table 4.2), with the results of an F test being used to determine whether the first linear regression coefficient was significantly different from zero. As the p values in all cases exceed 0.05, it is concluded that there are no significant linear trends in the basin-integrated Ekman transport at 36°N. Given that the NCEP/NCAR Reanalysis extends back to 1948, it would thus appear that there has been no change in the mean value of Ekman transport during the last 60 years.

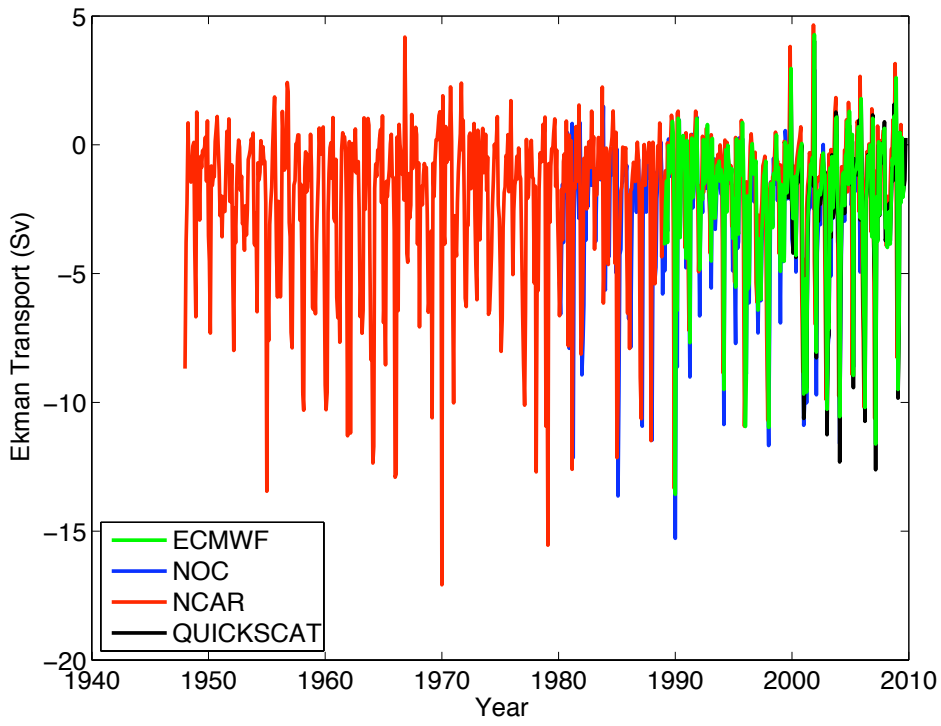

Figure 4.1: Zonally integrated Ekman transport at 36°N, based on four estimates of wind stress from the ECMWF Interim Reanalysis (1989-2009), the NOC Climatology (1980-2005), the NCEP/NCAR Reanalysis (1948-2009) and the QUICKSCAT Scatterometer (1999-2009).

Wind stress product	Mean Ekman Transport (Sv)	Standard deviation of Ekman transport (Sv)
ECMWF	−2.16	3.03
NOC	−2.85	3.07
NCEP/NCAR	−1.79	2.95
QUICKSCAT	−2.52	3.20

Table 4.1: Mean and standard deviation of the zonally integrated meridional Ekman transport at 36°N in the Atlantic for the period August 1999 to December 2005.

	Regression coefficients	F statistic	p value
ECMWF	$-0.0049/-2.3686$	0.2800	0.8715
NOC	$-0.0116/-2.8452$	1.2176	0.5971
NCEP/NCAR	$0.0069/-2.0177$	0.0262	0.2702
QUICKSCAT	$0.0816/-2.9183$	0.7020	0.4038

Table 4.2: Statistics of the four time series of zonally integrated Ekman transport at 36°N. The left hand column shows the linear regression coefficients a and b of the regression relationship $E = a(t - 2002) + b$, where t is time in years and E is the Ekman transport in Sv. The F statistic and associated p value express the probability that a is significantly different from zero.

For completeness, the regression analysis was repeated using only data from 2002 to 2008, the period over which we have estimated interior transport from the Argo float data (Table 4.3). Once again, no statistically significant trend was observed, though the three available products suggested a small reduction in the southward magnitude of around 1 Sv over the period (calculated from the first linear regression coefficients of Table 4.3).

In order to compare the consistency of the estimates from the four products, linear regression analyses were also conducted between all four individual time series for the overlapping portion of the time series (August 1999 to December 2005). The results are given in Table 4.4. In all cases, correlation coefficients between the products exceed 0.97 and the first linear regression coefficient is in the range 0.93 to 1.07, indicating a near one-to-one relationship between the Ekman transport estimates.

The latitudinal variability of Ekman transport in the subtropical North Atlantic is seen clearly in Figure 4.2. South of 32°N, the Ekman transport is directed northwards, coincident with the trade winds at these latitudes, whilst the midlatitude westerly winds north of 32°N lead to a southward Ekman transport, with a maximum value of 3 Sv close to 40°N. There is close agreement between all four products across the entire latitude range, with mean

	Regression coefficients	F statistic	p value
ECMWF	$0.2188/-2.94$	1.963	0.1650
NCAR	$0.2132/-2.56$	1.966	0.1647
QUICKSCAT	$0.2499/-3.32$	2.268	0.1360

Table 4.3: As Table 4.2, except for the period 2002 to 2008 only. The NOC time series is excluded as it ends in December 2005.

	NOC	**NCEP/NCAR**	**QUICKSCAT**
ECMWF	0.9798/0.9933/ −0.6969/0	0.9954/0.9682 0.3089/0	0.9933/1.0427 −0.2525/0
NOC	- -	0.9702/0.9309 0.8631/0	0.9737/1.0082 0.3605/0
NCEP/NCAR	- -	- -	0.9868/1.0650 −0.6066/0

Table 4.4: Statistics for the cross-correlation of the individual time series of the zonally integrated Ekman transport at 36°N in Sv. In each box, the first figure gives the correlation coefficient, the second and third figures are the linear regression coefficients a and b of the relationship $y = ax + b$ where y is the time series in the top row and x is the time series in the left hand column. The fourth figure displays the probability that the regression coefficient a is statistically different from zero, from the results of an F test. Values of zero indicate a probability of $< 1 \times 10^{-12}$. An assumption of statistical independence is made when calculating degrees of freedom, which is not strictly true for NCEP/NCAR and QUICKSCAT after 2002.

values not differing by more than 1 Sv.

Inspection of the mean wind stress fields for the period since 2002 (Figure 4.3) confirms the meridional pattern of Ekman transport observed in Figure 4.2. At 36°N, westerly winds dominate in the western part of the basin, with weaker north or northeasterly winds found east of 20°W, resulting in a *net* southward Ekman transport. South of 36°N, the northeasterly trade winds are found over an increasing proportion of the basin, resulting in northward Ekman transport across the entire basin south of 30°N. The region of Ekman convergence occurs near 31°N in the western basin, moving to 38°N in the eastern basin close to 20°W. The consistency of such a pattern between the four wind stress products is encouraging and suggests our estimate of Ekman transports at 36°N is robust.

Finally, the zonal structure of the Ekman transport is plotted (Figure 4.4). In line with the observations of the mean wind stress fields, the meridional Ekman transport is near zero between the eastern boundary and around 30°W, with relatively weak southward Ekman flow over the rest of the basin corresponding to the region of westerly winds. The rate of cumulation of the Ekman transport as the western boundary is approached, in line with the reduction in the strength of the westerlies to the west of 70°W. All four products are consistent in replicating this pattern.

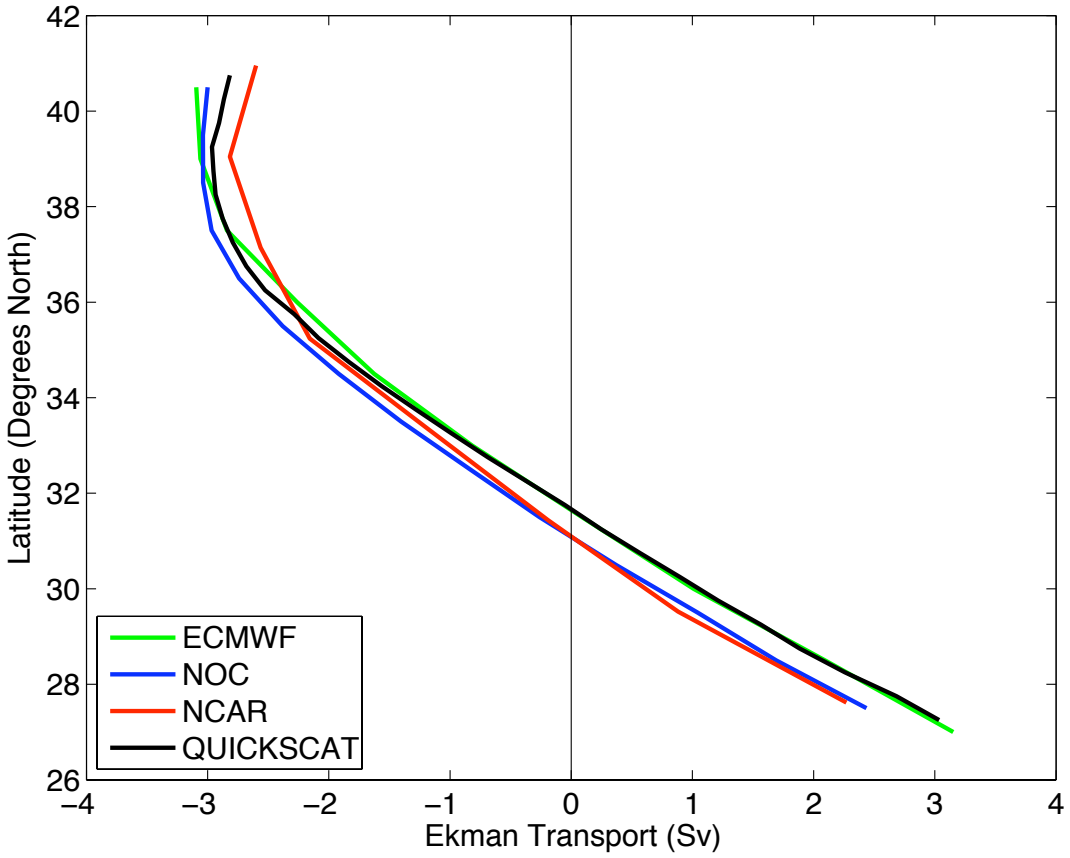

Figure 4.2: Mean zonally integrated Ekman transport, based on four estimates of wind stress from the ECMWF Interim Reanalysis (1989-2009), the NOC Climatology (1980-2005), the NCEP/NCAR Reanalysis (1948-2009) and the QUICKSCAT Scatterometer (1999-2009).

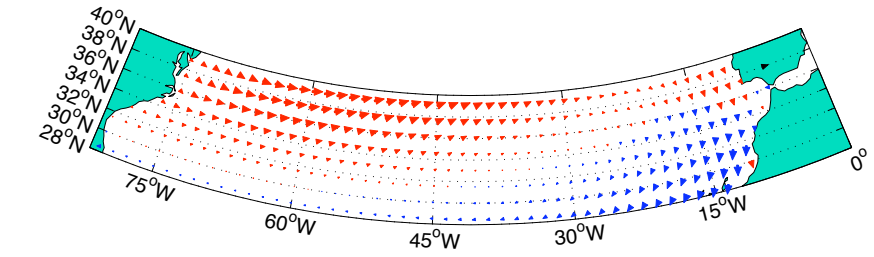

(a) ECMWF

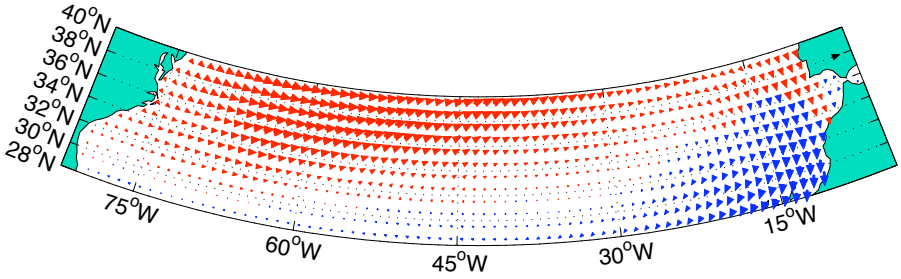

(b) NOC

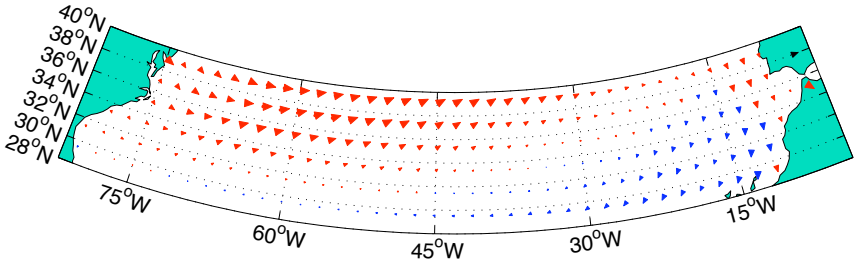

(c) NCEP/NCAR

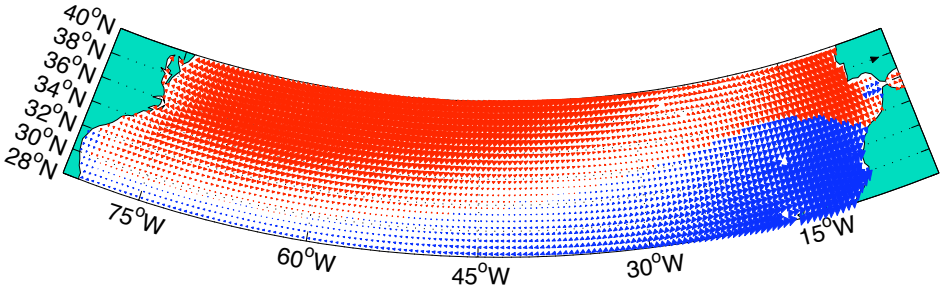

(d) QUICKSCAT

Figure 4.3: Mean wind stress fields for four different wind stress products in the region of the North Atlantic between 28°N and 40°N. Products and averaging period are (a) the ECMWF Interim Reanalysis (2002-2008), (b) the NOC Climatology (2002-2005), (c) the NCEP/NCAR Reanalysis (2002-2008) and (d) the QUICKSCAT Scatterometer (2002-2008). Note the differing resolution of the four wind stress products. Positive eastward-directed stress is plotted in red and negative westward-directed stress in blue. The black arrow plotted over Iberia corresponds to a wind stress of 0.5 Nm^{-2}.

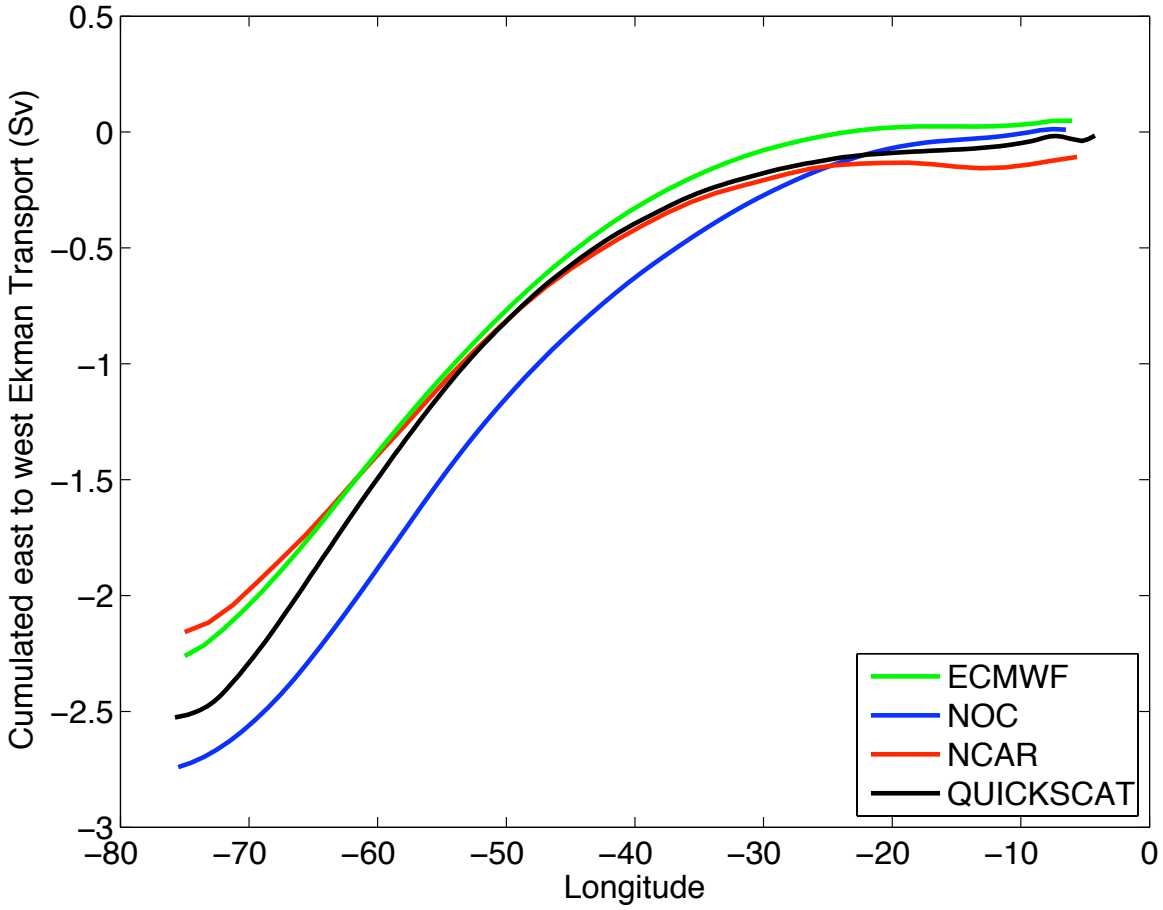

Figure 4.4: Cumulated mean east to west Ekman transport (Sv) at 36°N for four wind stress products for the periods in Figure 4.2.

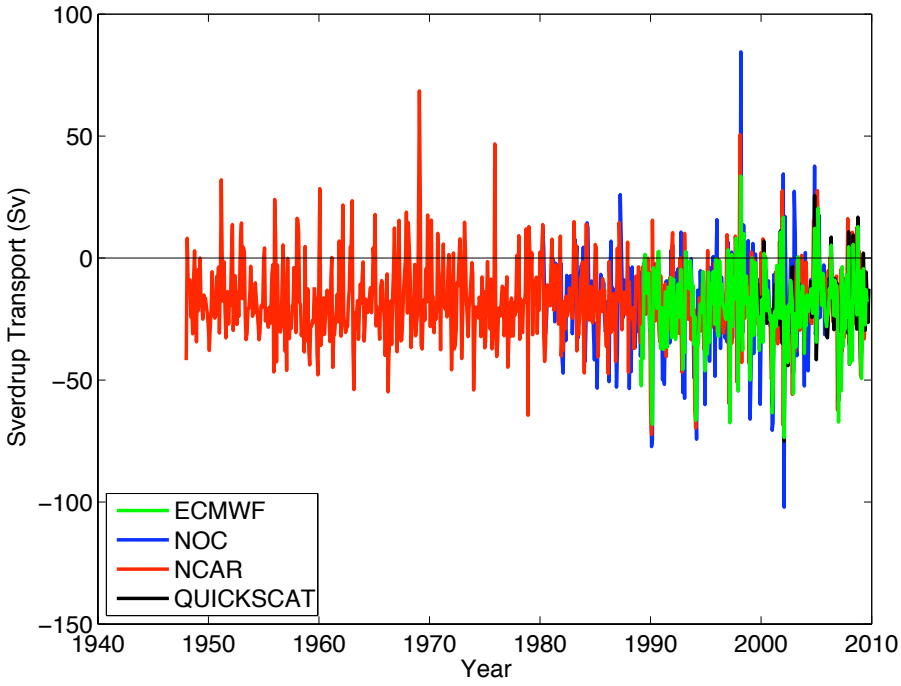

Figure 4.5: Zonally integrated Sverdrup transport at 36°N, based on four estimates of wind stress curl from the ECMWF Interim Reanalysis (1989-2009), the NOC Climatology (1980-2005), the NCEP/NCAR Reanalysis (1948-2009) and the QUICKSCAT scatterometer (1999-2009).

4.2.2 Sverdrup Transport

Monthly time series of basin-wide zonally integrated Sverdrup transports at 36°N are given in Figure 4.5. As with the Ekman transport, a close correlation is observed between the four products, whose mean values and standard deviations are given in Table 4.5. In the period for which the four products overlap, the mean Sverdrup transports agree to within 3 Sv and have a similar measure of standard deviation (between 15 Sv and 21 Sv). The standard deviation for Sverdrup transport is five to six times larger than the comparable measure for Ekman transport (Tables 4.1 and 4.5); the mean value is almost ten times larger.

The close correlation between the products is confirmed by a correlation analysis (Table 4.6). However, the values of the linear regression coefficients suggest there is not a simple one-to-one relationship between the product estimates. For instance, the second linear regression coefficient for QUICKSCAT vs. NOC is −10.54, indicating a large offset from zero, whilst the first coefficient (0.4921) indicates that a 1 Sv change in NOC-derived Sverdrup transport would only correspond to a 0.49 Sv change in the QUICKSCAT value.

A temporal linear regression analysis of all four products confirms that there is no long term trend in the zonally integrated Sverdrup transport at 36°N in the period since 1948 (Table 4.7). Once again, the regression was repeated for only the period between 2002 to 2008

Wind stress product	Mean Sverdrup Transport (Sv)	Standard deviation of Sverdrup Transport (Sv)
ECMWF	−20.54	15.68
NOC	−19.84	21.94
NCEP/NCAR	−17.56	16.18
QUICKSCAT	−20.31	15.65

Table 4.5: Mean and standard deviation of zonally integrated Sverdrup transport at 36°N in the Atlantic for the period August 1999 to December 2005.

	NOC	NCEP/NCAR	QUICKSCAT
ECMWF	0.694/0.971/0.106/0	0.899/0.927/1.491/0	0.935/0.933/ − 1.141/0
NOC	-	0.637/0.470/ − 8.242/0	0.690/0.492/ − 10.543/0
NCAR	-	-	0.839/0.812/ − 6.054/0

Table 4.6: As in Table 4.4, except for zonally integrated Sverdrup transport at 36°N in Sv. Once again, p values of zero represent values of less than 1×10^{-12}.

(Table 4.8), and no statistically significant linear trend was observed.

Figure 4.6 shows the latitudinal variability of Sverdrup transport within the subtropical Atlantic. Values of zonally-integrated transport reach a peak of between 20 Sv and 25 Sv between 30°N and 34°N, before weakening rapidly between 34°N and 40°N. As the Sverdrup transport at these latitudes is dominated by the meridional gradient in the eastward wind stress (the $-\partial\tau_x/\partial y$ term), such a latitudinal gradient in Sverdrup transport is easily understood with reference to the mean wind fields (Figure 4.3). The rapid transition that occurs between 30°N and 34°N from a region of easterly trade winds into a zone of midlatitude westerlies sets up a strong positive northward gradient in τ_x, thus driving a southward Sverdrup transport across the basin. In contrast, the region between 34°N and 40°N is one of more slowly increasing westerlies, causing a gradual reduction in the strength of the Sverdrup transport. North of 40°N, the Sverdrup transport gradually reduces to zero as the wind stress curl tends to zero at the maximum of the midlatitude westerlies (not shown).

All four products exhibit the same meridional pattern, although both NOC and QUICKSCAT estimates show larger southward transports between 28°N and 34°N and larger northward transports between 38°N and 40°N. It is probable that the reason for this discrepancy is the lower spatial resolution of the reanalysis products compared with those derived from ship-

	Regression coefficients	F statistic	p value
ECMWF	0.1183/ − 20.13	0.4474	0.5042
NOC	−0.1104/ − 19.79	0.5663	0.4523
NCEP/NCAR	−0.0413/ − 18.77	1.528	0.2168
QUICKSCAT	0.3902/ − 20.96	0.6305	0.4287

Table 4.7: As Table 4.2, but for the four time series of zonally integrated Sverdrup transport at 36°N in Sv. The form of the regression relationship is $S = a(t - 2002) + b$ where S is the Sverdrup transport and t is time in years.

	Regression coefficients	F statistic	p value
ECMWF	$0.1455/-22.503$	0.0623	0.6217
NCEP/NCAR	$0.9223/-21.465$	1.034	0.3122
QUICKSCAT	$1.2811/-24.9137$	2.1600	0.1457

Table 4.8: As Table 4.3, but instead for the zonally integrated Sverdrup transport at 36°N in Sv. The form of the regression relationship is $S = a(t-2002)+b$ where S is the Sverdrup transport and t is time in years.

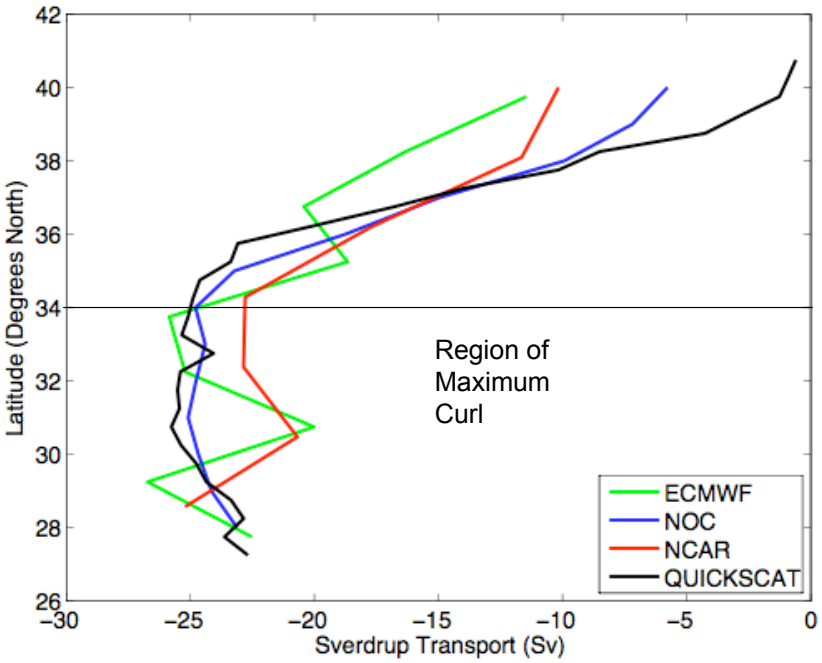

Figure 4.6: Mean zonally integrated Sverdrup transport, based on four estimates of wind stress from the ECMWF Interim Reanalysis (1989-2009), the NOC Climatology (1980-2005), the NCEP/NCAR Reanalysis (1948-2009) and the QUICKSCAT Scatterometer (1999-2009).

board measurements (NOC) or satellite measurements (QUICKSCAT). NOC, for instance, incorporates over 30 million in-situ meteorological reports worldwide. This means that the sharpest gradients in wind stress tend to be smoothed out, thus reducing the size of the transport maximum between 30°N and 34°N. Despite this reservation, it is encouraging that the products agree to within 3 Sv (12%) at 36°N.

4.3 Spectral Estimation and Empirical Orthogonal Function Analysis

It is known that both wind stress and wind stress curl fields vary over a range of timescales from hourly to decadal, and over a variety of space scales from localised phenomena to basin-scale changes. The largest time and space scales of variability include a reported 8 TW global increase in energy flux into the ocean from the atmosphere between 1950 and 2000, as a result of increased wind speeds (Thorpe, 2006), and the North Atlantic basin-wide variability in the wind stress related to the NAO (Marshall et al., 2001). In order to disentangle this broad spectrum of variability and isolate the scales of variability relevant to our study (seasonal to multiannual), spectral and empirical orthogonal function analysis were employed on the underlying wind stress and wind stress curl fields that determine the magnitude of the Ekman and Sverdrup transports (Equations 4.5 and 4.7).

Whilst this analysis does reveal the dominant timescales of wind stress and wind stress curl variability, it does not determine the timescales over which the theoretical Sverdrup balance holds in controlling the mass transport of the ocean. This separate issue is dealt with in more length in Section 5.1.

4.3.1 Spectral Analysis

The purpose of spectral estimation is to "partition the variance of a time series as a function of frequency" (Emery and Thomson, 1998), and it is thus employed in our study to determine the dominant periods of wind stress and wind stress curl variability. The spectral analysis was conducted on monthly mean wind stress values from all four wind stress products (NOC Climatology, QUICKSCAT data, ECMWF and NCEP/NCAR Reanalyses) in the latitude band 28°N to 40°N. Initial investigations were carried out using the time periods for each product given in Table 4.9, though this was later extended to the full length of each available time series.

Spectral Considerations

Extensive experimentation was carried out to determine the optimum spectral estimation method from which to estimate the dominant frequencies of variability in both sets of data. In the following section, the choices made are illustrated using NOC wind stress curl data,

Product	Time Interval
ECMWF Interim	January 1989 to April 2009
NOC	January 1980 to December 2005
NCAR	January 1980 to June 2009
QUICKSCAT	August 1999 to September 2009

Table 4.9: Date intervals used in initial spectral analysis investigations of wind stress and wind stress curl data for four different wind stress products. Note the QUICKSCAT scatterometer failed after September 2009.

although the conclusions reached about the suitability of each spectral method were made after examination of both zonal wind stress and wind stress curl data, and after examination of all four wind stress products. All the spectra presented have a y axis displaying spectral density multiplied by frequency, thus converting the power per unit frequency into variance. The spectra are variance conserving, meaning that by integrating under the curves the original variance of the data set is recovered.

Spectral estimation techniques fall into two general categories. Parametric techniques, such as the Burg and Yule-Walker methods (Burg, 1975; Marple, 1987), rely on fitting a model spectrum to the observed spectrum, whilst nonparametric methods, such as those using conventional Fourier transformation to estimate a periodogram, do not make any assumptions about the underlying structure of the variance in frequency space. As a meteorological field such as wind stress is complex and its noise structure is known imprecisely, it is not possible to use parametric methods, because fitting an overly simple autoregressive model can seriously degrade the spectral estimate (Emery and Thomson, 1998). Furthermore, the relatively short length of any of the time series (< 60 years) compared with the possible timescales of variability (months to decades) reinforces the argument for using nonparametric methods as these techniques produce a more robust spectral estimate in these circumstances.

The simplest nonparametric technique uses the entire time series to estimate the Fourier components and calculates the power in each frequency accordingly. This provides a high frequency resolution to the spectral estimate, but this comes at the expense of the statistical reliability of the estimates. For instance, when the demeaned and detrended NOC wind stress curl is examined using a simple periodogram method (Figure 4.7), it is observed that the upper 95% confidence limit is an order of magnitude larger than the spectral estimate itself. A further problem is that the simple periodogram method uses a simple box window that is truncated at either end of the time series. This means the dataset has endpoint discontinuities that cause 'ringing' in the dataset. This occurs because energy leaks into side-lobes causing power to be lost into neighbouring frequency bands (Press et al., 1996).

In order to minimise these problems, two techniques that reduce the variance of the power estimate were trialled. The first, known as the Thomson multitaper method (Thomson, 1982), uses a number of orthogonal data tapers over the whole length of the time series and averages across the resulting spectra to give a single spectral estimate. The normalised power

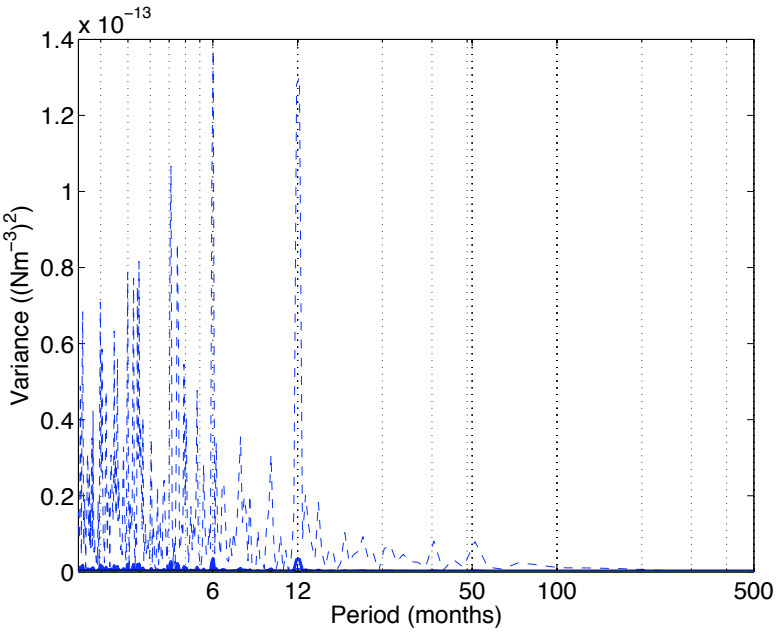

Figure 4.7: Variance preserving power spectrum for the basin mean of the wind stress curl in the latitude band 28°N to 40°N from the NOC Climatology. The period is January 1980 to December 2005 and the spectrum is calculated using the simple periodogram method and a single box window function. The solid line denotes the variance and the dashed lines the upper and lower confidence intervals at 2.5% and 97.5%. Note the extremely large uncertainties on the estimates.

spectra derived using the Thomson multitaper method for both 4 and 6 tapers are shown in Figure 4.8. The use of different length tapers is again a trade-off between maximising the frequency resolution and minimising the uncertainty.

Despite the differences between the individual realisations, there is a clear peak of spectral power in wind stress curl at 12 months, which is statistically significant at the 95% level. There is also a non-significant 6 month peak. Moreover, raised power is found at 4 months and 2 months (the Nyquist frequency). No strong variability at periods greater than 12 months is observed.

The second technique used to improve the accuracy of the power estimate is the Welch periodogram method. Once again, this method sacrifices resolution for spectral accuracy. However, unlike the multitaper method, it achieves this by dividing the demeaned and detrended time series into a number of overlapping windows over which it independently estimates the power spectrum, before averaging these together into a single estimate. The number of windows (chosen by the user) is a compromise between the requirement for spectral accuracy and the lowest frequency that one wishes to resolve (periods longer than the window length cannot be evaluated using this method). Moreover, the Welch method allows different window shapes to be used that can minimise the effects of ringing. These alternative windows have more tapered shapes at the edges that reduce leakage into side lobes. Experimentation using the Welch method was done using 4, 8 and 16 windows

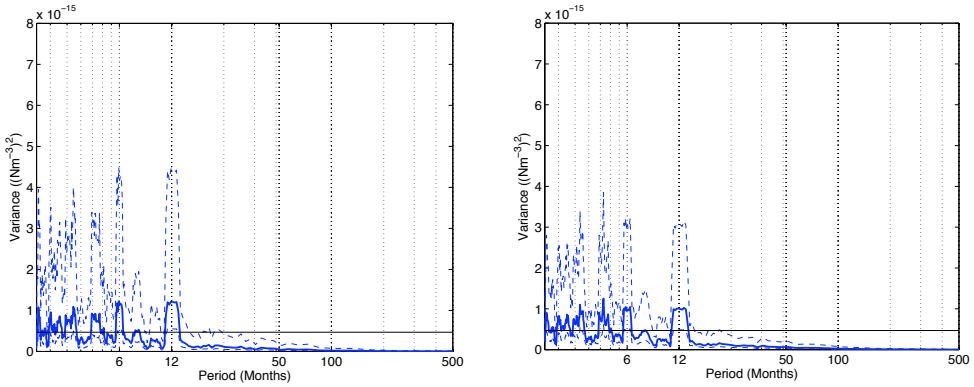

(a) 4 tapers (b) 6 tapers

Figure 4.8: Variance-preserving power spectra of NOC wind stress curl for the period January 1980 to December 2005 calculated using the Thomson multitaper method and (a) 4 tapers; (b) 6 tapers. The solid blue line denotes the variance and the dashed blue lines the upper and lower confidence intervals at 2.5% and 97.5%. With the larger number of tapers, the accuracy of the spectral estimate improves (note the narrower confidence intervals) but the frequency resolution is degraded (note the increasing width of the annual peak). The mean variance of the spectrum is indicated by the solid black horizontal line in each plot.

respectively. For the NOC wind stress curl data, and a 50% window overlap, this gave window lengths of 125 months, 69 months and 37 months (Figure 4.9).

In agreement with the Thomson multitaper method, peaks in power in this series are found at 12 months, 6 months, 4 months and 2 months (the Nyquist frequency). Considering Figure 4.9a, only the peak at annual frequency has a 95% confidence interval that does not encompass the mean value of variance and hence it is only this peak that is statistically distinct from the background noise. In both the 8 and 16 window cases (Figure 4.9b and 4.9c), none of the observed peaks are found to be statistically different from a background white noise, though the size of the confidence interval is much smaller. 8 windows appears to be a suitable compromise between resolution and accuracy: the 4 window case has very large error bars whilst the 16 window case results in an over-smoothed spectrum (e.g. the annual peak is spread over 4 months). Further experimentation was also carried out with a variety of different window types (e.g. Hann, Bartlett and Kaiser windows), but the underlying spectral structure again remained similar.

Some work was also carried out to determine the correct size of the confidence intervals for each spectral estimate. Whilst the MATLAB Spectral Analysis Toolbox provides error bars for each spectrum based on a chi-squared distribution (Kay, 1976), these are determined solely by the number of windows and do not take into account the overlap percentage. Whilst using overlapping windows is advantageous for minimising loss at the edge of a window, it does reduce the number of independent spectral estimates and hence the degrees of freedom for determining confidence intervals. For instance, using 8 windows and a 50% overlap only provides 4 independent sets of data. Hence, for each spectral estimate, the error bars were determined by using the same window length but zero overlap. The ratio of

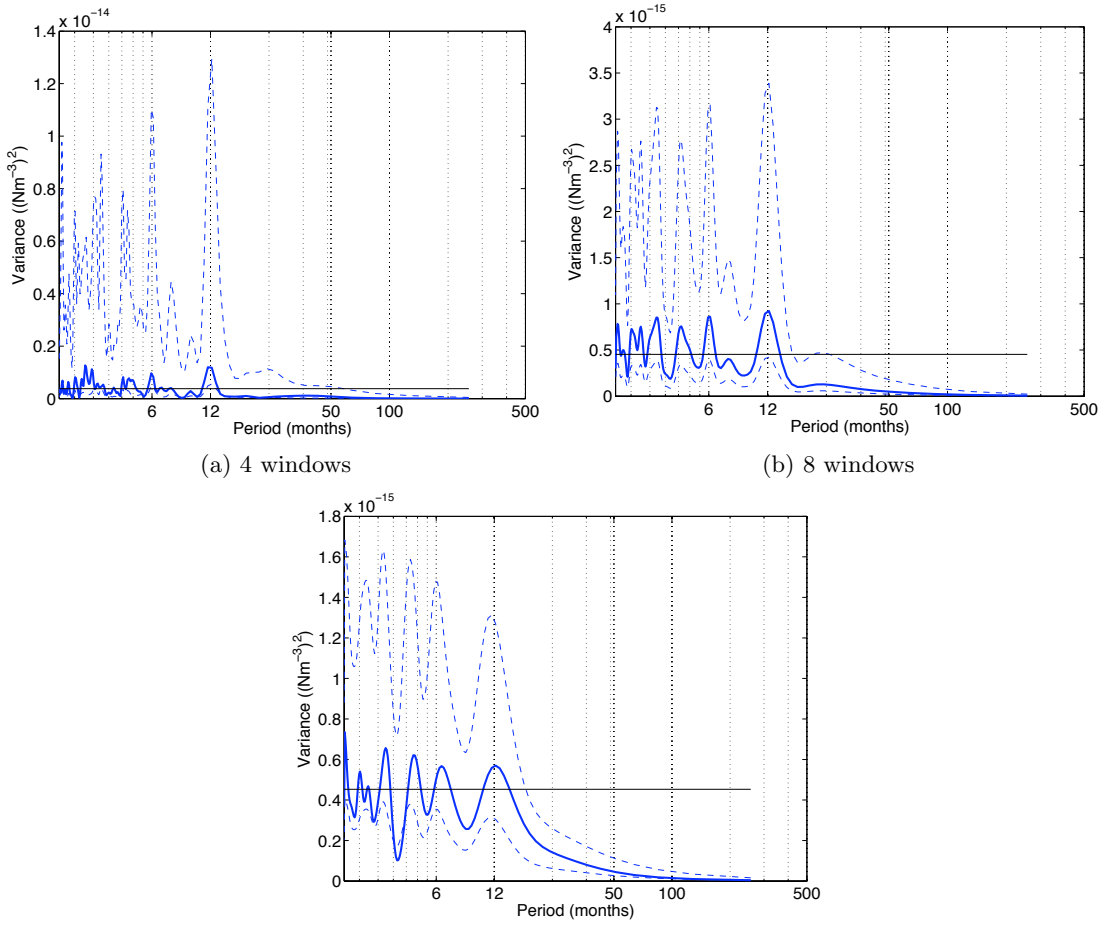

(a) 4 windows

(b) 8 windows

(c) 16 windows

Figure 4.9: Variance-preserving power spectra of NOC wind stress curl for the period January 1980 to December 2005 calculated using the Welch method with different Hamming window lengths: (a) four 125-month windows; (b) eight 69-month windows and (c) sixteen 37-month windows (50% overlap in each case). The solid blue line denotes the variance and the dashed blue lines the upper and lower confidence intervals at 2.5% and 97.5%. As the number of windows increases, the accuracy of the spectral estimate improves (note different vertical scales) but the frequency resolution is degraded. Furthermore, the lowest resolvable frequency also increases as the periodogram does not provide accurate spectral estimates for periods longer than the window length. The mean variance of the spectrum is indicated by the solid black horizontal line in each plot.

the upper and lower confidence intervals to the spectral estimate for the zero overlap case were then calculated. Finally, these ratios were then applied to the spectral estimate for the 50% overlap case to obtain the true size of the error bars.

Unless otherwise stated, all subsequent estimates are made using the Welch method with eight Hamming windows and a 50% overlap. This equates to window lengths of 55 months, 69 months, 164 months and 27 months for ECMWF, NOC, NCEP-NCAR and QUICKSCAT respectively.

Spectral Estimates of Zonal Wind Stress

The zonal wind stress (τ_x) is the dominant variable in determining the meridional Ekman transport at 36°N, and it has already been shown that the majority of the southward Ekman transport at 36°N occurs west of 30°W (Section 4.2.1). It was thus decided to produce spectral estimates over three areas, to examine how the dominant frequencies vary within the subtropical North Atlantic. These areas were:

1. The entire North Atlantic between 28°N and 40°N. The mean wind stress across the basin for each timestep is calculated and the spectral estimate produced from the resulting time series.

2. The same domain, but divided into regions west and east of 30°W.

3. The wind stress at 36°N only.

These are given in Figures 4.10, 4.11, 4.12 and 4.13 respectively. The spectral estimate over the entire basin (Figure 4.10) shows a statistically significant peak at annual period in three of the four products (NOC, NCEP/NCAR and ECMWF), with a weaker indication of raised power at semi-annual period. Examining the spectra for the region west of 30°W (Figure 4.11), both annual and semi-annual cycles in the westerly winds are significant in these three products. By contrast, for the region east of 30°W (Figure 4.12) where northeasterly winds predominate (Figure 4.3), the annual and semi-annual cycles are not statistically significant, with more of the variance concentrated at shorter periods (2-4 months). It is important to note the different vertical axis scales on Figures 4.11 and 4.12, showing that the variance in the western basin is larger at all frequencies than that found near the eastern boundary. This conclusion is supported by Figure 4.14, which displays the standard deviation of the zonal wind stress for the NOC Climatology. Examination of the spectra for the 36°N line alone (Figure 4.13) shows very similar results to the full basin estimate, with statistically significant peaks in three of the products at 12 months, and no clear evidence of variability on timescales longer than one year.

The phase of the dominant annual cycle is illustrated clearly in Figure 4.15, which is a box-plot of mean wind stress values across the entire basin at 36°N. The eastward-directed wind stress is at a maximum during the winter months (especially February) and at a minimum

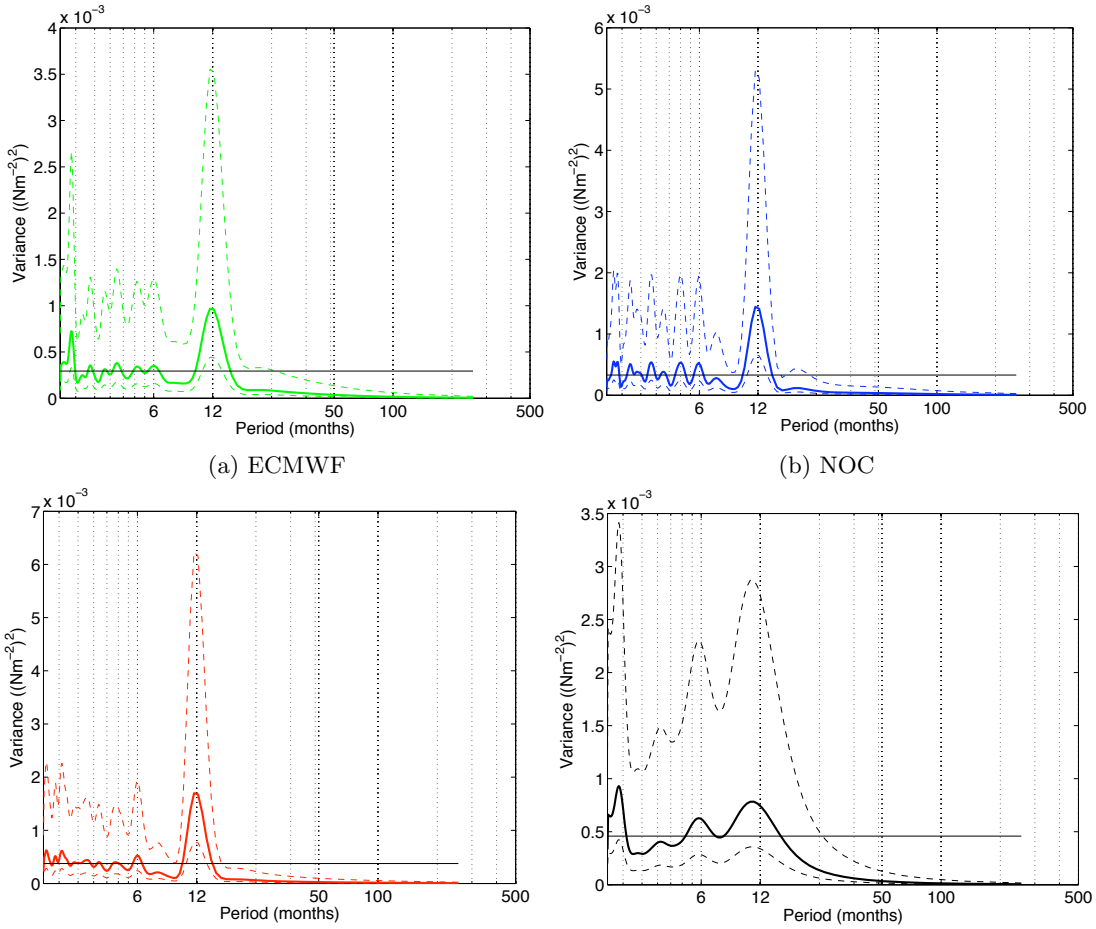

(a) ECMWF (b) NOC

(c) NCEP/NCAR (d) QUICKSCAT

Figure 4.10: Normalised Welch power spectrum (8 windows, 50% overlap) of the basin-averaged zonal wind stress for 28°N to 40°N. The top row shows results for (a) the ECMWF Reanalysis (January 1989-April 2009) and (b) the NOC Climatology (January 1980-December 2005). The bottom row shows results for (c) the NCEP/NCAR Reanalysis (January 1948-June 2009) and (d) the QUICKSCAT Scatterometer (August 1999-September 2009). The solid line denotes the variance (power multiplied by frequency) and the dashed lines the upper and lower confidence intervals of the spectral estimate at 2.5% and 97.5%. The black horizontal line denotes the mean variance. The annual peak is not significant for QUICKSCAT, most likely because of the short time series length.

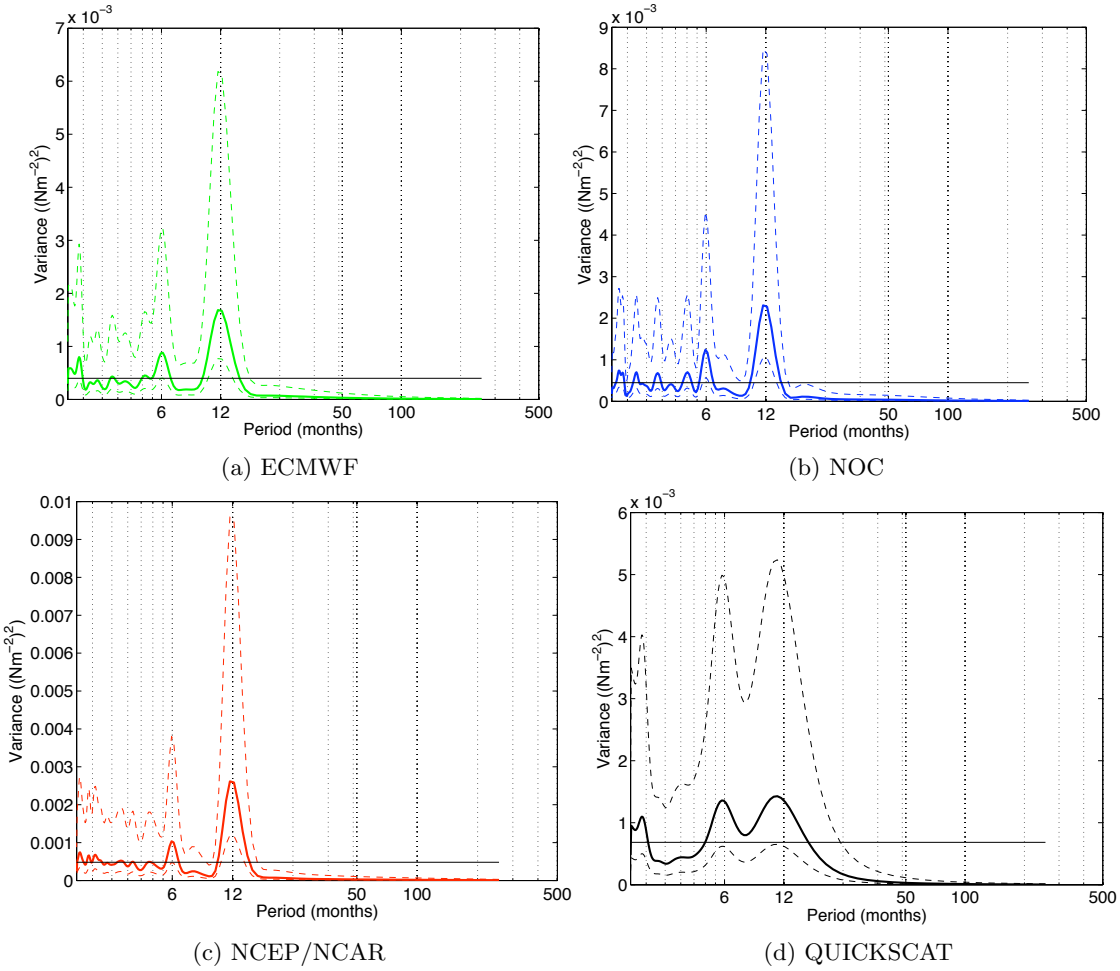

(a) ECMWF

(b) NOC

(c) NCEP/NCAR

(d) QUICKSCAT

Figure 4.11: As Figure 4.10, but restricted to the region between 30°W and the western boundary. The solid line denotes the variance (power multiplied by frequency) and the dashed lines the upper and lower confidence intervals of the spectral estimate at 2.5% and 97.5%. The black horizontal line denotes the mean variance.

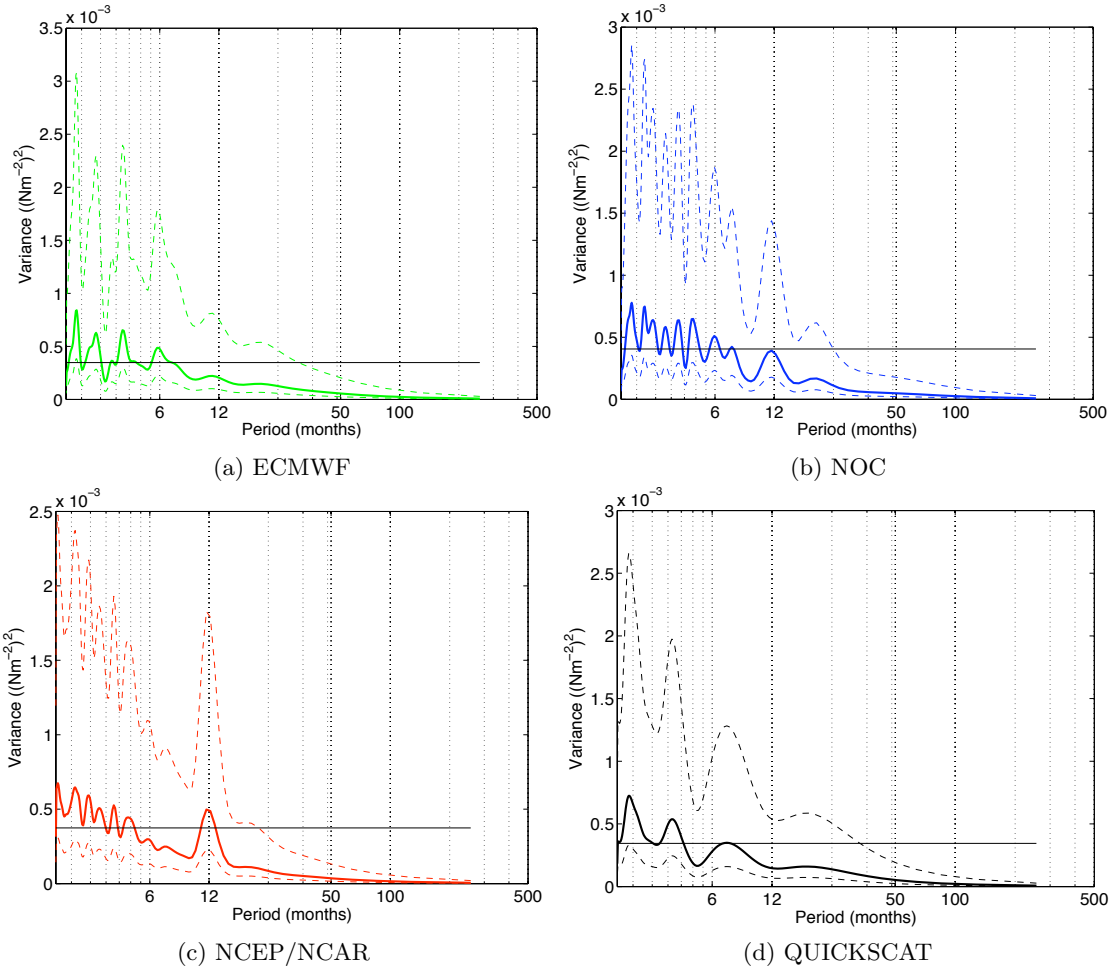

(a) ECMWF

(b) NOC

(c) NCEP/NCAR

(d) QUICKSCAT

Figure 4.12: As Figure 4.10, but restricted to the region between 30°W and the eastern boundary. The solid line denotes the variance (power multiplied by frequency) and the dashed lines the upper and lower confidence intervals of the spectral estimate at 2.5% and 97.5%. The black horizontal line denotes the mean variance.

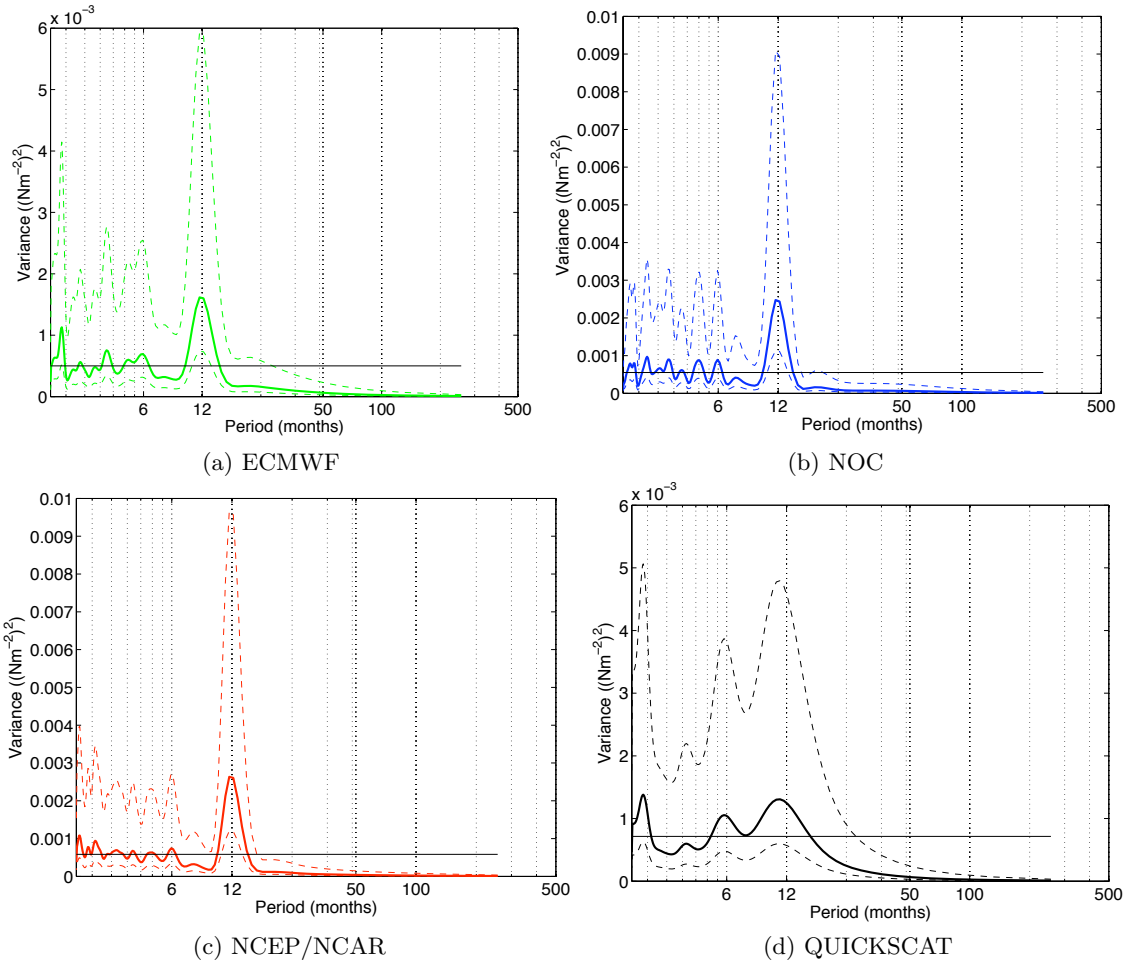

Figure 4.13: As Figure 4.10, but restricted to the 36°N line only. The solid line denotes the variance (power multiplied by frequency) and the dashed lines the upper and lower confidence intervals of the spectral estimate at 2.5% and 97.5%. The black horizontal line denotes the mean variance.

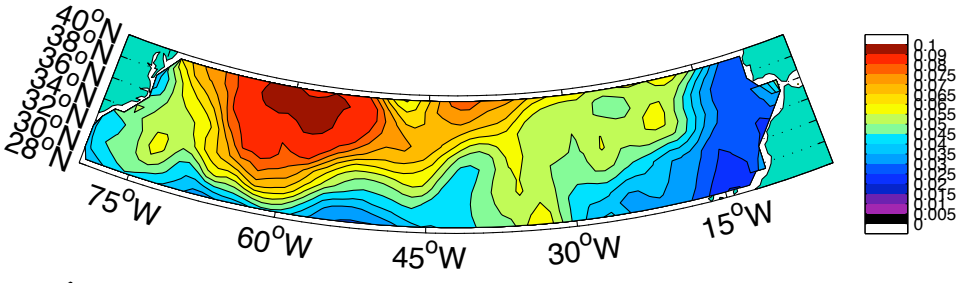

Figure 4.14: Standard deviation of the zonal component of wind stress (in Nm^{-2}) for the period 2002-2007 for NCEP/NCAR Reanalysis. Note the increasing standard deviation with latitude, and the increased standard deviation over the western part of the basin close to 60°W, especially north of 35°N.

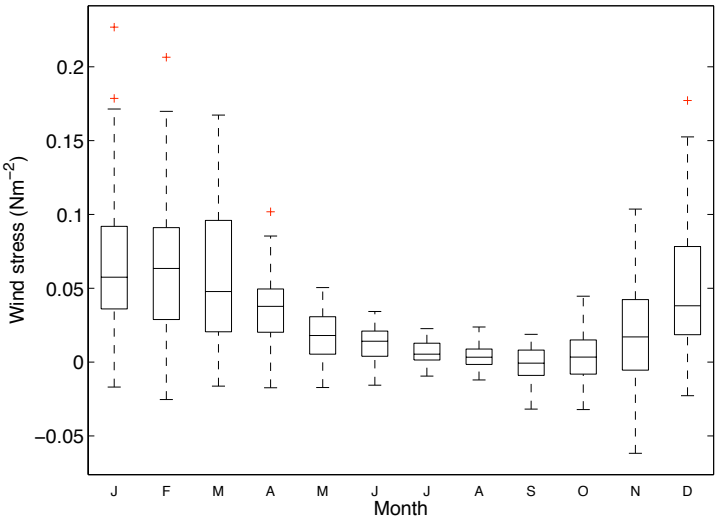

Figure 4.15: Boxplot of zonal wind stress at 36°N (in Nm^{-2}) for the period 1948-2009 for the NCEP/NCAR Reanalysis. Note the larger values and the greater variability during the winter months. The boxes show the lower (Q_1) and upper quartiles (Q_3) and median value, with the upper whiskers extending to furthest data point that lies within the region $Q_3+1.5(Q_3-Q_1)$ and the lower whiskers extending to the further data point that lies within the region $Q_1 - 1.5(Q_3 - Q_1)$. Outliers are displayed in red.

in late summer. This causes a winter-time maximum in southward Ekman transport. The semi-annual cycle seen in the western part of the basin is not apparent in this diagram.

Spectral Estimates of Wind Stress Curl

As with the zonal wind stress, power spectra of wind stress curl are evaluated across the entire northern subtropical North Atlantic, for the regions west and east of 30°W and along the 36°N line only (Figures 4.16, 4.17, 4.18 and 4.19). Once again, 30°W is the approximate longitude separating the relatively weak Sverdrup transport close to the eastern boundary from the more rapid southward transport in the western basin. It therefore remains an appropriate boundary to separate the basin.

The spectral estimate across the entire basin (Figure 4.16) contains an annual peak for all four products, though it is not statistically distinguishable from a white power spectrum at the 95% confidence level. This annual cycle is particularly weak in the QUICKSCAT product, most likely because of the relatively short length of the QUICKSCAT series compared with the other products, meaning that the signal to noise ratio is smaller. Some evidence of a semi-annual cycle can also be distinguished in all four spectral estimates. There is also a relatively larger proportion of the power at high frequencies than in the zonal wind stress spectra, with several non-significant peaks in the 2 to 4 month period range.

After splitting the basin into regions west and east of 30°W (Figures 4.17 and 4.18), two clear observations can be made. Firstly, as in the case of the zonal wind stress, both annual

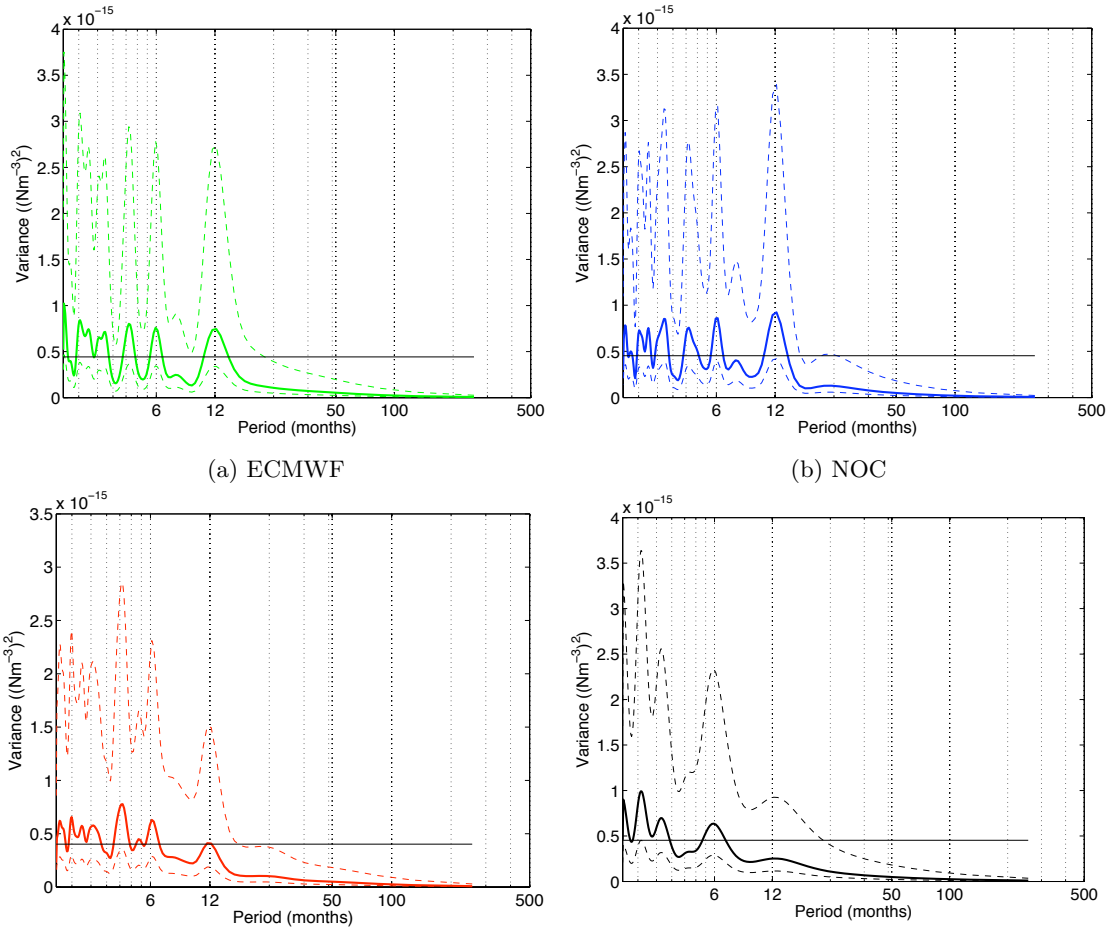

(a) ECMWF (b) NOC

(c) NCEP/NCAR (d) QUICKSCAT

Figure 4.16: Variance preserving Welch power spectrum (8 windows, 50% overlap) of the basin-averaged wind stress curl for 28°N to 40°N. The top row shows results for (a) the ECMWF Reanalysis (January 1989-April 2009) and (b) the NOC Climatology (January 1980-December 2005). The bottom row shows results for (c) the NCEP/NCAR Reanalysis (January 1948-June 2009) and (d) the QUICKSCAT Scatterometer (August 1999-September 2009). The solid line denotes the variance (power multiplied by frequency) and the dashed lines the upper and lower confidence intervals of the spectral estimate at 2.5% and 97.5%. The black horizontal line denotes the mean variance.

and semi-annual peaks are more distinguishable in the western basin, with two of the four estimates showing statistically significant peaks at the 95% level at twelve-month period. In the eastern basin, the annual and semi-annual peaks are almost entirely absent, as the signal to noise ratio is higher here. Secondly, the concentration of power at high frequencies (less than 4 months) noted for the whole-basin spectra is most noticeable in the eastern part of the basin, particularly for NOC, NCEP/NCAR and QUICKSCAT. This variance is larger than the annual cycle, and suggests that high-frequency changes in wind stress curl close to the eastern boundary is an important source of variability in the Sverdrup transport field of this region.

Restricting the analysis to the 36°N latitude line only (Figure 4.19) yields similar results to the analysis for the full 28°N to 40°N latitude band. The spectral peak at 12 months is a

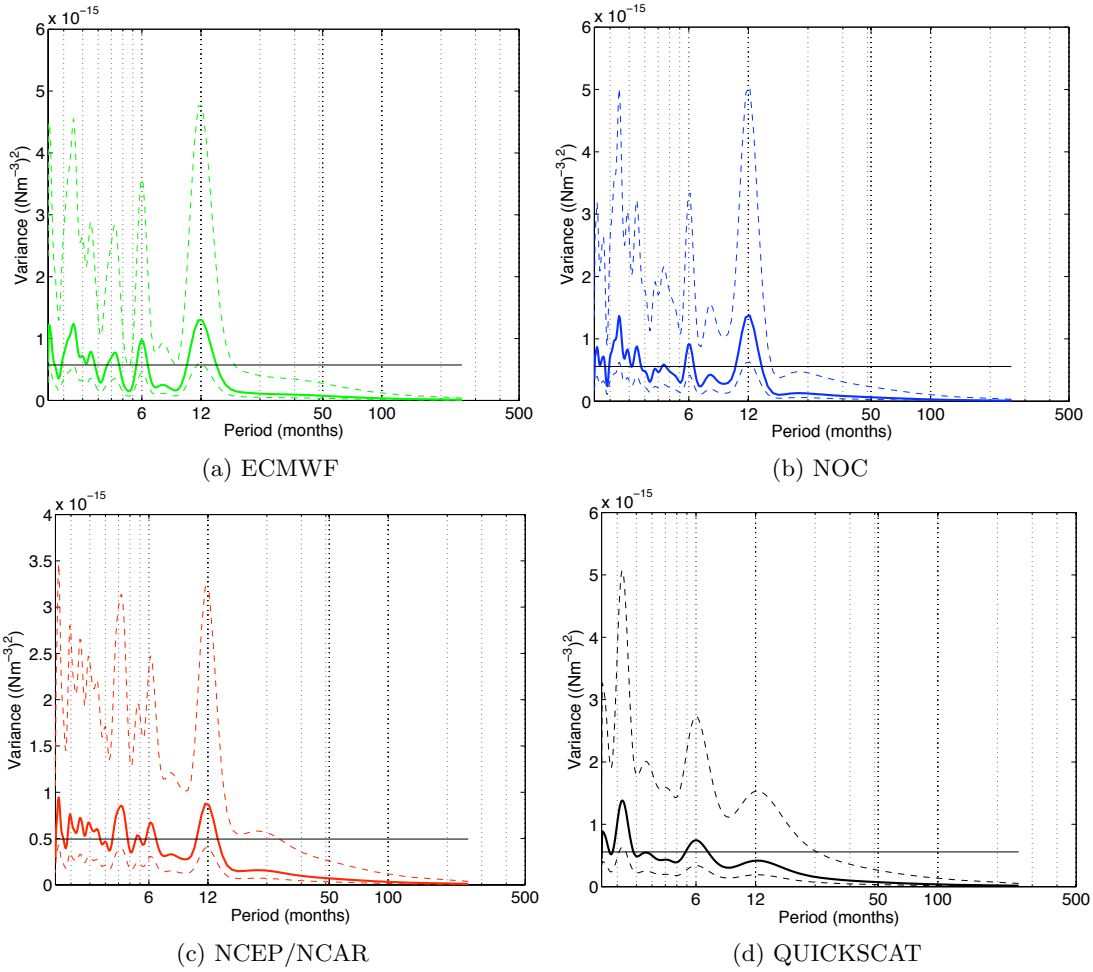

(a) ECMWF (b) NOC

(c) NCEP/NCAR (d) QUICKSCAT

Figure 4.17: As Figure 4.16, but restricted to the region between 30°W and the western boundary. The solid line denotes the variance (power multiplied by frequency) and the dashed lines the upper and lower confidence intervals of the spectral estimate at 2.5% and 97.5%. The black horizontal line denotes the mean variance.

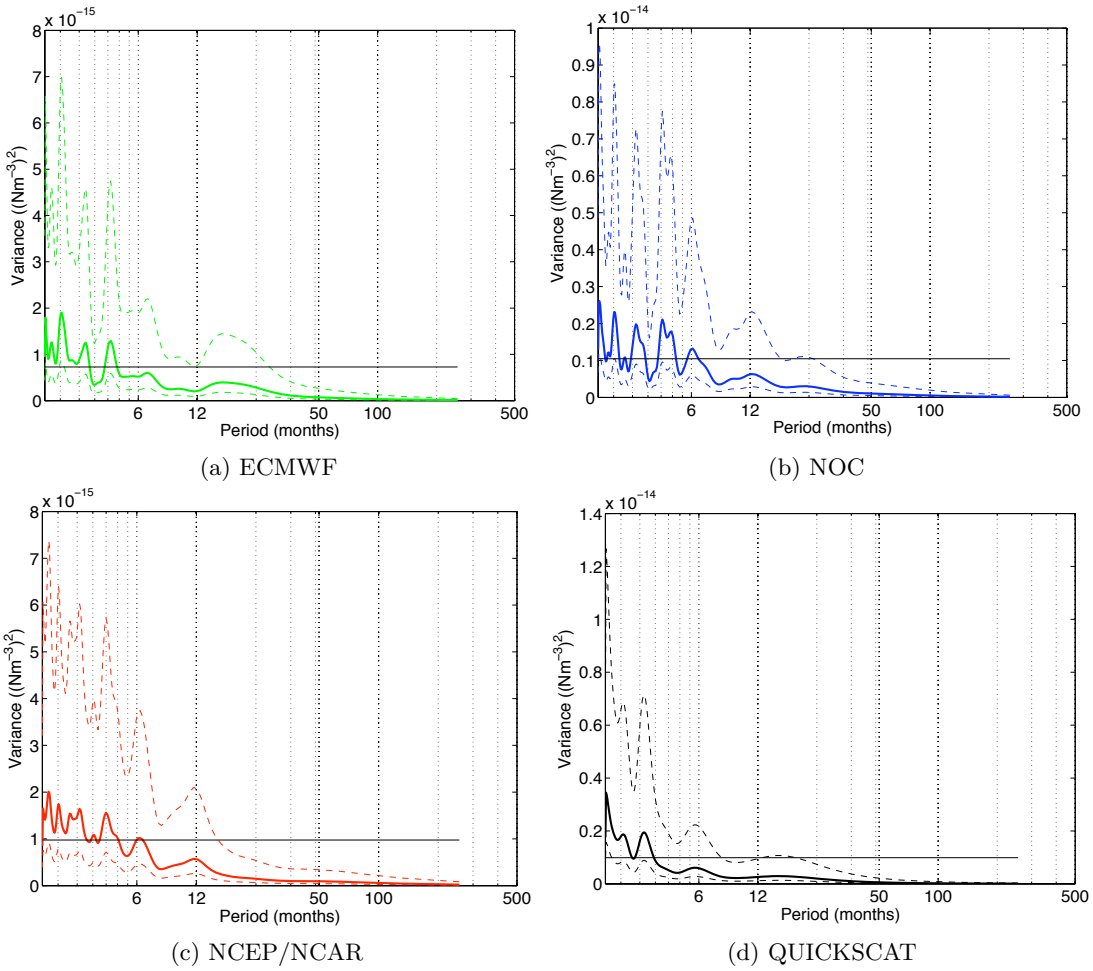

(a) ECMWF (b) NOC

(c) NCEP/NCAR (d) QUICKSCAT

Figure 4.18: As Figure 4.16, but restricted to the region between 30°W and the eastern boundary. The solid line denotes the variance (power multiplied by frequency) and the dashed lines the upper and lower confidence intervals of the spectral estimate at 2.5% and 97.5%. The black horizontal line denotes the mean variance.

little weaker than for the full latitude band, and not statistically distinguishable from the background noise. Two of the products, NOC and NCEP/NCAR, show larger variance at the high-frequency end of the spectrum than in the case of the full latitude band.

Throughout this analysis, it has been shown that dominant frequencies are generally more difficult to isolate from wind stress curl than from zonal stresses. It is likely that this is because curl is more variable over small spatial scales raising the noise of the dataset, making it more difficult to detect annual or semi-annual signals.

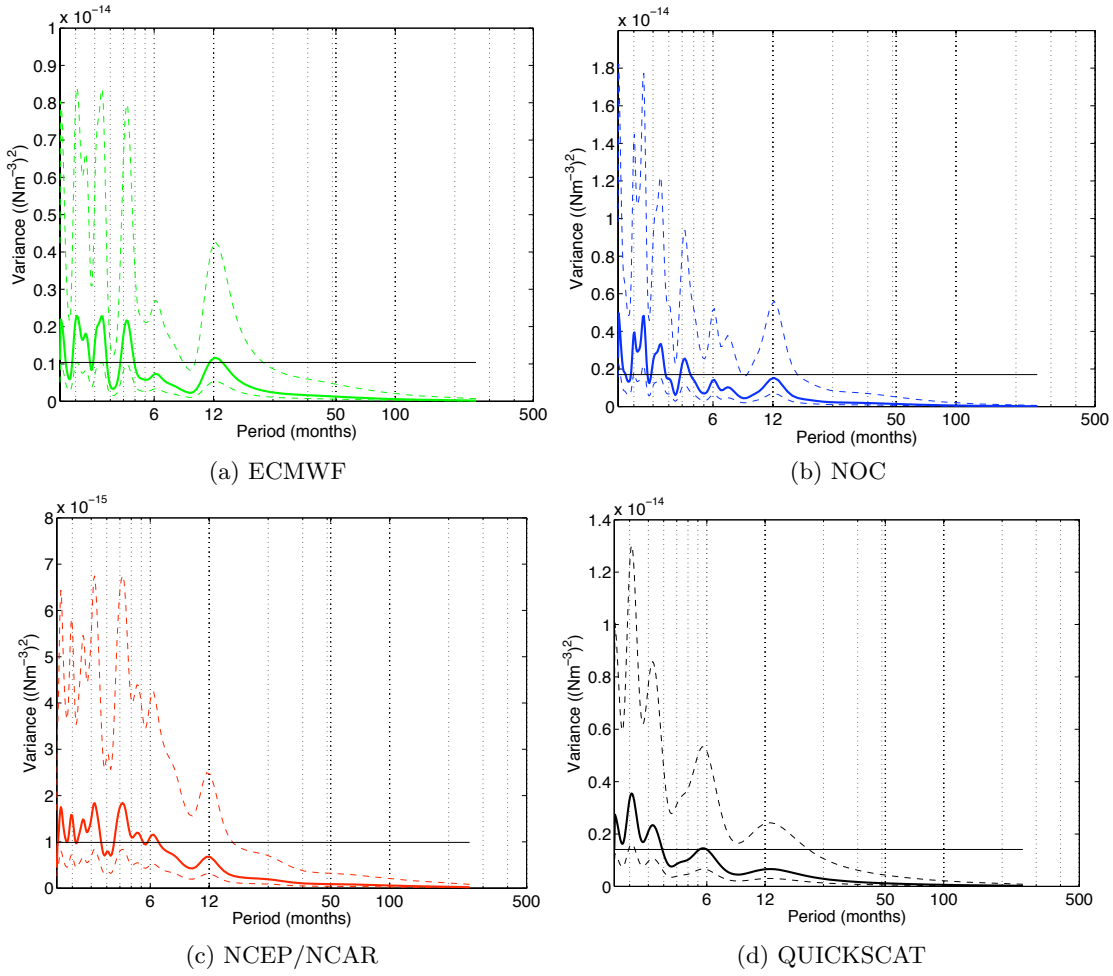

Figure 4.19: As Figure 4.16, but restricted to the 36°N line only. The solid line denotes the variance (power multiplied by frequency) and the dashed lines the upper and lower confidence intervals of the spectral estimate at 2.5% and 97.5%. The black horizontal line denotes the mean variance.

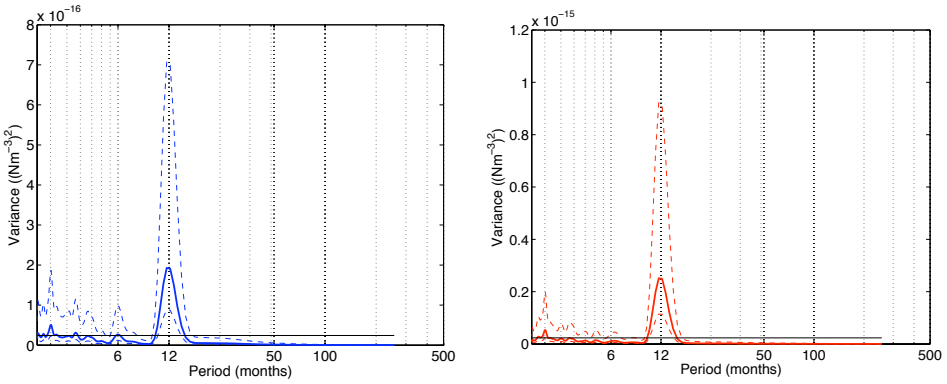

(a) NOC (b) NCEP/NCAR

Figure 4.20: As Figure 4.16, but using the spatially-averaged $\frac{d\tau_y}{dx}$ term only. The solid line denotes the variance (power multiplied by frequency) and the dashed lines the upper and lower confidence intervals of the spectral estimate at 2.5% and 97.5%. The black horizontal line denotes the mean variance. The left panel shows the result for the NOC Climatology (1980-2005) and the right panel shows the result for NCEP/NCAR Reanalysis (1980-2008).

In all four spectra, there is no evidence of strong variability at timescales longer than 12 months. In order to determine the importance of the individual terms of the wind stress curl equation ($\partial\tau_y/\partial x$ and $\partial\tau_x/\partial y$) in setting the spectral properties of the wind stress curl field, the power spectra of $\partial\tau_y/\partial x$ and $-\partial\tau_x/\partial y$ are investigated separately. It is found that the meridional gradient of zonal wind stress is the more important term in determining both the timescale and magnitude of variability, although a clear annual cycle can be found in the spectra for both individual terms (Figures 4.20 and 4.21). As each term only contains one spatial derivative, the high-frequency noise is reduced making annual cycles in both individual plots more distinct.

Once again, the sign of the annual cycle is revealed by means of a boxplot (Figure 4.22). Negative wind stress curl values reach a maximum in January, suggesting the southward Sverdrup transport is greatest during winter. This conclusion is consistent with a strengthening of both the midlatitude westerlies and easterly trades during winter, increasing the meridional gradient in the zonal wind stress. However, winter is also the period of greatest variability in wind stress curl values, with values sometimes being more positive than those found during summer. The weakest southward Sverdrup transport occurs in August. Therefore both Ekman and Sverdrup transports have wintertime maxima and late-summer minima. The size of these cycles are quantified in Section 4.3.3.

Spectral Estimates for the Period 1999 to 2005

For both the zonal wind stress and the wind stress curl fields, the power spectra are also calculated over much shorter periods, in order to test the robustness of the conclusions and the agreement between the individual products. In particular, the spectral analysis conducted above is repeated for the period August 1999 to December 2005 only, during

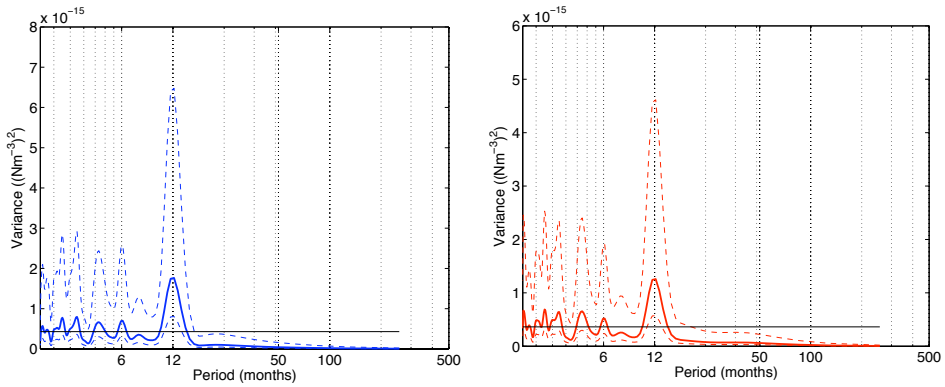

(a) NOC (b) NCEP/NCAR

Figure 4.21: As Figure 4.16, but using the spatially-averaged $-\frac{d\tau_x}{dy}$ term only. The solid line denotes the variance (power multiplied by frequency) and the dashed lines the upper and lower confidence intervals of the spectral estimate at 2.5% and 97.5%. The black horizontal line denotes the mean variance. The left panel shows the result for the NOC Climatology (1980-2005) and the right panel shows the result for NCEP/NCAR Reanalysis (1980-2008). Note the different vertical scales when compared with Figure 4.20.

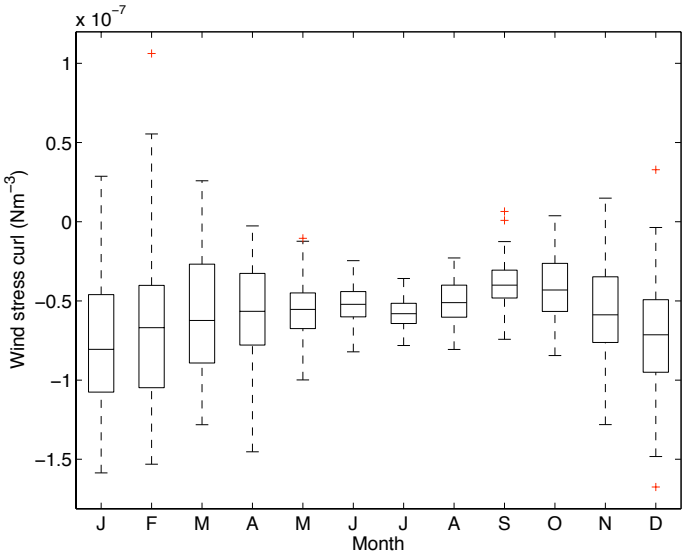

Figure 4.22: Boxplot of wind stress curl at 36°N (in Nm^{-3}) for the period 1948-2009 for the NCEP/NCAR Reanalysis. Note the more negative wind stress curl and the greater variability during the winter months. The boxes show the lower (Q_1) and upper quartiles (Q_3) and median value, with the upper whiskers extending to furthest data point that lies within the region $Q_3 + 1.5(Q_3 - Q_1)$ and the lower whiskers extending to the further data point that lies within the region $Q_1 - 1.5(Q_3 - Q_1)$. Outliers are displayed in red.

which data for all four products are available. Owing to the short length of the time series, only 4 overlapping windows are used for this realisation.

For the zonal wind stress (Figure 4.23), the resolution of the spectrum is poorer, owing to the reduced length of the time series, but the overall shape is similar, with a broad annual peak remaining the dominant feature. Raised power is also found at 6 months, but this is not statistically significant. For the wind stress curl (Figure 4.24), the resolution is again poorer, though the general pattern of increased variance at high frequency remains. The annual cycle, already a more muted peak than in the case of the zonal wind stress, is almost entirely absent, apart from in the ECMWF time series. Resolving periods longer than one year is difficult in these spectra, largely because the short time series length and number of windows precludes accurate spectral estimates for periods longer than 38 months.

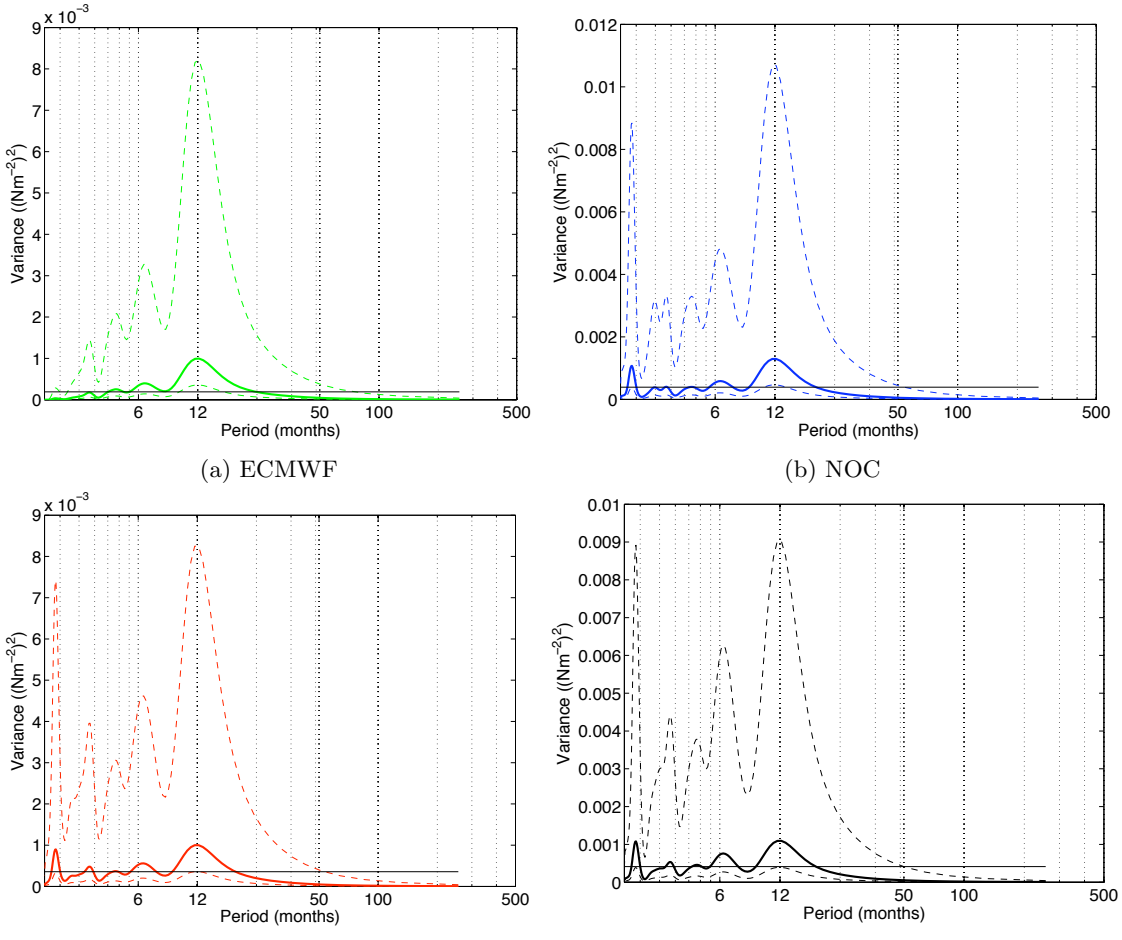

Figure 4.23: Normalised Welch power spectrum (4 windows, 50% overlap) of the spatially-averaged zonal wind stress for 28°N to 40°N for the period August 1999 to December 2005 only. The top row shows results for (a) the ECMWF Reanalysis and (b) the NOC Climatology. The bottom row shows results for (c) the NCEP/NCAR Reanalysis and (d) the QUICKSCAT Scatterometer. The solid line denotes the variance (power multiplied by frequency) and the dashed lines the upper and lower confidence intervals of the spectral estimate at 2.5% and 97.5%. The black horizontal line denotes the mean variance.

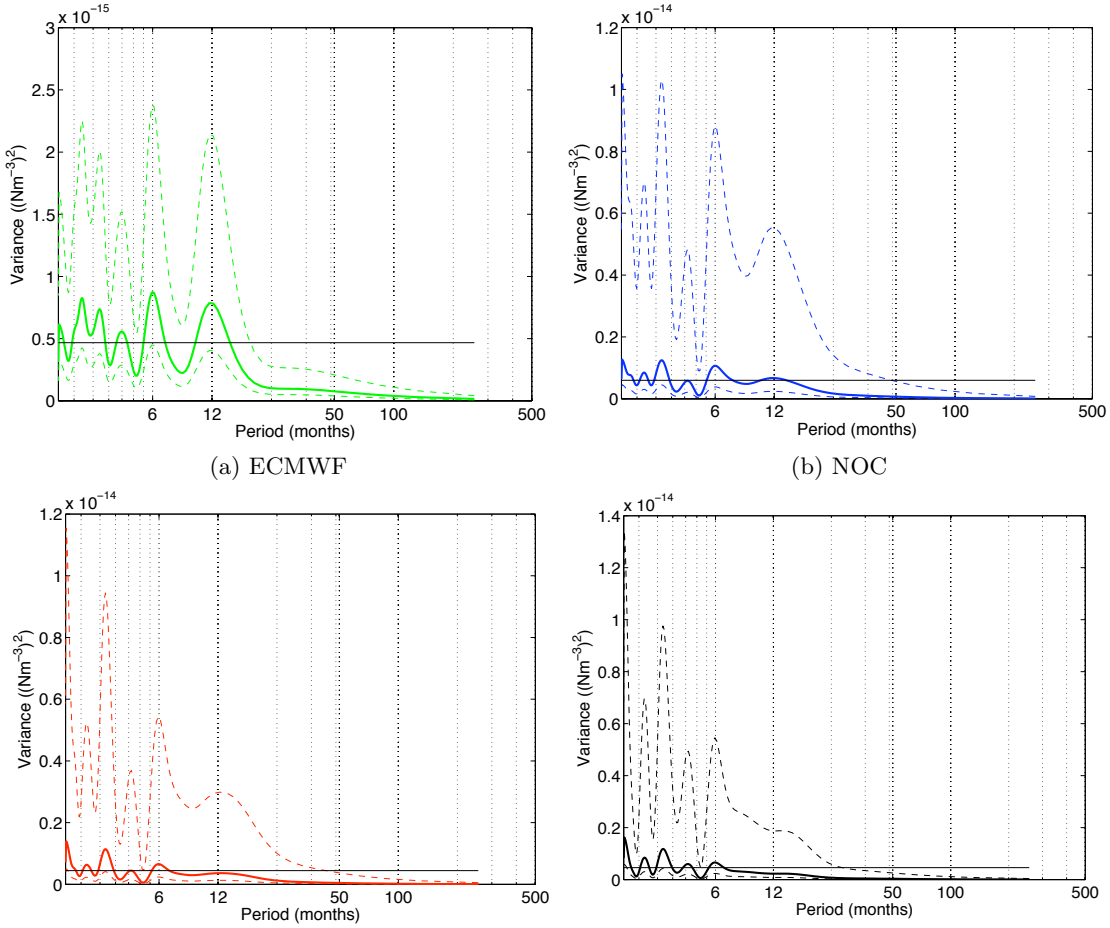

Figure 4.24: As Figure 4.23, except for wind stress curl. The solid line denotes the variance (power multiplied by frequency) and the dashed lines the upper and lower confidence intervals of the spectral estimate at 2.5% and 97.5%. The black horizontal line denotes the mean variance.

However, despite the differences observed in the shorter time series, the general characteristics of the spectra remain similar, suggesting the prominent timescales of variability have remained the same during the last 60 years. In conclusion, the annual cycle is the dominant period affecting the magnitude of both the Ekman and Sverdrup transport in the subtropical North Atlantic. This cycle is less pronounced in the case of wind stress curl, with enhanced variability in curl at the high frequency end of the spectrum (2-4 months), particularly in the eastern basin. Significant variability at timescales longer than 1 year is not evident in any of the power spectra. Multi-annual variability is revisited in Section 4.4 in reference to variability driven by the North Atlantic Oscillation.

4.3.2 Empirical Orthogonal Function Analysis

Empirical orthogonal function analysis was employed in this study as a method of identifying the spatial patterns of variability associated with the principal timescales described above. The remainder of this section is divided as follows. The theoretical considerations applicable

to the technique and methods used in this study are described, followed by separate results sections for the zonal wind stress and wind stress curl.

Theoretical Considerations

EOF analysis provides a compact description of the spatial and temporal variability of a data set by expressing it in terms of a number of independent modes, each of which has associated eigenvalues (describing the amount of the variance the mode contains) and eigenvectors. In practice, EOFs for large data sets such as wind stress data are deduced using a singular value decomposition (SVD) that does not require the calculation of a covariance matrix. This SVD (Kelly, 1988) is expressed as follows:

$$\mathbf{D} = \mathbf{U} \cdot \mathbf{S} \cdot \mathbf{V^T} \tag{4.9}$$

where **D** is the two-dimensional data matrix (e.g. the time series of zonal wind stress/wind stress curl measurements), consisting of P rows (spatial points) and Q columns (temporal values). **U** is a P $\times$ Q column-orthogonal matrix containing the right singular vectors of **D** and **V** is a Q $\times$ Q square matrix containing the left singular vectors of **D**. **S** is a diagonal matrix containing the singular scalar values in the diagonal position and zeros elsewhere. From this decomposition, **U** contains the eigenvectors and the time-dependent amplitude of each eigenvector (**A**) is given by:

$$\mathbf{A} = \mathbf{V} \cdot \mathbf{S} \tag{4.10}$$

Prior to computing our empirical orthogonal functions, the time series of zonal wind stress and wind stress curl at each point were both demeaned and detrended. Many discussions of EOF analysis (e.g. Emery and Thomson (1998)) argue for normalising the time series by dividing the demeaned and detrended values by their standard deviation (in a point-by-point fashion) to ensure that the variance from no one data point dominates the analysis. To test whether this step was necessary for our data, the standard deviations of both the zonal wind stress and wind stress curl across the 28°N and 40°N latitude domain are examined. The standard deviation of the zonal wind stress (Figure 4.25) suggests that the variance increases in the northern and western parts of the basin, but that no one point dominates the variability. The standard deviation of the curl (Figure 4.26) suggests a region of very strong variability close to the eastern boundary in both the ECMWF and NCEP/NCAR Reanalyses, though this feature is not found in either of pure observational products. The reason for this is unclear, though a previous study (Kanzow et al., 2010) observed similar increased wind stress curl variability very close to the boundary caused by seasonal reversal of the WSC (also seen in Figure 4.37).

This result suggests that normalisation might be a necessary step before computing the

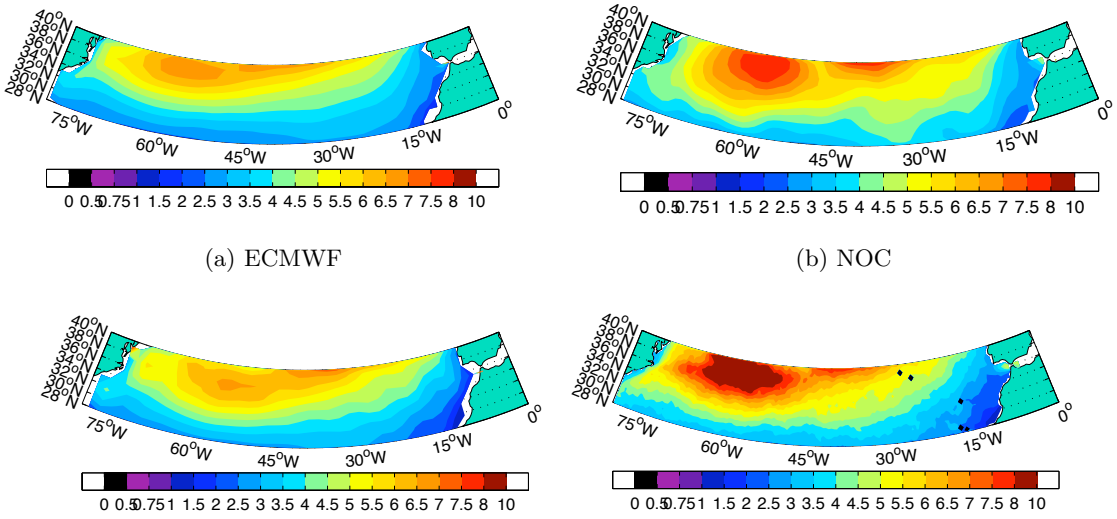

(a) ECMWF

(b) NOC

(c) NCEP/NCAR

(d) QUICKSCAT

Figure 4.25: Standard deviation of zonal wind stress field (in $\times 10^{-2}$ Nm^{-2}) for the four wind stress products over the full length of their time series. The top row shows results for (a) the ECMWF Reanalysis (January 1989-April 2009) and (b) the NOC Climatology (January 1980-December 2005). The bottom row shows results for (c) the NCEP/NCAR Reanalysis (January 1948-June 2009) and (d) the QUICKSCAT Scatterometer (August 1999-September 2009).

eigenvectors, particularly for the curl. As a result, a sensitivity study was conducted on both the zonal wind stress and the wind stress curl data by computing the leading EOFs from both the normalised and non-normalised data set (Figures 4.27, 4.28, 4.29 and 4.30).

It is apparent from Figures 4.27 and 4.28 that the three leading empirical orthogonal functions for the zonal wind stress are only slightly sensitive to whether or not the data have been normalised prior to performing the singular value decomposition. In each case, the spatial patterns are rather similar, suggesting normalisation is not a required step. In contrast, the results of the EOF analysis on the wind stress curl (Figures 4.29 and 4.30) show that normalisation of the field prior to the singular value decompostion does substantially affect the outcome. The largest differences are found in EOF1, where the non-normalised values lead to large positive and negative regions close to either boundary, which dominates the underlying basin-wide pattern. Moreover, the second EOF in the normalised case (Figure 4.30b) is completely absent from Figure 4.29. The percentage of variance explained by each mode is also different, with the three non-normalised modes accounting for 51% of the variance and the three normalised modes explaining 41%. Further description and physical interpretation of the individual results is given below, but all subsequent results for both zonal wind stress and wind stress curl include the normalisation step.

A final consideration is the use of EOF analysis to determine variability at periods longer than one year. As limitations in the spatial distribution of the Argo data mean that only annual estimates of interior transports are available, the detection of variability in either the wind stress or wind stress curl (and thus the Ekman or Sverdrup transport) with periods

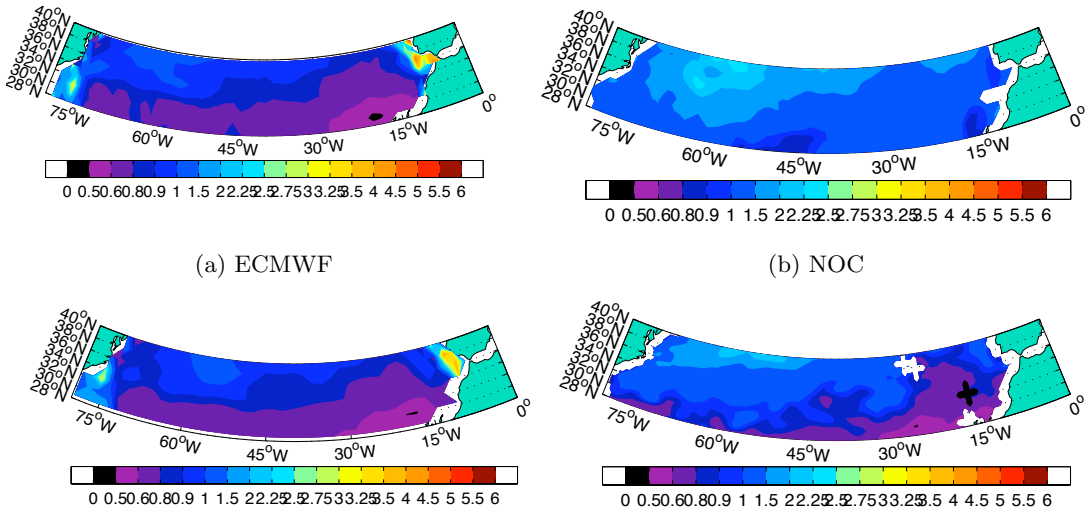

(a) ECMWF

(b) NOC

(c) NCEP/NCAR

(d) QUICKSCAT

Figure 4.26: As Figure 4.25, except for the wind stress curl (in $\times 10^{-7}$ Nm^{-3}).

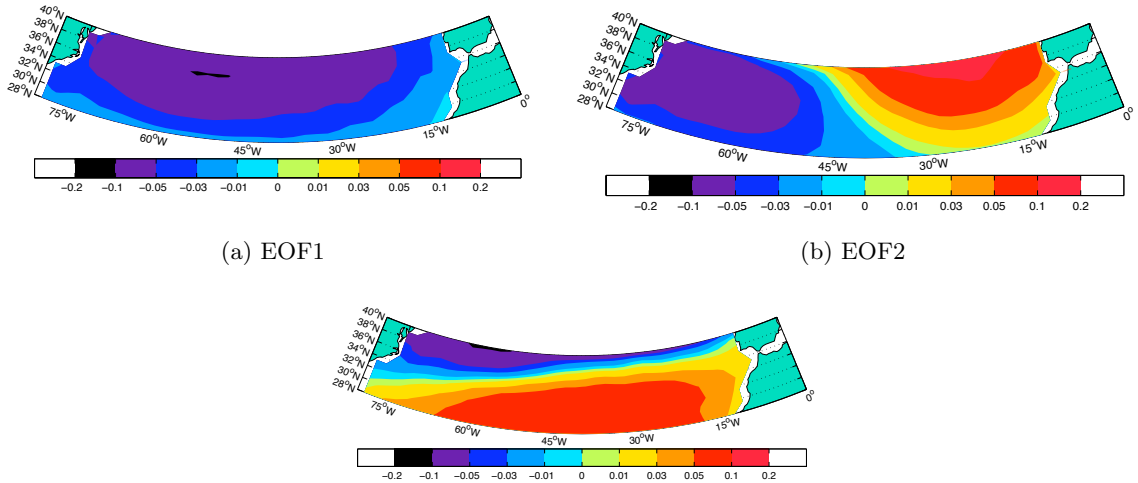

(a) EOF1

(b) EOF2

(c) EOF3

Figure 4.27: Spatial pattern of the first three EOFs of the demeaned and detrended zonal wind stress derived from the NCEP/NCAR Reanalysis for the period January 1948 to June 2009. The three modes comprise 59%, 13% and 9% of the variance respectively.

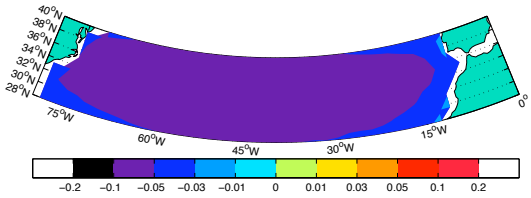

(a) EOF1

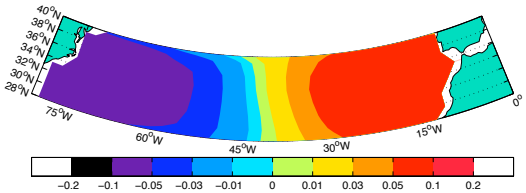

(b) EOF2

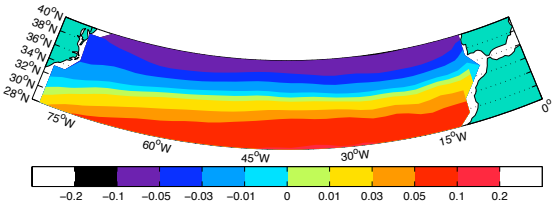

(c) EOF3

Figure 4.28: As Figure 4.27, except using normalised wind stress data. The three modes comprise 52%, 14% and 12% of the variance respectively.

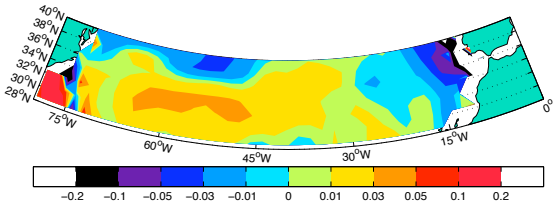

(a) EOF1

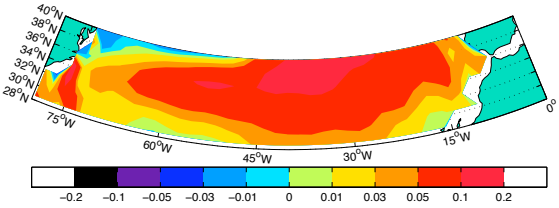

(b) EOF2

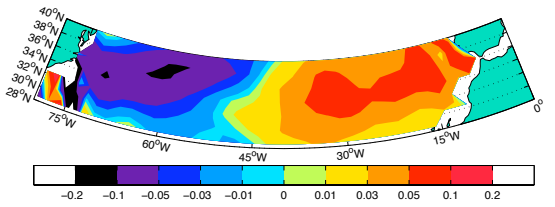

(c) EOF3

Figure 4.29: Spatial pattern of the first three EOFs of the demeaned and detrended wind stress curl derived from the NCEP/NCAR Reanalysis for the period January 1948 to June 2009. The percentage of variance explained was 29.06% for EOF1, 12.74% for EOF2 and 9.03% for EOF3.

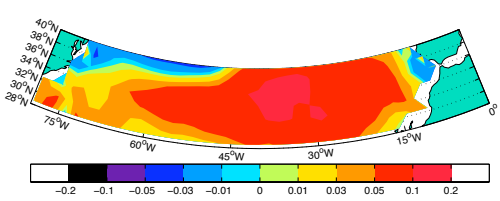

(a) EOF1

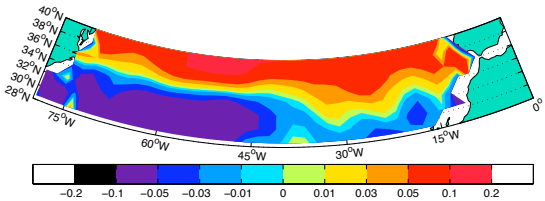

(b) EOF2

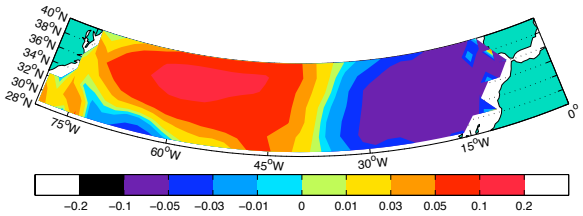

(c) EOF3

Figure 4.30: As Figure 4.29, except using normalised wind stress curl data. The percentage of variance explained was 19.82% for EOF1, 12.15% for EOF2 and 9.68% for EOF3.

longer than 12 months is of significant interest to our study. However, the spectral analysis of zonal wind stress and wind stress curl data detailed in Section 4.3.1 did not reveal any strong variability at periods longer than one year. In order to investigate further, it was decided to filter both data sets to remove all variability with periods shorter than 1 year. A variety of different filters were tried, including a twelve-month moving average, but it was eventually decided to use a fifth-order low pass Butterworth filter with a cutoff frequency of 1 year^{-1}. This filter has the advantage of a flat spectral response in the passband (i.e. the period greater than 12 months). Spectral analysis of the two filtered time series (not shown) reveals that the filter successfully suppresses almost all the variability at subannual frequencies.

The time series of the basin-averaged zonal wind stress and wind stress curl for the four products are shown in Figures 4.31 and 4.32, with the filtered time series overlaid in red. For the zonal wind stress, the four products agree well and show no long-term trend over their respective periods. Mean zonal wind stress values are close to 0.02 Nm^{-2} in all cases, with standard deviation in the raw data being approximately 0.03 Nm^{-2}. The one-year low pass filtered time series has a substantially lower standard deviation, around 0.009 Nm^{-2}, suggesting that any Ekman transport variability on timescales longer than one year can be masked by the size of the annual and semi-annual signals. A similar conclusion is reached with reference to the wind stress curl, where the standard deviation of the raw time series (around 3.3×10^{-8} Nm^{-3}) is twice as large as the standard deviation of the one-year low pass filtered time series (around 1.5×10^{-8} Nm^{-3}). Again, visual inspection of the time series suggests good agreement between the individual products, in line with the high degrees of correlation found between Sverdrup transports in Section 4.2.2.

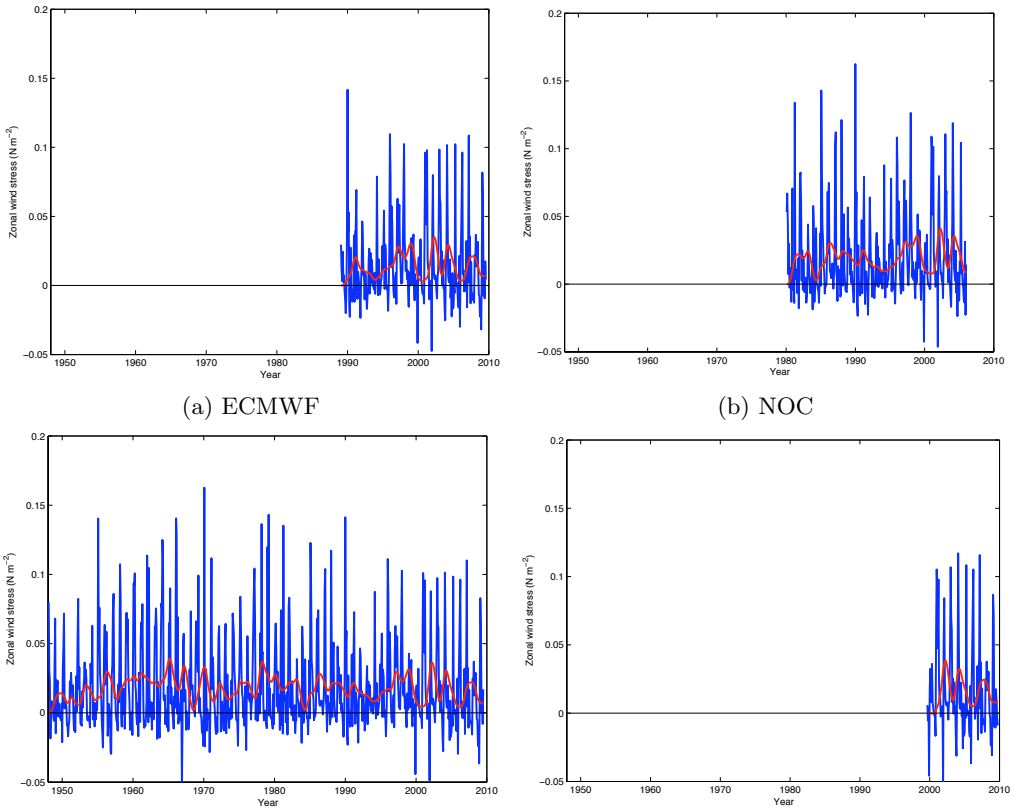

(a) ECMWF (b) NOC

(c) NCEP/NCAR (d) QUICKSCAT

Figure 4.31: Time series of basin-averaged zonal wind stress (in Nm^{-2}) in the latitude band 28°N to 40°N in blue, with a twelve month low pass Butterworth filtered time series overlaid in red. Products are (a) the ECMWF Reanalysis, (b) the NOC Climatology, (c)the NCEP/NCAR Reanalysis and (d) QUICKSCAT scatterometer data.

EOFs of Zonal Wind Stress

The three leading empirical orthogonal functions of the zonal wind stress in the latitude band 28°N to 40°N were therefore calculated for the four wind stress products. The spatial patterns exhibited are remarkably consistent, despite the differing spatial resolution and lengths of the individual time series. The result for NCEP/NCAR was already presented in Figure 4.28 and the result for the NOC Climatology is shown in Figure 4.33. Results for the ECMWF Reanalysis and QUICKSCAT are not shown, but are very similar in both their spatial pattern and principal component time series. The percentage of variance explained by each mode is given in Table 4.10.

The first mode, which explains between 43% and 52% of the variance, is the basin-wide mode associated with the annual cycle. The principal component time series of EOF1 (not shown) exhibits a strong spectral peak at 12 months and, in line with the annual cycle previously shown in Figure 4.15, reaches a maximum in late winter (February to March) a minimum in late summer. EOF2, which exhibits an east-west dipole across the basin, explains between 14% and 19% of the variance. No obvious dominant timescale is attached to this mode, although power spectra of the EOF2 time series (not shown) have a suggestion

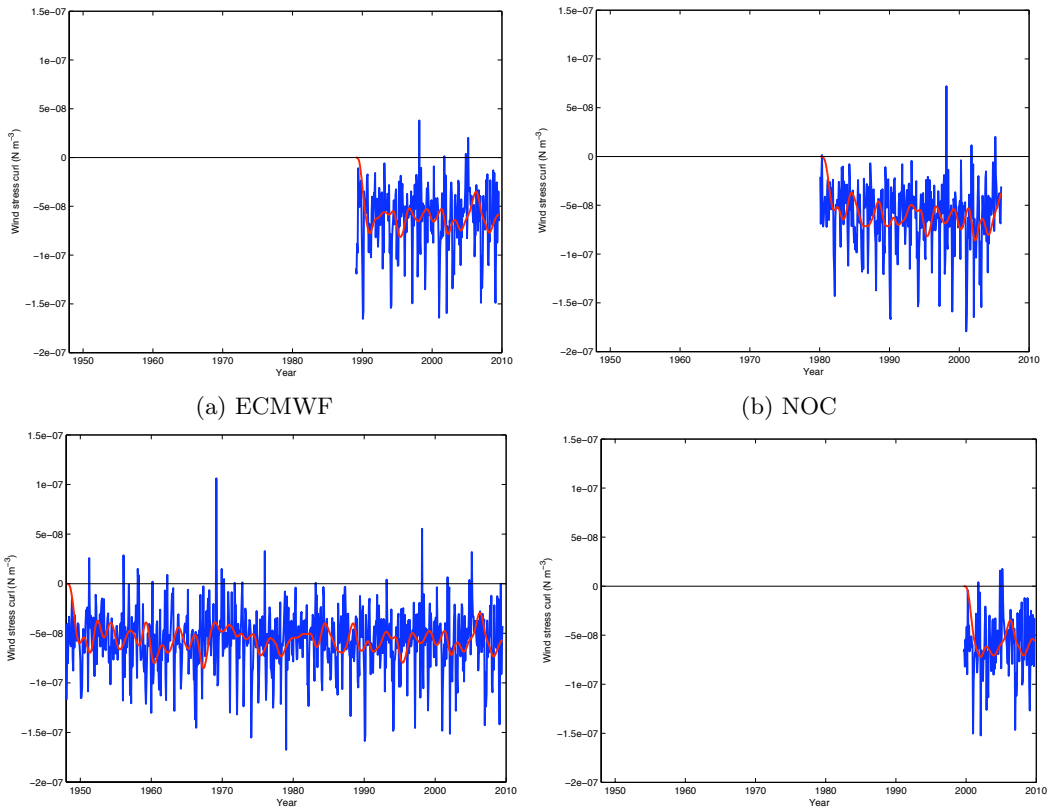

(a) ECMWF (b) NOC

(c) NCEP/NCAR (d) QUICKSCAT

Figure 4.32: Time series of basin-averaged wind stress curl (in Nm^{-3}) in the latitude band 28°N to 40°N in blue, with a twelve month low pass Butterworth filtered time series overlaid in red. Products are (a) the ECMWF Reanalysis, (b) the NOC Climatology, (c) the NCEP/NCAR Reanalysis and (d) QUICKSCAT scatterometer data.

of raised power at 6 months, particularly in the case of the ECMWF Reanalysis and NOC Climatology. The final pattern, explaining 10% to 12% of the variance, is a north-south basin-wide dipole.

The three leading modes for the 12 month low-pass filtered zonal wind stress data are shown in Figure 4.34 for the ECMWF Reanalysis. The spatial pattern and principal component time series (not shown) for the other products are very similar. The first mode, which explains between 42% and 52% of the variance (Table 4.11), is in phase across the entire domain, with peak values generally found towards the centre of the basin. This mode is therefore reminiscent of the annual cycle observed in Figure 4.33 for the EOF performed

	EOF1	**EOF2**	**EOF3**
ECMWF	48.6	18.2	12.5
NOC	43.3	16.7	10.1
NCEP/NCAR	51.7	14.2	11.8
QUICKSCAT	47.2	18.5	11.2

Table 4.10: Percentage of variance explained by three leading EOFs for zonal wind stress field of the 28°N to 40°N region of the North Atlantic.

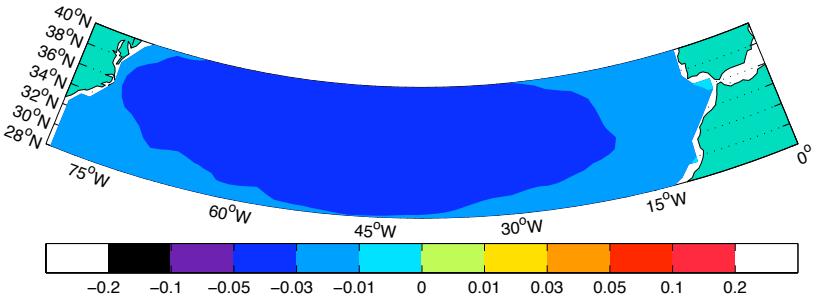

(a) EOF1

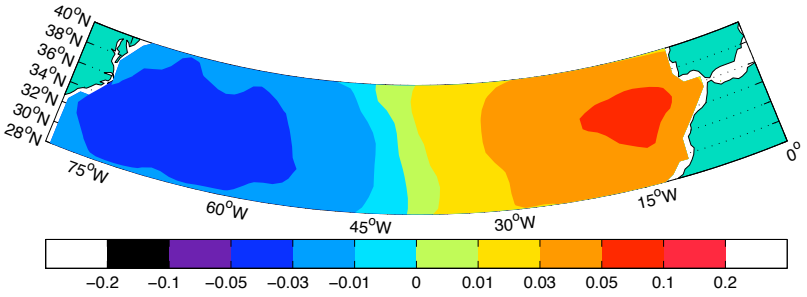

(b) EOF2

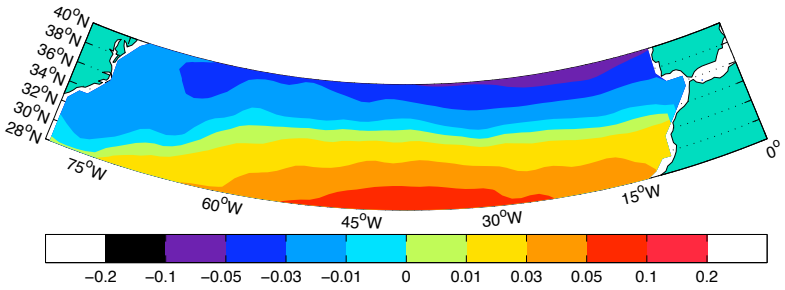

(c) EOF3

Figure 4.33: Spatial pattern of the first three EOFs of the demeaned, detrended and *normalised* zonal wind stress derived from NOC Climatology for the period January 1980 to December 2005. The percentage of variance explained was 43.28% for EOF1, 16.66% for EOF2 and 10.10% for EOF3.

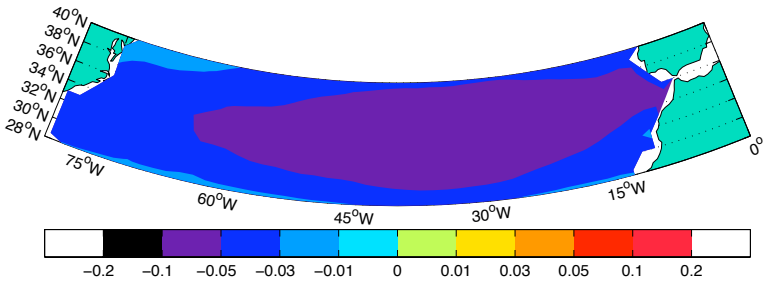

(a) EOF1

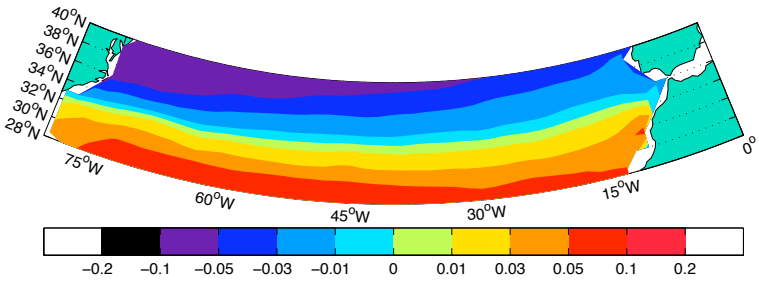

(b) EOF2

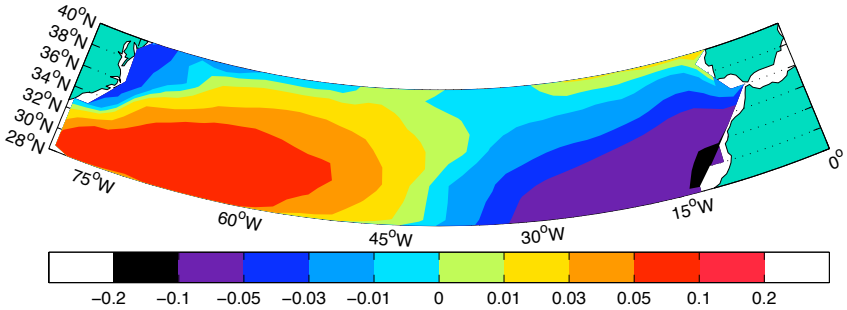

(c) EOF3

Figure 4.34: Spatial pattern of the first three EOFs of the 12-month Butterworth filtered zonal wind stress derived from the ECMWF Reanalysis for the period July 1989 to November 2008. The first six months (January to June 1989) and the final six months (November 2008 to April 2009) of the series were truncated as part of the filtering procedure. The filtered data are detrended, demeaned and normalised prior to the singular value decomposition. The percentage of variance explained was 51.53% for EOF1, 21.29% for EOF2 and 8.17% for EOF3.

	EOF1	EOF2	EOF3
ECMWF	51.5	21.3	8.2
NOC	41.8	14.8	12.6
NCEP/NCAR	45.3	16.6	11.8
QUICKSCAT	52.5	21.5	9.5

Table 4.11: Percentage of variance explained by three leading EOFs for the 12-month low pass filtered zonal wind stress field of the 28°N to 40°N region of the North Atlantic.

	EOF1	EOF2	EOF3
Monthly	Full basin change	East-west dipole	North-south dipole
12-month low pass	Full basin change	North-south dipole	East-west dipole

Table 4.12: Summary of type of EOF patterns observed for the time series of zonal wind stress.

on the unfiltered data. It would thus appear that at periods longer than one year, by far the most important type of variability are coherent changes in wind stress across the entire subtropical North Atlantic. It has been suggested that the pressure and circulation changes associated with the North Atlantic Oscillation could be responsible for variability in the wind stress fields on periods longer than 12 months, and an in-depth analysis of the relationship between Mode 1 and the NAO is given in Section 4.4.

The second EOF mode in all four products consists of a north-south dipole pattern across the entire basin. Two of the products (NCEP/NCAR Reanalysis and the NOC Climatology) suggest the pattern is actually southwest to northeast oriented, with the southern maximum centred close to 28°N, 50°W. On the other hand, the second mode in QUICKSCAT has southeast to northwest orientation with the southern maximum located around 25°W, much closer to the eastern boundary. Nevertheless, the principal component time series of the four products are qualitatively similar. Mode 2 typically explains between 15% and 21% of the variance.

The third EOF mode for all four EOF realisations comprises an east-west oriented dipole. For the two products with the longest temporal coverage – the NOC Climatology and the NCEP/NCAR Reanalysis – the centres of action are located immediately north of the Canary Islands at the eastern boundary and close to the centre of the subtropical gyre at 36°N, 65°W. The other products yield slightly different configurations (e.g. ECMWF has the western centre much further south) but the essential structure is similar. This mode explains between 8% and 13% of the variance.

It is clear from this analysis that at periods both longer than and shorter than one year, the most significant modes of variability in the subtropical North Atlantic are basin-scale changes. For both the filtered and the unfiltered data sets, the first three EOF modes have accounted for around 70 to 80% of the variance, suggesting that the pattern is adequately described in a fairly low number of discrete spatial patterns. A summary of the leading EOFs for the zonal wind stress is given in Table 4.12.

EOFs of Wind Stress Curl

The three leading empirical orthogonal functions of the wind stress curl in the latitude band 28°N to 40°N were calculated for the four wind stress products. The results for the NCEP/NCAR Reanalysis, the NOC Climatology and the ECMWF Reanslysis are given in Figures 4.30, 4.35 and Figure 4.36 respectively. It is immediately apparent that the percentage of variance explained by each mode is much lower than for the zonal wind stress analysis (Table 4.13). For instance, the first mode explains only between 8% and 22% of the variance depending on the wind product used. Given that the wind stress curl is composed of two derivatives, the data set is more noisy, thus reducing the signal to noise ratio and minimising the proportion of variance explained by the leading EOFs.

The first mode of variability in all four products comprises a positive centre of action in the eastern central part of the basin, with small negative regions close to both the eastern boundary and the Gulf Stream. This mode, which represents the annual cycle in wind stress curl, confirms that the negative wind stress curl in the middle of the basin intensifies during winter, driving a stronger southward Sverdrup transport across the region (Figure 4.22). However, the cycle is reversed in the boundary regions. To investigate this further, Figure 4.37 shows a boxplot of the annual cycle of spatially averaged wind stress curl in the region east of 10°W. Wind stress curl values are positive throughout the year in this region, due mainly to a weakening southerly wind stress as one moves eastward into the mouth of the Mediterranean Sea. However, during the summer months, especially July and August, the magnitude of the positive curl is reduced. Nevertheless, the central basin intensification of negative curl during the winter months remains the dominant signal.

	EOF1	**EOF2**	**EOF3**
ECMWF	22.3	11.2	9.1
NOC	8.6	5.0	4.1
NCAR	19.8	12.1	9.7
QUICKSCAT	17.9	9.8	8.7

Table 4.13: Percentage of variance explained by three leading EOFs for the wind stress curl field of the 28°N to 40°N region of the North Atlantic.

The second and third modes explain relatively small proportions of the variance (Table 4.13). The second mode shows a north-south dipole across the width of the basin, whilst the third mode exhibits an east-west dipole, although the details of the spatial pattern do vary between the individual products.

The three leading modes of variability for the 12-month low pass Butterworth filtered wind stress curl are given in Figure 4.38 for the NCEP/NCAR Reanalysis. The first mode is once again a basin-wide in-phase pattern, with a peak value generally close to 35°W. This indicates that, as in the case of the zonal wind stress, variability at timescales longer than one year is dominated by basin-scale changes. This mode accounts for between 12% and 46% of the variance depending on which product is analysed (Table 4.14) but the spatial

	EOF1	EOF2	EOF3
ECMWF	36.0	13.2	8.2
NOC	12.3	8.2	7.4
NCAR	23.3	12.2	8.2
QUICKSCAT	45.8	9.8	8.7

Table 4.14: Percentage of variance explained by three leading EOFs for the 12-month Butterworth filtered wind stress curl field of the North Atlantic between 28°N and 40°N.

pattern of variability is similar.

The second and third modes exhibit more complex spatial patterns and there is some disagreement between the individual products as to their exact configuration. For example, whilst both the NCEP/NCAR and the ECMWF Reanalyses exhibit an east-west dipole in Mode 2, the centres of maximum variability are in different locations. Furthermore, the results for the NOC Climatology show a very complicated small-scale pattern of variability across the basin that is not obviously related to any physical mechanism (not shown). However, given the relatively small proportion of the variance explained by these modes, it is likely that the patterns are only reflecting background noise within the data set and not real physical modes of variability.

In conclusion, the EOF analysis of the wind stress curl has confirmed the presence of a strong annual cycle in the basin, which causes a maximum in negative wind stress curl across the centre of the basin during winter. However, the boundary regions, particularly close to the Gulf Stream and the outflow from the Mediterranean, show an antiphase relationship with the centre of the basin. When compared with the annual cycle in zonal wind stress, the annual cycle of curl explains a smaller proportion of the total variance. At periods longer than 12 months, the leading mode of variability is a basin-wide coherent pattern centred close to 40°W. The lower modes all explain less than 15% of the variance.

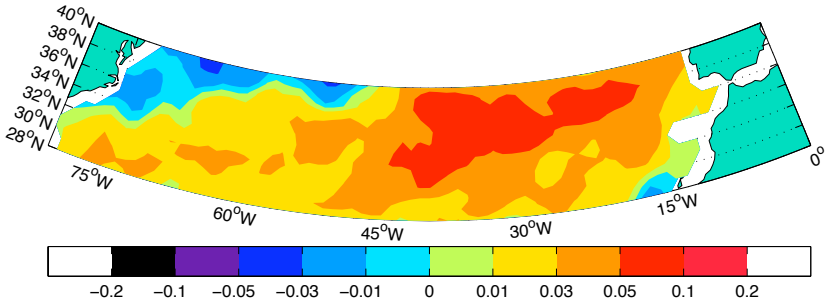

(a) EOF1

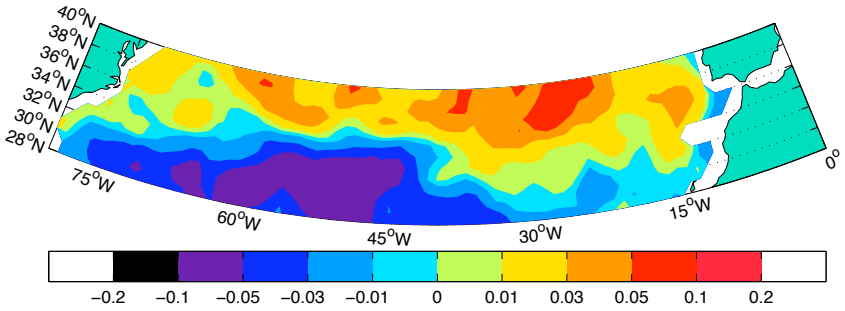

(b) EOF2

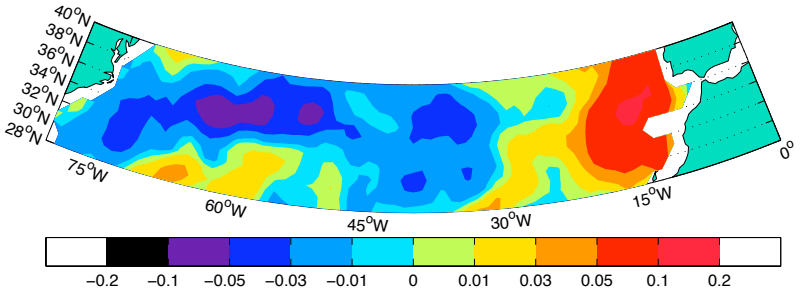

(c) EOF3

Figure 4.35: Spatial pattern of the first three EOFs of the demeaned, detrended and normalised wind stress curl derived from the NOC Climatology for the period January 1980 to December 2005. The percentage of variance explained was 8.6% for EOF1, 5.0% for EOF2 and 4.1% for EOF3.

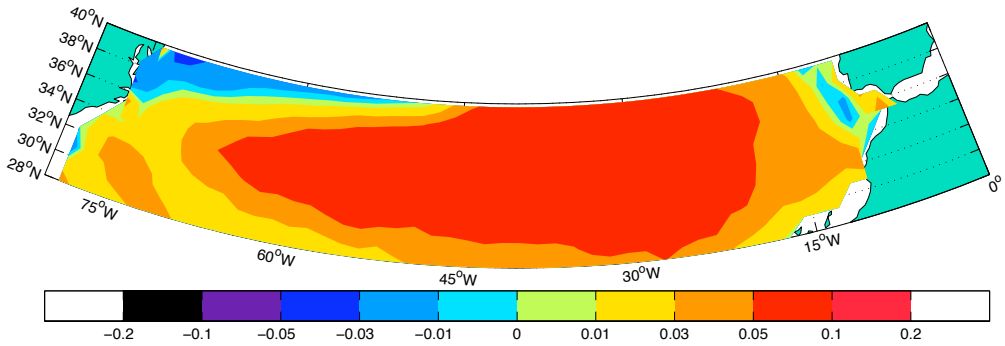

(a) EOF1

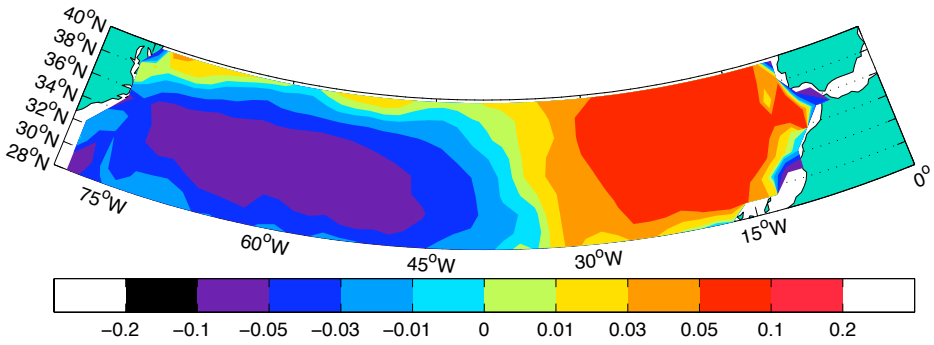

(b) EOF2

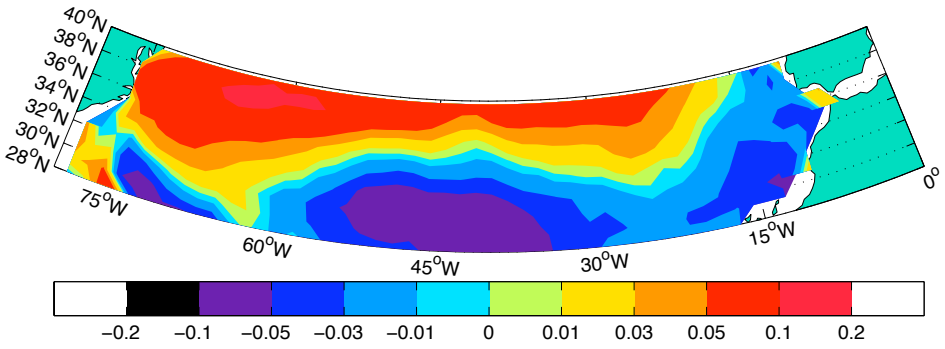

(c) EOF3

Figure 4.36: Spatial pattern of the first three EOFs of the demeaned, detrended and normalised wind stress curl derived from the ECMWF Reanalysis for the period January 1989 to April 2009. The percentage of variance explained was 22.3% for EOF1, 11.2% for EOF2 and 9.1% for EOF3.

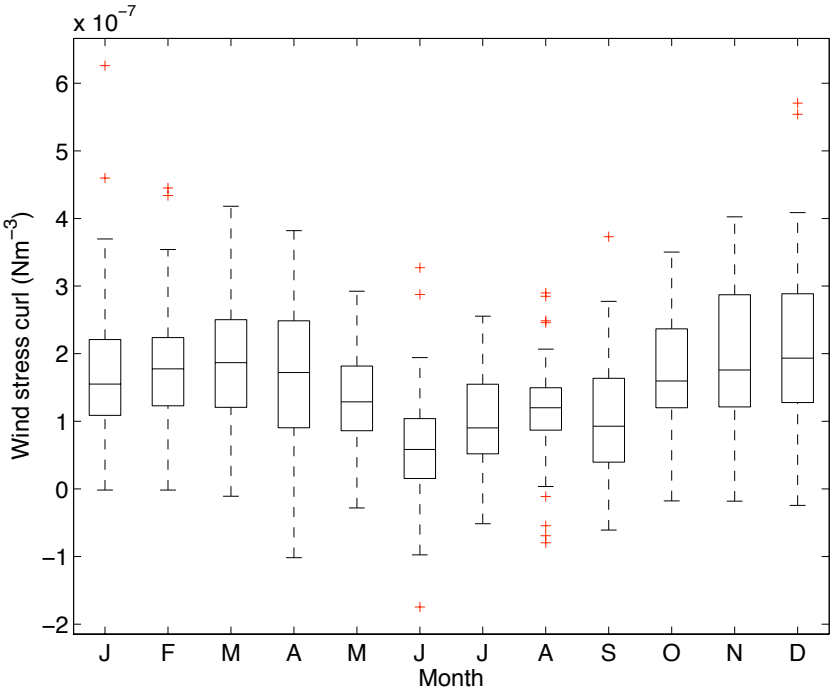

Figure 4.37: Boxplot of spatially averaged wind stress curl in the region east of 10°W (in Nm^{-3}) for the NCEP/NCAR Reanalysis (1948-2009). Note the less positive wind stress curl values during the summer months, meaning the eastern boundary has a reversed seasonal cycle of curl compared to the interior of the basin. The boxes show the lower (Q_1) and upper quartiles (Q_3) and median value, with the upper whiskers extending to furthest data point that lies within the region $Q_3 + 1.5(Q_3 - Q_1)$ and the lower whiskers extending to the further data point that lies within the region $Q_1 - 1.5(Q_3 - Q_1)$. Outliers are displayed in red.

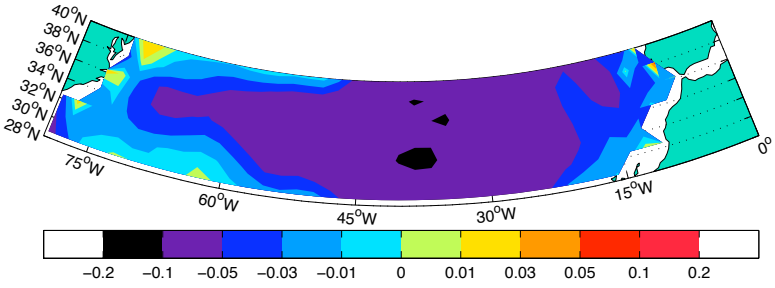

(a) EOF1

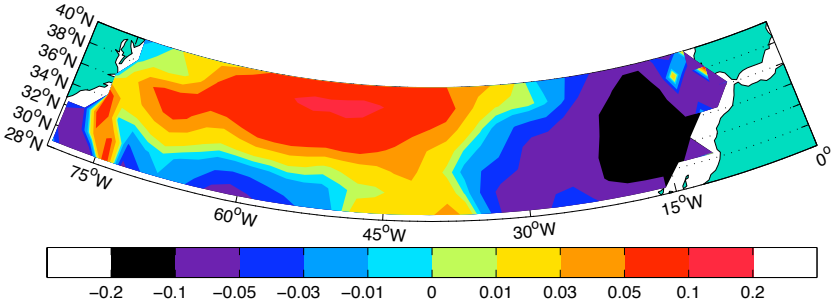

(b) EOF2

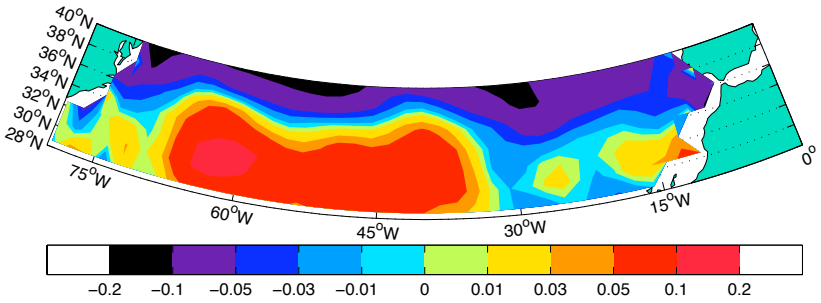

(c) EOF3

Figure 4.38: Spatial pattern of the first three EOFs of the 12-month Butterworth filtered wind stress curl derived from the NCEP/NCAR Reanalysis for the period July 1948 to March 2009. The first six months (January to June 1948) and the final six months (March to September 2009) of the series were truncated as part of the filtering procedure. The filtered data are detrended, demeaned and normalised prior to the singular value decomposition. The percentage of variance explained was 23.3% for EOF1, 12.2% for EOF2 and 8.2% for EOF3.

4.3.3 Quantifying the Variability in Ekman and Sverdrup Transports

Having identified the largest modes of variability, it is possible to quantify the *size* of the Ekman and Sverdrup transport variability at 36°N that is attributable to each mode of variability. As before, both the raw data and the 12-month low passed data are considered.

Ekman Transport Variability

Firstly the empirical orthogonal functions of the raw zonal wind stress were examined. For each EOF, a series of steps was followed in order to obtain an estimate of the variability in Ekman transport caused by each mode:

1. Time series of detrended, demeaned and normalised zonal wind stresses were obtained at each grid point within the four products. This was achieved by multiplying the leading empirical orthgonal functions by their relevant principal component time series.

2. The results for each grid point were then multiplied by their standard deviation in order to restore the correct variability to the time series.

3. The results along the 36°N line were then extracted and each EOF τ_x value made negative and divided by ρf to obtain a demeaned Ekman transport per unit width.

4. The transport values were then integrated across the basin width to obtain a time series of Ekman transport anomalies attributable to each mode.

The time series of Ekman transport anomalies attributable to EOF1 are given in Figure 4.39 (with the mean values found in Table 4.1). The four products are in close agreement in their overlapping period and confirm that the timescale of variability for this mode is annual. The standard deviation of these time series varies between 2.73 Sv and 3.11 Sv, suggesting that the annual strengthening and weakening of the westerlies at 36°N alters the Ekman transport by this amount. The standard deviations for this mode and for Modes 2 and 3 are found in Table 4.15. The results confirm that the basin-wide annual cycle of wind stress is by far the most important control on the magnitude of the Ekman transport at 36°N. Moreover, Mode 2, the east-west dipole pattern of wind stress, has very little effect on the zonally integrated Ekman transport, because an increase in Ekman transport in the eastern basin is compensated for by a reduction in the western basin, and vice versa. However, the second EOF may be important in altering other fluxes such as heat transport, as the $v'T'$ term may be affected by the zonal structure of the Ekman transport. The third EOF only contributes between 0.3 Sv and 0.7 Sv, less than a quarter of the size of the annual cycle.

The same Ekman transport variability estimate was made using the EOF analysis of the 12-month filtered zonal wind stress data. The time series attributable to EOF1 is shown in Figure 4.40 and the standard deviations for the three leading modes are given in Table 4.16. Several important observations can be made:

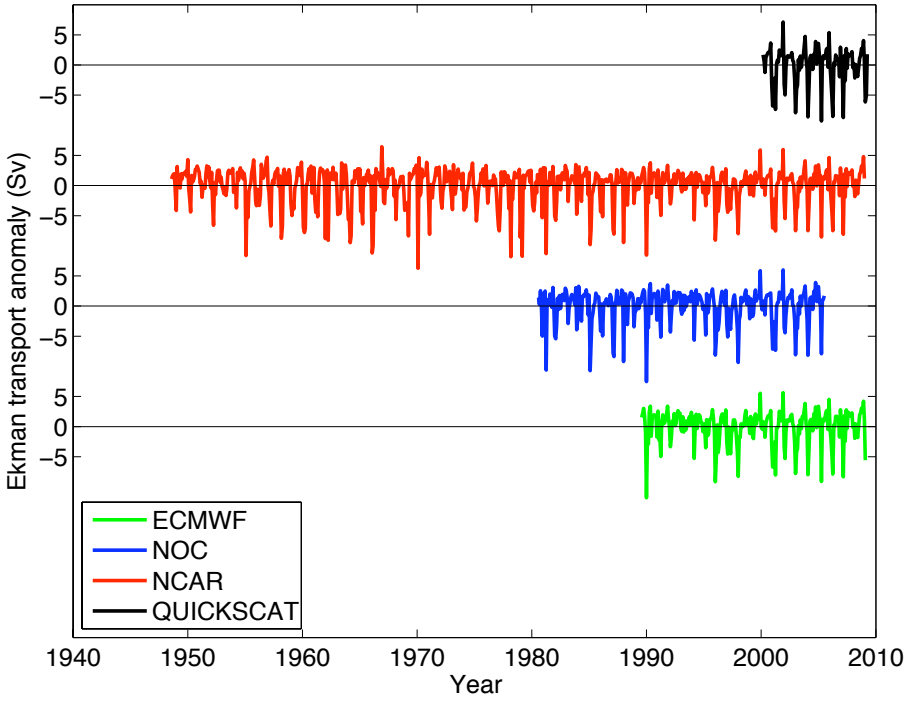

Figure 4.39: Time series of the Ekman transport anomalies at 36°N in Sv from the first EOF of the zonal wind stress in the band 28°N to 40°N.

	EOF1	**EOF2**	**EOF3**
ECMWF	2.73	0.15	0.63
NOC	2.81	0.029	0.71
NCAR	2.97	0.0035	0.29
QUICKSCAT	3.11	0.26	0.72

Table 4.15: Standard deviation (in Sv) of the zonally integrated Ekman transport anomaly time series at 36°N associated with the three leading empirical orthogonal functions of the zonal wind stress field.

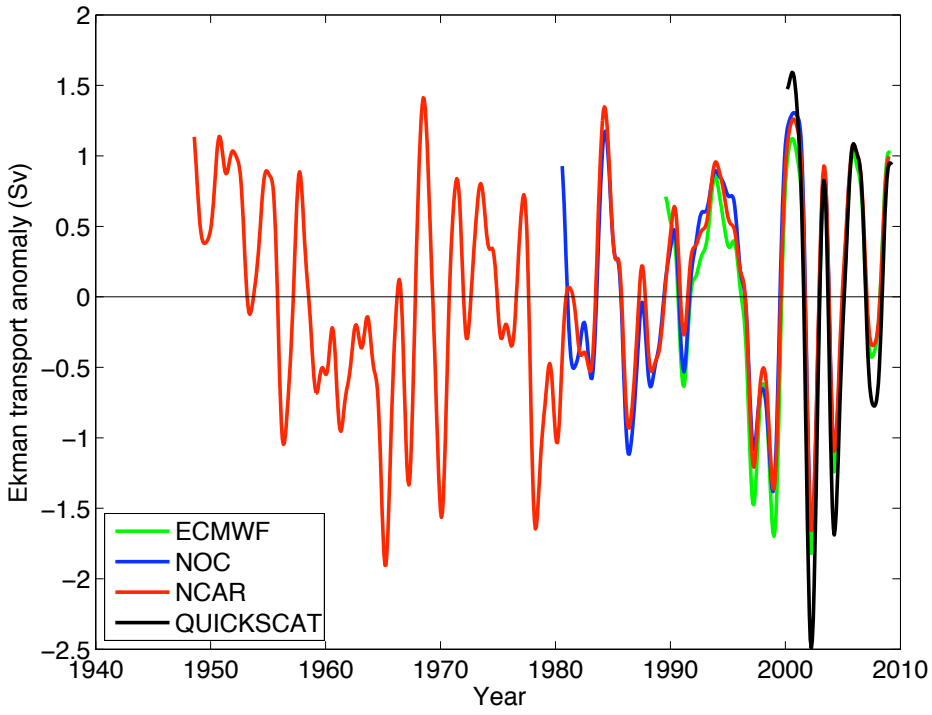

Figure 4.40: Time series of the Ekman transport anomalies at 36°N in Sv from EOF1 of the 12-month low pass filtered zonal wind stress in the band 28°N to 40°N.

1. Variability on timescales longer than one year is much smaller than the annual cycle. Whilst the annual cycle in Ekman transport has a standard deviation of close to 3 Sv, the largest mode of variability at timescales longer than one year produces Ekman transport changes of around 1 Sv.

2. The north-south dipole that characterises EOF2 yields an Ekman transport standard variability of less than 0.25 Sv.

3. The east-west dipole of EOF3 yields an Ekman transport variability of less than 0.2 Sv.

4. The variability arising from EOF2 and EOF3 is likely to be below the measurement error in the wind stress products. Whilst no formal error bounds are available for ECMWF, NCEP/NCAR or NOC (version 1), QUICKSCAT does contain an error bound for wind stress. Simple visual inspection of the data at 36°N suggests that the size of this error is around 10%, meaning that zonally integrated changes of less than 0.2 Sv are unlikely to be detected by this analysis.

	EOF1	EOF2	EOF3
ECMWF	0.78	0.23	0.0097
NOC	0.72	0.094	0.18
NCAR	0.72	0.065	0.067
QUICKSCAT	1.09	0.21	0.078

Table 4.16: Standard deviation of the zonally integrated Ekman transport anomaly time series at 36°N associated with the three leading empirical orthogonal functions of the 12 month low-pass filtered zonal wind stress field.

	EOF1	EOF2	EOF3
ECMWF	13.7	0.69	7.44
NOC	13.2	5.61	5.53
NCAR	11.2	7.91	2.48
QUICKSCAT	11.7	8.43	1.53

Table 4.17: Standard deviation in Sv of the zonally integrated Sverdrup transport anomaly time series at 36°N associated with the three leading empirical orthogonal functions of the wind stress curl field.

Sverdrup Transport Variability

The same procedure was followed as for the Ekman transport variability outlined above. For both the raw wind stress curl data and for the 12-month low-pass filtered data, time series of Sverdrup transport anomalies were computed at 36°N for the first three modes. The time series of the raw transport anomalies from the first mode are given in Figure 4.41, with the standard deviation of the transport anomalies for the first three modes given in Table 4.17. There is a clear agreement between the four products, with the dominant frequency being at 1 year^{-1}. The standard deviations of these time series are between 11.7 Sv and 13.7 Sv, implying a strong annual cycle. Mode 2 accounts for a smaller proportion of the variability in the Sverdrup transport, but still has a standard deviation of between 0.7 Sv and 8.4 Sv, depending on the product used. It is notable that the ECMWF estimate of standard deviation (0.7 Sv) is much lower than for the other products. This occurs because of the slightly different spatial structure of the mode in this product (Figure 4.36). Whilst NOC, NCEP/NCAR and QUICKSCAT have a consistent sign across the whole of the basin at 36°N (e.g. Figure 4.30), the spatial pattern for the ECMWF Reanalysis at 36°N has a different sign either side of 45°W, meaning that changes in the eastern basin are compensated for by changes in the western basin when computing the zonally integrated transport.

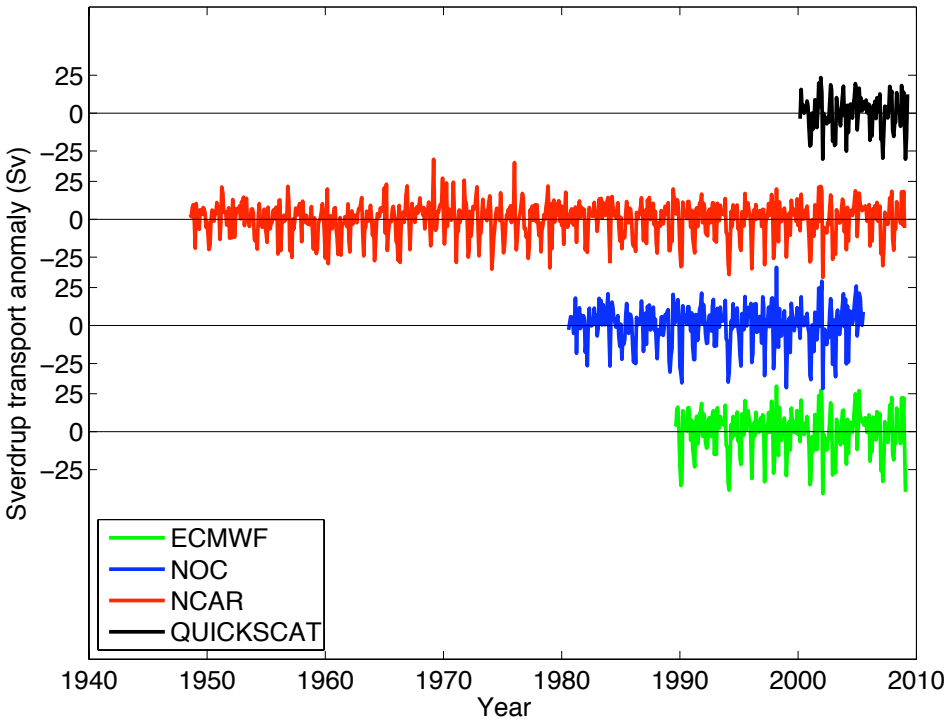

Figure 4.41: Time series of the Sverdrup transport anomalies at 36°N in Sv from the EOF1 of the wind stress curl in the band 28°N to 40°N.

For the 12-month filtered wind stress curl data (Table 4.18 and Figure 4.42), two observations can be made:

1. As with the zonal wind stress data, the interannual variability is generally much smaller in magnitude than the annual cycle. The size of the Mode 1 variability on timescales longer than 12 months is typically 3 to 4 Sv, compared with an annual cycle of 11 to 13 Sv. However, a notable exception is the result obtained for the QUICKSCAT data. In this case, the magnitude of the Mode 1 internannual variability is roughly the same as the annual cycle (13.5 Sv cf. 11.7 Sv). The reason for this increased variability is likely to be related to the short time series length of QUICKSCAT increasing the noise of the data. Nevertheless, the relatively short length of the QUICKSCAT filtered time series (less than 10 years) means the estimates of variability on timescales longer than 1 year must be treated with caution.

2. The disagreement in the spatial configuration of Modes 2 and 3 between the individual products, outlined in Section 4.3.2, means that the standard deviations in Sverdrup transport resulting from these modes are not easily comparable. Nevertheless, the standard deviations for these modes are all less than 4 Sv (Table 4.18).

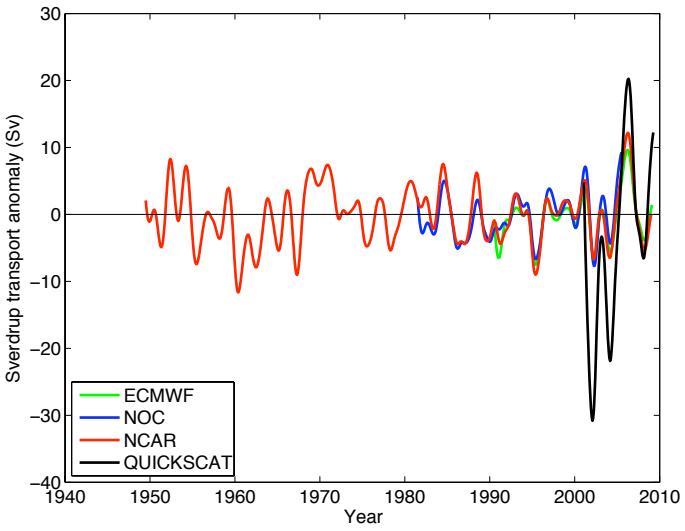

Figure 4.42: Time series of the Sverdrup transport anomalies at 36°N in Sv from EOF1 of the 12-month low pass filtered wind stress curl in the band 28°N to 40°N.

	EOF1	**EOF2**	**EOF3**
ECMWF	3.53	1.58	1.81
NOC	3.27	1.03	2.68
NCAR	4.19	3.92	0.82
QUICKSCAT	13.5	9.82	1.63

Table 4.18: Standard deviation in Sv of the zonally integrated Sverdrup transport anomaly time series at 36°N associated with the three leading empirical orthogonal functions of the 12-month low pass filtered wind stress curl field.

Wind stress product	Time period for NAO Regression
ECMWF	July 1989 to June 2008
NOC	July 1980 to June 2005
NCAR	July 1980 to June 2008
QUICKSCAT	February 2000 to June 2008

Table 4.19: Time periods over which the regression between Butterworth low-pass filtered zonal wind stress/wind stress curl and the low-pass filtered NAO were conducted for each product.

4.4 Relationships with the North Atlantic Oscillation

For both the zonal wind stress and the wind stress curl, the leading mode of variability at periods longer than 1 year is a basin-wide change in the strength of the stress or curl. The size of this pattern suggests that a large-scale mode of atmospheric variability controls the wind fields. The North Atlantic Oscillation, outlined in Chapter 2, is the strongest likely candidate as it is the main mode of pressure variability in the Northern Hemisphere. In this section, a regression analysis is conducted between the values of 12-month low-pass filtered zonal wind stress/wind stress curl and 12-month low-pass filtered NAO values from the National Oceanic and Atmospheric Administration's Climate Prediction Centre. The results of this analysis then permit a quantification of the Ekman and Sverdrup transport anomalies at 36°N associated with changes in the NAO. Finally, a regression analysis is conducted between the three leading EOFs of the filtered zonal wind stress/wind stress curl and the filtered NAO time series.

4.4.1 North Atlantic Oscillation Regression Analyses

Initially, regression analyses are conducted between the filtered zonal wind stress fields and the filtered NAO time series (Figure 4.43). The periods over which these regressions are conducted are displayed in Table 4.19. In each case the first and last six months of the available data are truncated to avoid filtering edge effects biasing the regression estimate. In order to calculate statistical significance for the correlation coefficients (Figure 4.43), an effective number of degrees of freedom has to be calculated, as data points from each filtered time series are not statistically independent. This is achieved by calculating an integral time scale for both the NAO and wind stress time series using an autocorrelation function, from which an effective number of degrees of freedom is inferred. In each case, the lower number of degrees of freedom was selected and used to test the significance of the correlation coefficient at the 95% level (Emery and Thomson, 1998).

A negative correlation exists between the magnitude of the zonal wind stress and the NAO index in all four products, indicating that when the NAO index is positive, the westerly winds that dominate across much of the basin are weakened, with a consequent weakening in the southward Ekman transport. In the ECMWF and NCEP/NCAR Reanalyses, along with the NOC Climatology, the correlation is statistically significant (at the 95% level) over

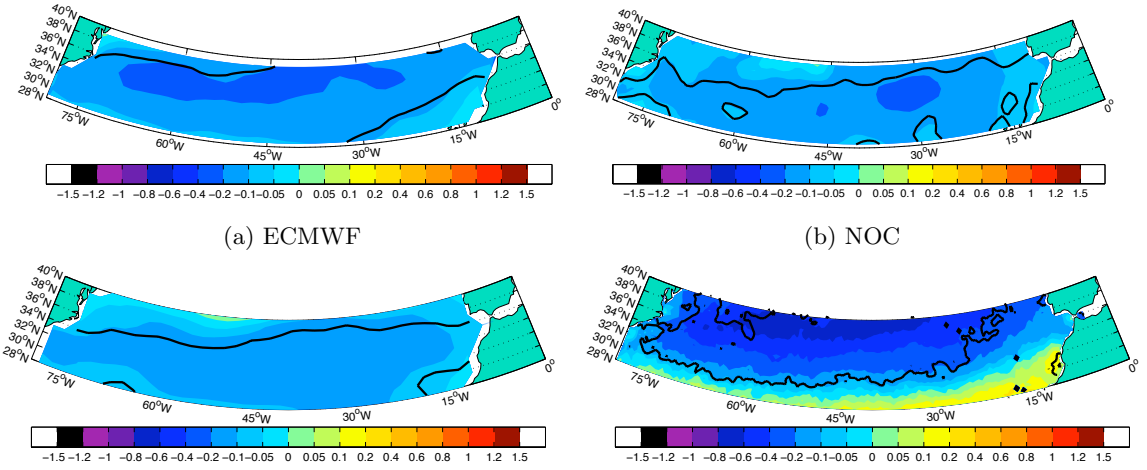

(a) ECMWF (b) NOC

(c) NCEP/NCAR (d) QUICKSCAT

Figure 4.43: First linear regression coefficient a ($\times 10$) (in colour) from the regression of 12-month low-pass filtered zonal wind stress (in Nm^{-2}) on 12-month low-pass filtered NAO index (i.e. $\tau = a \times \mathrm{NAO} + b$). The black contours indicate regions where the p value for the null hypothesis that the correlation coefficient is not distinguishable from zero falls below 0.05. The wind stress products are (a) the ECMWF Reanalysis, (b) the NOC Climatology, (c) the NCEP/NCAR Reanalysis and (d) the QUICKSCAT Scatterometer.

much of the latitude band, with the exception of regions close to the northern edge of the domain and a smaller zone close to the Canary Islands. At 36°N, the negative correlations are generally significant east of 45°W. East of 30°W, where winds are generally north to north easterly in direction, the negative correlation is strong, suggesting the winds have a stronger westward component under positive NAO conditions. The size of the linear regression coefficients is similar in ECMWF, NOC and NCEP/NCAR, but they tend to be larger in QUICKSCAT as this product has the strongest mean winds (Figure 4.6). Moreover, some positive correlations are observed towards the southern end of the domain with this product. This result is consistent with the larger interannual variability observed in the leading EOF of the 12-month low pass filtered zonal wind stress (Table 4.16).

A similar regression map is presented in Figure 4.44 for the relationship between the low-pass filtered wind stress curl and the low-pass filtered NAO. A more complex pattern is observed than in the zonal wind stress regression, although several important features can be identified. Firstly, positive correlations tend to dominate the region south of 34°N in all the products, suggesting that the negative wind stress curl in this latitude band becomes more positive as the phase of the NAO becomes more positive. Consequently, the southward Sverdrup transport decreases with increasing NAO. North of 34°N, the reverse pattern is observed, with negative linear regression values found across much of the basin. These imply that as the NAO becomes more negative, the southward basin-wide Sverdrup transport decreases. Thirdly, the region of statistically significant regression at the 5% level is more restricted geographically than in the zonal wind stress regression (Figure 4.43). Finally, QUICKSCAT exhibits a slightly different regression pattern to the other products, with

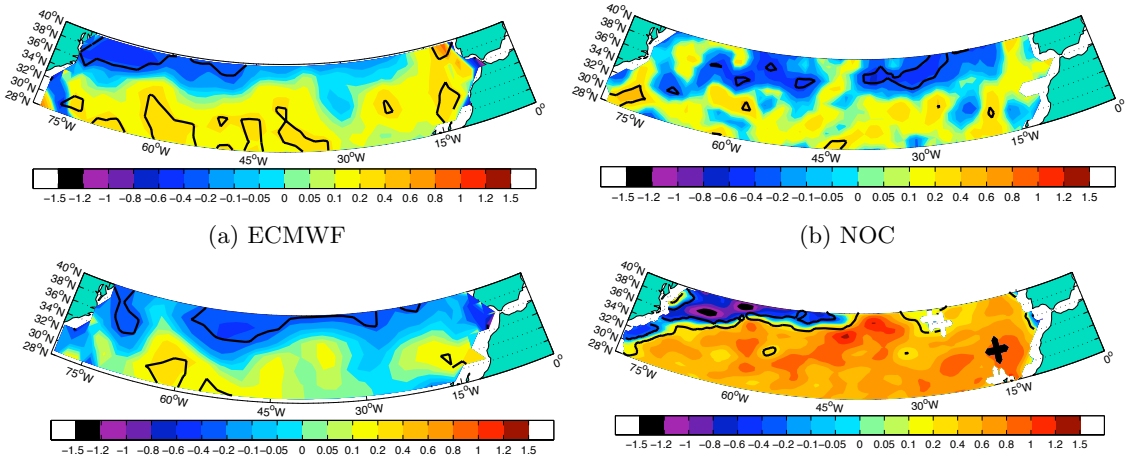

(a) ECMWF (b) NOC

(c) NCEP/NCAR (d) QUICKSCAT

Figure 4.44: First linear regression coefficient ($\times 10^7$) (in colour) from the regression of 12-month Butterworth low-pass filtered wind stress curl (in Nm^{-3}) on 12-month Butterworth low-pass filtered NAO index. The black contours indicate regions where the p value for the null hypothesis that the correlation coefficient is not distinguishable from zero falls below 0.05. The wind stress products are (a) the ECMWF Reanalysis, (b) the NOC Climatology, (c) the NCAR/NCEP Reanalysis and (d) the QUICKSCAT Scatterometer (bottom right).

NAO value	+1	+0.77	0	−0.66	−1
ECMWF	−0.94	−1.26	−2.34	−3.25	−3.74
NOC	−1.81	−2.04	−2.82	−3.49	−3.83
NCEP/NCAR	−0.93	−1.18	−2.02	−2.75	−3.11
QUICKSCAT	0.30	−0.36	−2.56	−4.44	−5.42

Table 4.20: Zonally integrated Ekman transport at 36°N for several NAO values based on regression coefficients shown in Figure 4.43.

strong positive correlation extending right to the northern edge of the domain east of 45°W.

To examine the impact of these regression results on the total Ekman and Sverdrup transports at 36°N, the coefficients at the nearest grid points to 36°N are used to estimate the zonally integrated meridional Ekman and Sverdrup transports at this latitude for a range of NAO values (Tables 4.20 and 4.21). Transports are estimated at NAO = 0.77 and NAO = −0.66 as these are the highest and lowest 12-month filtered NAO time series observed in the 28 year record, occurring in September 1990 and July 2000 respectively.

NAO value	+1	+0.77	0	−0.66	−1
ECMWF	−21.5	−20.9	−18.8	−17.0	−16.1
NOC	−22.1	−21.1	−17.9	−15.1	−13.6
NCEP/NCAR	−21.5	−20.6	−17.4	−14.7	−13.3
QUICKSCAT	−4.5	−7.72	−18.4	−27.5	−32.2

Table 4.21: Zonally integrated Sverdrup transport at 36°N for several NAO values based on regression coefficients shown in Figure 4.44.

For the Ekman transport time series, increased southward Ekman transport is observed with a more negative phase of the NAO. Using the two most extreme values of NAO observed during the 28-year time series, the state of the NAO is associated with an Ekman transport change of between 1.5 Sv and 4.1 Sv. This is substantially smaller than the size of the annual cycle (which has a *standard deviation* of up to 3 Sv, see Table 4.15). It is likely that the 4.1 Sv range calculated from QUICKSCAT data is an overestimate given that the length of the QUICKSCAT filtered time series regression is less than 9 years.

For the Sverdrup transport time series, both Reanalysis products and the NOC Climatology suggest that an increased southward Sverdrup transport is associated with a more positive NAO. Over the length of the NAO time series, the total range of variability associated with changes in the NAO is between 3.9 Sv and 6 Sv, again substantially smaller than the annual cycle (Table 4.17). Interestingly, the QUICKSCAT data shows the opposite pattern, with increased southward Sverdrup transport as the NAO decreases, in line with the more northerly extent of the positive regression values seen in Figure 4.44. Again, in spite of the improved spatial resolution of QUICKSCAT, the short length of time series compared to the timescale of interest suggests these regression coefficients may be unreliable.

In order to understand more thoroughly how the NAO-induced variability affects the size of both the Ekman and Sverdrup transports, Figure 4.45 displays the mean composite NOC-derived wind stress for the 10 months with the highest and 10 months with the lowest 12-month low pass filtered NAO values. It is initially surprising that the positive NAO state was observed to produce weaker westerlies north of 34°N, as a positive state of the NAO is generally considered to enhance the midlatitude westerlies and the strength of the North Atlantic storm track. Nevertheless, previous modelling work by Eden and Jung (2001) yielded a similar result. They suggested that positive NAO conditions cause an anticyclonic circulation anomaly centred on the subpolar front close to 40°N. A near identical-result was also observed by Marshall et al. (2001) based on a regression of the NCEP/NCAR Reanalysis winds onto the wintertime NAO index of Hurrell (1995). The positive midlatitude westerly wind stress anomaly commonly attributed to a positive state of the NAO is actually found north of 45°N (Marshall et al.'s Figure 2).

The final observation – that an increased North Atlantic Oscillation is associated with an increased southward Sverdrup transport at 36°N – is also supported by Figure 4.45. In the NAO negative case (bottom panel), the southward extension of the belt of strong westerly winds in the western basin causes a reduction in the meridional gradient of easterly stress, and a concomitant weakening of the southward Sverdrup flow. In contrast, when the NAO is in positive phase (top panel), the band of westerlies weaken in the region near 36°N, causing an increase in the meridional gradient of easterly wind stress, and a strengthening of the Sverdrup transport.

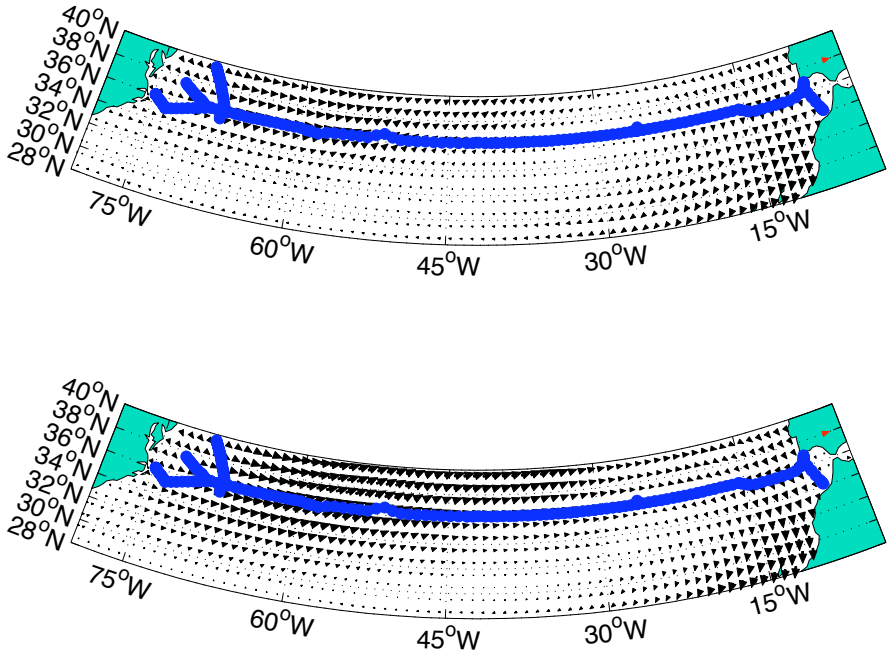

Figure 4.45: Mean wind stress field from the NOC Climatology for the 10 months with the highest 12-month low pass filtered NAO index (top) and the 10 months with the lowest 12-month low pass filtered NAO index (bottom). The red arrow over Iberia indicates a wind stress of 0.5 Nm^{-2}.

4.4.2 Regression Analyses with the Empirical Orthogonal Functions

A regression analysis is also conducted between the three leading principal component time series and the NAO for the 12-month low pass filtered zonal wind stress and wind stress curl. The aim is to determine the spatial modes of variability excited by the North Atlantic Oscillation. Once again, the reduced number of degrees of freedom associated with the time series filtering are accounted for when estimating the p values.

Zonal Wind Stress

The results for the regression of EOF1 onto the NAO index using the time periods given in Table 4.19 are presented in Table 4.22. The results suggest a strong positive correlation between the time series of EOF1 amplitudes and the filtered North Atlantic Oscillation. The R^2 values imply that the NAO index explains between 28% and 45% of the variance of Mode 1, indicating that the NAO accounts for the basin-wide change in zonal wind stresses associated with this mode (Table 4.12). Even taking into account the reduced number of degrees of freedom caused by using filtered time series, the correlations are statistically significant at the 1% level.

Relatively strong negative correlations (between -0.30 and -0.52) are also found between

	Regression coefficients	Correlation coefficient	p value	R^2 value
ECMWF	$22.69/-2.79$	0.536	8×10^{-4}	0.28
NOC	$34.43/-4.33$	0.601	3×10^{-5}	0.36
NCEP/NCAR	$19.90/-1.06$	0.603	6×10^{-6}	0.36
QUICKSCAT	$108.85/-6.15$	0.672	0.0015	0.45

Table 4.22: The two linear regression coefficients, the correlation coefficient and associated p value and the R^2 value for the regression of EOF1 of the 12-month low pass filtered zonal wind stress onto the 12-month low pass filtered NAO.

the NAO time series and the time series of EOF2 amplitudes, implying that the NAO time series might also be partly responsible for setting up the north-south dipole pattern that characterises this mode (Table 4.23). Given the relatively larger impact of the NAO on the wind stress field towards the northern part of this domain (as shown in Figure 4.45), this result is to be expected. Nevertheless, the R^2 values are much weaker than in Mode 1, suggesting that the NAO only accounts for between 9% and 27% of this mode's variability. Despite the NAO correlating in a positive sense with EOF1 amplitudes and negatively with EOF2 amplitudes, no correlation is observed between Mode 1 and Mode 2 as EOF analysis identifies modes that are independent of one another.

	Regression coefficients	Correlation coefficient	p value	R^2 value
ECMWF	$-10.09/1.23$	-0.370	0.020	0.14
NOC	$-12.56/1.58$	-0.368	0.030	0.14
NCEP/NCAR	$-5.95/0.401$	-0.297	0.057	0.09
QUICKSCAT	$-54.74/2.39$	-0.523	0.011	0.27

Table 4.23: The two linear regression coefficients, the correlation coefficient and associated p value and the R^2 value for the regression of EOF2 of the 12-month low pass filtered zonal wind stress onto the 12-month low pass filtered NAO. Only the NCEP/NCAR Reanalysis does not produce a statistically significant correlation at the 5% level.

The regression results for EOF3 (not shown) suggest that a weak correlation exists between the NAO time series and Mode 3 amplitudes, although the R^2 values are extremely small (less than 0.1). The east-west dipole is therefore unlikely to be NAO-related.

Wind Stress Curl

In the case of the wind stress curl, the relationship between the individual modes and the NAO index is more difficult to interpret. For EOF1, which generally has a centre in the middle to eastern part of the basin, no clear correlations can be found with the time series of the low-pass filtered NAO (Table 4.24). In light of the opposing signs of the correlation in the northern and southern part of the domain (Figure 4.44), it is not particularly surprising that the NAO time series does not correlate with this basin-wide mode. However, the NAO time series does exhibit stronger correlations (with statistically significant regression

	Regression coefficients	**Correlation coefficient**	**p value**	**R^2 value**
ECMWF	$1.56/-0.170$	0.046	0.78	0.002
NOC	$1.16/-0.145$	0.040	0.81	0.001
NCEP/NCAR	$0.118/-0.336$	0.020	0.97	4×10^{-6}
QUICKSCAT	$39.7/-2.54$	0.29	0.17	0.08

Table 4.24: The two linear regression coefficients, the correlation coefficient and associated p value and the R^2 value for the regression of EOF1 of the 12-month low pass filtered wind stress curl onto the 12-month low pass filtered NAO.

coefficients at the 5% level) in Modes 2 and 3. Unfortunately, the spatial configuration of these modes differs between the individual products, meaning that interpreting which modes of spatial variability are excited by the NAO is difficult. In all four products, however, the third mode exhibits a quasi- north-south dipole pattern, which for ECMWF, NOC and NCEP/NCAR correlates strongly with the low pass-filtered NAO (Table 4.25). Although this mode only accounts for 7 to 9% of the variability, the result confirms the previous observation of opposing regression signs in the northern and southern parts of the domain (Figure 4.44).

	Regression coefficients	**Correlation coefficient**	**p value**	**R^2 value**
ECMWF	$9.93/-1.22$	0.55	5.4×10^{-4}	0.30
NOC	$8.38/-1.05$	0.37	0.018	0.14
NCEP/NCAR	$9.89/-0.816$	0.66	1.5×10^{-6}	0.434
QUICKSCAT	$-24.2/0.480$	0.35	0.10	0.12

Table 4.25: The two linear regression coefficients, the correlation coefficient and associated p value and the R^2 value for the regression of EOF3 of the 12-month low pass filtered wind stress curl onto the 12-month low pass filtered NAO.

In conclusion, the results indicate that the NAO affects the magnitude of both Ekman and Sverdrup transports on timescales longer than 12 months, but that the modes of variability excited by the NAO are different in each case. For the zonal wind stress, a positive NAO weakens the strength of the westerly wind stress across the basin, leading to a weaker southward Sverdrup transport. The NAO primarily affects the first EOF (a basin-wide change in zonal wind stress) but also influences the north-south dipole pattern of EOF2, implying that zonal wind stress changes are larger towards the northern end of the domain. In contrast, the NAO affects the wind stress curl differently. North of 34°N, an increased NAO causes an increase in southward Sverdrup transport (Table 4.21), whilst to the south of this latitude this relationship is largely reversed. This change in sign coincides with the overall increase in southward Sverdrup transport to the north of 34°N observed in Figure 4.6. The regions of statistical significance are substantially smaller than for the zonal wind stress. In this case, the NAO primarily affects EOF3, which generally exhibits a north-south dipole in all the products. The NAO does not show strong correlation with the near basin-wide EOF mode 1 (Table 4.24). Overall, the strength of the correlation is much weaker for

WSC than for zonal wind stress, with EOF3 only accounting for between 7 and 9% of the variance.

4.5 Conclusions

In this chapter, the dominant timescales of variability of both zonal wind stress and wind stress curl fields have been revealed and the relationship to Ekman and Sverdrup transports at 36°N explored. In both cases, the annual cycle is the largest component of the variability, leading to a basin-wide change in the strength of the zonal wind stress (strongest in winter) and a near basin-scale change in the magnitude of the wind stress curl (largest in the central basin in winter). Some evidence for higher frequency variability at 2 to 4 months is also observed in the spectral analysis of wind stress curl. The annual cycles translate into winter maxima in both the Ekman transport and Sverdrup transport at 36°N. The size of the annual cycle, as measured by the standard deviation of the first EOFs, is close to 3 Sv for the Ekman transport and near 12 Sv for the Sverdrup transport. Given that the Sverdrup transport includes contributions from both the Ekman and geostrophic components (Equation 4.8), the annual cycle in the geostrophic component, inferred from the difference in these estimates, should be around 9 Sv. The annual cycle in the size of the interior transport estimated from Argo floats is discussed in Section 5; the 9 Sv change calculated here should be clearly detectable if wind is the dominant control on its size.

On timescales longer than one year, the main modes of variability are basin-scale changes in the size of the zonal wind stress and wind stress curl. In the case of the zonal wind stress, this accounts for around 45% of the variability, whilst the first EOF of the wind stress curl accounts for only around 15% of the variability. In terms of transport changes, these modes account for around 1 Sv of Ekman transport variability and 4 Sv of Sverdrup transport variability at 36°N. Therefore, the interannual variability is roughly one-third of the size of the annual cycle. The size of the geostrophic interannual variability, calculated from the difference of the Sverdrup and Ekman components, is thus close to 3 Sv.

The role of the NAO in driving interannual variability in both Ekman and Sverdrup transports has also been examined. A strong correlation is found between the basin-wide changes in the zonal wind stress and the state of the low-pass filtered NAO, implying a stronger southward Ekman transport during negative phases of the oscillation. In the period since 1980, it is estimated that the NAO could account for changes of up to 4 Sv in the Ekman transport (note this is a range, not a standard deviation). In contrast, the wind stress curl shows a more complex pattern of NAO-dependency, with positive (negative) NAO values supporting more southward Sverdrup transport in the region north (south) of 34°N. Furthermore, the NAO does not correlate with the first EOF of 12-month low pass filtered wind stress curl, but does exhibit statistically significant correlations with other modes, in particular the north-south dipole in Mode 3. We therefore conclude that whilst the NAO is responsible for changes in the magnitude of both Ekman and Sverdrup transports, the

relationship is stronger and clearer for the Ekman transport.

One aspect that has not been investigated fully here is the correlation between individual modes of zonal wind stress versus wind stress curl variability. This is potentially important, especially for periods greater than 12 months where the NAO is the dominant control on the basin-scale wind field. Pursuing this line of investigation more actively would further enhance understanding of the atmospheric circulation changes related and unrelated to NAO-type variability and the associated ocean response.

The close agreement between wind stress products derived using different methodologies in the latitude band 28 to 40°N is pleasing and suggests that our findings are robust. Results from the QUICKSCAT Scatterometer sometimes differ from the other products; we believe this is caused by a combination of an improved spatial resolution but a relatively short time series length (less than 10 years), which acts to reduce the signal to noise ratio throughout the basin.

Chapter 5

Synthesis

In the first part of this chapter, the results obtained in Chapters 3 and 4 are discussed in order to test the hypothesis that changes in the observed wind stress curl field account for the annual and interannual variability in the interior transport of the Atlantic at 36°N. The extensive literature concerning the validity of the Sverdrup relation in the North Atlantic is discussed in Section 5.1, before the formal hypothesis testing is conducted in Section 5.2. In line with earlier studies, it is shown that the Sverdrup relation alone is insufficient to account for either the mean value or variability in the total basin-wide geostrophic transport. However, the relationship does successfully predict the baroclinic transport in the region east of 40°W, though it is not capable of describing the the year-to-year variability. Other sources of transport variability forced by wind stress curl variability are discussed briefly in section 5.2.3.

In the second part, a comprehensive error analysis of our interior and Gulf Stream transport estimates is conducted (Sections 5.3 and 5.4). In the case of the southward interior transport, it is demonstrated that despite potentially large shear errors resulting from OI mapping error of the θ/S fields, these are partly density-compensating, meaning that the vertically integrated transport error is small (order 2 Sv). This lends support for attempting direct density mapping of the section (Section 5.3.6). However, despite the use of subsurface displacements averaged over several years, uncertainty in the choice of background velocity remains very large, with the barotropic component above 1000 dbar estimated to be -15.6 ± 34.2 Sv (the error bar representing two standard deviations from the mean). Errors in the Gulf Stream transport estimates arise both from uncertainty in the regression relationship that links the total transport with sea surface height differences and from altimeter instrumental errors themselves. In reality, the instrumental uncertainty is small, causing transport errors of less than 1 Sv, whilst the RMS error in the regression relationship for the 0 to 1000 dbar time series is 4.3 Sv. The Gulf Stream time series above 1000 dbar is thus accurate to within 6 Sv.

The third part of the chapter concerns the relationship between Gulf Stream transport at the Line W section and wind stress/WSC fields in the subtropical North Atlantic (Section 5.5).

Whilst at monthly timescales there appears to be a correlation between the Gulf Stream transport and the wind stress curl immediately to the east, it cannot unequivocally be established that this relationship is robust given that both time series are short and contain strong annual cycles. A similar conclusion is reached by a lag correlation analysis with local meridional and zonal wind stress. Results are then presented from the OCCAM model that imply that first baroclinic mode Rossby waves are an important source of variability in the density field in both the interior of the basin and at the western boundary at 36°N. This confirms previous work conducted by Hirschi et al. (2009) which argued for Rossby waves controlling the mid-ocean transport variability at 26°N, and also supports a previous study by Anderson and Corry (1985) who argued that the Rossby wave transit time set the upper frequency bound on the validity of the Sverdrup balance. Some comments are also given explaining how a modelling study could be used to investigate the importance of the Sverdrup balance in setting the interior transport and to understand the physical mechanisms that moth link variability in wind stress/WSC to Gulf Stream volume transport.

In the final sections (5.8 to 5.10), our results are drawn together to provide an estimate of the total mean northward volume transport above 1000 dbar at the 36°N/Line W section. This is compared with results form previous studies and the remaining uncertainties outlined. A summary of the main results is then provided, before an examination of the broader implications of our research for monitoring the circulation at 36°N. Three separate but related fields of study are discussed. Firstly, the potential for synthesising Line W and Argo measurements to estimate the MOC on annual and seasonal timescales is evaluated, to improve previous estimates obtained by Hernandez-Guerra et al. (2010) and Willis (2010). Secondly, the possibility of lengthening the Gulf Stream time series is considered, both to improve the reliability of the seasonal cycle calculations and to investigate mechanisms forcing the boundary current transport variability. Finally, the use of Argo and Line W data to create synthetic sections from which long term changes in heat content and meridional heat transport is critically assessed, with reference to ongoing work within the MONACO group of the RAPID-WATCH programme (Ivchenko et al., 2008).

5.1 Previous Work in the North Atlantic

The earliest tests of the relation derived by Sverdrup (1947) were conducted in the Pacific. Reid (1948) used observed climatological winds in the 10°S to 25°N latitude band to calculate the zonal and meridional mass transport of the upper kilometre. A close agreement was found with the observed transport, except in the region very close to the Equator.

Almost thirty years later, the validity of the relationship in the North Atlantic was tested systematically for the first time. For six different latitude sections (8°N, 16°N, 24°N, 32°N, 53.5°N and 59°N) , Leetmaa et al. (1977) used the wind stress tabulations of Bunker (1976) to calculate the zonally integrated meridional Sverdrup transport and compared the result to estimates of geostrophic shear from cruise data along these latitudes. At the subtropical

latitudes of 24°N and 32°N, a close correspondence was observed between the wind stress curl and hydrographic data in the eastern 4000 km of the North Atlantic. At 24°N, they proposed that mass conservation occurred by a 30 Sv northward transport in the Gulf Stream being compensated by a 30 Sv southward interior flow. At 32°N, 27 Sv of southward Sverdrup transport was found in the interior, smaller than that found by geostrophic measurements but within the errors of the method. They thus concluded that the Sverdrup relationship accounts for most of the interior transport, with negligible transport at depths greater than 1500 dbar.

However, almost since its publication, this paper has attracted substantial criticism. Wunsch and Roemmich (1985) observed that the simple balance between 30 Sv of northward Gulf Stream flow and 30 Sv of southward interior flow at Florida Straits omitted the southward flowing lower limb of the overturning circulation (the Deep Western Boundary Current). Whilst Leetmaa's scheme required zero net motion above 1000 m, calculations from cruise sections in 1957 and 1981 suggested a net northward flow of 19 Sv above 1000 m, meaning that the northward Gulf Stream flow must be returned by a combination of interior and overturning pathways (Roemmich and Wunsch, 1985). Hence, at 24°N, the wind stress curl matched the transport well in the eastern two-thirds of the basin, but it overestimated the zonal integral of transport above $\sigma_\theta = 27.4$ in both 1957 and 1981, as some of the southward transport is provided by the DWBC. At 36°N, Roemmich and Wunsch (1985) observed that the wind stress *overestimated* the southward transport on the eastern side of the basin but *underestimated* the transport integrated between the eastern boundary and the outer edge of the Gulf Stream. Furthermore, the relation did have self-consistency issues (Wunsch and Roemmich, 1985), specifically that the vertical velocity profile obtained by integrating $w_z = \beta v/f$ downward from the surface Ekman pumping velocity yielded v and w of opposite signs. This was shown to be inconsistent with the positive vertical velocity that would be observed from northward bottom flow over a shoaling seafloor. In summary, Wunsch and Roemmich (1985) concluded that 'the evidence for Sverdrup balance in the North Atlantic would appear to be slight'.

Despite this scepticism, modelling work has provided support for the relationship. For instance, Anderson and Corry (1985) suggested that the Sverdrup balance was a valid approximation to the long-term mean southward transport and compensated the 30 Sv of northward transport in the Florida Current. Their investigation focused on the temporal fluctuations in the strength of the Florida Current, and specifically the observation that the annual maximum of southward Sverdrup transport did not correspond with the annual maximum in Florida Straits transport, which occurs during summer. Furthermore, they argued that on annual or shorter periods, Sverdrup balance does not hold, with boundary current variability instead controlled by barotropic Rossby waves generated by $\mathrm{curl}_z(\tau/H)$, where H is the ocean depth. However, their work did not focus on transport in the interior where one might expect the theoretical relationship to have a more direct effect.

More recently, a further reanalysis of the theoretical Sverdrup relation has taken place at

25°N as part of the RAPID-WATCH programme using the ECCO state estimate (Thomas et al., 2010). In this analysis, the transport derived from wind stresses within ECCO was compared to modelled ocean transport in the top 1000 m in a box centred on 25°N. Averaged over the period 1992 to 2007, the zonally integrated transport was 88% of that predicted by the Sverdrup balance, though the pointwise deviation across the basin was larger in many cases. It was also found that the presence of a mid-depth level of no motion meant that the Sverdrup balance was a valid approximation for the interior transport despite significant deep flows in the Deep Western Boundary Current. Although vortex stretching in the bottom boundary layer of the ocean was also found to induce vertical velocities, these are generally decoupled from the surface meaning that the balance holds by assuming a level of no motion at intermediate depths.

In new observational work, the transports inferred from a single section inverse of the 2005 36°N section were compared with the Sverdrup transport derived from the NOC Climatology (McDonagh et al., 2010). In line with Wunsch's earlier study, it was found that the Sverdrup relation overestimated the transport in the eastern basin and understimated it in the region west of 40°W. Our study contributes to this existing body of literature by investigating empirically the applicability of the relation on both a year-to-year and season-to-season basis.

5.2 Hypothesis Testing

Two hypotheses are now tested. Firstly, does the Sverdrup minus Ekman transport (Equation 4.8) account for the total geostrophic interior transport across the basin and its zonal structure? Secondly, does the annual and interannual variability in the Sverdrup minus Ekman flow explain the year-to-year and season-to-season variability in the interior transport? In Chapter 4, it was found that the overall Sverdrup minus Ekman transport had a seasonal variability (as measured by the standard deviation) of approximately 9 Sv (with a maximum in late winter) and an interannual variability of around 3 Sv. The veracity of these figures is now tested using the independently-obtained transport estimates. In each case, the geostrophic transport was evaluated both above 1000 dbar and above $\sigma_\theta = 27.38$. The justification for using $\sigma_\theta = 27.38$ is that it typically forms the deepest outcropping isopycnal in the subtropical gyre and is thus the density range over which one might expect the transport to be directly influenced by the wind stress curl.

5.2.1 The Mean Transport

To answer the first question, the east to west cumulated geostrophic transport above $\sigma_\theta = 27.38$ for the six years was calculated, assuming a zero reference velocity at $\sigma_\theta = 27.38$. The background velocity calculated from the Argo float trajectories was initially excluded due to its uncertainty (more details in Section 5.3.4). Figure 5.1 shows this geostrophic transport

alongside the annual mean east to west cumulated Sverdrup minus Ekman transport for each year. In line with earlier work at 36°N (McDonagh et al., 2010), the geostrophic transport from the integrated to 67.6°W is generally larger than the predicted Sverdrup transport (the exceptions being in 2002, when there is least confidence in the accuracy of the interior transport, and in 2007). Whilst the range of integrated Sverdrup minus Ekman transports is between 12 and 22 Sv, the interior transport above $\sigma_\theta = 27.38$ is between 13 and 35 Sv. Moreover, several features of the velocity sections, such as the large northward transport anomaly close to 42°W in 2003 (Figure 5.1b) which was attributed to a single eddy in Section 3.1.1, are clearly not caused by wind stress curl.

Splitting the basin at 40°W, two different regimes can be identified. East of this longitude, the geostrophic transport roughly follows that predicted by the Sverdrup relation (Figure 5.2), whilst west of 40°W, the cumulated transport commonly exceeds the Sverdrup transport by up to 15 Sv. The exception is in 2007, when the total cumulated geostrophic estimate is close to that predicted by the Sverdrup equation. The result in the eastern basin is different to that reached by McDonagh et al. (2010), who found that the cumulated transport was generally *less* than that reached by the Sverdrup equation. The reason for this discrepancy is the lack of Argo data very close to the eastern boundary, which means our analysis may have missed the northward flow in all layers east of 10°W observed in the 2005 cruise section. This flow was found to be largest in magnitude in the MW layer, implying that this flow is not caused by Sverdrup dynamics.

The analysis was also repeated to *include* the reference velocity at 1000 dbar, as derived in Section 3.3. When this barotopic component is included, the discrepancy between the Sverdrup and interior transport in the western basin increases, with total interior transports of between 28 and 56 Sv. Examining the mean transport per unit depth profile from this realisation (Figure 5.3) reveals that velocities at 1000 dbar are weakly southward in both basins. Above 800 m, the transport is stronger in the western basin, with greater vertical shear than east of the Mid-Atlantic Ridge. The contribution of the reference velocity is examined at greater length in Section 5.3.4.

The explanation for the east-to-west cumulated interior transport exceeding the value predicted by the Sverdrup relation is most likely related to Gulf Stream recirculation, in particular the Worthington gyre. (Worthington, 1976). This feature, found south of the Gulf Stream and north of Bermuda, is estimated to recirculate up to 100 Sv of the full-depth Gulf Stream transport. Using Worthington's diagrams, approximately 28 Sv is recirculated above $\theta = 7$°C, the closest isotherm to $\sigma_\theta = 27.38$. Adding this component to the mean Sverdrup minus Ekman flow (12 to 22 Sv) yields a transport range of 40 to 50 Sv that is much closer to that directly observed by the optimal interpolation including the reference velocity component. It is thus likely that both the wind-driven transport *and* the recirculation contribute to the size of the interior flow.

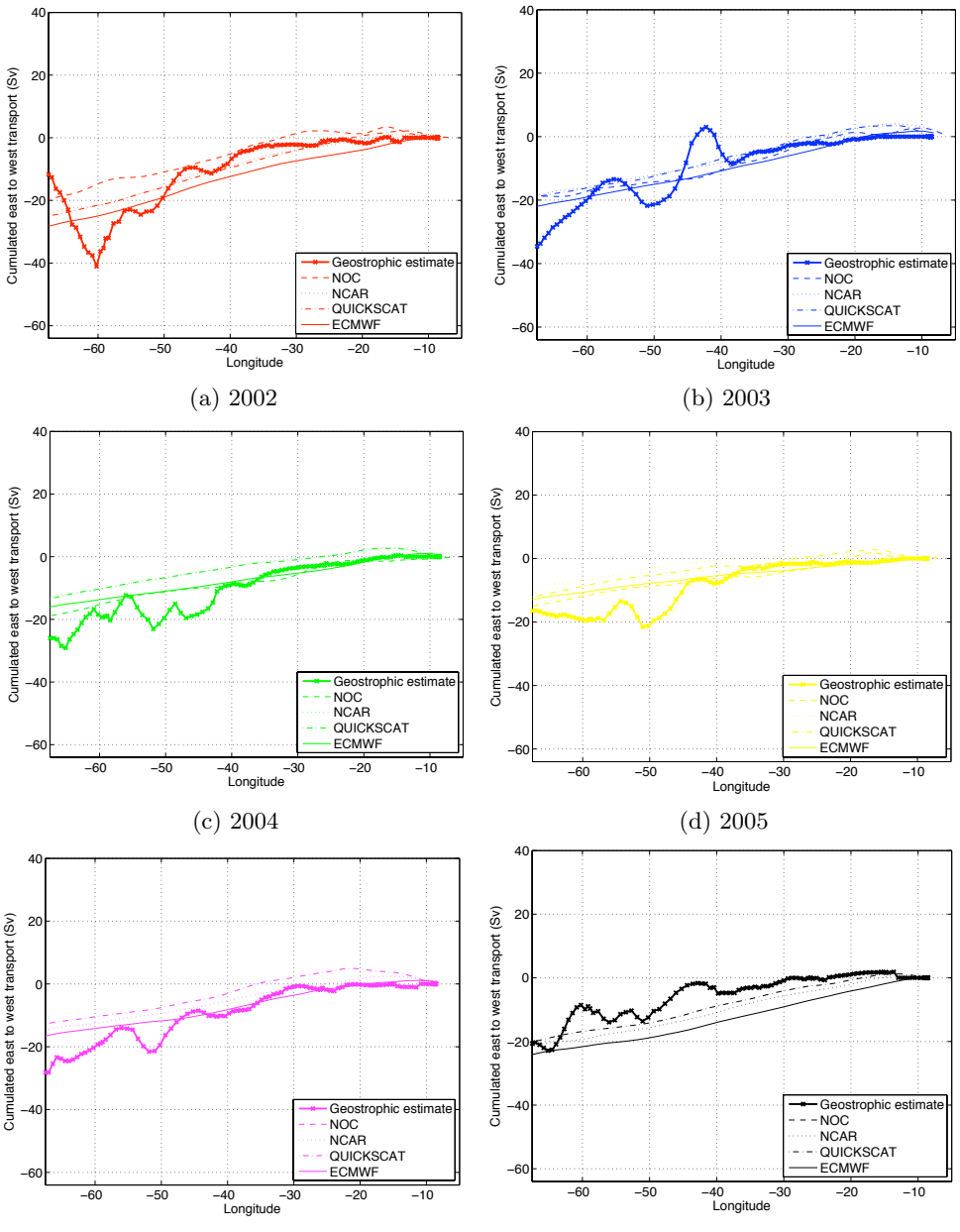

(a) 2002 (b) 2003

(c) 2004 (d) 2005

(e) 2006 (f) 2007

Figure 5.1: East to west cumulated geostrophic transport above $\sigma_\theta = 27.38$ from the optimal interpolation, compared with the east to west cumulated Sverdrup minus Ekman transport from each wind stress product. A zero velocity is assumed at $\sigma_\theta = 27.38$.

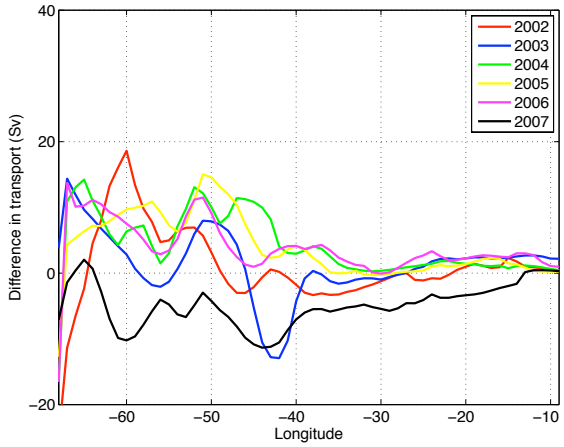

Figure 5.2: Difference between east to west cumulated geostrophic transport above σ_θ = 27.38 from the optimal interpolation and the east to west cumulated Sverdrup minus Ekman transport from each wind stress product. Whilst values are generally close to zero east of 40°W, the geostrophic transport above σ_θ = 27.38 is generally larger than that predicted by the Sverdrup relation west of the Mid-Atlantic Ridge.

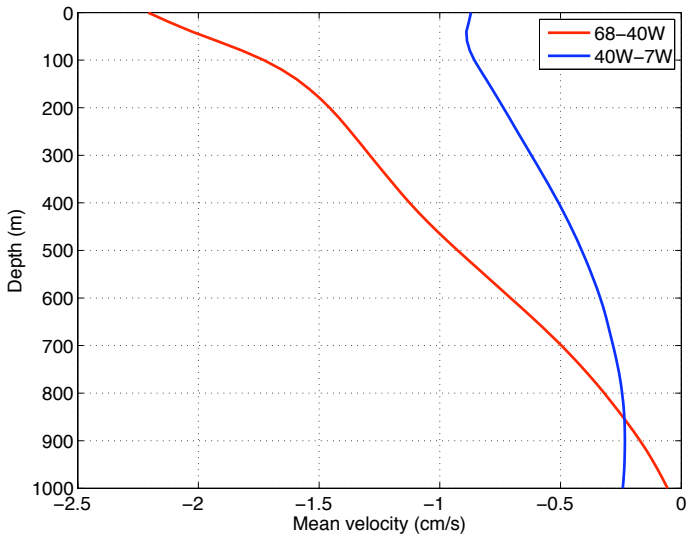

Figure 5.3: Mean interior geostrophic velocity between the surface and 1000 m for the western basin (in red) and the eastern basin (in blue) for the period 2002 to 2007, including the reference velocity at 1000 dbar. Whilst both velocity profiles decay with depth, neither become very close to zero at 1000 m suggesting the Sverdrup relation alone does not set the mean size of the interior flow.

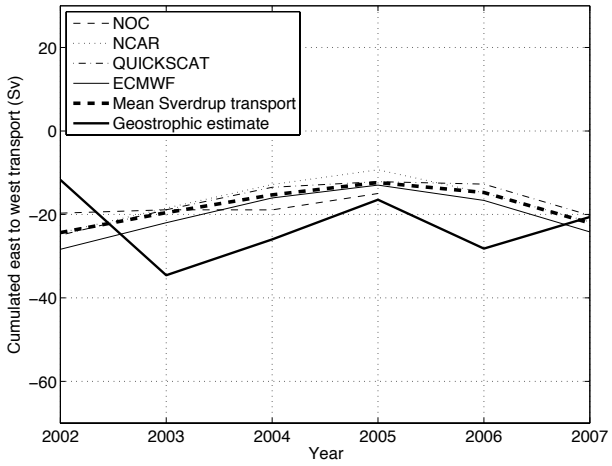

Figure 5.4: Comparison of the southward east-to-west cumulated geostrophic transport ($\sigma_\theta < 27.38$) at 36°N from the OI and the east-to-west cumulated Sverdrup minus Ekman transport from four wind stress products for the years 2002 to 2007. The westward limit of integration is 67.6°W and a zero velocity is assumed at $\sigma_\theta = 27.38$. A mean of the four Sverdrup minus Ekman transport estimates is also plotted and regression statistics between this estimate and the geostrophic transport are provided in Table 5.1. Note that no NOC estimate is available after 2005.

5.2.2 Interannual and Seasonal Variability

Although the Sverdrup relation does not explain the total cumulated transport of the interior, it remains possible that wind stress curl variability controls the interannual and seasonal variability in the transport. To assess this second hypothesis, Figure 5.4 shows the southward transport cumulated to 67.6°W (immediately offshore of the Gulf Stream) above $\sigma_\theta = 27.38$ (zero velocity at this level) with the Sverdrup transport, cumulated westwards to the same position, shown for each wind stress product. Visual inspection of Figure 5.4 disappointingly shows no correlation between the Sverdrup minus Ekman transport and the interior transport. Very similar results are observed using 1000 dbar as the lower integration limit. The relationship was tested for statistical significance by a regression analysis and F test. The results using both the transport above $\sigma_\theta = 27.38$ and above 1000 dbar are given in Table 5.1, but in both cases no statistically significant relationships were established at the 5% level. Therefore, on an interannual basis, it does not appear that the curl of the wind stress is the controlling influence on the strength of the interior transport.

When the geostrophic and Sverdrup transports are examined on a season-by-season basis (Figure 5.5 and Table 5.2), once again no statistically significant correlation is observed. Whilst the interior geostrophic flow reaches a southward maximum in spring, the Sverdrup minus Ekman flow generally peaks in winter. The exception to this rule is the NOC Climatology, which does show the zonally integrated Sverdrup transport reaching a southward maximum during spring. Furthermore, the size of the annual cycle in Sverdrup transport is much smaller than that for the geostrophic transport. The annual range of Sverdrup transports (from the mean of the four products) is 4.6 Sv. In contrast, the range of geostrophic

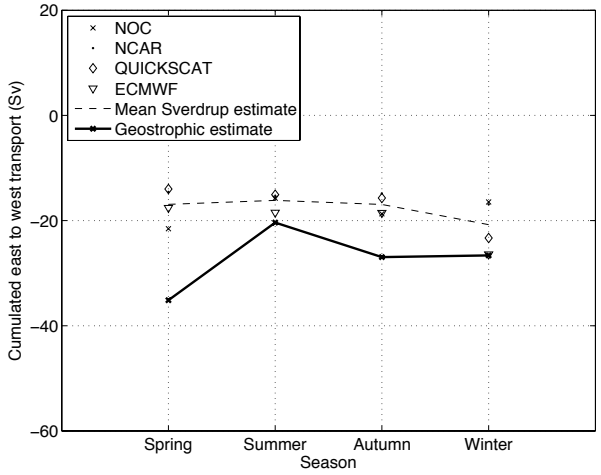

Figure 5.5: As Figure 5.4, but for the four seasons (data taken from the period 2001 to 2007).

Range of geostrophic transport integration	**Correlation coefficient**	**Regression coefficients (a and b)**	**R^2 value**	**F statistic**	**p value**
$\sigma_\theta < 27.38$	-0.264	$-0.470/-31.42$	0.070	0.300	0.613
$0-1000$ dbar	-0.294	$-0.637/-39.35$	0.086	0.377	0.572

Table 5.1: Linear regression statistics for the regression of zonally integrated Sverdrup minus Ekman transport (mean of four wind stress products) on zonally integrated interior transport from the OI (assuming zero velocity at $\sigma_\theta = 27.38$ or 1000 dbar). The relationship expressed by the regression coefficients is: Geostrophic transport (in Sv) $= a\times$ (Sverdrup minus Ekman) $+b$. Six years of data are used (2002 to 2007), giving 5 degrees of freedom.

Range of geostrophic transport integration	**Correlation coefficient**	**Regression coefficients (a and b)**	**R^2 value**	**F statistic**	**p value**
$\sigma_\theta < 27.38$	0.0728	$0.212/-23.52$	0.0053	0.0107	0.9272
$0-1000$ dbar	0.0616	$0.192/-29.47$	0.0038	0.0076	0.9384

Table 5.2: Linear regression statistics for the regression of zonally integrated Sverdrup minus Ekman transport (mean of four wind stress products) on zonally integrated interior transport from the OI (assuming zero velocity at $\sigma_\theta = 27.38$ or 1000 dbar). The relationship expressed by the regression coefficients is: Geostrophic transport (in Sv) $= a\times$ (Sverdrup minus Ekman) $+b$. The data are divided by season (including data from the years 2001 to 2007), giving 3 degrees of freedom.

estimates is 16.8 Sv.

The Gulf Stream recirculation in the western basin has already been discussed and, as a result, it is perhaps unsurprising that wind stress variations from year-to-year and season-to-season are not the only control on the zonally integrated transport. However, given that Sverdrup balance holds reasonably well in the region east of 40°W, one might expect the variability here to be largely wind stress controlled. To test this assertion, the analysis was repeated for the eastern basin only (excluding the barotropic reference velocity). The results for each individual year are given in Figure 5.6a, but again no positive correlation between the Sverdrup minus Ekman transport and the geostrophic transport is observed on an interannual basis. Indeed, the correlation coefficient (-0.687) suggests a negative correlation, although the very small number of degrees of freedom means that this is not significant at the 5% level (p-value = 0.056). Repeating the analysis for the individual seasons (Figure 5.6b) *does* yield a positive correlation coefficient (0.914). Moreover, the first linear regression coefficient of the relationship is close to one (1.163), suggesting there is a simple one-to-one relationship between the seasonal Sverdrup transport and the geostrophic transport in the eastern basin. However, the number of degrees of freedom (3) once again means that this relationship is not significant at the 5% level (p-value = 0.086). As already emphasised, the analysis is inhibited to some extent by the lack of Argo floats close to the eastern boundary, meaning that the narrow band of northward velocities observed in the 2005 cruise section east of 10°W would be missed by our analysis if the feature was permanent. This narrow current is not thought to be in Sverdrup balance, meaning that its inclusion might weaken the correlation observed in Figure 5.6b.

A complex picture thus emerges from this analysis. Whilst the seasonal Sverdrup minus Ekman and geostrophic flows are *not* correlated when cumulated across the entire basin (Table 5.2), there may be a weak correlation on a seasonal basis in the region east of 40°W. In Chapter 4, it was found the annual cycle of wind stress curl was the strongest mode of variability, with a maximum in January and a minimum in summer; it is hence unsurprising that the seasonal cycle is well-reproduced in the eastern basin where the balance appears to approximate most closely the total transport. Interestingly, the spectral analysis suggested that the annual cycle of WSC was larger in the western basin than in the eastern basin (Figures 4.17 and 4.18), yet no correlation between Sverdrup transport and the geostrophic transport is found in this region. However, given the probable role of Gulf Stream recirculation in setting the size of the transport field of the western basin, the lack of correlation in this region should perhaps be expected. Relatively weak variability in wind stress curl at periods greater than 12 months is likely to account for the lack of correlation between the Sverdrup and geostrophic transports on interannual and longer timescales. For instance, the first EOF of the 12-month low pass filtered WSC only accounted for between 12 and 46% of the variance (Table 4.14).

In conclusion, the Sverdrup minus Ekman transport alone is not sufficient to explain either the mean size of the interior transport above $\sigma_\theta = 27.38$ or the variability in its magnitude

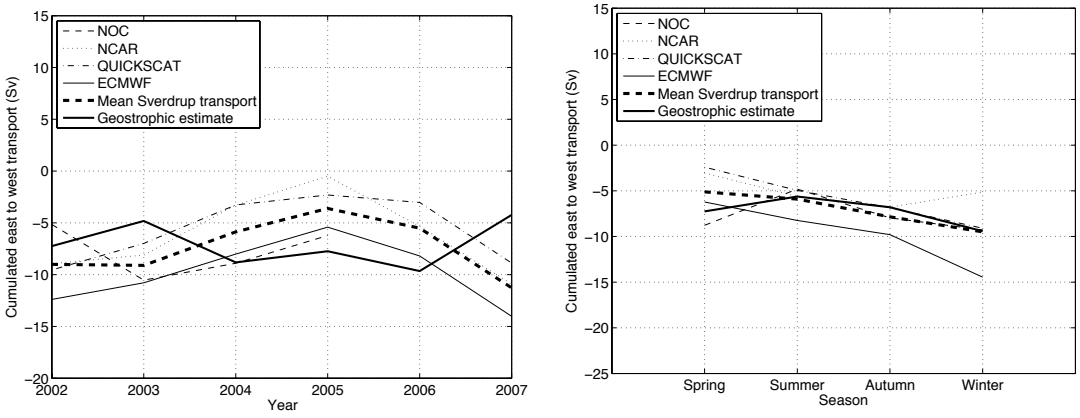

(a) Annual estimates (b) Seasonal estimates

Figure 5.6: Comparison of the east-to-west cumulated geostrophic transport east of 40°W from the OI and the east-to-west cumulated Sverdrup minus Ekman transport from four wind stress products for (a) the years 2002 to 2007 and (b) the four seasons. Integration of the Sverdrup minus Ekman transport is to 40°W. A mean of the four Sverdrup minus Ekman transport estimates is also plotted.

from year-to-year. However, it does successfully predict the mean size of the baroclinic transport in the region east of 40°W and there is a weak correlation between the seasonal estimates of Sverdrup minus Ekman transport and geostrophic transport in this region. Given the discrepancies towards the western end of the section (Figure 5.2), it is likely that variability in the size of the recirculation plays a crucial role in controlling the magnitude of the interior flow.

5.2.3 Other Wind Stress Effects

Despite the general lack of correlation between the *zonally integrated* Sverdrup minus Ekman transport and the interior gyre transport at annual timescales, wind stress curl has other more localised effects that can affect water mass characteristics. Of principal importance is the effect of WSC on Ekman pumping. As outlined in Section 4.2.2, 36°N lies just to the north of the region of maximum Ekman convergence caused by the opposing signs of the Ekman transport north and south of 31°N (Figure 4.2). This convergence causes subduction of light surface water masses, causing isopycnals to heave downwards and an accompanying increase in dynamic height. When wind stress curl is enhanced at 36°N, downward Ekman velocities increase causing an intensification of pumping; when the curl weakens the velocities decrease and the positive dynamic height anomaly reduces in magnitude. These processes need not affect the entire basin simultaneously, but can cause local temperature and salinity anomalies that affect the total size of the zonally integrated interior transport. This is particularly important when regions at each end of the section are affected, as the zonal gradient in dynamic height can alter, causing a change in the zonally integrated baroclinic transport.

Evidence of Ekman pumping altering the properties and/or transport of the subtropical

North Atlantic is found in several previous studies. It was already discussed in Section 1.8 that Leadbetter et al. (2007) found evidence of increased (decreased) Ekman downwelling at times of positive (negative) NAO, causing a warming of the upper 800 m of the ocean, particularly in the western basin. Our NAO results (Figure 4.45) support this observation, with the stronger southward Sverdrup transport during periods of positive NAO driving an increased Ekman downwelling at the western end of the section. However, in order to test the importance of this process in driving interior transport changes on interannual timescales, the vertical velocities associated with positive and negative phases of the NAO should be quantified. This would be achievable within an ocean model such as OCCAM where u, v and w are defined at every gridpoint.

In addition to direct forcing of the thermocline by wind stress curl variability, several studies have highlighted the potential for Ekman downwelling to trigger westward propagating first baroclinic mode Rossby waves. At decadal timescales, Sturges and Hong (1995) found that open ocean wind stress curl close to 36°N in an ocean model led to Rossby wave speeds of around 2 cms^{-1} and cause sea level variability of up to 10 cm. Furthermore, DiNezio et al. (2009) found that 3-year low pass filtered Florida Straits transport was correlated with WSC variability near the eastern boundary, triggering Rossby waves that propagated westward across the basin at speeds over double those of the theoretical Rossby wave relationship. Kanzow et al. (2010) also provides evidence that annual wind stress curl variability close to the Canary Islands causes a springtime maximum and autumn minimum in Ekman downwelling in that region, which could explain the 2.2 Sv annual cycle in the mid-ocean transport with a maximum in spring and minimum in autumn.

The contribution of Rossby waves to both interior and Gulf Stream transport variability at 36°N is analysed in more detail in Section 5.6. However, this study does not specifically examine the role of Ekman pumping in driving interannual changes in the geostrophic transport outlined in Chapter 3. It is possible that the decrease in the temperature of much of the western basin between 2003 and 2005 was driven by decreased Ekman pumping close to the western end of the section in response to the reduced southward wind stress curl in this period (Figure 5.4). However, until the western basin WSC forcing and the accompanying Ekman convergence has been quantified, the source of interannual T/S changes within the basin remains highly speculative.

5.3 Errors in the Interior Transport Estimates

In order to test the robustness of the interannual and seasonal estimates of interior transport, a comprehensive analysis of errors was required. Two major sources of error were identified. The first originates from the temperature and salinity mapping error of the OI, discussed in detail in Section 3.1. A mapping error variance is produced by the OI representing the uncertainty in the temperature and salinity estimate resulting from the data-grid and data-data covariance (Figures 3.5 and 3.6). How this translates into a geostrophic shear

uncertainty is outlined in Section 5.3.1. The second error is the uncertainty in the background reference velocity derived from the Argo and Line W velocities, which is discussed at length in Section 5.3.4. Given that only carefully checked delayed mode temperature and salinity profiles were used, the uncertainties resulting from instrument error are generally small (0.01°C for temperature and 0.01°C for salinity), which are an order of magnitude smaller than the mapping errors found in Figures 3.5 and 3.6.

5.3.1 Geostrophic Shear Errors

The following method was used as a way of obtaining an upper bound on the possible errors of interior transport shear. Error variances (σ^2) in Figures 3.5, 3.6, 3.20 and 3.21 were converted into error deviations (σ) (by taking the square root) and then used to estimate a maximum and minimum possible dynamic height at the surface relative to 1000 dbar. The dynamic height anomaly at any point results from the squared sums of the temperature and salinity contributions:

$$D' = \sqrt{D'^2_T + D'^2_S} \tag{5.1}$$

where D' is the dynamic height anomaly, D'_T is the dynamic height anomaly resulting from the temperature error and D'_S is the dynamic height anomaly resulting from the salinity error. Using the maximum temperature and minimum salinity yields the potential positive dynamic height anomaly, whilst the minimum temperature and maximum salinity yields the potential negative dynamic height anomaly. For the moment, errors in T and S are assumed to be perfectly anticorrelated to yield an upper bound on the dynamic height error; this is shown in subsequent sections to be a pessimistic assumption, with many of the T/S errors being correlated and density compensated.

Two mapping points at either end of the interior transport section were then selected. At the eastern boundary, the mapping point at 13.4°W was chosen as it is the first point having data to as deep as 1000 dbar in all years. At the western end of the section, the longitude of 67.6°W was chosen, this being the point at which the zonal 12°C isotherm gradient becomes negative (the criterion used in Section 3.4 to define the western limit of the interior flow). Using the maximum and minimum dynamic heights at these two points, the maximum and minimum geostrophic shear between these points was calculated, assuming a level of no motion at 1000 dbar. The range of possible transports resulting only from the θ/S uncertainty at the western end of the section was also calculated.

The results for each year and season are given in Figure 5.7. In each case, the total error in the interior transport is very large, with a 90 Sv range in 2002 and a 70 Sv range in 2007. The errors at the western end of the section only yield an error of 35 Sv in 2002 and 20 Sv in 2007. Total errors for the seasonal results are smaller (a range of around 55 Sv in each season) because the mapping errors for temperature and salinity are smaller

as there are more contributing data points (Figures 3.20 and 3.21). Whilst these errors do appear huge, seemingly casting doubt on our entire methodology for estimating the interior transport, these errors are an *absolute upper bound* on the total error and do not reflect the *likely* magnitude as the T and S errors are in reality well-correlated. It is unfeasible that the entire water column between the surface and 1000 dbar would be biased both cold and salty or warm and fresh by the maximum error deviation. Such a situation would require the errors to be perfectly correlated over the entire depth and would produce an unrealistic temperature and salinity structure different to anything actually observed on the 36°N section. The minimum interior circulation estimate in almost all years is in fact northward, clearly an unrealistic situation given our knowledge of the circulation of the subtropical North Atlantic.

Given that this method can only give us an upper bound to the mapping uncertainty, an alternative approach was adopted to achieve a more likely estimate of the size of the interior transport error, outlined below.

Error Estimate from Cruise Data

The geostrophic shear error estimate involved using the Argo data collected during the period of the 2005 cruise occupation to estimate the temperature and salinity along the section, as outlined in Section 3.1.1 (the ±0 month case). For this realisation of the OI, we have two independent estimates of error in the interpolation:

1. The OI yields mapping error estimates for both temperature and salinity. These were converted to error deviations by taking the square root of the error variances.

2. A second estimate of error is the difference between the CD171 cruise section and the interpolated temperature and salinity fields. Given the zonal length scale of the interpolation (350 km) and the station spacing (typically between 50 and 70 km), it was decided to compare the interpolated fields with a 5 point moving average of the cruise data, as we do not expect the OI to resolve small-scale eddy variability at scales shorter than the decorrelation length scale.

The vertically averaged magnitude of the potential temperature OI deviation and the vertically averaged difference between the OI potential temperature and the 5-point moving average cruise potential temperature are both shown in Figure 5.8. Over most of the basin, the OI mapping error (1) exceeds the size of the error independently obtained from the cruise estimate (2), suggesting the actual error in geostrophic shear is likely to be much smaller than suggested by Figure 5.7. Only in the Gulf Stream region, west of 68°W, do the mapping errors underestimate the actual error in potential temperature, most likely because the OI fails to capture the highly complex temperature structure in this region.

The vertical structure of the difference between the two lines in Figure 5.8 is given in Figure 5.9. This plot emphasises that the interpolation error is much larger than the 'actual'

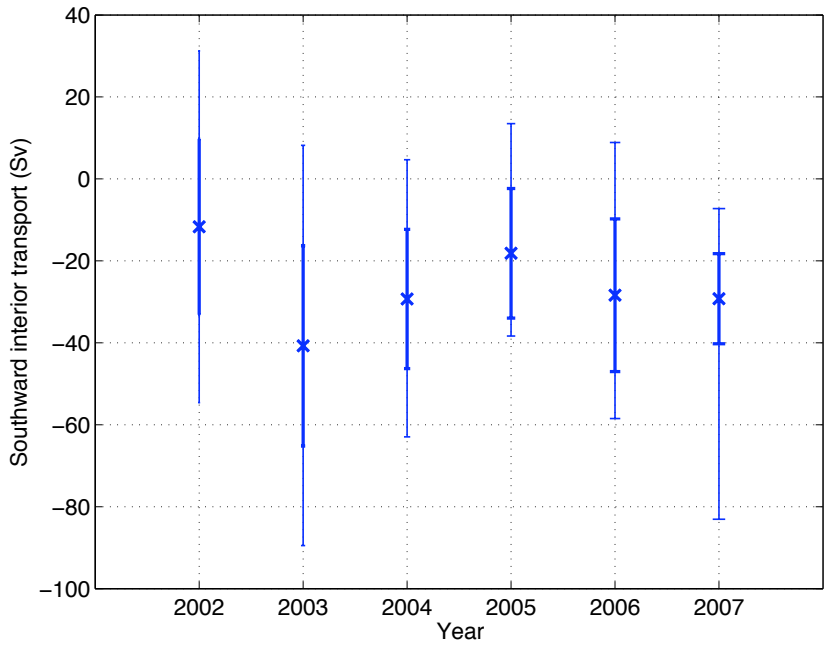

(a) Annual Interior Transport Estimates

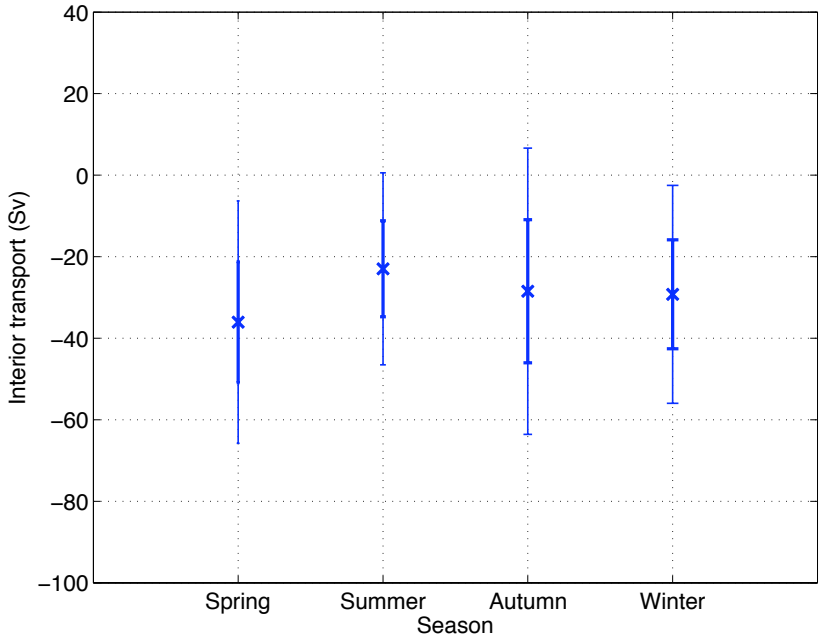

(b) Seasonal Interior Transport Estimates

Figure 5.7: Interior transport above 1000 dbar relative to a level of no motion at 1000 dbar. The bold error bars show the range of possible interior transports given the temperature and salinity mapping errors at 67.6°W, whilst the feint error bars show the total range of interior transports given the errors at both ends of the section.

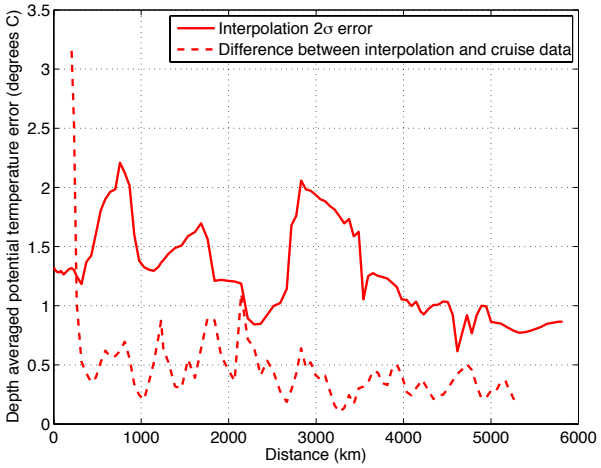

Figure 5.8: The vertically averaged potential temperature difference in the top 1000 dbar between the ±0 month optimal interpolation of the Argo data and the 5 point moving average CD171 cruise data (dashed line), along with the 2σ potential temperature error diagnosed by the OI (solid line).

	Total interior transport (Sv)
Cruise estimate	−36.6
5 point m.a. cruise estimate	−35.1
±0 month Argo interpolation	−33.4

Table 5.3: Three estimates of total east-to-west interior transport above 1000 dbar, assuming a level of no motion at that level. The difference between the transport estimate for the 5 point moving average cruise data and the Argo estimate is only 1.7 Sv.

error in most of the top 1000 dbar, especially in the western basin where the majority of the transport variability arises. Similar analyses were performed for salinity (Figure not shown). In this case, the mapping error exceeded the 'actual' error by at least four times across the entire basin away from the Gulf Stream. Given these results, the interior transport error is likely to be much smaller that that suggested in Figure 5.7. In order to test the assertion, it was decided to estimate the total east-to-west accumulated transport above 1000 dbar from both the cruise data and the ±0 month interpolation (Figure 5.10). It is shown that, in spite of the temperature errors, the difference in accumulated transport between the Argo interpolation and the cruise data is relatively small (1.7 Sv). Indeed, integrating from the eastern boundary to 67.6°W (the point used previously for interior transport calculations), the total transport varies very little (Table 5.3). The large difference in accumulated transport in the Gulf Stream occurs because of insufficient data in this region in the relatively short time window of 1st May to 15th June 2005.

In view of the results in Table 5.3 and 5.10, it is clear that despite very large errors in the geostrophic shear being possible, the real magnitude of the error in the geostrophic shear estimate caused by mapping errors is small. This occurs for two reasons. Firstly, very large errors would require a high degree of depth correlation in the θ or S errors (e.g. the entire water column between the surface and 1000 dbar is too warm, or too salty). To investigate

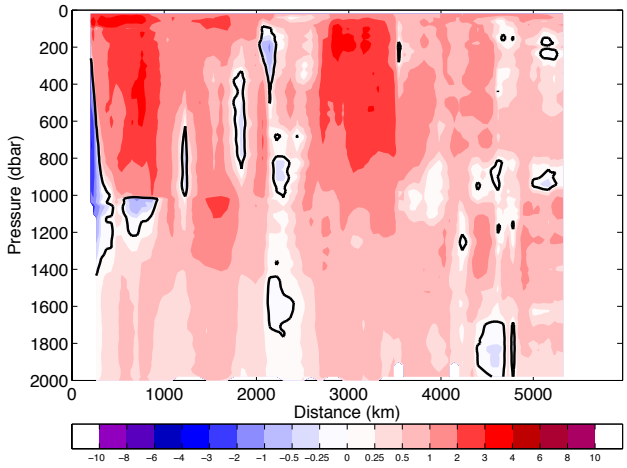

Figure 5.9: The difference between the OI 2σ mapping potential temperature error for the ± 0 month case and the 'actual' error of the OI (the absolute difference between the OI and the 5 point moving average CD171 potential temperature).

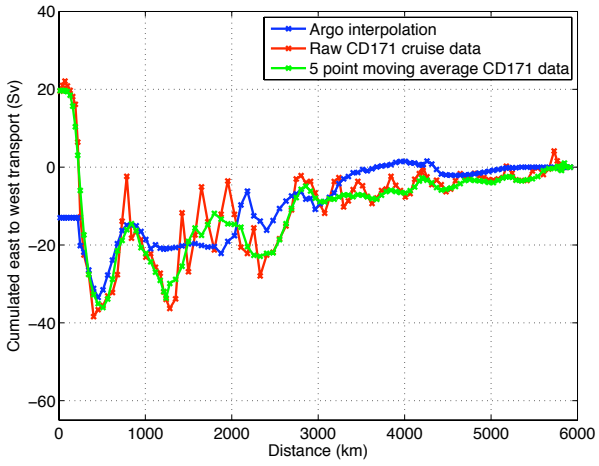

Figure 5.10: East to west cumulated geostrophic transport above 1000 dbar, assuming a level of no motion at that pressure horizon. The three estimates are from the ± 0 month Argo float interpolation (in blue), the CD171 cruise data (in red) and a five-point moving average of the cruise data (in green).

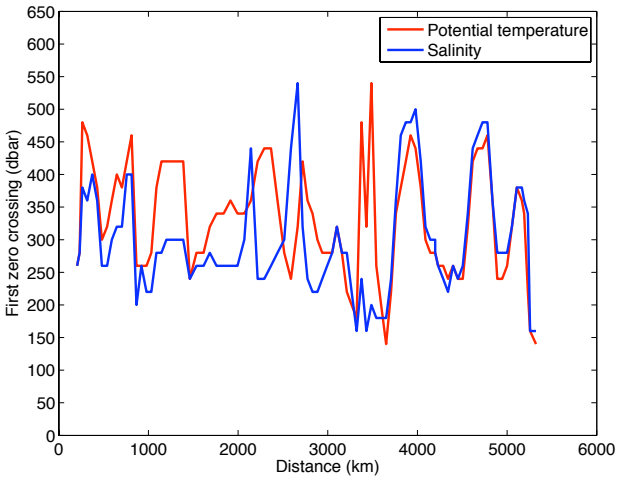

Figure 5.11: Vertical decorrelation length scales from the difference between the ±0 month OI realisation and the 5-point moving average cruise data. Results are plotted for both potential temperature and salinity by distance from the westernmost station (in km).

the extent of depth correlation in the errors, a spatial autocorrelation of the difference between the OI and the 5 point moving average cruise data (Figure 3.13a) was performed for both potential temperature (Figure 5.9) and salinity. The extent of autocorrelation of θ or S in depth was determined by the first zero crossing of the ACF at each mapping point. The longitudinal distribution of these vertical scales is presented in Figure 5.11. The mean decorrelation depth scale was only 330 dbar for potential temperature and 300 dbar for salinity, though significant longitudinal variation was found in these values. Scales as short as 150 dbar are found in the eastern basin close to 30°W, whilst values of over 500 dbar are found just to the west of the Mid-Atlantic Ridge. Fortunately, at both ends of the interior transport section, the errors have a relatively short decorrelation length scale (270 dbar to 320 dbar at 67.6°W and 150 dbar by the eastern boundary). As a result, the entire water column between the surface and 1000 bar is not likely to be biased warm/cold or fresh/salty, helping to explain the small overall error in transport (1.7 Sv from Table 5.3). However, it is notable that in regions with longer length scales (e.g. close to 1200 km/ 58°W), there is a larger disagreement in the estimated transport from the Argo data compared with the cruise data (Figure 5.10), of up to 15 Sv.

The second reason for the errors being much smaller than Figure 5.7 would suggest is that the θ and S errors are strongly correlated, with positive potential temperature errors being associated with positive salinity errors and vice versa (see Figures 3.13a and 3.13c). As these changes have opposing effects on density, it may be that the errors at least partially compensate for one another, reducing the geostrophic shear error between the two ends of the section. The size of the correlation between the θ and S errors is shown in Figure 5.12; it exceeds 0.45 across the entire basin. Given this strong correlation, further consideration is given in Section 5.3.6 to direct mapping of density to eliminate the issue of compensating errors.

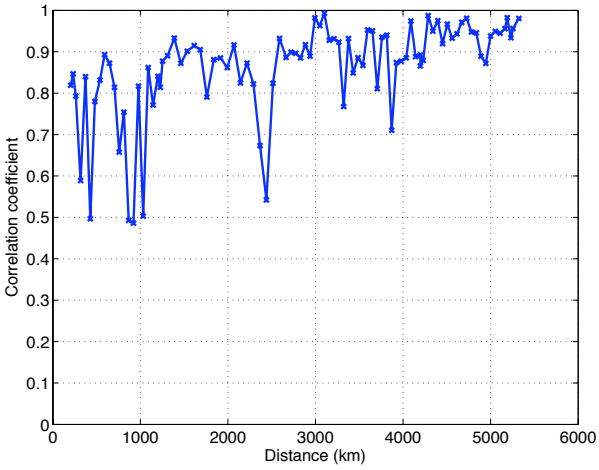

Figure 5.12: Correlation coefficient between cruise minus OI ±0 month potential temperature and cruise minus OI ±0 month salinity for the top 1000 dbar at each mapping point.

5.3.2 Size of Density Compensation

In order to investigate the compensating effect of potential temperature and salinity errors, the transport value for the ±0 month interpolation in Table 5.3 was recalculated using only the potential temperature error (Figure 3.13a) and assuming no salinity error. The compensatory nature of the relationship was analysed by evaluating the overall density change at each end of the section using the linearised equation of state:

$$\frac{\rho}{\rho_0} = 1 - \alpha dT + \beta dS \tag{5.2}$$

where α and β are the thermal expansion and haline contraction coefficients respectively, and dT and dS are the (correlated) T and S errors, provided by the difference between the ±0 month OI and the 5 point moving average cruise data. ρ_0 represents the reference density. For each 20 bar pressure level at each section of the section, rho/rho_{zero} was calculated. The combined effect of temperature and salinity changes was then converted into an equivalent temperature change only, using:

$$\alpha dT = \frac{1 - \frac{\rho}{\rho_0}}{\alpha} \tag{5.3}$$

At the western end of the section, including the effect of salinity changes reduced the depth-averaged temperature error from −0.16°C to −0.09°C, whilst at the eastern end of the section the effective error is reduced from 0.02°C to 0.01°C. The total cumulated transport using only the temperature error was 32.6 Sv, compared with 33.4 Sv when both T and S errors are included (Table 5.7). This suggests that the transport error would be around 40% larger (around 2.5 Sv) were it not for the compensating effect of T and S errors.

5.3.3 Geostrophic Shear Errors Summary

An independent estimate of geostrophic shear error has been made using the difference between the OI and cruise derived θ/S fields. This yields a 1.7 Sv cumulated transport error. Whilst the mapping error variance from the OI shows that much larger errors are possible, the strong density compensation between θ and S along with the short length scales of θ and S errors limits the size of the absolute transport uncertainty. The analysis suggests that larger errors are possible in the region between 40°W and 60°W (Figure 5.10) because of mesoscale eddies. However, by using an entire year's data for our OI estimates (Figures 3.3 and 3.4), much of this variability is likely to be removed.

5.3.4 Reference Velocity Errors

The second major source of error arises from uncertainty in the reference velocity field derived from the Argo float trajectories and Line W velocity measurements. Integrated across the interior part of the section (the eastern boundary to 67.6°W) and in the upper 1000 dbar of the water column, this barotropic contribution accounts for 15.6 Sv of the southward transport (Figure 3.36). An initial estimate of the size of the error in the background velocity is made by considering the standard error of the cross-track velocities in each of the boxes ($\sigma/\sqrt{n}$, where n is the number of trajectory measurements contributing to the velocity estimate at each point). The standard errors for both u and v velocities are plotted in Figure 5.13. Across all the interior of the basin, the zero u and v velocity falls within the standard error of our estimates. Moreover, there is reason to believe that the standard error actually underestimates the size of the possible error, as the standard error calculation assumes that each measurement of velocity is independent. In reality, a simple temporal decorrelation of all u and v velocities collected to form the estimate in Figure 3.35 suggests that u velocities with a temporal separation of less than 14 days and v velocities with a temporal separation of less than 10 days cannot be viewed as statistically independent. Such a conclusion accords with other work by Hadfield et al. (2007), who used a 10 day temporal decorrelation length scale.

If the maximum and minimum values of cross track velocities along the cruise track are used throughout the section (from the standard errors), a huge range of possible barotropic transports is observed, from 163 Sv southwards to 134 Sv northwards. However, as with the geostrophic shear, such huge uncertainties would require errors to be perfectly correlated in the x direction across the entire basin. Moreover, these errors would need to have a long temporal decorrelation (several years), which has already been shown to be unrealistic. The short spatial scales of u and v were confirmed by a simple autocorrelation analysis of the YoMaHa and Line W velocities in the period 2002 to 2008. All the u and v velocities from the boxes in Table 3.4 were considered. These velocities were linearly interpolated onto 0.25° of longitude grid points (roughly 25 km) along 36°N and detrended and demeaned. The spatial autocorrelation functions of both u and v velocities were then evaluated. For

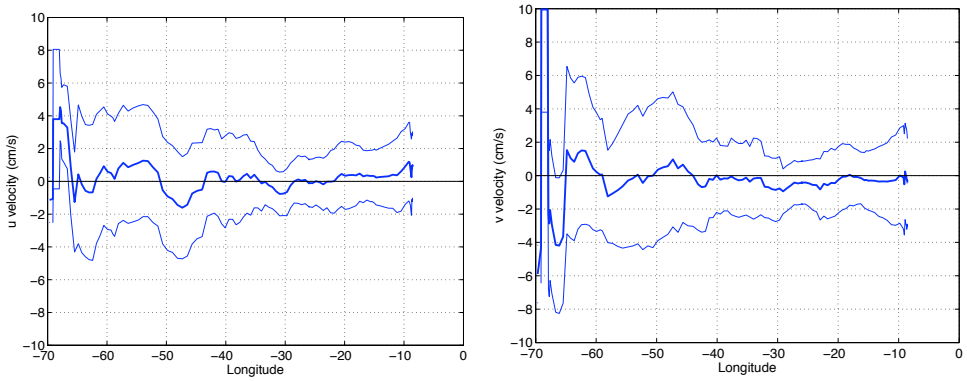

(a) u velocities (b) v velocities

Figure 5.13: Mean and standard errors of u and v velocities at 1000 dbar used in the transport estimates in Chapter 3.

the u velocity, a scale of 89 km was found, whilst the v velocity scale was 112 km. Given that the station spacing of the interior of the interpolated section is between 50 km and 70 km, the errors between every second station are effectively random, meaning that there would not be a systematic bias of the entire section's velocities.

Unfortunately, it is not possible to test the accuracy of the background velocity estimate by reference to a independent data set, as there were insufficient subsurface Argo trajectories collected during the period of cruise CD171 to compare with the lowered ADCP measurements. An alternative approach was instead adopted. For each mapping point across the section at which the reference velocity was estimated (Figure 3.36), the standard error at that point was identified. For each point, a random number was then generated from a normal distribution with mean zero and standard deviation of one, which was then used to scale the standard deviation. This scaled standard deviation was then applied at each point to create a different reference velocity field, with the resulting velocities being cumulated east to west as far as 67.6°W and throughout the top 1000 dbar. This process was repeated 10000 times in a Monte-Carlo type approach in order to estimate the range of possible barotropic transports. The resulting mean and standard deviation was -15.6 ± 17.1 Sv. We thus conclude that, in a strict statistical sense, the barotropic velocity field is not different from zero, though the field is unlikely to be northward. This result is a major limitation on the accuracy of our interior transport estimate and demonstrates that, even at the current Argo sampling density, the float displacement data cannot be used on their own to obtain a reliable barotropic transport estimate. Nevertheless, this result does not affect the year-to-year estimates of *variability* as these only reflect density-driven changes. Furthermore, because of the agreement between our interior transport estimate and those derived previously from cruise and Argo data (Hernandez-Guerra et al., 2010; McDonagh et al., 2010), we continue to include the barotropic component of -15.6 Sv in our interior transport estimate (though not when performing the comparison with the Sverdrup transport in Section 5.2).

5.3.5 Total Error Estimates

In light of the discussion in Sections 5.3.1 and 5.3.4, the total error in our seasonal and annual interior transport estimates is ±36 Sv (two standard errors from the mean). However, the vast majority of this error is in the barotropic component (±34 Sv), with the baroclinic variability correct to ±2 Sv.

The issue of sampling uncertainty has not been quantitatively examined. Specifically, one would like to know whether our 'annual' and 'seasonal' estimates of interior transport are good representations of the annual or seasonal mean, and to what extent they are temporally or spatially biased. Our OI scheme (Equation 2.4) did not include a temporal weighting term as it was unclear how this should be formulated (e.g. should more weight be given to measurements from one part of the year compared with another to compensate for the fact that there are a smaller number absolute measurements in that period?). A relatively even distribution of data was observed in Table 3.1 for each year for the basin as a whole, but the conclusion does not necessarily hold true for every longitude band. This is a potentially important limitation for a zonally integrated quantity such as volume transport, where the accumulated value is strongly dependent on the available data at either end of the section. It has already been noted that relatively few Argo profiles are found west of 50°W in 2002 (Section 3.1.1), meaning that the background climatology becomes increasingly important to the overall solution.

The final source of uncertainty comes from the choice of background climatology itself, as this can influence the solution, especially in regions where Argo data are lacking. To investigate the likely impact of the choice of climatology on the interior transport, the 2002 year was repeated using the WOA05 Annual Climatology, as it was in this year when Argo data were most sparse. The difference in the potential temperature and salinity fields is plotted in Figure 5.14. Overall, the difference in both fields is remarkably small, with the largest difference in temperature being only 0.3°C and in salinity only 0.03. In both cases, the differences are well within the combined mapping errors of the two realisations. The change in zonally integrated interior transport above 1000 dbar is only 0.1 Sv, meaning that our transport estimates are robust and this does not contribute a substantial term to the error budget.

A further improvement to the analysis would be to test other climatologies, such as the 0.5° WOCE Global Hydrographic Climatology which combines data from the World Ocean Database 1998 with WOCE data (Gouretski and Koltermann, 2004). To avoid the production of water masses with spurious T/S characteristics, data in this product are averaged onto potential density surfaces below the top 100 m, as opposed to the isobaric averaging using in the World Ocean Atlas. It would therefore be a useful exercise to compare the results using WOA to those using the isopycnally-averaged WOCE GHC.

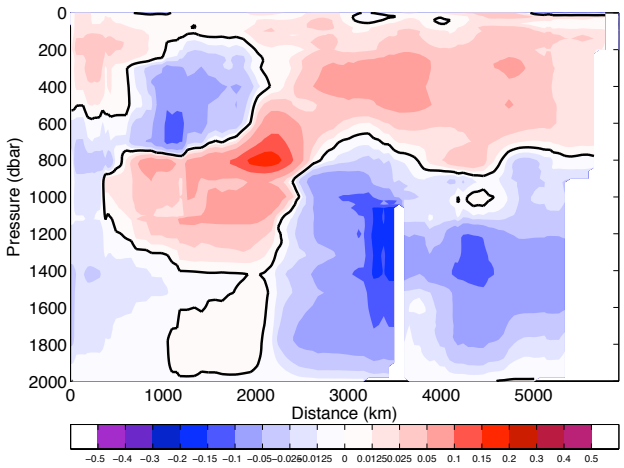

(a) Potential temperature difference between interpolation using WOA01 and WOA05 (WOA01 minus WOA05).

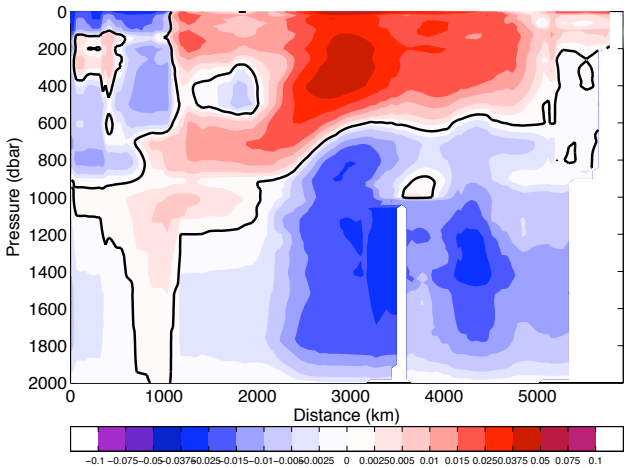

(b) Salinity difference between interpolation using WOA01 and WOA05 (WOA01 minus WOA05).

Figure 5.14: Difference in interpolated fields caused by using a different background climatology (WOA01 versus WOA05) for the year 2002. Note the colour bars on these plots are considerably reduced in range when compared with Figure 3.15.

5.3.6 An Alternative Approach

Given the strong correlation observed between the temperature and salinity errors, with the resulting density compensation, an alternative approach would be to map density directly. A similar OI method could be used, with density anomalies calculated from all Argo profiles relative to a background density calculated from World Ocean Atlas temperature, salinity and depth. This would have the advantage of reducing the error estimates considerably and avoids the problem of dealing with temperature/salinity covariances. Furthermore, it might also be expected that the decorrelation length scales of density on pressure surfaces would be longer than those for salinity or potential temperature, owing to the compensating effect of the T/S errors. A form of direct density mapping has been used successfully by Willis (2010) when estimating the MOC at 41°N that uses zonal scales of up to 891 km. Use of these larger scales would permit allow a higher temporal resolution to the time series to the interior transport estimates as the volume of available data for inclusion within the mapping scheme would be increased.

Whilst adopting this approach would therefore be advantageous for quantifying the transport field at 36°N, it does not allow us to separate the effects of temperature and salinity changes in the basin on the size and/or zonal structure of the interior transport (Section 3.1.2). Separate θ and S mapping would therefore continue to be an important supplement to density mapping to investigate the role of property changes in driving baroclinic transport variability.

5.4 Errors in the Gulf Stream Transport Time Series

Two main sources of uncertainty exist in the Gulf Stream transport time series. The first arises from the error of the regression relationships derived in Table 3.8. The RMS errors for the 0 to 1000 dbar, 0 to 2000 dbar and full depth Gulf Stream transport are 4.3 Sv, 11.4 Sv and 31.2 Sv respectively. The increasing error as the range of depth integration increases reflects the weakening of the regression relationship as transport changes at deeper levels are more baroclinic in nature and not manifested in SSH differences (Table 3.8).

Given the instrumental error in the JASON altimeter measurements, estimated as 3.9 cm (`http://topex-www.jpl.nasa.gov/mission/jason-1.html`), it was decided to assess the magnitude of the total error in Gulf Stream transport in the top 2000 dbar. This was carried out by adding or subtracting 7.8 cm (2×3.9) from the observed SSH difference for each altimeter pass, and then recalculating the Gulf Stream transport using the same regression relationship but the modified SSH differences. The results, shown in Figure 5.15, show that the impact of altimeter errors is fairly small. Using the minimum possible SSH difference, the mean 0 to 2000 dbar Gulf Stream transport in the period 2002 to 2008 is 104.2 Sv, whilst using the maximum possible SSH difference yields a mean transport of 111.6 Sv. The total Gulf Stream transport in the upper 2000 db is thus 107.9 ± 3.7 Sv.

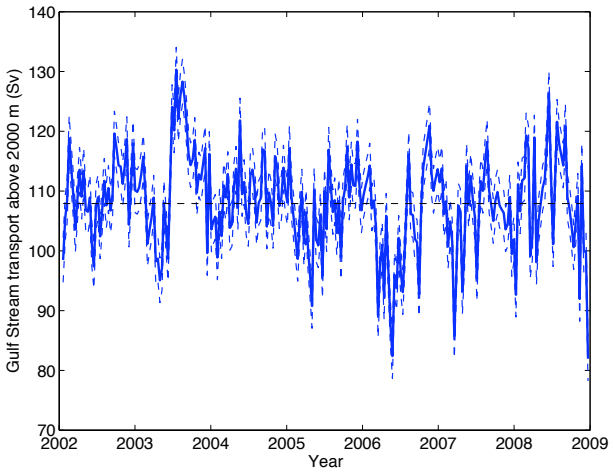

Figure 5.15: Gulf Stream transport in the upper 2000 dbar inferred from sea surface height differences from the JASON altimeter. The upper and lower values (blue dashed lines) represent the range of transport values that result from instrumental error in the altimeter.

Using the same instrumental error values, the size of the error bars for transport in the upper 1000 dbar was 6 Sv. The larger error for transports in this depth range occurs as a result of its larger first linear regression coefficient (77.05 cf. 47.76), as documented in Table 3.8.

Combining both RMS and instrument errors, the total size of the Gulf Stream transport error in the top 1000 bar is therefore around 10.3 Sv, or 12% of the total mean transport.

5.5 Reconciling the Gulf Stream Transports and Sverdrup Balance

As already discussed in Section 5.1 with reference to the Florida Current (Anderson and Corry, 1985), the Sverdrup balance does not explain fluctuations in Gulf Stream transport over annual and subannual periods. This result is confirmed for the Line W Gulf Stream transport by Figure 5.16, which displays the correlation coefficient between the wind stress curl in the subtropical North Atlantic and the time series of 0 to 2000 dbar western boundary current transports from the altimeter. If the Sverdrup balance did compensate for the Gulf Stream on a month-by-month basis, one would expect a band of negative correlations extending across the interior of the Atlantic close to 38°N at zero lag. In reality, none of the wind stress curl products exhibit such a pattern. However, all products do show a statistically significant negative correlation in the region offshore of Line W. In the cases of NOC, NCEP/NCAR and ECMWF wind products, the negative correlation is centred close to 60°W, roughly 700 km to the east of the Gulf Stream, with correlations peaking at around −0.3. In contrast, the higher resolution QUICKSCAT product has three correlation centres near 65°W, 60°W and 50°W respectively (Figure 5.16d). Other features, such as the band of positive correlation towards the eastern and southern part of the domain are also

seen in all the products, but only the negative correlation centre near 60°W is consistently found to be statistically significant at the 5% level.

Further experimentation was carried out to determine the lagged correlations of the time series with wind stress curl across the basin (Figure 5.17). The strong negative correlation observed near 60°W at zero lag is also found at both 1 month and 2 month lags, though the centre of the correlation is further east, centred generally at 45 to 60°W. By 3 months, the region of statistically significant correlation has disappeared in all the products. By this time, the NCEP/NCAR, NOC and QUICKSCAT products all show a positive wind stress curl correlation in the western basin south of 36°N, though the exact geographical configuration does differ.

The strong negative correlation to the east and northeast of the Gulf Stream section at Line W is potentially an interesting result when considered alongside previous work from the Florida Straits. Here, a number of model studies have suggested that the annual cycle of Florida Straits transport, with its maximum in July and minimum in October, is forced by wind stress over varying topography to the north and east of the straits. Anderson and Corry (1985) argue that the seasonal variation in transport is related to the integral of $\mathrm{curl}_z(\tau/H)$ along f/H isolines. As these lines move offshore to the east of Cape Hatteras (Figure 5.18), one might expect that variability in wind stress to the east of Line W might influence the Gulf Stream transport there, as suggested by our analysis. Furthermore, Böning et al. (1991) identified wind stress curl over the western North Atlantic as the main forcing mechanism of Florida Current variability. Other studies have invoked a combination of both local wind stress forcing in the vicinity of the Straits and more remote along-isobath wind stress forcing to drive both annual and higher-frequency variability (Fanning et al., 1994; Greatbatch et al., 1995). Specifically, Greatbatch et al. (1995) found that wind forcing in the immediate vicinity of the straits set the phase of the annual cycle, but that remote forcing (to the north of 35°N) accounted for the size of the transport variations.

To explore the relationship further, the mean wind stress curl for each product from the latitude-longitude box 38 to 40°N, 65 to 60°N was calculated by month and compared with the monthly mean Gulf Stream transport at Line W (Figure 5.19). The negative wind stress curl from the four products accurately is in phase with the annual cycle of the Gulf Stream. Only the two reanalysis products accurately predict the Gulf Stream minimum during March, whilst three of the four products imply a maximum in transport during September (when the maximum is in reality during August).

5.5.1 How Realistic is the Correlation?

At this point, it is worth asking how realistic the correlation between local wind stress curl and Gulf Stream transport at Line W might be, especially given the significant annual cycle in both components (Sections 3.5.3 and 4.3.1). An inferred correlation between these two time series is not necessarily indicative of a causal relationship, so care must be exercised

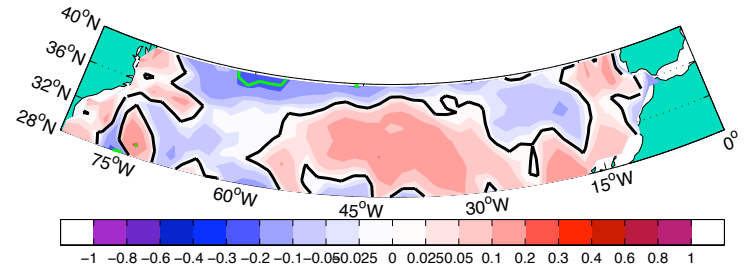

(a) ECMWF

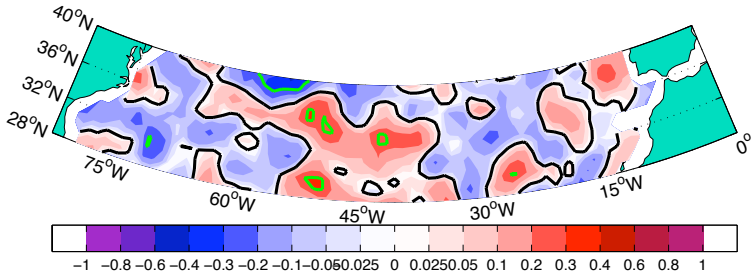

(b) NOC

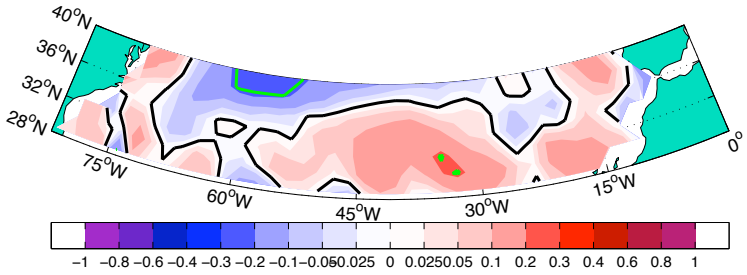

(c) NCEP/NCAR

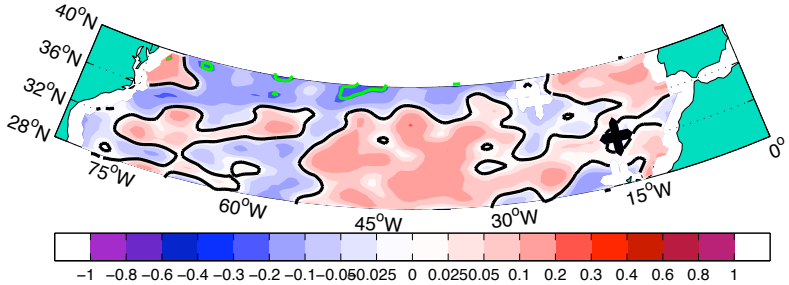

(d) QUICKSCAT

Figure 5.16: Correlation coefficient for the relationship between monthly local wind stress curl and monthly Gulf Stream transport inferred from the JASON altimeter at the Line W line. Four wind stress products are used and the period over which the relationship was calculated was 2002 to 2008, except for the NOC Climatology (2002 to 2005). The black contour is the zero line and the green contour displays the 5% significance line for rejecting the null hypothesis that the correlation coefficient is not significantly different from zero.The integral time scales for both the Gulf Stream transport and the WSC time series are less than 1 month across the basin, meaning that each observation can be treated as independent.

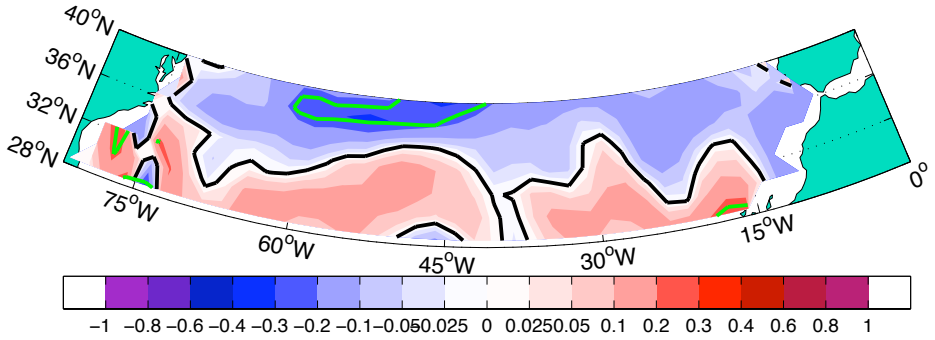

(a) 1 month

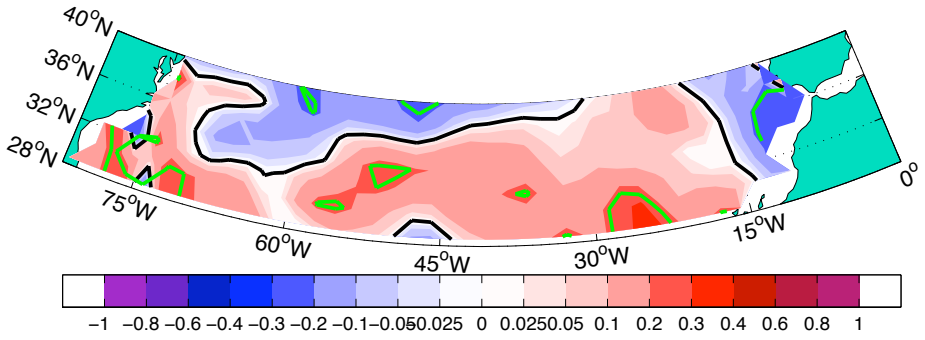

(b) 2 months

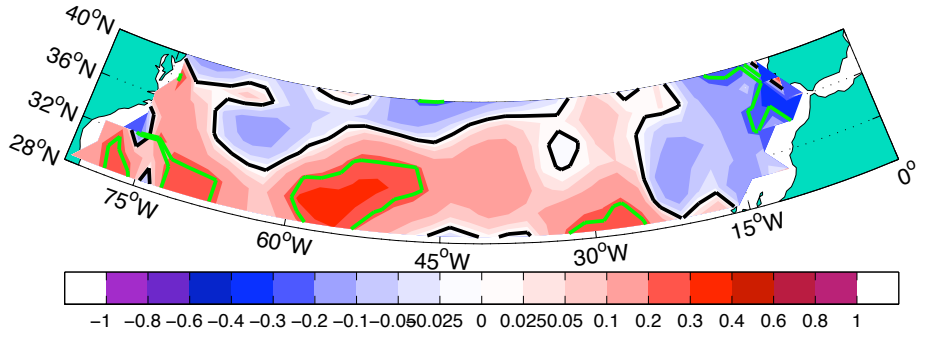

(c) 3 months

Figure 5.17: Correlation coefficients for the relationship between monthly wind stress curl and monthly Gulf Stream transport inferred from the JASON altimeter at the Line W line. The NCEP-NCAR Reanalysis is used for the wind stress curl, with differing time lags between 1 and 3 months. The black contour is the zero line and the green contour displays the 5% significance line for rejecting the null hypothesis that the correlation coefficient is not significantly different from zero.

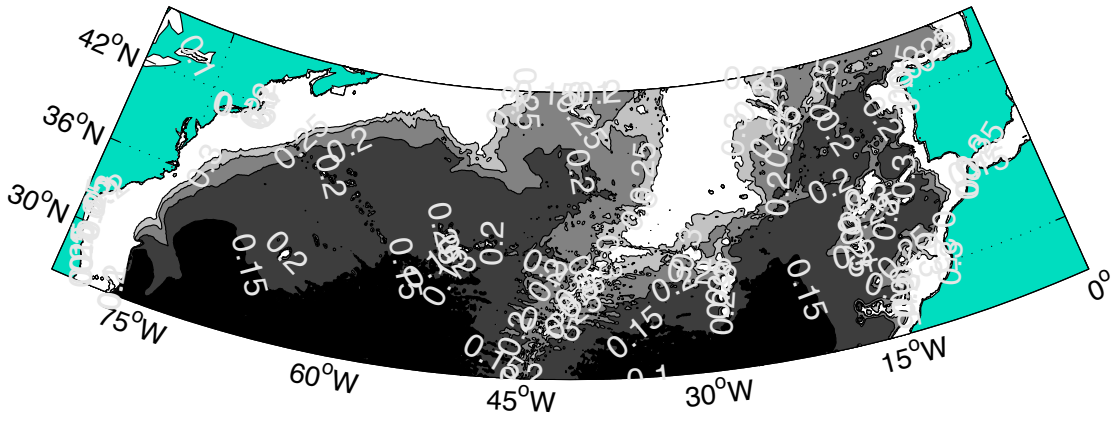

Figure 5.18: Map of f/H isolines in the subtropical North Atlantic, indicating that wind stress signals propagating along the topography would originate in the western basin to the east of Line W.

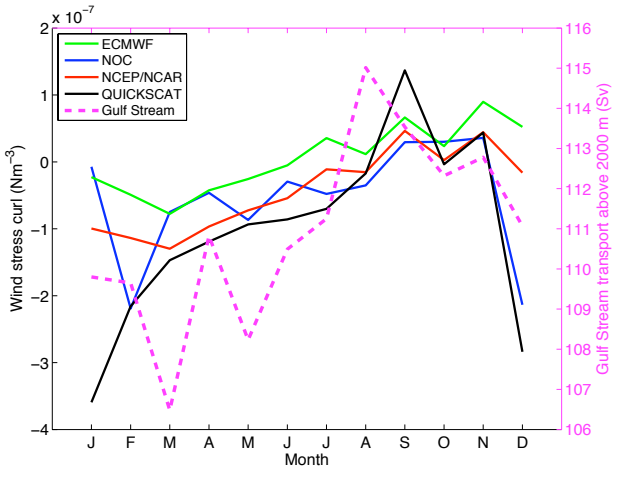

Figure 5.19: Mean Gulf Stream transport at Line W by month for the years 2002 to 2008, with the monthly mean negative wind stress curl in the box 38 to 40°N, 65 to 60°N overlaid. Note the monthly means for the NOC Climatology are for 2002 to 2005 only.

in the interpretation of Figures 5.16 and 5.17. Whilst the local nature of the correlation between wind stress curl and the Gulf Stream is suggestive of a relationship (Figure 5.19), especially given the lack of correlation elsewhere in the basin, an alternative approach is required if causation is to be established. Two alternative strategies are proposed.

Using the observational method, one could remove the mean annual cycle from each time series and correlate the residuals, thus deducing whether months with particularly strong (or weak) wind stress curl in the vicinity of Line W were correlated with enhanced or reduced Gulf Stream, after allowing for the seasonal cycle. Unfortunately, the short length of the Gulf Stream time series (7 years) precludes an accurate determination of the 'mean' seasonal cycle. However, this approach should be feasible once the Gulf Stream time series is extended to 17 years by incorporation of TOPEX/POSEIDON data into Figure 3.47. The second approach, which would complement the observational study and reveal the underlying mechanisms behind any correlations, would be to perform a model simulation (e.g. by applying an artificial large wind stress curl in different regions of an ocean general circulation model and examining the effect on the Gulf Stream volume transport). This is a similar method to that used by Greatbatch et al. (1995), who quantified the effect on the model Florida Straits transport of switching wind stress on or off in particular latitude bands. Given the large increase in the volume and quality of wind stress data since this study (see Chapter 4) and improved model resolution and physics, this should be a promising line of investigation.

5.5.2 Correlation between Wind Stress and the Gulf Stream at Line W

A similar correlation is not found at zero lag between Gulf Stream transport and zonal wind stress. The products generally concur on having negative correlations in the region west of 30°W and positive correlations near the eastern boundary (Figure 5.20a). However, only in the case of the NOC Climatology are any of these correlations statistically significant, suggesting the raw zonal stress does not influence the volume transport of the Gulf Stream on short timescales. However, if the Gulf Stream transport is regressed on a lagged time series of zonal wind stress, particularly between 2 and 4 months, the volume transport of the boundary current is observed to be anticorrelated with the zonal wind stress in the western part of the basin, with values of correlation reaching -0.5 in the vicinity of Line W itself (Figure 5.20b). However, if the lag is increased to 6 months, the negative correlation disappears, with a weak positive correlation instead being observed (Figure 5.20c). This is essentially a reversal of the 0 month map (Figure 5.20a), demonstrating the annual cycle related strengthening and weakening of the zonal wind stress.

A similar situation occurs when considering the regression of Gulf Stream transport on the meridional wind stress (Figure 5.21). At zero lag, no statistically significant correlations are found, but at lags between 1 and 6 months, a statistically significant positive correlation is found in the western basin, which gradually moves further east as the lag increases (by 6 months it is centred near 50°W).

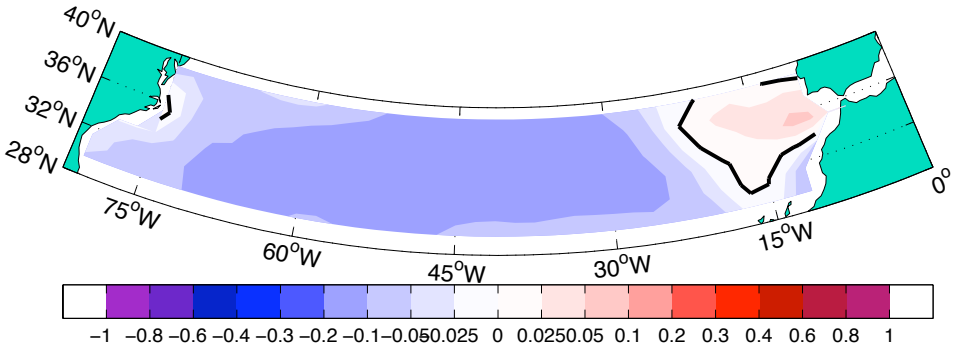

(a) 0 month

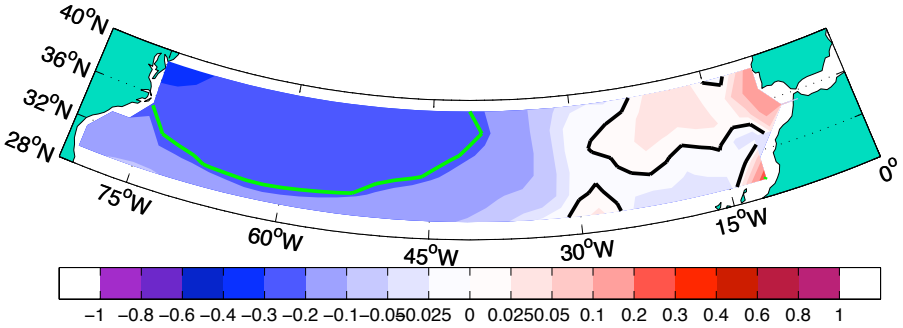

(b) 3 months

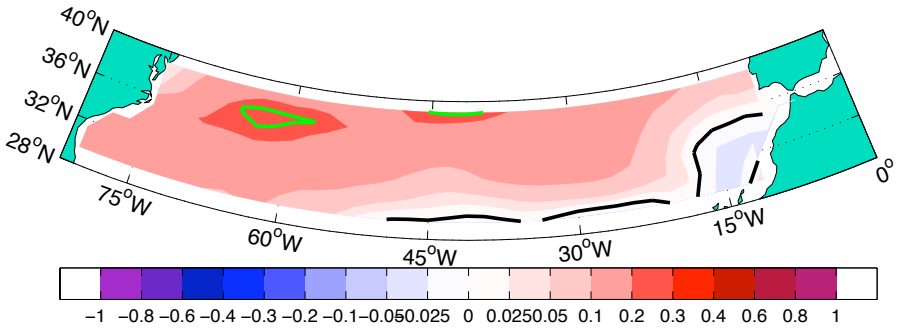

(c) 6 months

Figure 5.20: Correlation coefficients for the relationship between monthly zonal wind stress and monthly Gulf Stream transport inferred from the JASON altimeter at the Line W line. The NCEP-NCAR Reanalysis is used for the wind stress curl, with differing time lags between 0 and 6 months. The black contour is the zero line and the green contour displays the 5% significance line for rejecting the null hypothesis that the correlation coefficient is not significantly different from zero. The integral time scales for both the Gulf Stream transport and the zonal wind stress time series are less than 1 month across the basin, meaning that each observation can be treated as independent.

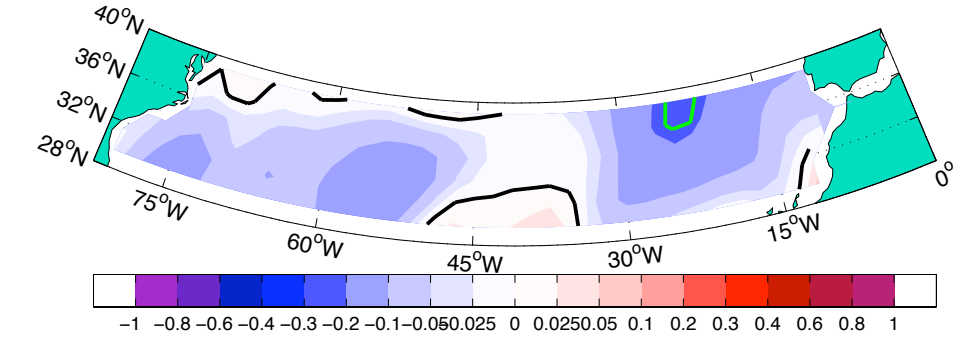

(a) 0 month

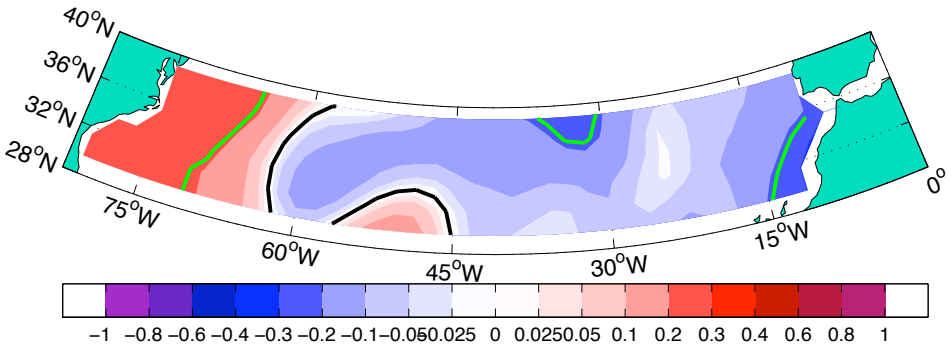

(b) 3 months

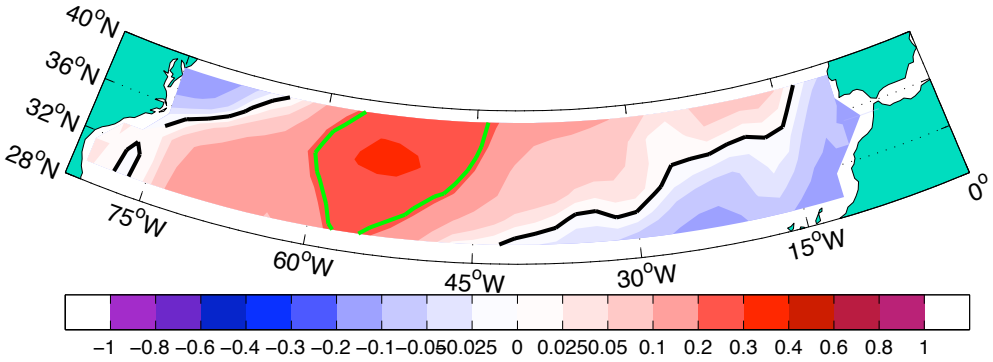

(c) 6 months

Figure 5.21: As Figure 5.20, except for meridional wind stress.

However, as in the case of the wind stress curl, these results are once again compromised by the strong annual cycle in each component, making it difficult to establish causation. Indeed, in such time series it is almost inevitable that at some time lag a statistically significant correlation will be observed. Despite these reservations, previous literature has argued that the Gulf Stream at Florida Straits is controlled by a number of wind stress-related mechanisms. For instance, Schott et al. (1988) found that sub-seasonal changes were almost certainly forced locally by meridional wind stress variability in the Straits, whilst seasonal changes could potentially be driven by remote wind stress curl forcing from the Caribbean or North Atlantic. However, they did not observe a similar lag between the state of the zonal/meridional wind stress and the transport change as we have observed, with the response to high-frequency wind stress forcing being largely instantaneous. An accurate determination of the physical processes controlling the Gulf Stream volume transport on monthly to annual timescales thus remains beyond the scope of this study, but our preliminary empirical evidence suggests that modelling efforts should continue to focus on the role of wind stress in the western basin of the North Atlantic.

Unfortunately, the time series of Line W Gulf Stream transports that has so far been constructed (7 years in length) remains too short for a comprehensive analysis of the *interannual* variability in Gulf Stream transport resulting from wind stress variability. However, using the regression relationship that has now been established, the Gulf Stream time series could feasibly be extended back to the start of the altimeter era in 1992. Unfortunately, high-resolution cruise crossings of the Gulf Stream were uncommon at this location before the Line W measurement programme. However, the 1997 A22 cruise (Section 2.3.3) could also be included in the regression analysis to ensure the size of the regression coefficients has not significantly changed over the last 15 years.

Elsewhere in the literature, several studies (Anderson and Killworth, 1977; Anderson and Corry, 1985) have suggested that, at decadal timescales, the Florida Straits transport is determined by the theoretical Sverdrup relation, with the balance holding at periods longer than the basin propagation time for first mode baroclinic Rossby waves (Chelton and Schlax, 1996). Early in the course of this project, a model analysis was conducted implying the importance of Rossby wave propagation in controlling the transport field within the basin at 36°N; these results are given below.

5.6 OCCAM Model Experiments

As a method of investigating the processes controlling transport variability and the connections between the interior and the western boundary, 19 years of model output were obtained from the $\frac{1}{4}^{\circ}$ OCCAM model, introduced in Section 2.8. Potential temperature and salinity fields were extracted at 35.9°N, in order to calculate the geostrophic shear relative to 1000 dbar at each model timestep. Validation of the T and S fields was undertaken by a simple comparison with WOA05 (Section 5.6.1), before calculating the dynamic height

field and geostrophic transport per unit width at each 5-day timestep to investigate the interannual variability (Section 5.6.2).

5.6.1 Model Validation

Use of this ocean general circulation model to investigate the mechanisms forcing interannual variability in the upper ocean transport implicitly assumes that the model successfully replicates both the mean state of the ocean and the variability in ocean parameters relevant to density-driven transport, especially temperature and salinity. Comparing the 1985 to 2003 mean temperature field from OCCAM with that from WOA05 (Locarnini et al., 2006) suggests the model captures the main temperature structure of the basin (Figure 5.22). The west-to-east gradient in SST, from 21°C at the centre of the gyre to 18°C adjacent to the eastern boundary, is found in both the climatology and the model. However, the mean model state has a warm bias of up to 3°C between the base of the mixed layer and 800 m depth east of 20°W. Moreover, the anomalous west-to-east shoaling of isotherms close to 68°W is not seen in the climatology and appears to result from too many cold core rings being shed from the simulated Gulf Stream. The standard deviation of the temperature fields (Figure 5.23) shows some agreement between the model and the climatology, though the model overestimates the actual temperature variability at 1000 m near the Mid-Atlantic Ridge whilst underestimating variability at 500 to 1000 m in the western basin.

A similar validation exercise was performed using OCCAM and WOA05 salinities (Antonov et al., 2006). Again, OCCAM captures the main features of the section (Figure 5.24), but has a Mediterranean Overflow that is both too shallow (by up to 600 m) and too salty (by up to 0.5). In addition, the model underestimates near surface salinity in the western basin by around 0.03. Other differences emerge when the standard deviation sections (Figure 5.25) are examined. The peak variability in the western basin is higher in OCCAM (0.4 compared with 0.3) but does not extend as far to the east, and the model also tends to overestimate the variability between 20°W and the Mid-Atlantic Ridge.

Further examination of the temperature field within the model reveals a long-term secular increase in temperature throughout the ocean interior in the period 1985 to 2003, with the increase being particularly large near the eastern boundary in the 200 to 800 dbar layer (3°C). A real increase in thermocline temperature had previously been observed between 1959 and 1981 cruise sections (Leadbetter et al., 2007), but both the magnitude and zonal extent of these changes was much smaller than that found within OCCAM (the maximum temperature increase of 2°C occurred between 50°W and 60°W only. Furthermore, these changes had largely reversed by the time of the 2005 CD171 repeat. Given this evidence, the changes observed are the attributable to model drift.

Mindful of several serious model limitations in representing both the mean state and variability of the T and S fields, especially in the region of the Mediterranean Water, we nevertheless chose to extract information about the magnitude and interannual distribution

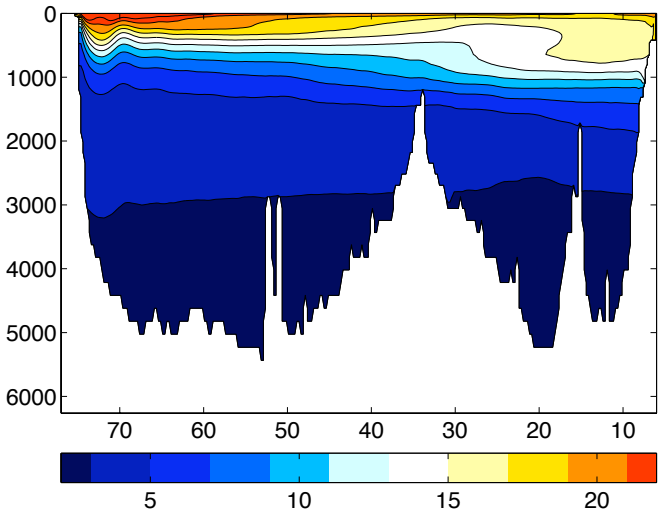

(a) OCCAM

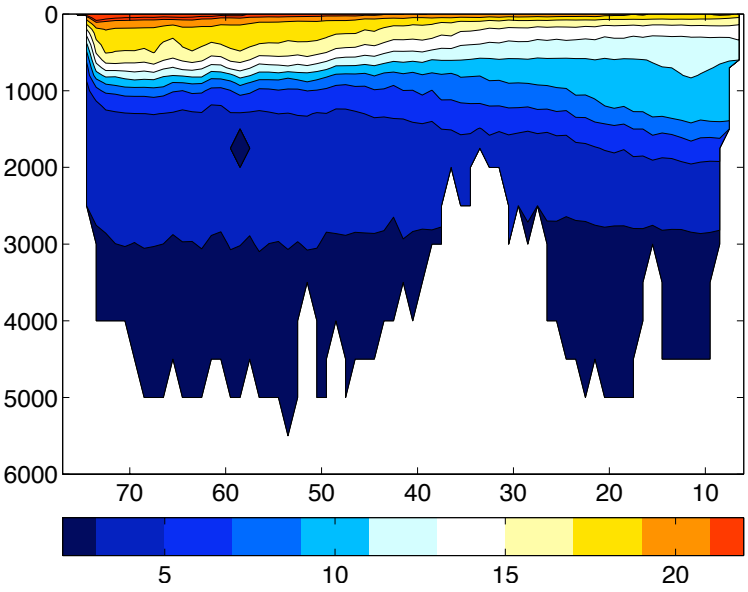

(b) WOA05

Figure 5.22: Mean temperature field at 35.9°N in the OCCAM model and *World Ocean Atlas 2005*. Longitude is on the x axis and pressure (in dbar) on the y axis.

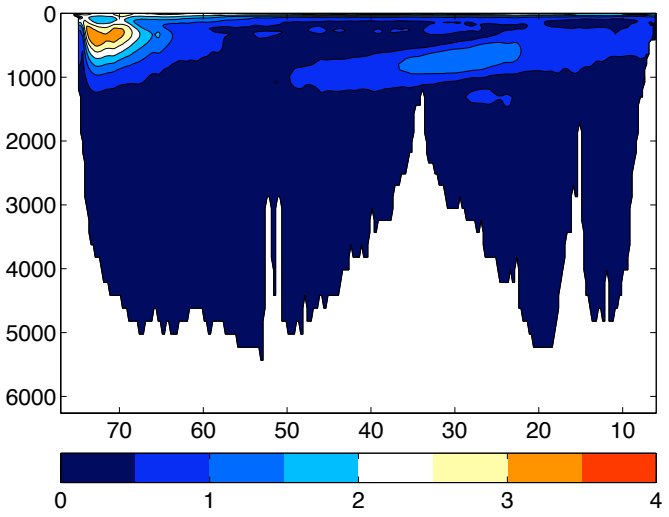

(a) OCCAM

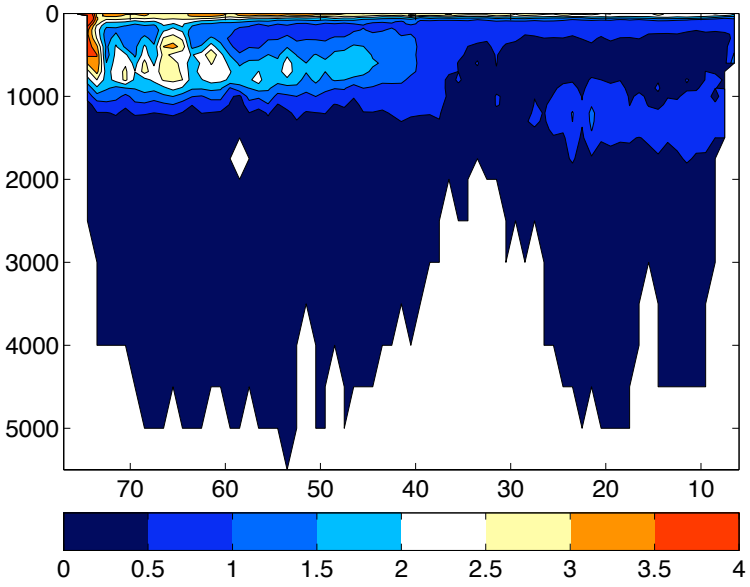

(b) WOA05

Figure 5.23: Standard deviation of the temperature field at 35.9°N in the OCCAM model and *World Ocean Atlas 2005*. Longitude is on the x axis and pressure (in dbar) on the y axis.

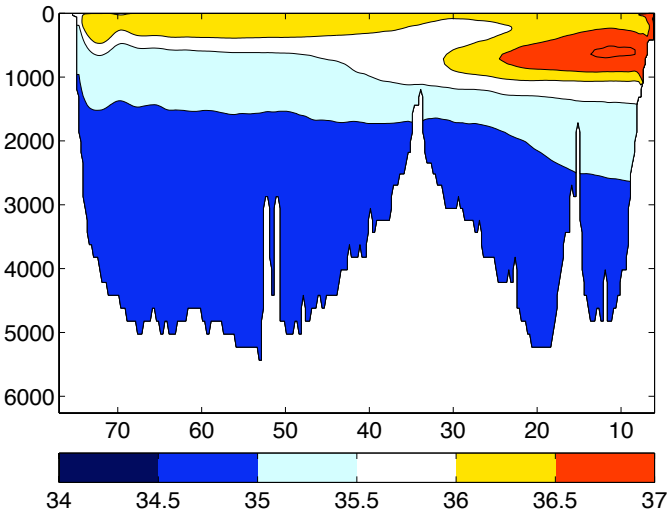

(a) OCCAM

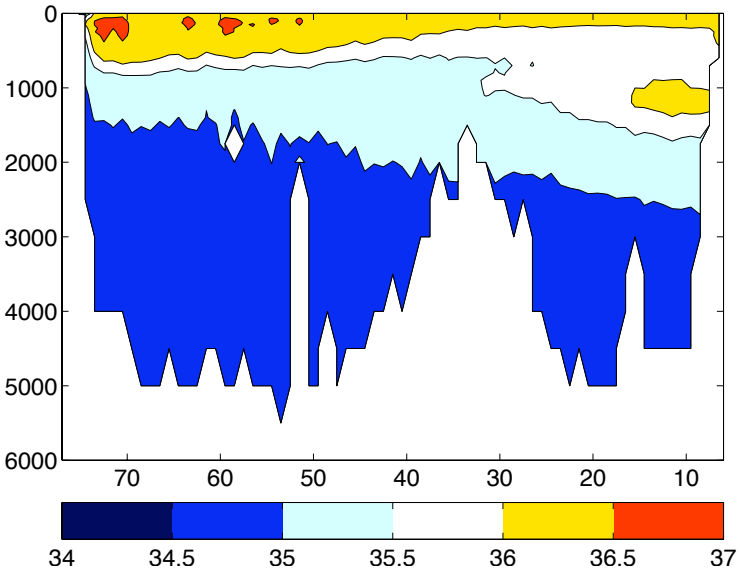

(b) WOA05

Figure 5.24: Mean salinity field at 35.9°N in the OCCAM model and *World Ocean Atlas 2005*. Longitude is on the x axis and pressure (in dbar) on the y axis.

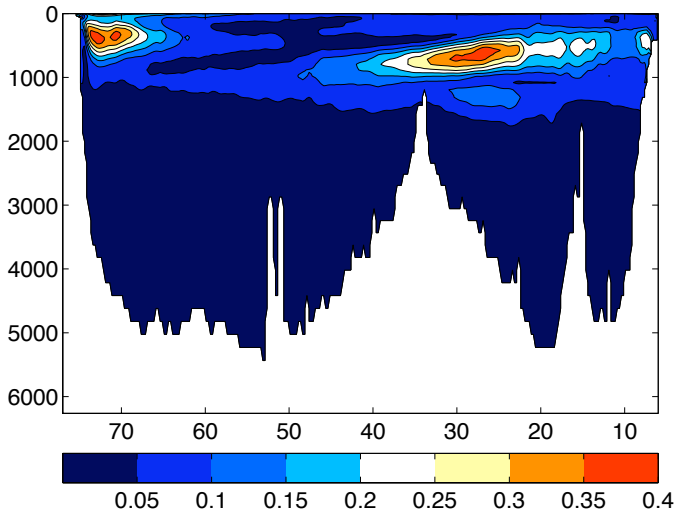

(a) OCCAM

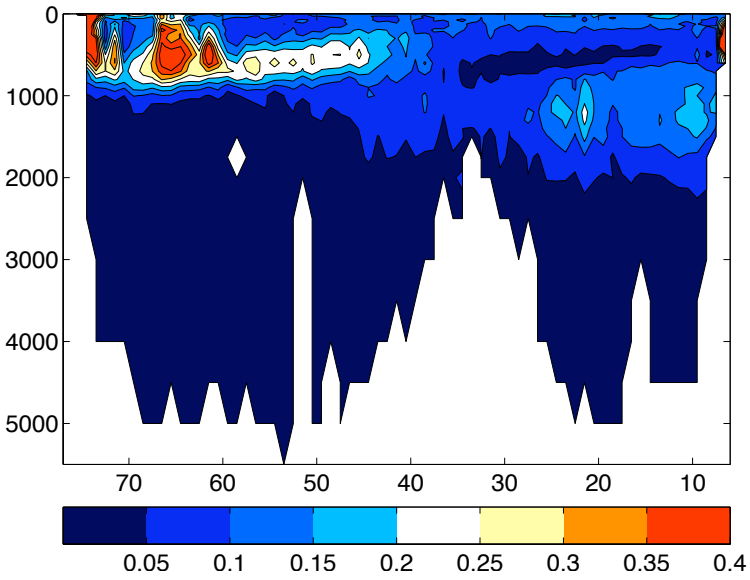

(b) WOA05

Figure 5.25: Standard deviation of the salinity field at 35.9°N in the OCCAM model and *World Ocean Atlas 2005*. Longitude is on the x axis and pressure (in dbar) on the y axis.

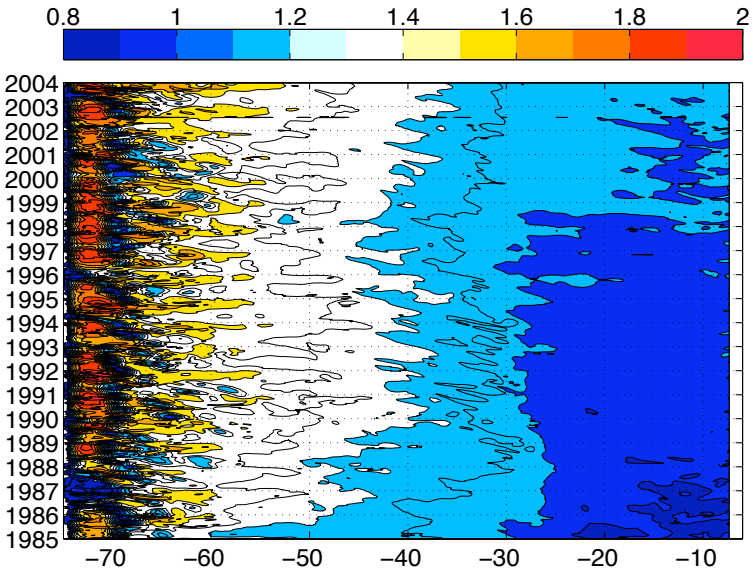

Figure 5.26: Dynamic topography (in dyn. m) at the surface relative to 1000 dbar along 35.9°N in the OCCAM model for the period 1985 to 2003. Longitude is given on the x axis and year on the y axis.

of interannual variability in the upper ocean transport field.

5.6.2 Model Dynamic Topography and Transport Variability

Using a reference level of 1000 dbar, the model dynamic topography at 35.9°N increases from around 1 dyn m. at the eastern boundary to 2 dyn m. at the core of the subtropical gyre (Figure 5.26). This is in line with previous estimates from the Argo data set (Figure 2.2).

If the reference level is changed to 1900 dbar and the top 200 dbar removed to exclude seasonal insolation effects, an interesting result emerges. Figure 5.27 shows the dynamic height anomaly (relative to the mean dynamic height at that location from the entire model run) at 200 dbar relative to 1900 dbar, plotted for every 5 day time slice from 1985 to 2003. A series of anomalies can be identified propagating westwards across the basin, which increase in magnitude close to the western boundary and, to a lesser extent, around the Mid-Atlantic Ridge. The anomalies take approximately 7 years to cross the entire ocean, implying a speed of around 2.5 cms^{-1}. Previous work examining the variability of the MOC (e.g. Hirschi et al. (2009)) has found similar features and attributed them to a series of baroclinic Rossby waves which transmit changes in the density field generated close to the eastern boundary westward across the North Atlantic. Wind-driven upwelling and downwelling appears to cause the elevation and lowering and isopycnals close to the eastern boundary (Köhl, 2005; Kanzow et al., 2010).

In order to test whether our observed anomalies are consistent with linear Rossby wave theory, the phase speed of first baroclinic mode Rossby waves at 36°N was calculated using

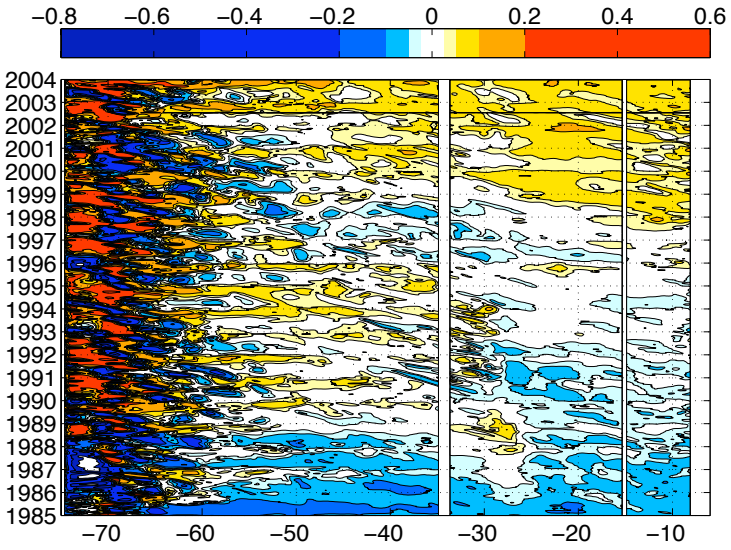

Figure 5.27: Anomaly from mean dynamic topography (in dyn. m) at 200 dbar relative to 1900 dbar along 35.9°N in the OCCAM model for the period 1985 to 2003. Longitude is given on the x axis and year on the y axis.

an equation derived from the dispersion relationship (LeBlond and Mysak, 1978):

$$C_{nx} = -\frac{\beta k_x^2}{k^2(k^2 + \frac{f^2}{gh_n})} \tag{5.4}$$

where C_{nx} is the phase velocity in the x direction, β is the meridional gradient of the Coriolis parameter f, k_x is the x component of the horizontal wavenumber k and h_n is the equivalent depth for the baroclinic mode n (1 in this case). Assuming the Rossby wave only propagates zonally, $k_x = k$. Using a typical Brunt-Vaisala frequency of 2×10^3 rad s^{-1} and an ocean depth of 5 km, $h_n = N^2h^2/gn^2\pi^2 = 1.03$ m.

The theoretical Rossby wave speed at 36°N for a wavelength of 1300 km (estimated from Figure 5.27) is found to be 2.6 cms^{-1}, in close agreement with the phase speed estimated from the propagation of geostrophic transport anomalies within the model (Figure 5.28). The time-longitude plots suggest that individual dynamic height anomalies tend to last between a few months and a year at a given location and thus might be an important source of interannual variability at this latitude.

The increase in the magnitude of the dynamic height anomalies both at the Mid-Atlantic Ridge near 35°W and at the western boundary warrants further discussion. In the case of the ridge, there is disagreement in the literature regarding the effect of topographic obstacles on Rossby wave propagation. Barnier (1988), for instance, found that the Mid-Atlantic Ridge acted as an effective barrier to low-frequency Rossby waves causing the eastern and western basin to have different low-frequency characteristics. Whilst Wang and Koblinsky (1994) also found that scattering occurred at the Mid-Atlantic Ridge, their model suggested that the ridge is an independent wave generation region in which barotropic and baroclinic com-

ponents are coupled to form new baroclinic waves. Furthermore, if these newly-generated waves did not have a sufficiently low frequency, the baroclinic signals generated were unable to propagate in the zonal direction and became trapped close to the ridge. They argued that this trapping mechanism could be the reason why observed variability tends to increase around topographic features such as mid-ocean ridges. This would provide a physically-plausible mechanism for our observations, but given the high sensitivity of topographic scattering and Rossby wave generation to model parameters in Wang's study, difficulties remain in correctly interpreting the results. Indeed Chu et al. (2007) recently observed long baroclinic Rossby waves in the North Atlantic using Argo subsurface tracks and temperature profiles but found only dissipation occurring at the ridge with no independent generation.

Amplification of Rossby wave activity near the western boundary has previously been observed in both the subtropical North Pacific and subtropical North Atlantic (Chelton and Schlax, 1996; Lin et al., 2005). Whilst Chelton and Schlax (1996) suggested that amplification in the Western Pacific was controlled topographically by the existence of Hawaii and Hess Ridges, the amplification region does not agree well with the topography and changes with time. Lin et al. (2005) instead suggested that baroclinic instability in the western basins (as defined by the meridional potential vorticity gradient) was the cause of Rossby wave amplification. In subtropical regions of both the North Atlantic and North Pacific, they demonstrated a spatial correlation between the zone of baroclinic instability and the zone of Rossby wave amplification. A third amplification mechanism, proposed by Osychny and Cornillon (2004), involves the interaction between the meandering western boundary current and the Newfoundland Ridge.

Whilst debate continues over the dynamics of planetary wave propagation in subtropical ocean basins, these results confirm that first baroclinic mode Rossby waves are a major source of interannual variability in the dynamic height field of OCCAM, accounting for variations of close to 1 dyn. m at 70°W over a few months. The waves are generated near the eastern boundary and propagate westward, becoming larger in magnitude as they move west of 60°W.

Figure 5.28 displays the vertically integrated transport in each quarter-degree of longitude (around 22.5 km), assuming a level of no motion at 1000 dbar. The Rossby wave signature is clearly visible on this figure, affecting the magnitude of both the interior transport *and* the model Gulf Stream as bands of alternating northward and southward flow propagate across the basin. For comparison with the Argo-derived baroclinic transport variability, these transport estimates are derived solely from the model T and S fields. Model u and v require rotation into geographical coordinates prior to analysis and have not been analysed here.

Integrating the transport from the eastern boundary to the position of maximum dynamic height at the centre of the gyre yields the time series of transport shown in Figure 5.29. The mean value of -26.8 Sv agrees quite closely with the baroclinic estimate of interior trans-

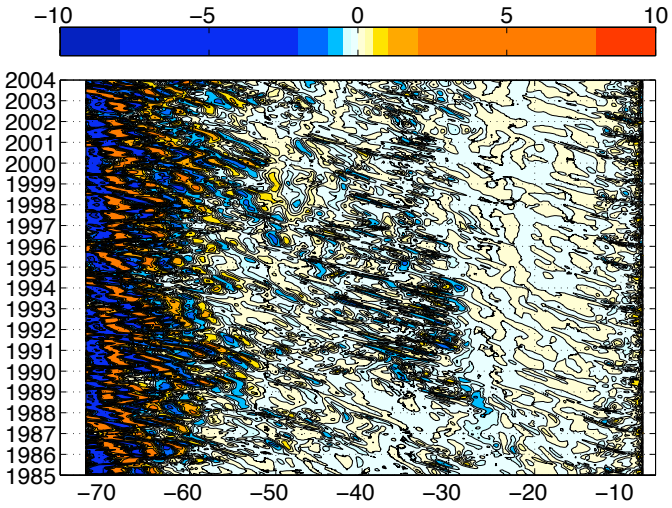

Figure 5.28: Time-longitude plot of vertically integrated meridional transport (in Sv) at 35.9°N for the OCCAM model run for 1985 to 2003. The level of no motion is set at 1000 dbar.

port derived from the observations, if the contribution of the reference velocity (−15.6 Sv) at 1000 dbar is discounted. Averaging the OCCAM transports into individual years, the standard deviation of the 19 annual estimates is close to 4.9 Sv. If the interior transport is instead integrated from east to west as far as 72.125°W (i.e. to a fixed position), the size of the standard of the 19 estimates is larger (10.5 Sv). This appears a little larger than the comparable observational estimate for 2003 to 2007 (7.7 Sv), but the observational time series is much shorter. Examination of five year model transport time series between 1985 to 2003 yields standard deviations of between 3 and 5 Sv, suggesting that the transport variability within OCCAM is slightly smaller than that actually observed.

Finally, a time series of Gulf Stream transports is extracted from OCCAM, again assuming a level of no motion at 1000 dbar (Figure 5.30). This time, the total transport above 1000 dbar is smaller than that at Line W, partly because the Gulf Stream crossing is further upstream and partly because strong northward transports still occur at 1000 dbar. Furthermore, the size of the variability of the OCCAM time series (subsampled at 10-day resolution) is again smaller than that observed in reality for similar time series lengths. For instance, the standard deviation of the altimeter-derived time series for the period 2002 to 2008 is 12.7 Sv, whilst the standard deviation for different seven-year time series of OCCAM model output (extracted from the period 1985 to 2004) is between 7 Sv and 9 Sv. This may be partly attributable to OCCAM Gulf Stream transports being evaluated further upstream; model transports at the Line W section have not yet been calculated. However, it is also probable that Rossby wave variability alone is insufficient to explain the magnitude of variability, or that the model does not properly capture the size of transport variability caused by Rossby waves.

The OCCAM analysis has therefore identified a possible source of variability in both interior

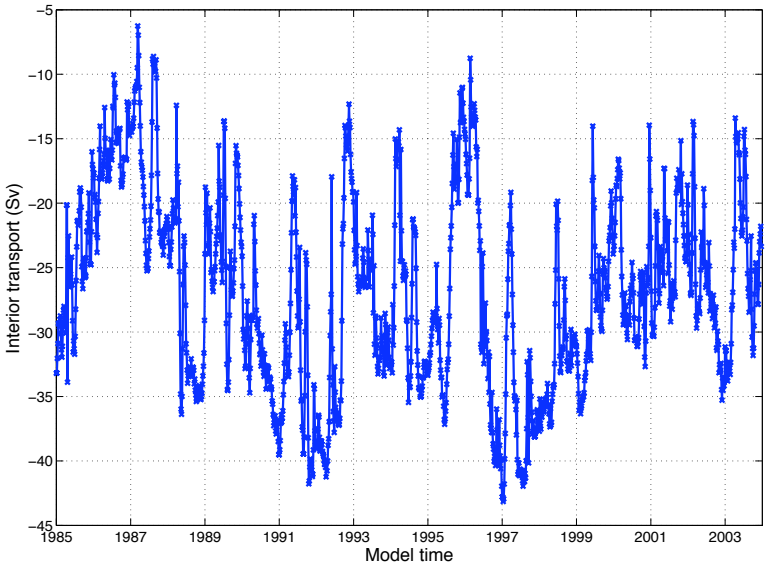

Figure 5.29: Time series of interior transport at 35.9°N derived from the OCCAM ocean model (1985-2003). The transport is integrated from the eastern boundary to the position of the maximum dynamic height in the gyre.

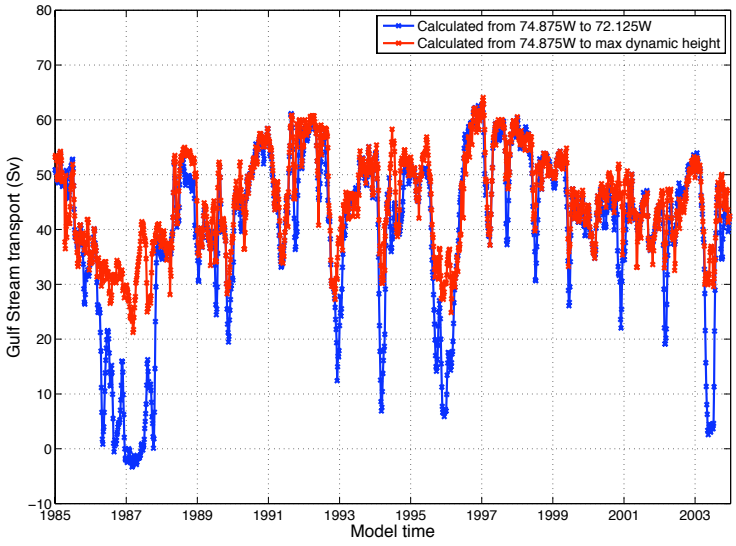

Figure 5.30: Two time series of Gulf Stream transport at 35.9°N derived from the OCCAM ocean model (1985-2003), assuming a level of no motion at 1000 dbar. The transport is evaluated either between fixed geographical points (blue line) or between the western boundary and the temporally-variant position of maximum dynamic height in the gyre (red line).

and Gulf Stream transports, namely the westward propagation of first baroclinic mode Rossby waves across the subtropical North Atlantic. However, given the model's limitations in accurately quantifying T/S variability at 36°N (Figures 5.23 and 5.25) and its tendency to drift, there are unresolved questions concerning the magnitude of transport changes caused by Rossby waves. Resolving the discrepancy between model and observed variability in both Gulf Stream and interior transports remains a key research priority.

5.7 Further Model Analyses

Whilst this study has been primarily observational in nature, the results from the OCCAM model suggesting a role for Rossby waves in controlling the interannual transport changes are encouraging and imply that high-resolution ocean models could be used to test other hypotheses in the thesis. Specifically, the OCCAM model could be used to test the hypotheses relating to Sverdrup balance in Section 5.2 and the correlations between Gulf Stream transport and wide stress/wind stress curl in Section 5.5. In the first case, an estimate of Sverdrup minus Ekman transport can be obtained for each timestep of the model from the prescribed ECMWF climatological wind stress (Section 2.8), or more ideally from a separate run of the model forced by ECMWF daily wind stress values. The zonally integrated Sverdrup minus Ekman value at 36°N could then be correlated with the total northward transport in the top 1000 bar calculated from the model v velocities. The effects of model drift that led to a basin-wide increase in dynamic height in the initial OCCAM model run (Figure 5.27) would have to be removed prior to the analysis. The effect of the bottom boundary (specifically wind stress curl over sloping topography) could be quantified in the model, allowing an assessment to be made of the frequency band over which Sverdrup theory holds and which other processes might be important, particularly at shorter timescales (e.g. Ekman pumping, barotropic variability). Whilst several limitations have been identified in the model, it has the strength of high spatial resolution at every timestep, making it a good option for a process study.

As already implied in Section 5.5.1, a modelling study is also likely to strengthen the analysis comparing Gulf Stream variability with wind stress/wind stress curl across the basin. Control and forcing experiments similar to those conducted previously by Böning et al. (1991) would identify the regions and timescales over which wind stress or WSC affects the size of the model Gulf Stream transport. Careful validation between the model transport and our altimeter-derived time series would be required to ensure the conclusions were applicable to the real Gulf Stream. Finally, the OCCAM model could also be used to support our length scale analysis in Chapter 2 as there are 19 years of model output at every grid point. The dependency of the decorrelation length scale on the time window (monthly, yearly etc.) could be assessed in detail with the OCCAM model to ensure the appropriate scale is applied for both seasonal and annual estimates at every pressure level.

Study	Latitude	MOC Transport	Comments
Hernandez-Guerra et al. (2010)	36°N	11.5 ± 3.1 Sv	Total transport above $\gamma_\eta = 27.38$
Willis (2010)	40 to 41.5°N	15.5 ± 2.4 Sv	Total transport above 1130 m
McDonagh et al. (2010)	36°N	16.6 Sv	Total transport above 1070 m

Table 5.4: Recent literature estimates of the strength of the MOC at or close to 36°N.

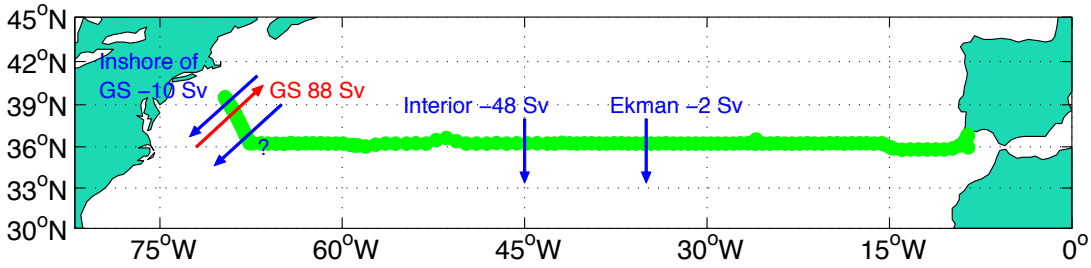

Figure 5.31: Schematic of MOC components at the 36°N/Line W section. The question mark between the Gulf Stream and the interior transport section reflects the unquantified transport discussed in the text.

5.8 Synthesis of Transport Estimates

From our individual transport estimates presented in Chapters 3 and 4, many of the components of the upper limb of the MOC have been quantified either at or close to 36°N. The Gulf Stream at Line W has a mean northward transport above 1000 dbar of around 87 Sv (Section 3.5), whilst the horizontal interior transport above 1000 dbar has a mean value of −48 Sv (using the mean of the four seasonal estimates, which weights each season equally). Including the contribution of the Ekman transport (around −2 Sv) and the estimated transport above 1000 dbar inshore of the Gulf Stream (around −10 Sv from the nine cruise sections), this would imply a total northward transport above 1000 dbar of around 28 Sv (Figure 5.31). This value appears large when compared with other estimates of overturning in this region of the North Atlantic (Table 5.4).

Some comments are warranted on the possible reasons for the discrepancy. Firstly, each of the other estimates has been obtained either on a single latitude line or as a box inverse between two latitude lines (Hernandez-Guerra et al., 2010). However, our estimate does not follow a line of constant latitude but relies on an interior transport estimated at 36°N and the remainder of the section (Gulf Stream and inshore) being evaluated at Line W. Nevertheless, given that smaller MOC values are obtained at both 36°N and 41°N, it does not seem likely that this is the source of the difference in transport. Two other possibilities are now examined in more detail.

The first possibility is that there is a missing component of southward transport between the offshore limit of the Gulf Stream and the 36°N latitude line in our analysis. It is not

possible to use the OI to estimate the transport here, as it had large errors in this region, and only four of the cruise sections (in November 2003, September 2004, April 2005 and October 2007) extend this far offshore (Figure 3.42). In most of the sections, the Gulf Stream has been crossed north of 36°N, with southward transport between the southern edge of the Stream and the 36°N. This southward transport (of up to 20 Sv in September 2004) is not quantified in our analysis. One way of including this component would be to attempt an altimeter-based analysis similar to that conducted with the Gulf Stream. However, the background mean dynamic height would have to be evaluated from other data, as only four Line W cruises extend into this region. One possibility would be to use the recent 1-minute Danish National Space Centre model (Andersen and Knudsen, 2009). Alternatively, it might be possible to construct a time series in the region immediately offshore of the Gulf Stream from the regular ADCP crossings of *M.V. Oleander* between Port Elizabeth and Bermuda, but this is limited by the depth range of the ADCP (maximum of around 800 m). In addition, both data quality and depth penetration on each individual ADCP section are dependent on both the number of scatterers and the sea state. A preliminary study of the data revealed that, in the period 2004 to 2008, an average of only 10 sections per year penetrated as deep as 200 m along the entire section, limiting the usefulness of the data for monitoring the size and structure of this transport.

The second reason for the discrepancy is the continuing uncertainty in the size of the 1000 bar reference velocity. Owing to the very noisy nature of the YoMaHa data set, the formal uncertainty remains very large (±34 Sv in Section 5.3.4). An improvement to this analysis could be to use altimetry data to reduce the noise in the float trajectories, a technique trialled successfully by Willis and Fu (2008).

In conclusion, this project has successfully quantified the most important components of the upper ocean transport above 1000 m, and with fairly modest additions to the analysis both the mean size and interannual variability in the MOC at this section should be quantifiable. Further discussion is provided in Section 5.10.

5.9 Conclusions

The main conclusions of the research are summarised below:

1. An optimal interpolation of temperature and salinity data from the Argo float array, in conjunction with reference velocity trajectories from the YoMaHa database, yields estimates of the geostrophic flow field of the North Atlantic at 36°N. Annual estimates of the zonally integrated transport between the offshore limit of the Gulf Stream and the eastern boundary vary from 36.2 Sv to 57.2 Sv southwards, with most variability originating in the Sargasso Sea. The mean interior transport above 1000 dbar (−48.0 Sv) agrees well both with previous cruise estimates (McDonagh et al., 2010) and with recent results from an Argo inverse of the North Atlantic (Hernandez-Guerra et al., 2010), both of which yield transports near −45 Sv (the latter study uses $\gamma_n < 27.38$ as

the density range). The size of the variability between individual years is broadly similar to the annual variability (7.7 Sv standard deviation cf. 6.6 Sv), with the strongest southward transport during spring. The size of the uncertainty in the transport field is formally very large (close to 40 Sv), because the reference velocities derived from the YoMaHa product are extremely noisy. However, the year-to-year and season-to-season baroclinic variability has a small error bar ±3.5 Sv, confirming that our conclusions about the density-driven horizontal gyre circulation are robust.

2. Examination of the dynamic height variability in layers from the OI confirms that the interannual variability in the baroclinic transport field of the interior is largely controlled by year-to-year changes in the vertical structure of the main thermocline, particularly in the western basin (Figure 3.27). In contrast, such displacement is not commonly observed in the eastern basin. The seasonal variability is more strongly controlled by the formation and erosion of the seasonal thermocline, with movement of the main thermocline being relatively less important (Figure 3.30).

3. Even after including both T/S and velocity measurements at 1000 dbar from the W1 and W3 moorings of the Line W array, the lack of data relative to the short length scales of variability near the western boundary leads to large errors in the transport in this region. An alternative strategy was instead adopted, which involved establishing an empirical relationship between the geostrophic transport of the Gulf Stream in the upper 1000 or 2000 dbar and the sea surface height difference across the Gulf Stream. This regression was then used to allow Gulf Stream transport to be inferred from a time series of sea surface height anomalies from the JASON altimeter. Successful application of this technique relies on transport changes occurring simultaneously across all ocean layers, a result confirmed by Figure 3.44 down to 1000 dbar. Using the difference between the maximum and minimum sea surface height in the region north of 36°N, the mean transport above 1000 dbar for the period 2002 to 2008 was 87.6 Sv and above 2000 dbar was 107.9 Sv. An annual cycle of magnitude 12 Sv is observed in the upper 2000 dbar, with the maximum transport occurring during August and the minimum in March. This result agrees with a previous study by Sato and Rossby (1995), who found a late-year maximum in transport from 130 histroical hydrographic cruises in this region. The mean value is larger than the solution transport reported by McDonagh et al. (2010) at 36°N, who calculated a 67.2 Sv transport in the top 1000 m. This study thus confirms that rapid increases in Gulf Stream transport take place downstream of Cape Hatteras (up to 10 Sv per 100 km).

4. As a means of identifying possible forcing mechanisms of variability in the interior transport and Gulf Stream, the zonal wind stress and wind stress curl (WSC) fields of the subtropical North Atlantic were examined in detail. The zonally integrated Ekman transport at 36°N for the period August 1999 to December 2005, the period during which data were available from all four wind stress products, was around 2 Sv southwards, contrasting with the 2 Sv of northward flow at the RAPID array latitude

of 26.5°N. The full-basin zonally integrated Sverdrup transport at 36°N was between 18 and 21 Sv southwards in the same period. 36°N lies slightly to the north of the region of maximum wind stress curl. To investigate the main modes of variability in both the zonal wind stress and WSC, spectral and EOF analyses were conducted. In the case of the zonal stress, the principal source of variability is a well-documented basin-wide annual cycle with the strongest westerly winds in February. A similar (but weaker) peak is found at annual frequency for the wind stress curl, implying a maximum southward Sverdrup transport in winter. On timescales longer than one year, basin-wide modes of variability are once again the most important, but the exact spatial configuration differs significantly between the individual wind stress products, particularly for WSC. Furthermore, the percentage of variance explained by the leading basin-wide EOF mode is small for the wind stress curl (only 15%).

5. At timescales longer than one year, it was found that the NAO is an important control on the zonal wind stress in the subtropical North Atlantic. A regression analysis (Figure 4.43) of 12-month low pass filtered zonal wind stress on a similarly filtered NAO time series implies a stronger (weaker) southward Ekman transport during negative (positive) phases of the NAO . This concurs with previous modelling work by Eden and Willebrand (2001). The relationship between the NAO and WSC is more complex, with a positive state favouring a more southward transport in the region north of 34°N and a weaker southward transport south of 34°N. Nevertheless, the regression relationship is not as strong as for the Ekman transport.

6. The Sverdrup minus Ekman flow, which from theory is meant to approximate the total upper ocean geostrophic transport, is in reality smaller than the total interior transport accumulated from the eastern boundary to 67.6°W. The discrepancy arises principally in the western basin, with the difference most likely attributable to the strong Gulf Stream recirculation at this latitude. After taking into account the proposed 28 Sv of recirculating transport above $\theta = 7$°C in the Worthington Gyre (Worthington, 1976), the transport estimates are more similar. Furthermore, the Sverdrup minus Ekman transport does agree with the interior transport east of the Mid-Atlantic Ridge to within 5 Sv. However, the Sverdrup minus Ekman transport does not successfully predict either the annual cycle in the interior transport (the theoretical relation predicts a maximum in winter whilst the actual maximum is in spring) or the size of the interannual variability.

7. Regression relationships between the Gulf Stream transport at Line W and wind stress/WSC within the basin suggest that the Gulf Stream volume transport is negatively correlated with wind stress curl immediately to the east at zero lag and negatively correlated with the local zonal wind stress at 1 to 3 months lag. However, the limited length of these time series and the fact that each of the time series contain significant annual cycles means that a causal relationship cannot be demonstrated. Further observational and modelling studies are required to establish the veracity of

these correlations and possible mechanisms linking the wind stress and Gulf Stream transport at Line W.

8. Whilst the limited length of the Gulf Stream time series determined so far (7 years) does not permit an easy determination of the controls on interannual and decadal Gulf Stream variability, results from the OCCAM model suggest an important role for first baroclinic mode Rossby waves. These propagate westwards across the basin, with their amplitude increased around the Mid-Atlantic Ridge and in the Gulf Stream. Model results show that the size of the transport anomalies caused by Rossby waves are probably too small to account for the observed variability in the interior transport and Gulf Stream. However, it is not clear whether this is an accurate result or is simply caused by the model failing to capture the size and/or mechanisms of real ocean variability.

5.10 Broader Implications

The results of this study have significant ramifications for several important areas of research. Firstly, some further comments are offered on the potential of the methods used for full-basin monitoring of the volume transports. Secondly, the value of the Gulf Stream transport time series is discussed in more detail before a brief examination of the importance of the results for constraining the heat budget of the North Atlantic.

As outlined in Section 5.8, whilst the Gulf Stream, interior and Ekman transport time series are important contributions to our understanding of ocean variability in the northern subtropical Atlantic, they do not by themselves yield full-basin transports of the upper 1000 dbar. Long-term monitoring of the MOC at 36°N is a more difficult problem than at 26°N, in part because the Gulf Stream is not separated by topography from the mid-ocean transport and in part because of the strong meandering of the western boundary current in this region. Nevertheless, it was argued in Section 5.8 that by incorporating estimates of the recirculation immediately offshore of the Gulf Stream into the analysis, it should be possible to reduce the discrepancy between the MOC estimate from this study and the existing literature values.

A further method of monitoring the MOC would be to use Line W to monitor the Gulf Stream and recirculation, a synthesised Argo section connecting Bermuda with the RAPID array moorings at the Mid-Atlantic Ridge at 26°N, and the existing RAPID array for the section between the eastern boundary and the Mid-Atlantic Ridge. This configuration would have the advantage of avoiding the Mediterranean outflow region at 36°N where Argo data coverage is sparse (e.g. Figure 3.3). However, given the paucity of Argo data in the region close to 26°N west of the Mid-Atlantic Ridge (Figure 2.1), this method is not likely to be successful at the present time. Unfortunately, the free-drifting nature of the Argo float array presents an inherent difficulty for estimating basin-averaged quantities such as volume or heat flux as regions can become either very densely or relatively poorly sampled. Whilst

this combination of Argo, Line W and RAPID does have the potential to monitor the MOC, research effort and coordination would be required to ensure the western basin was seeded with sufficient Argo floats throughout the duration of the programme. As has been demonstrated in this project, Argo does have the capability to yield at least annual and seasonal average sections of upper ocean geostrophic transport in the ocean interior. Therefore, the general approach of concentrated western boundary measurements supplemented with Argo floats in the interior is a sound approach where cost and/or logistical constraints prevent full-basin monitoring (e.g. at 24°S in the Atlantic). However, careful management of the Argo float array in these regions is needed to ensure a good temporal resolution of end point measurements.

A final complementary source of data that partly addresses the depth limitation of the Argo data for determining MOC changes is the RAPID-WAVE array (Elipot et al., 2010). This array of bottom pressure/inverted echo sounders, six of which are located on the bottom of Line W moorings, has now successfully yielded a time series of transports from 2004 to 2008 below and relative to 1000 m, on the principle that interannual changes in the MOC are largely controlled at the western boundary. Using the WAVE array data together with Argo/Line W altimetry estimates opens the possibility of monitoring both upper and lower limbs of the MOC at this latitude.

The novel time series of Gulf Stream transports presented in this thesis also presents a number of research opportunities. The time series could be easily extended back to 1992, yielding a 17 year record of transport above 1000 dbar or $\sigma_\theta = 27.38$. This would permit a more robust time series analysis to test whether the seasonal cycle deduced in Section 3.5.3 is a real or an artefact of the relatively short time series. Furthermore, 17 years of data would allow more accurate correlations to be determined with the wind stress/WSC, which in turn would provide observational evidence of the most likely mechanisms causing Gulf Stream variability. Accurate regression coefficients could also be determined with the low-frequency changes in the NAO, to evaluate the impact of this mode on transport at Line W. Further examination of the Gulf Stream from Line W cruise data could answer important questions such as the depth structure and transport of the inshore recirculation. In addition, the recent redeployment of a new GUSTO (Gulf Stream Transport Observations) mooring at the core of the Gulf Stream along Line W should yield more information about the depth structure of the boundary at this latitude. Unfortunately, a number of technical difficulties have affected this instrument, most recently in May 2010 when part of the mooring broke loose (Toole, personal communication).

Finally, results from this thesis can contribute significantly towards efforts to constrain the heat budget of the North Atlantic. The long debate over whether the subtropical North Atlantic forms a source or sink of heat was discussed in detail in Section 1.3. However, our findings also have direct relevance to a number of other unresolved questions. Firstly, our annual temperature, salinity and velocity sections obtained in Chapter 3 can be used to calculate the gyre component of meridional heat and freshwater transport on an interannual

timescale. Hadfield et al. (2007) has previously used objective maps of temperature in the North Atlantic to infer monthly changes in mixed layer heat content. Comparing these estimates with mixed layer heat content derived from the CD171 cruise yielded RMS errors of 10 to 20 Wm^{-2} when averaged over $10^\circ \times 10^\circ$ boxes away from the western boundary. Unfortunately, the error near the boundary is greater than 50 Wm^{-2}. Nevertheless, our T/S and velocity fields could be used to calculate a zonally integrated gyre heat and freshwater transport in the region east of 68°W. More recently, Wells et al. (2009), as part of the MONACO project, have estimated the various heat budget terms (storage, advection, diffusion and surface exchange) for the North Atlantic from 20°N to 60°N using a combination of interpolated Argo T/S and sea level heights (obtained via the Bernoulli Inverse Method) and NCEP/NOC heat fluxes and wind stress. It was established that, using the NOC fluxes, the heat budget was closed to within the error bounds in 13 out of the 20 $10^\circ \times 10^\circ$ boxes. Now that we have obtained the depth structure of the top 1000 dbar on an annual and seasonal basis at 36°N, a more refined heat and freshwater content analysis should be achievable.

Appendices

Appendix A

Study of Length Scales in the Subtropical North Atlantic

For completeness, further details of the analysis leading to our choice of interior zonal and meridional length scales (L_x and L_y) are given below. In order to understand the vertical structure of the length scales for each cruise and Argo realisation (Figures 2.7, 2.10, 2.11, 2.12 and 2.14), the detrended and normalised potential temperature and salinity anomalies at a number of pressure levels (20, 300, 500, 1000, 1500 and 1900 dbar) were plotted and examined.

A.1 Zonal Scales

A.1.1 Cruise Estimates

It was noted in Section 2.3.2 that differences in the vertical structure of the length scales occur between the CD171 cruise data and the Argo evaluation at 36°N. In the case of the cruise data (Figure 2.7a), a long potential temperature length scale of 550 km is found at 20 dbar, largely because the station-to-station variability in temperature is relatively small (Figure 2.8a). In contrast, the salinity length scale is much shorter as the station-to-station variability is larger, especially in the middle of the section (Figure 2.8c). This difference is most likely attributable to the short time window over which the observations were taken. As temperatures in the mixed layer are controlled over large regions by seasonal surface heat fluxes, the temperature scales in the top 100 dbar are much longer than those for salinity. Beneath this surface mixed layer, length scales for both variables decrease rapidly, with shorter scales at both 300 dbar and 500 dbar. This result might initially seem surprising, given that this is at the core of the subtropical mode water with a supposedly stable θ-S characteristic. However, our scales are evaluated on pressure surfaces and examination of the temperature and salinity anomalies reveals large variability from station-to-station, especially in the western basin. These anomalies are associated with strong eddy activity.

Specifically, a number of cold core rings, which contain cold and fresh water from north of the Gulf Stream, are found between 65°W and 50°W (Figure 2.8a).

Moving into the deeper water, the length scales stabilise at around 250 km below 900 dbar (Figure 2.7a), with substantial variability on short space scales across the entire basin (Figures 2.8a and 2.8c). Although the *absolute* size of the temperature and salinity anomalies decreases at depth (note that Figures 2.8a and 2.8c are normalised), internal waves cause strong vertical displacements of the isopycnals, especially as the stratification weakens in the deeper layers. The length scales thus remain similar throughout the intermediate and upper North Atlantic Deep Water layers down to 2000 dbar. The discrepancy in length scales for temperature and salinity between 950 dbar and 1100 dbar warrants further discussion. Being at the depth of the Mediterranean Outflow in the eastern basin, the difference might be presumed to be attributable to a difference in the outflow structure at the eastern boundary when compared to the climatology, possibly because of the presence of meddies (Armi and Zenk, 1984). However, closer examination of these pressure levels reveals that the source of the anomaly is actually found in the western basin, as separate plots of the length scales east and west of 40°W reveal that the difference in temperature and salinity scales only occurs west of the Mid-Atlantic Ridge (not shown). A comparison of the temperature and salinity anomalies in this depth range for the region between 68°W and 40°W reveals that the magnitude of the station-to-station variability close to the western boundary is smaller for salinity than for temperature in this depth range. In particular, the large positive temperature anomaly close to 60°W (Figure 2.8a at 1000 dbar) is much more muted in the salinity field. As a result, the length scales for salinity from this realisation are longer than for temperature. Nevertheless, it is important to bear in mind that this is derived from a single snapshot cruise section, so is unlikely to be a real feature of the decorrelation scales.

A.1.2 Argo Estimates

For the Argo-based estimates, the zonal length scales *increase* with depth, a reversal of the trend observed with the CD171 data. The reason for this trend is again revealed by referring to the gridded anomalies from which the autocorrelation functions were computed (Figures 2.8b and 2.8d). At 20 dbar, length scales are generally shorter than for the cruise data as the station-to-station variability is higher (data being taken from all seasons). However, as one moves to deeper levels, the length scales are larger than for the cruise realisation, because the effects of individual eddies are smoothed out by the large time window over which the Argo data are taken. This is most obvious in the western basin between 50°W and 65°W, where the variability over short distances (less than a few hundred kilometres) is substantially smaller than for the cruise realisation (e.g. compare the 1500 dbar anomalies on Figures 2.8a and 2.8b). Moreover, the Argo-based estimate is less susceptible to seasonal bias, which does strongly affect the individual cruise sections, especially in the surface layer.

It is also apparent from Figure 2.7b that potential temperature has a longer correlation scale than salinity below 1600 dbar. Examination of the raw anomalies (Figures 2.8b and 2.8d)

confirms that this is due to a large positive salinity anomaly close to station number 120 in the middle of the section that is not seen in the temperature field. Owing to the localised nature of this feature, it is likely to be caused by a single float profile and thus does not reflect a real difference in scales at this depth.

A.1.3 Reconciling the Differences

After uncovering the reasons for the differing vertical structure of the cruise and Argo realisations, it was decided that no robust difference in length scale could be detected between different pressure levels. In view of this, it was decided to adopt 350 km as the zonal scale throughout the interior of the basin.

A.2 Meridional Scales

A.2.1 Cruise Estimates

As outlined in Section 2.3.3, the meridional length scales are determined at 20°W, 52°W and 66°W by repeat occupations of WOCE lines A16, A20 and A22 respectively. The results of the autocorrelation analysis for the A16 section in years 1988 and 2003 were previously presented in Figures 2.11a and 2.11b, with a distinctly different pattern observed between the years. The earlier section exhibits a similar depth structure to the zonal CD171 section, with shortening length scales in the upper 1000 dbar and roughly constant scales between 1000 dbar and 2000 dbar. The later section has short ($\sim$ 150 km) length scales in the upper 400 dbar and between 1000 dbar and 1600 dbar, but longer scales between 400 dbar and 1000 dbar and below 1600 dbar. The interpretation of these differences is again assisted by the normalised anomalies at individual pressure levels given in Figures A.1 and A.2.

The large near-surface length scales in 1988 occur because of the main scales of variability are quite long (e.g. Figure A.1a shows that at 20 dbar the potential temperature anomaly is negative between 15°N and 30°N). Further down the water column, several large anomalies occur over relatively short distances, especially close to the mouth of the Mediterranean near 36°N. In 2003, it is apparent that at both 20 dbar and 1900 dbar, the length scales of variability are larger than at the other depth horizons shown (Figure A.2), consistent with Figure 2.11b that shows long length scales at both the top and bottom of the water column and generally shorter values elsewhere.

The results for the two cruises of the A20 section were discussed in some detail in Section 2.3.3, but some further comments on the A22 section are now warranted. In this case, the length scales were evaluated from two cruises in 1997 and 2003, with both years exhibiting increasingly long scales with increasing depth (Figures 2.14a and 2.14b). The only exception to this pattern occurs in 1997, when very long salinity scales of over 500 km are observed in the 1150 dbar to 1350 dbar pressure band. The reason for salinity having a much longer

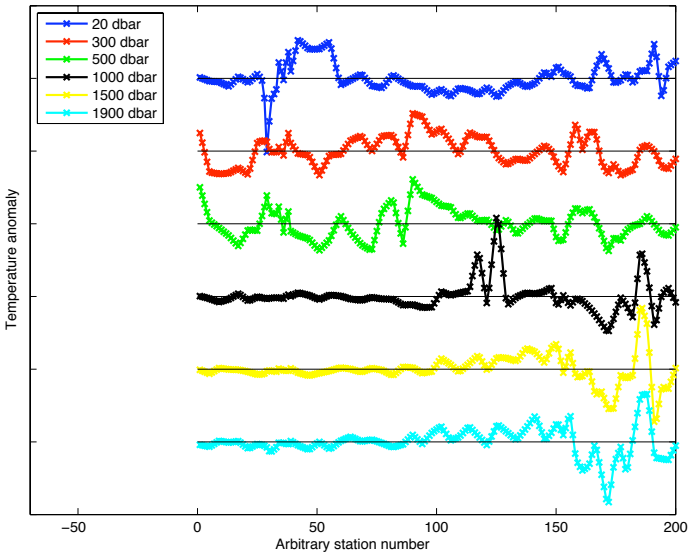

(a) Potential temperature

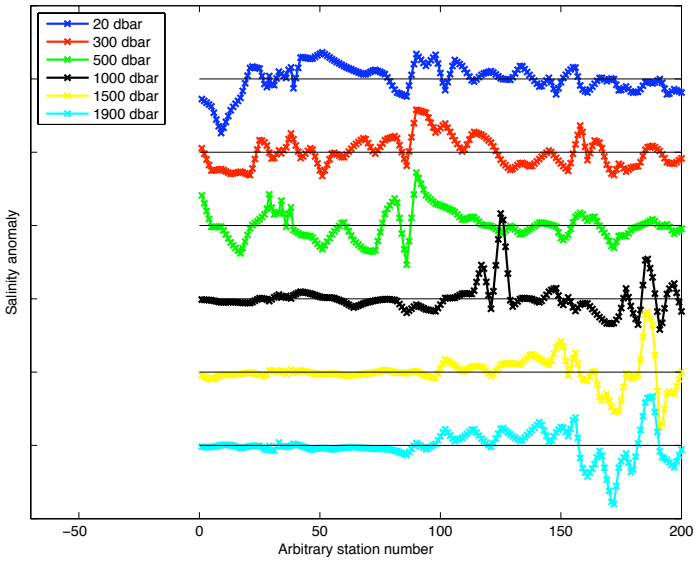

(b) Salinity

Figure A.1: Detrended potential temperature and salinity residuals for various pressure levels normalised by their standard deviation on the 1988 A16 section. The x axis is arbitrary station number from south to north, with Station 1 located at 5°N and Station 200 at 40°N.

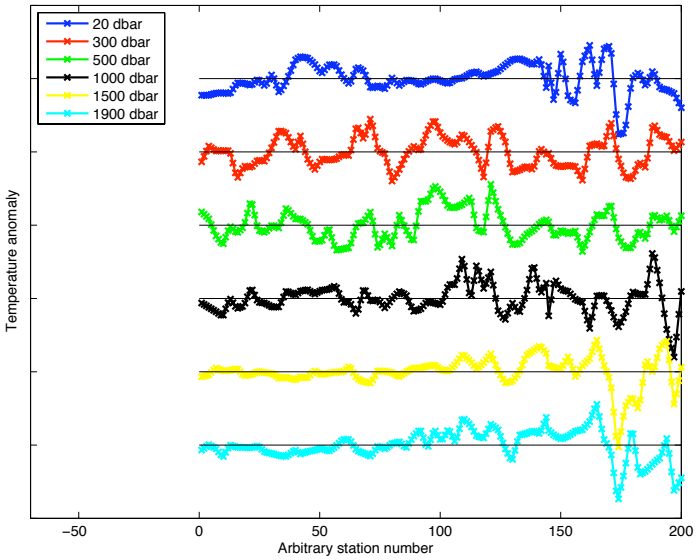

(a) Potential temperature

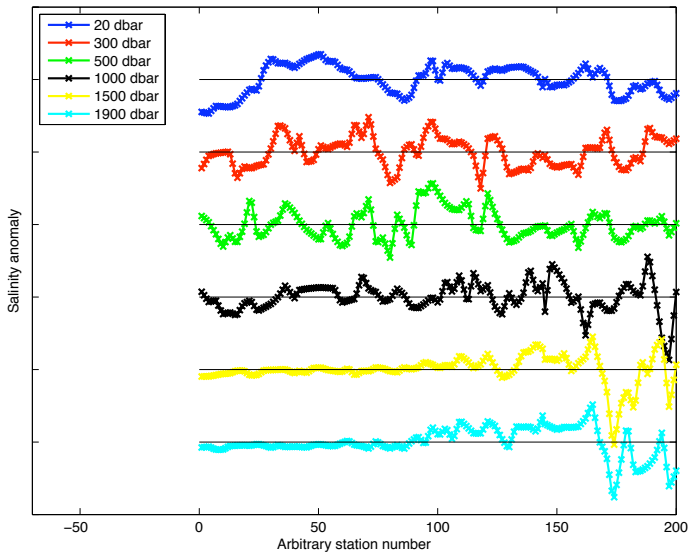

(b) Salinity

Figure A.2: Potential temperature and salinity residuals for various pressure levels normalised by their standard deviation on the 2003 A16 section. The x axis is arbitrary station number from south to north, with Station 1 located at 5°N and Station 200 at 40°N.

length scale than temperature at mid-depth is because a large positive anomaly that occurs in the temperature field close to the southern end of the section is not found in the salinity field (not shown here). However, this once again is found only on a single section and is unlikely to be indicative of a real difference in decorrelation scales.

A.2.2 Argo Estimates

A similar appraisal was conducted for the three meridional Argo realisations, using data collected from 2° either side of 20°W, 52°W and 66°W. At 20°W, where 979 Argo profiles were used to synthesise a 200 station section, length scales were small at all pressure levels (Figure 2.11c), with the shortness being attributable to very high levels of variability over short distances north of 35°N and below 1000 dbar (Figure A.3). This was also seen in the cruise data (Figure A.2) and represents meddies within the Mediterranean Water outflow causing large temperature and salinity anomalies in that region. It is notable that below 1400 dbar, the salinity scales are longer than the temperature scales, owing primarily to the more strongly positive temperature anomalies than found for salinity. Length scales for both temperature and salinity above the level of the Mediterranean Water are also longer, particularly in the 400 dbar to 700 dbar band, the core of the North Atlantic Central Water. This water mass is known to have relatively stable θ-S characteristics and is less susceptible than the Mediterranean Water to large eddy-related isopycnal displacements.

Length scales at 52°W were generally 100 to 200 km (Figure 2.12c), but those for salinity were much longer than for potential temperature in the pressure range 1000 dbar to 1600 dbar. The raw temperature and salinity anomalies suggest the difference is accounted for by much larger variability over short distance scales in the potential temperature field than in the salinity field in the northern part of the section around 37°N (see the 1000 dbar line in Figure A.4) . Examination of the autocorrelation function itself (not shown) nevertheless suggests that a zero crossing *almost* occurs for salinity close to 150 km, and we therefore conclude that a 100 km to 200 km length scale is likely for both temperature and salinity at all depths.

Finally, the length scales at 66°W were again in the range 100 to 200 km (Figure 2.14c), though between 1000 dbar and 1600 dbar, scales were generally much longer, especially for salinity (as large as 650 km). The increase in length scale in this depth range is attributable to the reduction in short-scale variability close to the northern end of the section (Figure A.5). A large positive salinity anomaly returns close to station 150 at 1900 dbar.

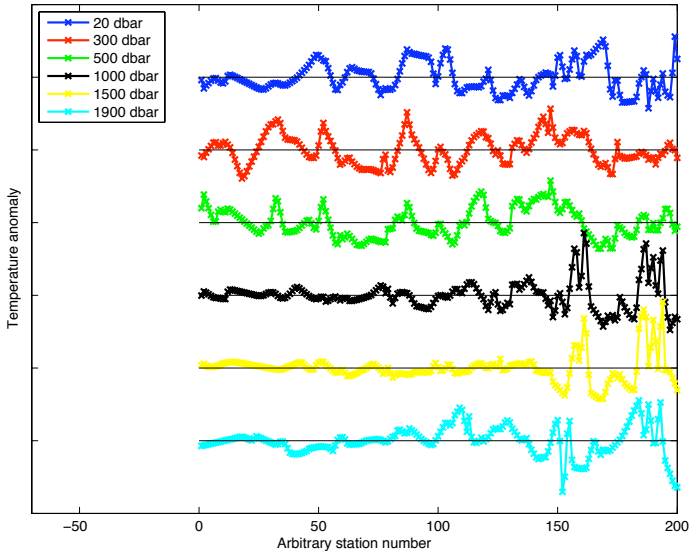

(a) Potential temperature

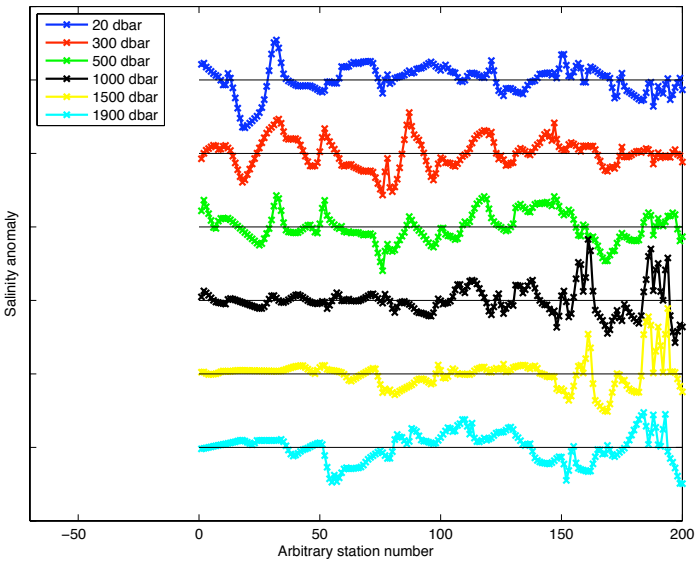

(b) Salinity

Figure A.3: Potential temperature and salinity residuals for various pressure levels normalised by their standard deviation derived from Argo profiles taken from 2° either side of 20°W. The x axis is arbitrary station number from south to north, with Station 1 located at 5°N and Station 200 at 40°N.

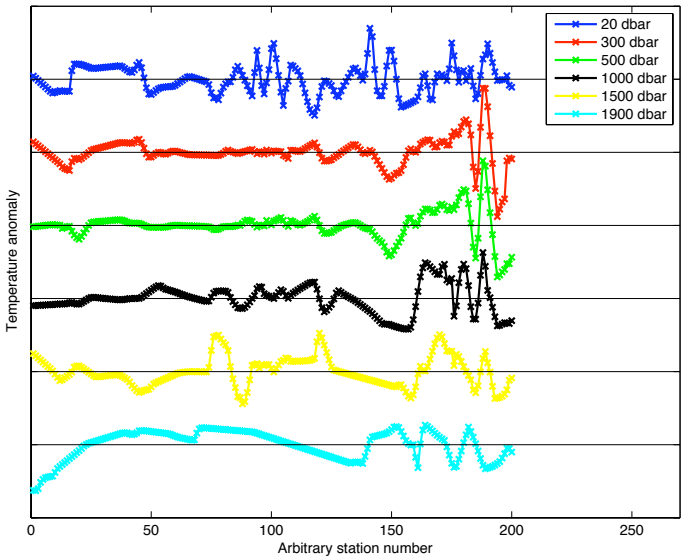

(a) Potential temperature

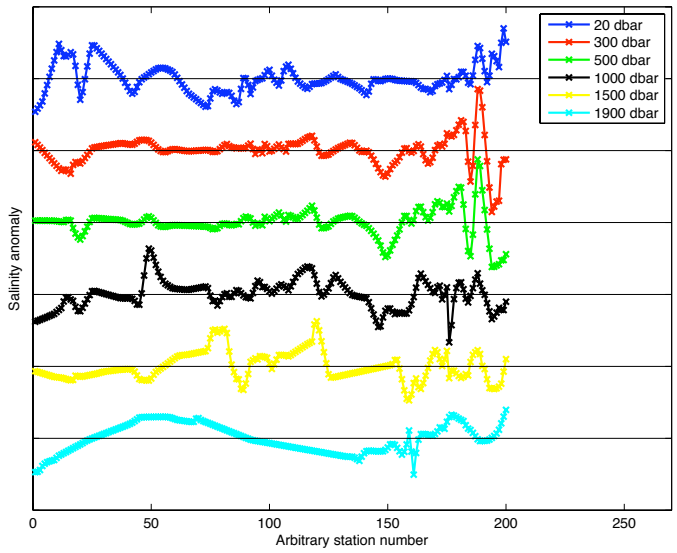

(b) Salinity

Figure A.4: Potential temperature and salinity residuals for various pressure levels normalised by their standard deviation derived from Argo profiles taken from 2° either side of 52°W. The x axis is arbitrary station number from south to north, with Station 1 located at 5°N and Station 200 at 41°N.

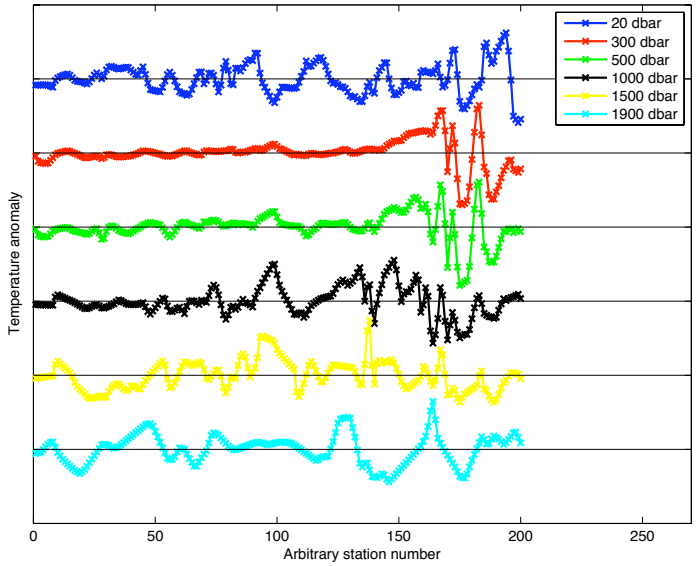

(a) Potential temperature

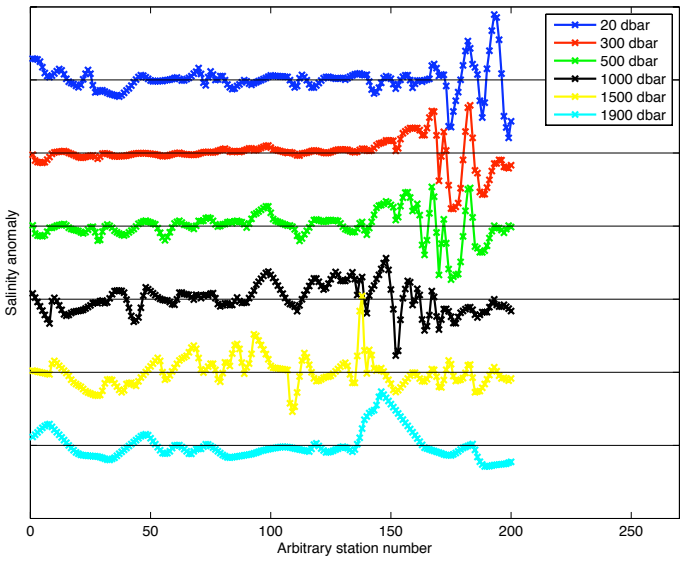

(b) Salinity

Figure A.5: Potential temperature and salinity residuals for various pressure levels normalised by their standard deviation derived from Argo profiles taken from 2° either side of 66°W. The x axis is arbitrary station number from south to north, with Station 1 located at 18°N and Station 200 at 39°N.

A.2.3 Reconciling the Differences

Despite the complexity in the vertical structure of the depth scales, it was decided to adopt a single meridional scale of 150 km. In most cases, the differences between realisations appeared to be caused either by the sampling strategy (e.g. all the cruise data being in a single month) or was an artefact of the mapping of the data onto the section. The alternative approach of mapping density directly was not tried in this study but would require a similar length scale study to obtain the appropriate decorrelation scales.

Bibliography

Alfutis, M. and P. Cornillon (2001): Annual and interannual changes in the North Atlantic STMW layer properties. *Journal of Physical Oceanography*, **31**(8), 2066–2086.

Álvarez, M., F. Pérez, D. Shoosmith and H. Bryden (2005): Unaccounted role of Mediterranean Water in the drawdown of anthropogenic carbon. *Journal of Geophysical Research Oceans*, **110**(C09S03), doi:10.1029/2004JC002633.

Andersen, O. and P. Knudsen (2009): DNSC08 mean sea surface and mean dynamic topography models. *Journal of Geophysical Research*, **114**(C11001), doi:10.1029/2008JC005179.

Anderson, D. and R. Corry (1985): Seasonal transport variations in the Florida Straits: A model study. *Journal of Physical Oceanography*, **15**, 773–786.

Anderson, D. and P. Killworth (1977): Spin-up of a stratified ocean with topography. *Deep Sea Research*, **24**, 709–732.

Antonov, J., R. Locarnini, T. Boyer and A. Mishonov (2006): *World Ocean Atlas 2005, Volume 2: Salinity*, US Government Printing Office.

Armi, L. and H. Stommel (1983): Four views of a portion of the North Atlantic subtropical gyre. *Journal of Physical Oceanography*, **13**, 828–857.

Armi, L. and W. Zenk (1984): Large lenses of highly saline Mediterreanean Water. *Journal of Physical Oceanography*, **14**, 1560–1575.

Atkinson, C., H. Bryden, J. Hirschi and T. Kanzow (2010): On the variability of Florida Straits and wind driven transports at 26N in the Atlantic. *Ocean Science Discussions*, **7**, 919–971.

AVISO Group (2008): AVISO and PODAAC User Handbook: IGDR and GDR Jason Products. Technical report, NASA/CNES.

Baringer, M. and J. Larsen (2001): Sixteen years of Florida Current transport at 27 degrees N. *Geophysical Research Letters*, **28**(16), 3179–3182.

Barnier, B. (1988): A numerical study into the influence of the Mid-Atlantic Ridge on non-linear first mode baroclinic Rossby Waves. *Journal of Physical Oceanography*, **18**(3), 417–433.

Berry, D. and E. Kent (2009): A new air-sea interaction gridded dataset from ICOADS with uncertainty estimates. *Bulletin of the American Meteorological Society*, **5**, 645–656.

Boehme, L. and U. Send (2005): Objective analyses of hydrographic data for referencing profiling float salinities in highly variable environments. *Deep Sea Research II*, **52**(3-4), 651–664.

Böning, C., R. Doscher and R. Budich (1991): Seasonal transport variation in the Western Subtropical North Atlantic: Experiments with an eddy-resolving model. *Journal of Physical Oceanography*, **9**, 1271–1289.

Bower, A. and H. Hunt (2000): Lagrangian observations of the Deep Western Boundary Current in the North Atlantic Ocean. Part II: The Gulf Stream Deep Western Boundary Current crossover. *Journal of Physical Oceanography*, **30**(5), 784–804.

Bower, A., M. Lozier, S. Gary and C. Böning (2009): Interior pathways of the North Atlantic meridional overturning circulation. *Nature*, **459**, 243–248.

Boyer, T., C. Stephens, J. Antonov, M. Conkright, R. Locarnini, T. O'Brien and H. Garcia (2002): *World Ocean Atlas 2001, Volume 2: Salinity.* NOAA Atlas NESDIS 50. US Government Printing Office.

Brennecke, W. (1911): Ozeanographischen Arbeiten der Deutschen Antarktischen Expedition. *Annalen der Hydrographie und Maritimen Meteorologie*, **39**, 642–647.

Bretherton, F., R. Davis and C. Fandry (1976): A technique for objective analysis and design of oceanographic experiments applied to MODE-73. *Deep Sea Research*, **23**, 559–582.

Bryan, K. (1969): A numerical method for the study of the circulation of the world ocean. *Journal of Computational Physics*, **4**(3), 347–376.

Bryden, H., L. Beal and L. Duncan (2005a): Structure and transport of the Agulhas Current and its temporal variability. *Journal of Oceanography*, **61**(3), 479–492.

Bryden, H., J. Candela and T. Kinder (1994): Exchange through the Strait of Gibraltar. *Progress in Oceanography*, **33**(3), 201–248.

Bryden, H. and S. Imawaki (2001): *Ocean Circulation and Climate*, Academic Press, pages 455–474.

Bryden, H., H. Longworth and S. Cunningham (2005b): Slowing of the Atlantic Meridional Overturning Circulation at 25 °N. *Nature*, **438**, 655–657.

Bryden, H., A. Mujahid, S. Cunningham and T. Kanzow (2009): Adjustment of the basin-scale circulation at 26N to variations in Gulf Stream, deep western boundary current and Ekman transports as observed by the Rapid array. *Ocean Science*, **5**, 421–433.

Buchan, A. (1895): Report on the scientific results of the voyage of H.M.S. Challenger during the years 1872-76, Physics and Chemistry. Technical report.
URL: *http://www.19thcenturyscience.org/HMSC/HMSC-INDEX/index-illustrated.htm*

Buchanan, J. (1884): Report on the scientific results of the voyage of H.M.S. Challenger during the years 1873-76, Physics and Chemistry. Technical report.
URL: *http://www.19thcenturyscience.org/HMSC/HMSC-INDEX/index-illustrated.htm*

Bunker, A. (1976): Computations of surface energy flux and annual air-sea interaction cycles of the North Atlantic Ocean. *Monthly Weather Review*, **104**, 1122–1140.

Burg, J. (1975): *Maximum entropy spectral analysis.* Ph.D. thesis, Department of Geophysics, Stanford University.

Carpenter, W. and J. Jeffreys (1870): Report on deep-sea researches carried on during the months of July, August and September 1870, in H.M.S. Porcupine. *Proceedings of the Royal Society (A)*, **19**, 146–221.

Chelton, D. and M. Freilich (2005): Scatterometer-based assessment of 10-m wind analyses from the Operational ECMWF and NCEP Numerical Weather Prediction Model. *Monthly Weather Review*, **133**(2), 409–429.

Chelton, D. and M. Schlax (1996): Global observations of oceanic Rossby Waves. *Science*, **272**(5259), 234–238.

Chu, P., L. Ivanov, O. Melnichencko and N. Wells (2007): On long baroclinic Rossby Waves in the tropical North Atlantic. *Journal of Geophysical Research Oceans*, **112**(C5), C05032.

Cox, M. (1984): A primitive equation 3-dimensional model of the ocean. GFDL Ocean Group Technical Report No. 1, Geophysical Fluid Dynamics Laboratory/NOAA, Princeton University.

Cunningham, S., T. Kanzow, D. Rayner, M. Baringer, W. Johns, J. Marotzke, H. Longworth, E. Grant, J. Hirschi, L. Beal, C. Meinen and H. Bryden (2007): Temporal variability of the Atlantic Meridional Overturning Circulation at 26°N. *Science*, **317**(5840), 935–938.

Curry, R. and M. McCartney (2001): Ocean gyre circulation changes associated with the North Atlantic Oscillation. *Journal of Physical Oceanography*, **31**, 3374–3400.

Davis, R., D. Webb, L. Regier and J. Dufour (1992): The Autonomous Lagrangian Circulation Explorer. *Journal of Atmospheric and Oceanic Technology*, **9**, 264–285.

Defant, A. (1941): Quantitative Untersuchungen zur Statik und Dynamik des Atlantischen Ozeans. Die absolute Topographie des physikalischen Meeresniveaus und der Druckflachen sowie die Wasserbewegungenim Raum des Atlantischen Ozeans. *In Wissenschaftliche Ergebnisse der Deutschen Atlantischen Expedition auf dem Forschungs - und Vermessungschiff Meteor, 1925-1927*, **6**, 191–260.

Deng, X., W. Featherstone, C. Hwang and P. Berry (2002): Estimation of contamination of ERS-2 and POSEIDON Satellite Radar Altimetry close to the coasts of Australia. *Marine Geodesy*, **25**(4), 249–271.

DiNezio, P. N., L. J. Gramer, W. E. Johns, C. S. Meinen and M. O. Baringer (2009): Observed Interannual Variability of the Florida Current: Wind Forcing and the North Atlantic Oscillation. *Journal of Physical Oceanography*, **39**(3), 721–736.

Eden, C. and T. Jung (2001): North Atlantic interdecadal variability: Oceanic response to the north atlantic oscillation (1865-1997). *Journal of Climate*, **14**(5), 676–691.

Eden, C. and J. Willebrand (2001): Mechanism of interannual to decadal variability of the North Atlantic Oscillation. *Journal of Climate*, **14**, 2266–2280.

Egbert, G., A. Bennett and M. Foreman (1994): TOPEX/POSEIDON tides estimated using a global inverse model. *Journal of Geophysical Research Oceans*, **99**, 24821–24852.

Ekman, V. (1905): On the influence of the Earth's rotation on ocean currents. *Arch. Math. Astron. Phys.*, **2**, 1–52.

Elipot, S., C. Hughes, M. Maqueda and R. Williams (2010): Meridional transport estimates from the RAPID-WAVE array.
URL: *http://www.liv.ac.uk/climate/research/elipot.pdf*

Emery, W. and R. Thomson (1998): *Data analysis methods in physical oceanography*. Pergamon.

Fanning, A., R. Greatbatch, A. DaSilva and S. Levitus (1994): Model-calculated seasonal tansport variations through the Florida Straits. *Journal of Physical Oceanography*, **24**(1), 30–45.

Fraile-Nuez, E. and A. Hernandez-Guerra (2006): Wind-driven circulation for the eastern North Atlantic Subtropical Gyre from Argo data. *Geophysical Research Letters*, **33**(L03601), doi:10.1029/2005GL025122.

Fratantoni, P. and R. Pickart (2003): Variability of the shelf break jet in the Middle Atlantic Bight: Internally or externally forced? *Journal of Geophysical Research Oceans*, **108**(C5), 3166.

Fuglister, F. (1960): *Atlantic Ocean Atlas of temperature and salinity profiles and data from the International Geophysical Year of 1957-1958*. Woods Hole Oceanographic Institution Atlas Series. Woods Hole Oceanographic Institution.

Ganachaud, A. (2003): Error budget of inverse box models: The North Atlantic. *Journal of Atmospheric and Oceanic Technology*, **20**(11), 1641–1655.

Gandin, L. (1963): *Objective analysis of meteorological field*. Gidrometeorologicheskoe Izdate'stvo, Leningrad.

Getzlaff, K. (2009): *Variability in the Southern Indian Ocean gyre circulation derived from Argo floats*. Ph.D. thesis, School of Ocean and Earth Science, University of Southampton. **URL:** *http://eprints.soton.ac.uk/69047/*

Gould, W. (1985): Physical oceanography of the Azores Front. *Progress in Oceanography*, **14**, 167–190.

Gouretski, V. and K. Koltermann (2004): WOCE Global Hydrographic Climatology, a Technical Report. Technical Report 35, Berichte des BSH.

Greatbatch, R., Y. Lu and B. DeYoung (1995): The variation of transport through the Straits of Florida: A barotropic model study. *Journal of Physical Oceanography*, **25**(11), 2726–2740.

Hadfield, R., N. Wells, S. Josey and J. Hirschi (2007): On the accuracy of North Atlantic temperature and heat storage fields from Argo. *Journal of Geophysical Research*, **112**, doi:10.1029/2006JC003825.

Haines, K., J. Blower, J.-P. Drecourt, C. Liu, A. Vivard, I. Astin and X. Zhou (2006): Salinity assimilation using S(T): Covariance relationships. *Monthly Weather Review*, **134**(759-771).

Halkin, D. and T. Rossby (1985): The structure and transport of the Gulf Stream at 73°W. *Journal of Physical Oceanography*, **15**, 1439–1452.

Hall, M. and H. Bryden (1982): Direct estimates and mechanisms of ocean heat transport. *Deep Sea Research*, **29**, 339–359.

Hernandez-Guerra, A., T. Joyce, E. Fraile-Nuez and P. Velez-Belchi (2010): Using Argo data to investigate the Meridional Overturning Circulation in the North Atlantic. *Deep Sea Research I*, **57**, 29–36.

Hirschi, J. and J. Marotzke (2007): Reconstructing the Meridional Overturning Circulation from boundary densities and the zonal wind stress. *Journal of Physical Oceanography*, **37**(3), 743–763.

Hirschi, J. J., P. Killworth, J. Blundell and D. Cromwell (2009): Sea surface height signals as indicators for ocean meridional mass transports. *Journal of Physical Oceanography*, **39**(3), 581–601.

Hogg, N. (1992): On the transport of the Gulf Stream between Cape Hatteras and the Grand Banks. *Deep Sea Research Part A*, **39**(7-8A), 1231–1246.

Hogg, N. and W. Johns (1995): Western boundary currents. *Reviews of Geophysics (supp.)*, **33**, 1311–1334.

Hogg, N., R. Pickart, R. Hendry and W. Smethie (1986): The Northern Recirculation Gyre of the Gulf Stream. *Deep Sea Research*, **33**, 1139–1165.

Hu, A., C. Rooth, R. Bleck and C. Deser (2002): NAO influence on sea ice extent in the Eurasian coastal region. *Geophysical Research Letters*, **29**(22), doi:10.1029/2001GL014293.

Hurrell, J. (1995): Decadal trends in the North Atlantic Oscillation: regional temperatures and precipitation. *Science*, **269**, 676–679.

Imawaki, S., H. Uchida, H. Ichikawa, M. Fukasawa, S. Umatani and the ASUKA Group (2001): Satellite altimeter monitoring of the Kuroshio transport south of Japan. *Geophysical Research Letters*, **28**(1), 17–20.

Iorga, M. and M. Lozier (1999): Signatures of Mediterranean outflow from a North Atlantic Climatology 1: Salinity and density fields. *Journal of Geophysical Research Oceans*, **104**(C11), 25985–26009.

IPCC (2007): *Contribution of Working Group I to the Fourth Assessment Report of the Intergovernmental Panel on Climate Change,* 2007. Cambridge University Press, Cambridge, United Kingdom and New York, USA.

Ivchenko, V., S. Danilov, D. Sidorenko, J. Schroter, M. Wenzel and D. Aleynik (2008): Steric height variability in the Northern Atlantic on seasonal and interannual scales. *Journal of Geophysical Research Oceans*, **113**(C11007), doi: 10.1029/2008JC004836.

Jacobsen, J. (1929): Contribution to the hydrography of the North Atlantic: The Dana Expedition 1921-22. *In The Danish Dana Expeditions 1920-22 in the North Atlantic and the Gulf of Panama*, **1**(3), 98pp.

Johns, W., T. Shay, J. Bane and D. Watts (1995): Gulf Stream structure, transport and Recirculation near 68-Degrees-W. *Journal of Geophysical Research Oceans*, **100**(C1), 817–838.

Josey, S., E. Kent and P. Taylor (1998): The Southampton Oceanography Centre ocean-atmosphere heat, momentum and freshwater flux atlas. Technical report, Southampton Oceanography Centre Report No. 6.

Joyce, T., J. Dunworth-Baker, R. Pickart, D. Torres and S. Waterman (2005): On the Deep Western Boundary Current south of Cape Cod. *Deep Sea Research II*, **52**, 615–625.

Joyce, T., R. Pickart and R. Millard (1999): Long term hydrographic changes at 52 and 66°W in the North Atlantic Subtropical Gyre and Caribbean. *Deep Sea Research II*, **46**, 245–278.

Kalnay, E., M. Kanamitsu, R. Kistler, W. Collins, D. Deaven, L. Gandin, M. Iredell, S. Saha and G. White (1996): The NCEP/NCAR 40-year reanalysis project. *Bulletin of the American Meteorological Society*, **77**(3), 437–471.

Kanzow, T., S. Cunningham, W. Johns, J. Hirschi, J. Marotzke, M. Baringer, C. Meinen, M. Chidichimo, C. Atkinson, L. Beal, H. Bryden and J. Collins (2010): Seasonal variability of the Atlantic Meridional Overturning Circulation at 26.5 degrees N. *Journal of Climate*, **23**(21), 5678–5698.

Käse, R. and W. Zenk (1996): *The Warmwatersphere of the North Atlantic Ocean*, Borntraeger, chapter 12, pages 365–396.

Kay, S. (1976): *Modern spectral estimation: theory and application*. Prentice Hall.

Kelly, K. (1988): Comment on 'Empirical orthogonal function analysis of advanced very high resolution radiometer surface temperature patterns in Santa Barbara Channel' by G.S.E Lagerloef and R.L. Berstein. *Journal of Geophysical Research*, **91**, 2633–2644.

Klein, B. and N. Hogg (1996): On the variability of 18 Degree Water formation as observed from moored instruments at 55 °W. *Deep Sea Research*, **43**(11-12), 1777–1806.

Köhl, A. (2005): Anomalies of meridional overturning: Mechanisms in the North Atlantic. *Journal of Physical Oceanography*, **35**, 1455–1472.

Kwon, Y. and S. Riser (2004): North Atlantic Subtropical Mode Water: A history of ocean-atmosphere interaction 1961-2000. *Geophysical Research Letters*, **31**(19), L19307.

Leadbetter, S., R. Williams, E. L. McDonagh and B. King (2007): A twenty year reversal in water mass trends in the Subtropical North Atlantic. *Geophysical Research Letters*, **34**(L12608), doi:10.1029/2007GL029957.

Leaman, K. and J. Harris (1990): On the average absolute transport of the Deep Western Boundary Currents east of Abaco Island, The Bahamas. *Journal of Physical Oceanography*, **20**(3), 467–475.

Leaman, K., E. Johns and T. Rossby (1989): The average distribution of volume transport and potential vorticity with temperature at 3 sections across the Gulf Stream. *Journal of Physical Oceanography*, **19**(1), 36–51.

Lebedev, K., H. Yoshinari, N. Maximenko and P. Hacker (2007): YoMaHa'07: Velocity data assessed from trajectories of Argo floats at parking level and at the sea surface. Technical Report 4(2), IPRC Technical Note.

LeBlond, P. and L. Mysak (1978): *Waves in the Ocean*. Elsevier.

Leetmaa, A., P. Niiler and H. Stommel (1977): Does the Sverdrup Relation account for the Mid-Atlantic circulation? *Journal of Marine Research*, **35**(1), 1–10.

Lin, X., D. Wu and Q. Li (2005): An amplification mechanism of intraseasonal long Rossby Wave in subtropical ocean. *Journal of Oceanography*, **61**(2), 369–378.

Locarnini, R., A. Mishonov, J. Antonov, T. Boyer and H. Garcia (2010): *World Ocean Atlas 2009, Volume 1: Temperature*, US Government Printing Office, chapter 1.

Locarnini, R., A. Mishonov, T. Boyer and H. Garcia (2006): *World Ocean Atlas 2005, Volume 1: Temperature*, US Government Printing Office, chapter 1.

Longworth, H. (2007): *Constraining variability of the Atlantic Meridional Overturning Circulation at* 25°N *from Historical Observations, 1980 to 2005.* Ph.D. thesis, School of Ocean and Earth Science, University of Southampton.
URL: *http://eprints.soton.ac.uk/48835/*

Lozier, M., M. McCartney and W. Owens (1995): The climatology of the North Atlantic. *Progress in Oceanography*, **36**, 1–44.

Lumpkin, R. and K. Speer (2003): Large-scale vertical and horizontal circulation in the North Atlantic Ocean. *Journal of Physical Oceanography*, **33**(9), 1902–1920.

Lumpkin, R. and K. Speer (2007): Global ocean meridional overturning. *Journal of Physical Oceanography*, **37**, 2550–2562.

Marple, S. (1987): *Digital spectral analysis.* Prentice-Hall.

Marshall, J., A. Andersson, N. Bates, W. Dewar, S. Doney, J. Edson, R. Ferrari, G. Forget, D. Fratantoni, M. Gregg and T. Joyce (2009): The CLIMODE Field Campaign observing the cycle of convection and restratification over the Gulf Stream. *Bulletin of the American Meteorological Society*, **90**(9), 1337–1350.

Marshall, J., H. Johnson and J. Goodman (2001): A study of the interaction of the North Atlantic Oscillation with ocean circulation. *Journal of Climate*, **14**(7), 1399–1421.

McCartney, M. and C. Mauritzen (2001): On the origin of the warm inflow to the Nordic Seas. *Progress in Oceanography*, **51**(1), 125–214.

McDonagh, E. L., P. McLeod, B. King, H. Bryden and S. Torres Valdes (2010): Circulation, heat and freshwater transport at 36N in the Atlantic. *Journal of Physical Oceanography, accepted.*

Mémery, L., M. Arhan, X. Alvarez-Salgado, M. M., H. Mercier, G. Castro and A. Rios (2000): The water masses along the western boundary of the south and equatorial Atlantic. *Progress in Oceanography*, **47**(1), 69–98.

Munk, W. (1950): On the wind-driven ocean circulation. *Journal of Meteorology*, **7**(2), 79–93.

Naeije, M., E. Schrama and R. Scharroo (2000): Radar Altimeter Database System (RADS): Towards a generic multi-satellite altimeter database system. USP-2 report 00-11, SRON/BCRS.

Niiler, P. and W. Richardson (1973): Seasonal variability of the Florida Current. *Journal of Marine Research*, **31**, 144–167.

Oka, E. (2005): Long-term sensor drift found in recovered Argo profiling floats. *Journal of Oceanography*, **61**(4), 775–781.

Oka, E. and K. Ando (2004): Stability of temperature and conductivity sensors of Argo profiling floats. *Journal of Oceanography*, **60**(2), 253–258.

Osychny, V. and P. Cornillon (2004): Properties of Rossby Waves in the North Atlantic estimated from satellite data. *Journal of Physical Oceanography*, **34**(1), 61–76.

Owens, W. and A. Wong (2009): An improved calibration method for the drift of the conductivity sensor on autonomous CTD profiling floats by θ-S climatology. *Deep Sea Research I: Oceanographic Research Papers*, **56**(3), 450–457.

Park, J., K. Kim, B. King and S. Riser (2005): An advanced method to estimate deep currents from profiling floats. *Journal of Atmospheric and Oceanic Technology*, **22**(8), 1294–1304.

Parker, C. (1971): Gulf Stream Rings in the Sargasso Sea. *Deep Sea Research*, **18**, 981–993.

Pena-Molino, B. and T. Joyce (2008): Variability in the slope water and its relation to the Gulf Stream path. *Geophysical Research Letters*, **35**(L03606), doi: 10.1029/2007GL032183.

Pickart, R. (1992): Water mass components of the North Atlantic deep western boundary current. *Deep Sea Research*, **39**(9), 1553–1572.

Pickart, R. and W. Smethie (1993): How does the Deep Western Boundary Current cross the Gulf Stream? *Journal of Physical Oceanography*, **23**(12), 2602–2616.

Pickart, R. and W. Smethie (1998): Temporal evolution of the deep western boundary current where it enters the sub-tropical domain. *Deep Sea Research I: Oceanographic Research Papers*, **45**(7), 1053–1083.

Press, W., S. Teukolsky, W. Wetterling and B. Flannery (1996): *Numerical Recipes in Fortran 90*, volume 2 of *Fortran Numerical Recipes*. Cambridge University Press.

Price, J., R. Weller and R. Schudlich (1987): Wind-driven ocean currents and Ekman Transport. *Science*, **238**, 1534–1538.

Prytherch, J. (2008): *Estimating subsurface currents from profiling floats: a new technique*. Master's thesis, School of Ocean and Earth Science, University of Southampton.

Rayner, D. and S. Cunningham (2005): Cruise report no 53: RRS Discovery Cruises D277/D278. Technical report, Southampton Oceanography Centre.

Reid, J. (1979): Contribution of the Mediterranean-Sea outflow to the Norwegian Greenland sea. *Deep Sea Research*, **26**(11), 1199–1223.

Reid, R. (1948): The equatorial currents of the eastern Pacific as maintained by the stress of the wind. *Journal of Marine Research*, **7**(2), 75–99.

Richardson, P. (1985): Average velocity and transport of the Gulf Stream. *Journal of Marine Research*, **43**, 83–111.

Richardson, P. (2008): On the history of meridional overturning circulation schematic diagrams. *Progress in Oceanography*, **76**, 466–486.

Richardson, P. and J. Knuass (1971): Gulf Stream and Western Boundary Undercurrent observations at Cape Hatteras. *Deep Sea Research*, **18**(11), 1089–1108.

Richardson, P., A. Strong and J. Knuass (1973): Gulf Stream eddies: Recent observations in the Western Sargasso Sea. *Journal of Physical Oceanography*, **3**(3), 297–301.

Richardson, W., W. J. Schmitz and P. Niiler (1969): The velocity structure of the Florida Current from the Straits of Florida to Cape Fear. *Deep Sea Research (supp.)*, **16**, 225–234.

Rintoul, S. and C. Wunsch (1991): Mass, heat, oxygen and nutrient fluxes and budgets in the North Atlantic Ocean. *Deep Sea Research*, **38**, S355–S357.

Rio, M. and F. Henrandez (2004): A mean dynamic topography computed over the world ocean from altimetry, in situ measurements, and a geoid model. *Journal of Geophysical Research Oceans*, **109**(C12032), doi:10.1029/2003JC002226.

Roemmich, D. (1980): Estimation of meridional heat flux in the North Atlantic by inverse methods. *Journal of Physical Oceanography*, **10**, 1972–1983.

Roemmich, D., O. Boebel, H. Freeland, B. King, P.-Y. Le Traon, R. Molinari, W. Owens, S. Riser, U. Send, K. Takeuchi and S. Wijffels (1998): On the design and implementation of Argo - an initial plan for a global array of profiling floats. Technical report, International CLIVAR Project Office ICPO Report No. 21.

Roemmich, D. and C. Wunsch (1984): Apparent changes in the climatic state of the deep North Atlantic Ocean. *Nature*, **307**(2), 447–450.

Roemmich, D. and C. Wunsch (1985): Two transatlantic sections: meridional circulation and heat flux in the subtropical North Atlantic Ocean. *Deep Sea Research*, **32**(6), 619–664.

Rogers, J. (1990): Patterns of low-frequency monthly sea level pressure variability (1899-1986) and associated wave cyclone frequencies. *Journal of Climate*, **3**, 1364–1379.

Rogers, J. (1997): North Atlantic storm track variability and its association to the North Atlantic Oscillation. *Journal of Climate*, **10**(7), 1635–1647.

Rossby, T., C. Flagg and K. Donohue (2005): Interannual variations in upper-ocean transport by the Gulf Stream and adjacent waters between New Jersey and Bermuda. *Journal of Marine Research*, **63**, 203–226.

Sato, O. T. and T. Rossby (1995): Seasonal and low frequency variations in dynamic height anomaly and transport of the Gulf Stream. *Deep Sea Research*, **42**(1), 149–164.

Schmitz, W. J. and W. Richardson (1968): On the Sources of the Florida Current. *Deep Sea Research (supp.)*, **38**, 379–409.

Schott, F., T. Lee and R. Zantopp (1988): Variability of Structure and Transport of the Florida Current in the period range of days to seasonal. *Journal of Physical Oceanography*, **18**(9), 1209–1230.

Semtner, A. (1974): A general circulation model for the world ocean. Technical report No.9, Department of Meteorology, University of California, Los Angeles.

Spall, M. (1996): Dynamics of the Gulf Stream Deep Western Boundary Current crossover: entrainment and recirculation. *Journal of Physical Oceanography*, **26**(10), 2152–2168.

Stephens, C., J. Antonov, T. Boyer, M. Conkright, R. Locarnini, T. O'Brien and H. Garcia (2002): *World Ocean Atlas 2001, Volume 1: Temperature*. NOAA Atlas NESDIS 49. US Government Printing Office.

Stommel, H. (1948): The westward intensification of wind-driven ocean currents. *Transactions of the American Geophysical Union*, **29**(2), 202–206.

Stommel, H. (1958): *The Gulf Stream*. Cambridge University Press.

Sturges, W. and B. Hong (1995): Wind forcing of the Atlantic thermocline along 32N at low frequencies. *Journal of Physical Oceanography*, **25**, 1706–1714.

Sverdrup, H. (1947): Wind-driven currents in a baroclinic ocean; with application to the equatorial currents of the eastern Pacific. *Proceedings of the National Academy of Sciences*, **33**(11), 318–326.

Sverdrup, H. U. (1942): *The Oceans: their physics, chemistry and general biology*. Prentice-Hall, New York.

Swallow, J. and L. Worthington (1961): Measurements of deep currents in the western North Atlantic. *Nature*, **179**, 1183–1184.

Talley, L. (2003): Shallow, intermediate and deep overturning components of the global heat budget. *Journal of Physical Oceanography*, **33**, 530–560.

Taylor, A. and J. Stephens (1998): The North Atlantic Oscillation and the latitude of the Gulf Stream. *Tellus*, **50A**, 134–142.

Thomas, M., A. de Boer, H. Johnson and D. Stephens (2010): Investigating the valdiity of the Sverdrup balance in determing the Meridional Overturning Circulation. In *Rapid Annual Science Meeting*.

Thomson, D. (1982): Spectrum estimation and harmonic analysis. *Proceedings of the IEEE*, **70**, 1055–1096.

Thorpe, S. (2006): *An Introduction to Ocean Turbulence*, Cambridge University Press, chapter 6.

Toole, J., R. Curry, T. Joyce, M. McCartney and B. Pena-Molino (2010): Transport of the North Atlantic Deep Western Boundary Currnet about 39N, 70W: 2004-2008. *Deep Sea Research, in press.*

Trenberth, K. and J. Caron (2001): Estimates of meridional atmosphere and ocean heat transports. *Journal of Climate*, **14**, 3433–3443.

Uppala, S., P. Kallberg, A. Simmons, U. Andrae, V. Bechtold, M. Fiorino and J. Gibson (2005): The ERA-40 Re-analysis. *Quarterly Journal of the Royal Meteorological Society*, **131**(612), 2961–3012.

Wang, L. and C. Koblinsky (1994): Influence of midocean ridges on Rossby Waves. *Journal of Geophysical Research Oceans*, **99**(C12), 25143–25153.

Warren, B. (1981): *Deep Circulation of the World Ocean*, MIT Press, chapter 3.

Webb, D., B. de Cuevas and A. Coward (1998): The first main run of the OCCAM global ocean model. Internal document No.34, Southampton Oceanography Centre.

Webster, F. (1961): A description of Gulf Stream meanders off Onslow Bay. *Deep Sea Research*, **8**, 130–143.

Wells, N., S. Josey and R. Hadfield (2009): Towards closure of regional heat budgets in the North Atlantic using Argo floats and surface flux datasets. *Ocean Science Discussions*, **6**, 95–128.

Willis, J. (2010): Can in situ floats and satellite altimeters detect long-term changes in Atlantic Ocean overturning? *Geophysical Research Letters*, **37**(L06602), doi:10.1029/2010GL042372.

Willis, J. and Fu (2008): Combining altimeter and subsurface float data to estimate the time-averaged circulation in the upper ocean. *Journal of Geophysical Research Oceans*, **113**(C12017), doi:10.1029/2008JC004841.

Willis, J., D. Roemmich and B. Cornuelle (2003): Combining altimetric height with broadscale profile data to estimate steric height, heat storage, subsurface temperature, and sea-surface temperature variability. *Journal of Geophysical Research*, **108**(C9), doi:10.1029/2002JC001755.

Wong, A., G. Johnson and W. Owens (2003): Delayed mode calibation of the autonomous CTD profiling float salinity data by $\theta-S$ climatology. *Journal of Atmospheric and Oceanic Technology*, **20**(2), 308–318.

Wong, A., R. Keeley and T. Carval (2009): *Argo Quality Control Manual Version 2.5*. Argo.

Wong, A. and B. King (2009): Report on Fourth Argo Delayed-Mode QC Workshop (DMQC-4). Technical report, CLS, Toulouse, France.

Worthington, L. (1959): The 18 degree water in the Sargasso Sea. *Deep Sea Research*, **5**, 297–305.

Worthington, L. (1976): On the North Atlantic Circulation. *Johns Hopkins Oceanographic Studies*, **6**, 1–110.

Wunsch, C. (1978): The North Atlantic Circulation west of 50 °W determined by inverse methods. *Reviews of Geophysics*, **16**(4), 583–620.

Wunsch, C. (2002): How did WOCE turn out? *WOCE Newsletter*, pages 4–9.

Wunsch, C. and D. Roemmich (1985): Is the North Atlantic in Sverdrup Balance? *Journal of Physical Oceanography*, **15**(12), 1876–1880.

Wüst, G. (1935): Schichtung und Zikulation des Atlantischen Ozeans, Die Stratosphäre des Atlantischen Ozeans. *Wiss. Erebn. Dt. Atlant. Exped. "Meteor"*, **6**, 109–288.